

# **Design and nondestructive imaging of a bioengineered vascular graft endothelium**

Bryce Matthew Whited

Dissertation submitted to the faculty of the Virginia Polytechnic Institute and State University in partial fulfillment of the requirements for the degree of

Doctor of Philosophy  
In  
Biomedical Engineering

M. Nichole Rylander (Chair)  
Yong Xu  
Aaron S. Goldstein  
Ge Wang  
Shay Soker  
Christopher G. Rylander

December 12<sup>th</sup>, 2012  
Blacksburg, VA

Keywords: Tissue engineering, vascular graft, nondestructive imaging, electrospinning, endothelial cells

Copyright 2012, Bryce Matthew Whited

# Design and nondestructive imaging of a bioengineered vascular graft endothelium

Bryce Matthew Whited

## **Abstract**

Cardiovascular disease is currently the leading cause of death in the U.S. that frequently requires bypass surgery using vascular grafts for treatment. Current limitations with fully synthetic grafts have led researchers to bioengineered alternatives that consist of a combination of vascular scaffolds and cells. A major challenge in creating a functional bioengineered vascular graft is development of a confluent endothelium on the lumen that is able to resist detachment under physiologic fluid flow. In addition, methodologies used to assess the growth and maturation of the endothelium in a noninvasive and dynamic manner are severely lacking. Therefore, the overall goal of this research is to advance the field of vascular tissue engineering by 1) creating methodologies to enhance EC adherence to a vascular graft and 2) development of a noninvasive and real-time imaging system capable of assessing the graft endothelium. To achieve these objectives, three separate studies were performed. In the first study, electrospun scaffold fiber diameter and alignment were systematically varied to determine their effect on endothelial cell (EC) morphology and adherence under fluid flow. ECs on uniaxially aligned nanofibers displayed elongated and aligned morphologies leading to higher adherence to the scaffolds under physiologic levels of fluid flow as compared to those on randomly oriented scaffolds. In the second study, a fiber optic based (FOB) imaging system was developed to image fluorescent ECs through a thick electrospun scaffold. Results demonstrated that the FOB imaging system was able to accurately visualize fluorescent ECs in a noninvasive manner through the thick and highly opaque scaffold. In the final study, the FOB imaging system was used to noninvasively quantify vascular graft endothelialization, EC detachment, and apoptosis through the vessel wall with greater imaging penetration depth than two-photon microscopy. Additionally, the FOB method was capable of continuously tracking EC migration and endothelialization of a bioengineered graft in a bioreactor. Overall, these results demonstrate that aligned scaffold topographies enhance EC adherence under fluid flow and the FOB imaging system is a promising tool to monitor endothelium development and response to fluid flow in a manner that has not previously been afforded using conventional imaging methods.

## **Author's Acknowledgements**

This work could not have been completed without the support and help from many fantastic colleagues. First, I would like to thank my advisor, Dr. Nichole Rylander, for obtaining funding for the research in addition to providing guidance and enthusiasm throughout my Ph.D. I would also like to thank my committee members who provided lab equipment and support for the research conducted. A special thanks goes to Dr. Matthias Hofmann who built the imaging system used for this research. I would also like to thank my fellow lab members and journal manuscript co-authors for great ideas and assistance with this research. Most of all, I would like to thank my wife, Elissa Whited, for her love, laughter and encouragement over the past 4 years, without which I would not have been able to complete the Ph.D. degree.

## **Attribution**

Several colleagues aided in the writing and research contained in this dissertation. A brief description of their contributions is included below.

*Marissa Nichole Rylander* is the primary advisor and committee chair for this research. She provided extensive guidance and comments for both the research and writing in this dissertation.

### **Chapter 3: A Fiber-Optic-Based Imaging System for Non-Destructive Assessment of Cell-Seeded Tissue-Engineered Scaffolds**

*Matthias C. Hofmann* built the imaging system used for the experiments and conducted the cell imaging, resolution and signal-to-noise ratio measurements. He also provided extensive writing and edits to the entire manuscript.

*Shay Soker* provided the GFP endothelial cells used for the cell imaging experiments and also provided extensive edits to the manuscript.

*Yong Xu* provided the lab space, equipment used for imaging, and also provided extensive edits to the manuscript.

### **Chapter 4: Dynamic, nondestructive imaging of a bioengineered vascular graft endothelium**

*Matthias C. Hofmann* built the imaging system used for the experiments.

*Shay Soker* provided the GFP endothelial cells used for the cell imaging experiments.

*Yong Xu* provided the lab space and equipment used for imaging.

### **Appendix A: Pre-osteoblast infiltration and differentiation in highly porous apatite-coated PLLA electrospun scaffolds**

*Jon Whitney* provided the Labview program used for quantifying cell infiltration for this study.

### **Appendix B: A Scanning-fiber-based Imaging Method for Tissue Engineering**

*Matthias C. Hofmann* conducted the imaging experiments for this study and was the primary writer for the manuscript.

*Yong Xu* was the primary investigator for this manuscript.

### **Appendix C: Real time imaging and characterization of bioengineered blood vessels within a bioreactor using OCT**

*Abhijit A. Gurjarpadhye* conducted the imaging for this study and was the primary writer for the manuscript.

*Christopher G. Rylander* was the primary investigator for this manuscript.

## Table of Contents

<b>Chapter 1 - Introduction</b> .....	<b>1</b>
<b>1.1 Overview</b> .....	<b>1</b>
<b>1.2 Clinical Significance</b> .....	<b>2</b>
<b>1.3 Vascular tissue engineering</b> .....	<b>3</b>
<b>1.4 Native arteries</b> .....	<b>4</b>
<b>1.5 Scaffolds for bioengineered vascular grafts</b> .....	<b>7</b>
<b>1.6 Electrospinning of bioengineered vascular grafts</b> .....	<b>10</b>
<b>1.7 Scaffold endothelialization techniques</b> .....	<b>12</b>
1.7.1 <i>In vitro</i> endothelialization .....	12
1.7.2 <i>In situ</i> endothelialization .....	13
<b>1.8 Fluid flow preconditioning of vascular grafts <i>in vitro</i></b> .....	<b>15</b>
<b>1.9 Methods to evaluate vascular grafts <i>in vitro</i></b> .....	<b>17</b>
1.9.1 Destructive methods.....	17
1.9.2 Nondestructive imaging methods.....	18
1.9.3 Confocal Microscopy .....	18
1.9.4 Two-Photon Microscopy.....	20
1.9.5 Optical Coherence Tomography .....	22
1.9.6 Bioluminescence imaging .....	23
1.9.7 Nondestructive imaging of vascular graft endothelialization .....	24
<b>1.10 Objective and Experimental Plan</b> .....	<b>26</b>
1.10.1 Chapter 1: The influence of nanofiber scaffold topography on endothelial cell morphology, alignment, and adhesion in response to fluid flow.....	26
1.10.2 Chapter 2: A Fiber-Optic-Based (FOB) Imaging System for Non-Destructive Assessment of Cell-Seeded Tissue-Engineered Scaffolds.....	27
1.10.3 Chapter 3: Dynamic, nondestructive imaging of a bioengineered vascular graft endothelium.....	27
<b>1.11 Material in Appendices</b> .....	<b>28</b>
<b>Chapter 2: The influence of nanofiber scaffold topography on endothelial cell morphology, alignment, and adhesion in response to fluid flow</b> .....	<b>29</b>
<b>2.1 Abstract</b> .....	<b>29</b>
<b>2.2 Introduction</b> .....	<b>30</b>
<b>2.3 Materials and Methods</b> .....	<b>32</b>
2.3.1 Scaffold Fabrication .....	32
2.3.2 Scaffold Characterization .....	32
2.3.3 Cell Culture and Cell Seeding.....	33
2.3.4 Cell Morphology and Alignment .....	33
2.3.5 Immunofluorescence Staining.....	34
2.3.6 Cell Adhesion Assays.....	34
2.3.7 Statistical Analysis .....	35
<b>2.4 Results</b> .....	<b>35</b>
2.4.1 Scaffold Topography.....	35
2.4.2 Cell Morphology and Alignment .....	38

2.4.3	Structural and cell-substrate protein expression and organization .....	40
2.4.4	EC Adhesion Under Fluid Flow .....	44
<b>2.5</b>	<b>Discussion .....</b>	<b>46</b>
<b>2.6</b>	<b>Conclusion .....</b>	<b>49</b>
<b>2.7</b>	<b>Acknowledgements .....</b>	<b>50</b>
<b>Chapter 3: A Fiber-Optic-Based Imaging System for Non-Destructive Assessment of</b>		
<b>Cell-Seeded Tissue-Engineered Scaffolds .....</b>		
<b>3.1</b>	<b>Abstract .....</b>	<b>53</b>
<b>3.2</b>	<b>Introduction.....</b>	<b>53</b>
<b>3.3</b>	<b>Materials and Methods.....</b>	<b>54</b>
3.3.1	Design Principle .....	54
3.3.2	Scaffold Fabrication .....	55
3.3.3	MIC Integration.....	55
3.3.4	Cell Culture and Scaffold Seeding .....	55
3.3.5	Excitation Light Delivery.....	55
3.3.6	Spectral measurements and signal-to-noise ratio (SNR).....	56
3.3.7	Confocal Laser Scanning Microscopy .....	56
3.3.8	Statistical Analysis and Mapping of Results.....	56
<b>3.4</b>	<b>Results.....</b>	<b>56</b>
3.4.1	Bioreactor .....	56
3.4.2	Procedure for Fiber Scanning and Fluorescence Mapping .....	56
3.4.3	Control Image Capture .....	57
3.4.4	Imaging Results and Image Analysis .....	57
3.4.5	Comparison with Confocal Microscopy .....	58
3.4.6	Mapping Resolution .....	58
3.4.7	Spectral Emission Response and Signal-to-Noise Ratio (SNR) .....	59
3.4.8	Dynamic Assessment of Cell Growth and Distribution .....	59
<b>3.5</b>	<b>Discussion .....</b>	<b>60</b>
<b>3.6</b>	<b>Conclusion .....</b>	<b>62</b>
<b>3.7</b>	<b>Acknowledgements .....</b>	<b>62</b>
<b>Chapter 4: Dynamic, nondestructive imaging of a bioengineered vascular graft</b>		
<b>endothelium .....</b>		
<b>4.1</b>	<b>Abstract .....</b>	<b>64</b>
<b>4.2</b>	<b>Introduction.....</b>	<b>65</b>
<b>4.3</b>	<b>Materials and Methods.....</b>	<b>67</b>
4.3.1	Vascular scaffold fabrication and micro-imaging channel (MIC) integration .....	67
4.3.2	Scaffold morphology.....	70
4.3.3	Cell culture and scaffold seeding .....	70
4.3.4	Excitation light delivery and FOB image acquisition .....	70
4.3.5	Nondestructive quantification of EC lumen coverage .....	71
4.3.6	Nondestructive quantification of EC detachment .....	72
4.3.7	Nondestructive quantification of EC apoptosis.....	72
4.3.8	Nondestructive quantification of graft endothelialization in response to scaffold fiber diameter.....	73
4.3.9	Two-photon microscopy .....	73
4.3.10	Statistical analysis .....	74

<b>4.4 Results and Discussion .....</b>	<b>74</b>
4.4.1 Nondestructive quantification of EC lumen coverage .....	74
4.4.2 Nondestructive quantification of EC detachment .....	76
4.4.3 Nondestructive quantification of EC apoptosis.....	78
4.4.4 Nondestructive quantification of graft endothelialization in response to scaffold fiber diameter.....	79
4.4.5 Two photon microscopy and comparison to conventional imaging methods.....	82
<b>4.5 Conclusion .....</b>	<b>87</b>
<b>4.6 Acknowledgements .....</b>	<b>87</b>
<b>Conclusions and Future Work .....</b>	<b>88</b>
<b>5.1 Conclusions.....</b>	<b>88</b>
<b>5.2 Future Work.....</b>	<b>89</b>
5.2.1 Incorporation of an aligned nanofiber lumen in a bioengineered vascular graft .....	90
5.2.2 Integration of FOB imaging into a fluid flow bioreactor .....	91
5.2.3 FOB imaging system to measure scaffold wall maturation .....	94
5.2.4 Conclusions .....	98
<b>Appendix A: Pre-osteoblast infiltration and differentiation in highly porous apatite-coated PLLA electrospun scaffolds .....</b>	<b>100</b>
<b>A.1 Abstract .....</b>	<b>101</b>
<b>A.2 Introduction .....</b>	<b>101</b>
<b>A.3 Materials and Methods .....</b>	<b>102</b>
A.3.1 Materials.....	102
A.3.2 Composite Scaffold Fabrication.....	102
A.3.3 PEO Fiber Removal .....	102
A.3.4 Scaffold Surface Mineralization .....	102
A.3.5 Scaffold Characterization.....	102
A.3.6 Mechanical Testing of Scaffolds.....	103
A.3.7 MC3T3-E1 Cell Culture and Cell Seeding .....	103
A.3.8 Assessment of Cell Infiltration .....	103
A.3.9 Cell Number .....	103
A.3.10 Alkaline Phosphatase Activity .....	103
A.3.11 Osteocalcin Content .....	103
A.3.12 Calcium Content .....	104
A.3.13 Statistical Analysis.....	104
<b>A.4 Results.....</b>	<b>104</b>
A.4.1 Scaffold Fabrication and Characterization.....	104
A.4.2 Mechanical Testing.....	104
A.4.3 Cell Infiltration into Mineralized PLLA scaffolds.....	104
A.4.4 Cell Number .....	105
A.4.5 ALP Activity .....	106
A.4.6 Osteocalcin Content .....	106
A.4.7 Calcium Content .....	106
<b>A.5 Discussion .....</b>	<b>107</b>
<b>A.6 Conclusion .....</b>	<b>110</b>
<b>A.7 Acknowledgements .....</b>	<b>110</b>

<b>Appendix B: A Scanning-fiber-based Imaging Method for Tissue Engineering .....</b>	<b>112</b>
<b>B.1 Abstract .....</b>	<b>114</b>
<b>B.2 Introduction .....</b>	<b>114</b>
<b>B.3 Materials and Methods .....</b>	<b>115</b>
B.3.1 Experimental Design .....	116
B.3.2 Scaffold Fabrication .....	116
B.3.3 MIC Integration .....	116
B.3.4 Excitation Light Delivery .....	116
<b>B.3.5 Incorporation of Fluorescent Sources .....</b>	<b>116</b>
B.3.6 Measuring the Scaffold Optical Properties .....	116
B.3.7 Imaging System .....	117
B.3.8 Fiber-Scanning and Fluorescence-Mapping Procedure .....	117
B.3.9 Excitation Spot Characterization .....	118
B.3.10 Spectrum Measurement .....	118
<b>B.3.11 Cell Culture Protocol .....</b>	<b>118</b>
<b>B.4 Results .....</b>	<b>118</b>
B.4.1 Excitation Spot Characterization .....	118
B.4.2 Phantom Optical Properties .....	119
B.4.3 Phantom Imaging Results .....	119
B.4.4 Imaging Resolution Analysis .....	120
B.4.5 Signal Vs. Noise .....	121
B.4.6 Endothelial Cell Imaging .....	122
<b>B.5 Discussion .....</b>	<b>122</b>
<b>B.6 Conclusion .....</b>	<b>123</b>
<b>B.7 Acknowledgements .....</b>	<b>123</b>
<b>Appendix C: Real time imaging and characterization of bioengineered blood vessels within a bioreactor using OCT .....</b>	<b>125</b>
<b>C.1 Abstract .....</b>	<b>125</b>
<b>C.2 Introduction .....</b>	<b>126</b>
<b>C.3 Materials and Methods .....</b>	<b>128</b>
C.3.1 Tissue-Engineered Blood Vessels .....	128
C.3.2 Bioreactor Design .....	129
C.3.3 Swept-Source OCT .....	130
C.3.4 OCT Image Acquisition .....	130
C.3.5 Resolution .....	131
C.3.6 Scaffold Thickness .....	131
C.3.7 Scattering Coefficient .....	132
<b>C.4 Results .....</b>	<b>133</b>
C.4.1 OCT Imaging .....	133
C.4.2 Scaffold Thickness .....	134
C.4.3 Scaffold Scattering Coefficient .....	134
C.4.4 Cell migration .....	135
<b>C.5 Discussion .....</b>	<b>136</b>
<b>C.6 Acknowledgements .....</b>	<b>138</b>
<b>References .....</b>	<b>140</b>

## List of Figures

	Page
<b>Figure 1.1</b> Depiction of a common tissue engineering approach to repair/replace diseased/damaged blood vessels. 1) Vascular cells are taken from the patient in need of treatment, 2) cells are expanded in vitro, 3) cells are seeded into three-dimensional scaffolds, 4) the scaffolds are then incubated under physiologic conditions (i.e. fluid flow) to allow cells to proliferate, differentiate and produce extracellular matrices, and finally, 5) the cell-seeded vascular grafts are implanted into the patient to provide a functional replacement.....	4
<b>Figure 1.2</b> Anatomy of an artery. ( <a href="http://en.wikipedia.org/wiki/File:Endothelial_cell.jpg">http://en.wikipedia.org/wiki/File:Endothelial_cell.jpg</a> - Creative Commons - GNU Free Documentation License.....)	6
<b>Figure 1.3</b> Forces acting on an EC under pulsatile blood flow.....	7
<b>Figure 1.4</b> Image of a fluid flow bioreactor used at the Wake Forest Institute for Regenerative Medicine to precondition bioengineered vascular grafts.....	16
<b>Figure 1.5</b> Bovine aortic ECs elongate and align with flow under physiologic levels of hemodynamic shear stress in vitro, but retain a polygonal morphology under no or low shear stress. (Reprinted with permission from The American Medical Association from [21])......	16
<b>Figure 1.6</b> Atomic force microscopy images of bovine aortic endothelial cells a) cultured under no flow, and b) after exposure to 12- dynes/cm <sup>2</sup> shear stress in steady laminar flow. Flattened profiles of aligned ECs give rise to smaller spatial variations of shear stress and stress gradients at the EC surface. Arrow indicates direction of flow. Gray micrometer scale in b indicates height of cell surface referenced to lowest point (at junctions between cells). (Reprinted from Davies et al. 1995 – Reprint permission not required for this use [19]).....	17
<b>Figure 1.7</b> A) A standard fluorescence microscope utilizes an optical path that provides uniform illumination of the sample. Fluorescence from the focal plane, as well as from out-of-focus planes, reaches the detector. B) A confocal microscope provides focused illumination of a point within a sample, which is then imaged through a pinhole in front of the detector. Most out-of-focus light from other imaging planes does not reach the detector because of the pinhole. C) A typical fluorescence microscope image of a thick human bladder section, and D) the same section as imaged by a confocal microscope (both 60X). (Reprinted with permission from Mary Ann Liebert, Inc. [72]).....	20
<b>Figure 1.8</b> A simplified Jablonski fluorescence diagram showing a) 1, b) 2 and c) 3 photon excitation. Once the excited state has been reached, the fluorescence emission (i.e. 460 nm) is exactly the same for all three modalities of excitation. (Creative commons attribution license – Reprinted from [74]).....	21
<b>Figure 1.9</b> Diagram of fluorescence excitation volume in a 3D sample (yellow), where a) fluorescence (green) is generated throughout the excitation (blue) light path in confocal	

microscopy, and b) fluorescence (green) is confined to a small volume with two-photon excitation in the excitation path (red). (Reprinted with permission from Mary Ann Liebert, Inc. [72]).....21

**Figure 1.10** Options for imaging a bioengineered vascular graft endothelium. A) Image of a pulsatile bioreactor used to precondition a bioengineered electrospun vascular scaffold. B) Schematic representation of imaging the endothelium of a bioengineered vascular scaffold in a pulsatile bioreactor using microscope-based imaging techniques such as confocal/multi-photon microscopy. Blue arrows represent excitation light and green arrows represent fluorescence emission. Microscope-based techniques have a limited capacity to image the endothelium of a vessel due to the highly scattering nature of the vascular scaffold wall and limited working distance of the objectives. C) Schematic representation of imaging the endothelium using endo-microscopy techniques. To accomplish this, an endo-microscope must be inserted into the lumen of the vessel, which may cause abrasion on the lumen surface, introduce sterility concerns, and occlude fluid flow. D) Schematic representation of the FOB imaging system integrated into a pulsatile bioreactor. Excitation light is guided into the scaffold wall and fluorescence emission is collected from outside the bioreactor. Using this technique, it is possible to image the endothelium through the thick vessel wall in a dynamic manner without disturbing the vessel during preconditioning in a bioreactor.....25

**Figure 2.1:** Representative SEM images of electrospun PCL/collagen scaffolds. A 3 x 3 scaffold property matrix was formed by systematically varying fiber diameter (100-nm, 300-nm, and 1200-nm) and degree of fiber alignment (random, semi-aligned, and fully-aligned).....37

**Figure 2.2:** Fiber diameters for scaffolds electrospun from various polymer solution concentrations (5%, 10%, and 15% w/v) and fabrication parameters with varying degrees of fiber alignment. An “\*” indicates a statistical difference from the 5% (w/v) group, and a “#” indicates statistical difference from the 10% (w/v) group ( $p < 0.05$ ) ( $n = 250$  fibers for each group).....38

**Figure 2.3:** Representative images of Calcein AM stained ECs on electrospun scaffolds. Cells displayed a more cuboidal morphology on random nanofiber scaffolds as compared to scaffolds with defined fiber alignment, where cells were elongated and aligned with the direction of fiber orientation. Cells on 1200-nm scaffolds displayed a rounded morphology, no preferred orientation, and appear to have infiltrated into the scaffold (white arrows).....39

**Figure 2.4:** Quantitative analysis of a) cell area, b) aspect ratio, and c) length of long axis of Calcein AM stained ECs on electrospun scaffolds. Cell area was significantly greater on 100-nm and 300-nm scaffolds when compared to 1200-nm scaffolds. Cell aspect ratio and length of long axis were significantly increased on aligned 100-nm and 300-nm scaffolds as compared to random and 1200-nm scaffolds. An “\*” indicates a statistical difference from the 1200-nm scaffold group, and a “#” indicates statistical difference from the random scaffold group ( $p < 0.05$ ) ( $n \geq 10$  images per group).....40

**Figure 2.5:** Representative fluorescent images of cytoskeletal F-actin organization for ECs on scaffolds with varying fiber diameters and orientations. F-actin (red) was organized at the periphery of cells on random 100-nm and 300-nm scaffolds, but was located throughout the cells

in thick bundles parallel to nanofiber orientation on 100-nm and 300-nm fully-aligned scaffolds.....41

**Figure 2.6:** Representative fluorescent images of VE-cadherin (green), showing that the cell-cell adhesion protein was strongly expressed at the periphery of cells where cell-cell contact occurred on 100-nm and 300-nm scaffolds. VE-cadherin was not, however, expressed in cells on 1200-nm scaffolds.....42

**Figure 2.7:** Staining for vinculin revealed that cells on aligned scaffolds displayed a considerably higher level of vinculin than cells on random scaffolds.....43

**Figure 2.8:** The total area covered by vinculin in each image was quantified using image analysis. The results show that cells on aligned scaffolds expressed 2-3 times the amount of vinculin than cells on random scaffolds. A “#” indicates a statistical difference from the random scaffold group ( $p < 0.05$ ) ( $n = 9$  images per group).....44

**Figure 2.9:** Percentage of cells that remained adherent to the 100-nm and 300-nm scaffolds during 60 min of a) 20 dyne/cm<sup>2</sup> and b) 40 dyne/cm<sup>2</sup> continuous hydrodynamic shear stress. c) Percentage of cells adherent to the scaffolds after 60 min of continuous hydrodynamic shear stress. Values marked with the same letter are not significantly different ( $p < 0.05$ ).....46

**Supplemental Figure 2.1:** Normalized histograms of fiber angle for scaffolds electrospun with varying fiber diameters and fiber orientations (grey bars) ( $n = 250$  fibers for each group). Degree of fiber alignment systematically increased with an increase in mandrel rotation rate. Curves represent the wrapped normal distribution (Equation 2.1).....51

**Supplemental Figure 2.2:** Normalized histograms of cell angle for ECs seeded on scaffolds with varying fiber diameters and fiber orientations (grey bars) ( $n \geq 10$  images per group). Cell alignment systematically increased with fiber alignment on 100-nm and 300-nm scaffolds. Curves represent the wrapped normal distribution (Equation 2.1).....51

**Figure 3.1.** Experiment design: (A) A thin and flexible MIC is embedded into the scaffold wall allowing controlled local delivery of fluorescence excitation light. By scanning the excitation light across the lumen of the vessel and capturing the cell-emitted fluorescence responses from the exterior surface, the original cell distribution of the luminal surface can be reconstructed via signal processing. All imaging hardware for FOB imaging is denoted “imaging system” in the figure and is located outside of the exterior surface. (B) For quantitative comparison with the control images, a planar scaffold was fabricated to allow direct-line-of-sight access to the luminal surface using a conventional optical microscope (control image camera). Both before and after unwrapping, the imaging system for FOB imaging remains the same. The control image camera captured images of cell distribution using conventional, direct-line-of-sight, fluorescence microscopy. Such images were denoted as control images and used to validate our FOB imaging method. The model scaffold in (B) can be regarded as the result of “unwrapping” the tubular scaffold in (A).....54

**Figure 3.2.** Vascular scaffold model fabrication and bioreactor design: (A) PDLA was electrospun into a 300  $\mu\text{m}$  thick scaffold mat. (B) A MIC was embedded into PDLA by heat sintering two 3 cm  $\times$  2 cm rectangular scaffold mats together. (C) Through heat sintering, a planar scaffold was fabricated with a luminal surface simulating blood vessel lumen and an exterior surface where diffused photons are collected to form fluorescence-mapped images using the FOB imaging method. (D) Microscope image of a fiber micro-mirror inserted into a MIC. The blue arrow indicates the direction of the excitation light. Through movement of the fiber, the excitation light was selectively delivered into the scaffold. (E) A photograph of the custom bioreactor designed to house the scaffold while simultaneously enabling external access to the MIC.....55

**Figure 3.3.** Image mapping procedure and scanning system: (A) Illustration of a 2D pixel grid on the luminal surface of the scaffold containing a GFP-labeled EC (represented by the green oval) and the excitation spot (represented by the blue circle). (B) A schematic drawing illustrating the principle of the FOB imaging method. Through fiber micro-mirror delivery via a MIC, a micron-scale excitation spot is generated on the luminal surface. Within any given excitation spot, a different amount of green fluorescence is generated depending on whether a GFP-labeled EC overlaps with the local excitation spot. An EM-CCD camera is used as a sensitive detector to capture the portion of fluorescence light that transmits through the scaffold to the exterior surface. The amount of fluorescence detected by the EM-CCD camera is then assigned to the corresponding imaging pixel. After sequentially scanning the excitation spot over all imaging pixels within the ROI followed by assigning fluorescence intensity measured by EM-CCD camera to each imaging pixel, a fluorescence-mapped image is obtained that depicts the distribution of GFP-labeled ECs on the luminal surface. Note that all imaging instruments required for this process are located on the side of the exterior surface. (C) An illustration of fluorescence-mapped image that corresponds to the configuration shown in (A). (D) Photograph of the imaging system showing the bioreactor on the heated platform. The micro-mirror position inside the MIC is controlled by the scanning stages in the figure.....57

**Figure 3.4.** Fluorescence mapping results and comparison: (A.1-3) Control images obtained through direct line-of-sight image acquisition. (B.1-3) An ROI measuring 300 x 300  $\mu\text{m}$  above the MIC was selected on each scaffold and fluorescence-mapped image was obtained using the fiber-scanning algorithm. The fluorescence signals were captured on the exterior surface of the scaffold to demonstrate the capability of mapping cells through  $\sim$ 500  $\mu\text{m}$  thick PDLA scaffolds. A total of 75 image pairs (25 pairs per scaffold) were obtained and evaluated for this experiment.....58

**Figure 3.5.** Statistical validation of the fluorescence-mapping method: Mean absolute error (MAE) and root mean squared error (RMSE) histograms for comparison between pairs of fluorescence-mapped and control images for each scaffold. The mean  $\pm$  std. dev. of the MAE and RMSE between the three scaffolds was 5.83%  $\pm$  0.88% and 10.26%  $\pm$  1.14%, respectively.....59

**Figure 3.6.** Imaging depth comparison to CLSM: (A) Diagram of direct-line-of-sight CLSM-image to visualize “actual” GFP EC distribution. (B) The sample is then reversed to image the luminal surface through the electrospun PDLA scaffold with the CLSM. Three scaffolds with thickness  $d = 100, 230,$  and  $460 \mu\text{m}$  were used. (C) Direct-line-of-sight CLSM-image of GFP

ECs on the luminal surface. (D) ECs on the luminal surface when imaged through the thickness of a 100  $\mu\text{m}$ -thick scaffold. Individual ECs could not be identified when imaging through (E) 230  $\mu\text{m}$  and (F) 460  $\mu\text{m}$  thick scaffolds. The FOB method could, however, detect ECs on the luminal surface through a  $\sim 500$   $\mu\text{m}$  thick scaffold (H). Comparison with a direct-line-of-sight image (G) confirms the accuracy of the fluorescence-mapped image.....59

**Figure 3.7.** Image Mapping Resolution: FWHM of the excitation spot on the luminal surface for micro-mirror launching angles  $\theta = -45^\circ$  to  $+45^\circ$  (mean  $\pm$  std. dev. of  $n = 5$  trials). This plot indicates that the resolution of the system is best when the excitation light is launched directly towards the luminal surface ( $\theta = 0$ ) and deteriorates by  $\sim 1/2$  when the fiber micro-mirror is rotated to  $\theta = \pm 45^\circ$ .....60

**Figure 3.8.** Signal-to-noise ratio characterization: (A) Comparison of the spectral emission response signal of the ECs and background noise caused by scaffold autofluorescence from 450-750 nm. Comparison of the cell response to the background noise gives the signal-to-noise ratio (SNR). (B) Representative EM-CCD camera images taken from the exterior surface when (1) the excitation spot was on a cell or (2) placed on an area void of cells (scaffold autofluorescence) 60

**Figure 3.9.** Dynamic imaging: (A) to (D): Four fluorescence-mapped images were taken in the same ROI at a 30 minute interval to demonstrate the dynamic imaging capability. The red lines serve as a visual aid to track the relative movement of cells between successive images. Images in (E) to (G), which are taken at a 30 minute time interval in another ROI, suggest that we can use our imaging method to monitor cell cytokinesis.....61

**Figure 4.1.** Vascular scaffold fabrication, MIC integration, and FOB imaging method. A-C) Illustration of the layer-by-layer electrospinning fabrication technique used to embed MICs within the wall of the vascular scaffold to facilitate imaging. D,E) Images of a vascular scaffold with MICs embedded within the wall. F) Image of a vascular scaffold sectioned lengthwise to validate endothelium imaging (half-vessel scaffold). G) Image of the fiber optic micro-mirror inserted within an MIC. Light is directed at a  $90^\circ$  angle relative to the fiber optic to allow excitation of ECs on the lumen of the vascular graft. H) Photograph of the vascular scaffold during an imaging experiment with the fiber-guided excitation light on. I) Schematic of the fiber optic imaging method used to create FOB images through the scaffold wall. Excitation laser light was guided to the fiber optic micro-mirror to excite GFP-ECs on the lumen of the vascular scaffold. The excitation spot created by the laser light was incrementally rastered on the lumen surface and GFP fluorescence was measured through the scaffold wall using an EMCCD detector. Linking the excitation spot to the GFP fluorescence values enabled fluorescence mapping to create a fiber optic-based (FOB) image. A corresponding control image was obtained by direct-line-of-sight control camera to validate the imaging method on half-vessel scaffolds.69

**Figure 4.2.** Quantification of GFP-EC proliferation and lumen coverage. A) A vascular scaffold sectioned lengthwise was seeded with GFP-ECs and 3 separate 1 mm x 250  $\mu\text{m}$  areas of the graft were imaged daily until the lumen reached confluency at Day 4 (representative images shown). B) Images were analyzed to quantify the amount of cell coverage on the vascular lumen ( $n = 3$  images/time point). The results show that there is good agreement between amount of cell coverage for the FOB images, obtained through scaffold wall, and direct-line-of-sight control

images at each time point. Data are presented as mean  $\pm$  one standard deviation and values marked with the same letter are not significantly different ( $p < 0.05$ ).....75

**Figure 4.3.** Quantification of GFP-EC detachment and apoptosis. A) Representative images of a near confluent endothelium that was subjected to a dilute concentration (1  $\mu\text{M}$ ) of trypsin EDTA to induce cell detachment from the lumen. An area of 250  $\mu\text{m}$  x 250  $\mu\text{m}$  was continuously scanned to image GFP-EC detachment from the lumen over time. B) Extent of GFP-EC detachment from the lumen was quantified by analyzing the area of cell coverage from the fluorescent images ( $n = 3$  images/time point). The FOB and corresponding control images had equivalent amounts of cell coverage at each time point. C) A near confluent endothelium was exposed to varying concentrations of camptothecin to induce GFP-EC apoptosis. A red fluorescent annexin-V conjugate was then added to visualize the extent of EC apoptosis on the vascular scaffold lumen. Three different 500  $\mu\text{m}$  x 250  $\mu\text{m}$  areas were imaged to detect both GFP and red fluorescent annexin-V (apoptotic cells) on each scaffold for each condition. Results showed that varying levels of GFP-EC apoptosis could be noninvasively imaged and B) the fraction of apoptotic cells could be quantified through the scaffold wall using the FOB imaging method ( $n = 3$  images/condition). Data are presented as mean  $\pm$  one standard deviation and values marked with the same letter are not significantly different ( $p < 0.05$ ).....77

**Figure 4.4.** Effect of lumen topography on graft endothelialization. Full-vessel grafts with varied electrospun fiber diameters were fabricated to study the effect of lumen fiber diameter and varying topography on EC proliferation and endothelialization. A) Mean fiber diameters of 3.32  $\mu\text{m}$ , 1.00  $\mu\text{m}$  and 0.36  $\mu\text{m}$  were electrospun by varying electrospinning parameters as shown in Table 4.1. After cell seeding, three separate 500  $\mu\text{m}$  x 250  $\mu\text{m}$  areas of each vascular graft were imaged daily to assess luminal coverage and EC growth over time. Representative FOB images of GFP-EC coverage are shown for each scaffold fiber diameter at B) Day 0, C) Day 3, and D) Day 7. E) After FOB imaging on Day 7, scaffolds were removed from the bioreactor, sectioned in half, stained for F-actin (red) and cell nuclei (blue), and imaged using a conventional fluorescence microscope to provide a comparison to the FOB images at Day 7. F) A total of  $n = 3$  scaffolds for each fiber diameter were imaged, and  $n = 3$  areas (500  $\mu\text{m}$  x 250  $\mu\text{m}$ ) for each scaffold, yielding a total of  $n = 9$  images for each scaffold group every day. The FOB imaging method provided a noninvasive, accurate measurement of vascular graft lumen endothelialization over time. Data are presented as mean  $\pm$  one standard deviation.....81

**Figure 4.5.** Imaging penetration depth: comparison of FOB imaging method to Two-photon microscopy. A) EC-seeded half-vessel scaffolds were imaged with a two-photon microscope in direct-line-of-sight to the lumen. B) Representative image of GFP-ECs in direct-line-of-sight to the vessel lumen. C) The two-photon microscope was then used to image GFP-ECs on the lumen through the wall of vascular scaffolds of varying thicknesses ( $t = 95, 230$  and  $520 \mu\text{m}$ ). Images of GFP-ECs on the vessel lumen through a D) 95  $\mu\text{m}$  and E) 230  $\mu\text{m}$  thick scaffold. Although cells were visible through the 95  $\mu\text{m}$  thick scaffold, GFP-ECs could not be resolved through the 230 and 520  $\mu\text{m}$  thick scaffolds. The FOB imaging method, however, was capable of resolving individual GFP-ECs through a  $\sim 510 \mu\text{m}$  thick scaffold wall (G) and the overall cell distribution of the same region of interest matched very closely to the direct-line-of-sight fluorescence image (F).....84

<b>Supplemental Figure 4.1.</b> Dynamic imaging of graft endothelialization. A full-vessel scaffold was seeded with GFP-ECs and a 500 $\mu\text{m}$ x 250 $\mu\text{m}$ section of the lumen was sequentially imaged at 2 hr intervals for a 3-day period. The figure shows the scaffold lumen at A) 2 hr, B) 10 hr, C) 20 hr, D) 30 hr, E) 40 hr, F) 50 hr, G) 60 hr, H) 70 hr, and I) 80 hr after seeding and J) corresponding plot of GFP-EC coverage over time. In this Figure, GFP-ECs are actively migrating along the surface of the lumen and each image can be analyzed to provide a real-time assessment of EC coverage.....	86
<b>Figure 5.1</b> A negatively charged mandrel with insulating gaps will alter the electric field between the positively charged polymer jet and negatively charged mandrel to produce axially aligned nanofibers for the vascular graft lumen. Once the aligned lumen has been established, the mandrel will be pushed together to remove the insulating gap to produce randomly oriented nanofibers for the vessel wall (adapted from zhu et al. [167]).....	91
<b>Figure 5.2</b> Design and fabrication of an imaging-compatible fluid flow bioreactor. A) Schematic of the fluid flow bioreactor, B) construction of the bioreactor, C) Image of the constructed fluid flow bioreactor, D) bioreactor connected to the media reservoir and centrifugal pump, E) FOB image of GFP-ECs on the lumen after seeding, and F) OCT cross-section image of the vessel wall.....	93
<b>Figure 5.3</b> Schematic representation of imaging both the endothelium and maturation of the vessel wall using the FOB imaging system.....	95
<b>Figure 5.4</b> Fluorescence images of GFP-ECs, mKate-ECs and Collagen Type 1.....	96
<b>Figure 5.5</b> Total fluorescence measured by the FOB imaging system as a result of varied concentration of collagen type I in PCL vessels.....	97
<b>Figure 5.6</b> Histological sections of PCL vessels seeded with CH310T1/2 cells over time reveal that A) cell-mediated collagen deposition (blue) increases over time in conjunction with B) cell colonization of the vessel wall towards the lumen of the vessel.....	98
<b>Figure A.1.</b> Offsetting syringes resulted in a graded fiber sheet ranging from 0 to 100 mass % PLLA along the mandrel length as determined by PEO mass loss (n = 3 scaffolds per mandrel location).....	104
<b>Figure A.2.</b> Representative SEM images of (A) a pure PLLA scaffold (0% PEO), (B) pure mineralized PLLA scaffold (0% PEO), (C) 3:1 blend of PEO:PLLA before PEO fiber removal (75% PEO), (D) 3:1 blend of PEO:PLLA after PEO fiber removal and mineralization, (E) close-up SEM image of apatite surface on a PLLA fiber, and (F) EDXS confirms that the biomimetic apatite contains calcium and phosphorous at a Ca/P ratio of approximately 1.4. Inset bars represent 20 $\mu\text{m}$ in images A, B, C, D and 2 $\mu\text{m}$ in image E.....	105
<b>Figure A.3.</b> (A) Porosity and (B) pore diameter of mineralized PLLA scaffolds with varying initial PEO content. A “*” indicates a significant difference (p < 0.05) between groups (n = 5).....	106

**Figure A.4.** (A) Elastic modulus and (B) ultimate tensile strength for pure PLLA and mineralized PLLA scaffolds with varying PEO content (% mass loss) after PEO fiber removal. A “\*” indicates a significant difference ( $p < 0.05$ ) between groups ( $n = 5$ ).....106

**Figure A.5.** Polarized bright field images of the DAPI-stained cell-seeded scaffold cross-sections (left) were used to demarcate the scaffold edges and measure scaffold thickness. The corresponding fluorescent image (center) was used to evaluate cell infiltration depth into the mineralized PLLA scaffolds. The image to the right is a combined bright field polarized and fluorescent image overlay. Scale bar = 400  $\mu\text{m}$ .....107

**Figure A.6.** Representative fluorescent images of mineralized PLLA cell-seeded scaffolds with 0 – 75% initial PEO content at days 1, 10, and 21 showing increased cell infiltration with both increased time and initial PEO content. Scale bar = 400  $\mu\text{m}$ .....107

**Figure A.7.** Cell infiltration into mineralized PLLA scaffolds as a function of PEO content at (A) 1, (B) 10, and (C) 21 days after cell seeding. Cell number and cell migration distance from the edge of the scaffold are displayed as % total cells that are in measured regions through the thickness of the scaffold. A “\*” indicates a significant difference ( $p < 0.05$ ) between groups. 108

**Figure A.8.** Average cell infiltration depth into the mineralized PLLA scaffolds at 1, 10, and 21 days after cell seeding. Cell infiltration was found to increase as a function of both time and PEO content. A “\*” indicates a significant difference ( $p < 0.05$ ) between groups.....108

**Figure A.9.** Amount of cells per scaffold construct or TCPS control sample at days 3, 7, 14 and 21 after cell seeding as determined by the PicoGreen assay kit ( $n = 4$ ).  $3 \times 10^4$  cells were seeded onto the scaffolds or TCPS control wells at day 0. A “\*” indicates a significant difference ( $p < 0.05$ ) from the TCPS control.....108

**Figure A.10.** Intracellular ALP activity of scaffold/cell constructs or TCPS control samples over time ( $n = 4$ ). Results are normalized per cell as determined by the DNA assay. A “\*” indicates a significant difference ( $p < 0.05$ ) from the TCPS control; a “#” indicates a significant difference ( $p < 0.05$ ) from the mineralized PLLA scaffold.....109

**Figure A.11.** Secreted OCN protein from scaffold/cell constructs or TCPS control samples ( $n = 4$ ). Results are normalized per cell as determined by the DNA assay. A “\*” indicates a significant difference ( $p < 0.05$ ) from the TCPS control; a “#” indicates a significant difference ( $p < 0.05$ ) from the pure PLLA scaffold.....109

**Figure A.12.** Total calcium content for each cell/scaffold construct and TCPS control sample ( $n=4$ ). Calcium levels of mineralized scaffolds without cells (control scaffolds) were assayed at each time point and subtracted from the background ( $n=4$ ). Results are normalized per cell as determined by the DNA assay. A “\*” indicates a significant difference ( $p < 0.05$ ) from the TCPS control; a “#” indicates a significant difference ( $p < 0.05$ ) from the pure PLLA scaffold.....109

**Figure B.1** (a) A pulsatile flow bioreactor for in vitro incubation of bioengineered carotid artery scaffolds developed by one of the authors. Bioreactors often require a hermetically enclosed chamber that is incompatible with standard optical imaging methods. (b) A vascular scaffold embedded with a MIC for non-destructive, scanning-fiber-based imaging. (c & d) depict design of a planar optical phantom that imitates a tubular carotid artery scaffold graft for future in vitro (no neck skin) or in vivo (with neck skin) studies. As shown in (c), a MIC is directly embedded within the wall of the scaffold. Through the MIC, we can deliver highly localized excitation light to a ROI on scaffold lumen and generate a fluorescent signal. Part of the fluorescent signal is captured by an external detector for image reconstruction. (d) An optical phantom model was designed to mimic the experimental configuration in (c). The phantom is designed such that we can verify our fluorescence mapping results using the direct-line-of-sight images obtained by a control camera.....115

**Figure B.2** (a) A thinly woven PDLLA scaffold mat was electrospun and then cut into 3 cm × 2cm rectangular mats. The optically turbid scaffold architecture is shown in the scanning electron microscope image. The PDLLA phantom was fabricated by placing MICs between two scaffold mats and heat sintering them together. (b) A microscope image of a fiber micro-mirror inserted into a MIC. (c) The 90° reflection of the excitation light at the polished fiber tip is used for local delivery and scanning of excitation light within the ROI.....116

**Figure B.3** (a) Schematic and (b) photograph of the scanning-fiber-based imaging system. (c) Diagram of the imaging procedure. Using the fiber mirror, we can locally deliver excitation light to a point within the ROI (excitation spot). The excitation spot is moved within the ROI by rotating and translating the fiber mirror. By scanning the excitation spot according to a pixel grid, we can map the intensity responses into a digital grid to obtain fluorophore distribution.....117

**Figure B.4** Excitation spot characterization. The plot lines are in 1 degree increments and the error is shown at every 4th point to prevent overcrowding. Error bars represent ± one std. dev. centered at the mean of the 5 trials. (a) The FWHM of the excitation spot intensity profile on scaffold lumen is shown with respect to launching angle  $\theta$ . The insets depict the actual excitation spot profile with  $|\theta|$  equal to 0°, 20°, and 40°, respectively. (b) The intensity of the profile (summed pixels) shows a diminishing excitation spot strength at increasing angles  $|\theta|$ . (c) The excitation spot profile center position on the R axis is shown to behave nearly linearly with respect to  $|\theta|$ . From the results, we find that  $R(\theta) = 3.33 \times \theta$  based on a linear fit (red).....119

**Figure B.5.** (a) The scattering coefficient ( $\mu_s$ ) of PDLLA is found to be roughly double that of porcine skin over the 450 nm – 700 nm range. The results also show that scattering events ( $\mu_s$ ) dominate over absorption events ( $\mu_a$ ) by more than two orders of magnitude. (b) The MFP for PDLLA and for porcine skin.....119

**Figure B.6** Results of fluorescence mapping. (a.1) A schematic showing how we obtain a direct-line-of-sight control image of the scaffold lumen. (a.2) A example of a control image. (b.1) Configuration for fluorescence mapping through the 0.5 mm thick PDLLA scaffold. (b.2) Mapping result through 0.5 mm PDLLA. (b.3) The spatial distribution of fluorescence signals on the bottom surface of the phantom, as captured by the EMCCD camera. The fluorescent signals were generated by the same ROI in (b.2) under illumination by the external excitation light. (c.1)

Configuration for fluorescence mapping through the same 0.5 mm thick PDLLA scaffold and a piece of 3 mm thick porcine skin. (c.2) Results of fluorescence mapping through 0.5 mm PDLLA + 3 mm skin. (c.3) Fluorescence image on the bottom surface of the porcine skin as captured by the EMCCD camera. We notice further “blurring” of the fluorescent signal in c.3, yet the result of fluorescence mapping in c.2 remain the same as the result in b.2., which was obtained using only PDLLA scaffold.....120

**Figure B.7** The resolution of the scanning-fiber-based-method is modeled by convolving the control image with a variable Gaussian PSF creating a theoretical mapped image. By finding the least mean square error of the difference between the theoretical and experimental results, we find the approximate resolution of the system. The result suggests that the imaging resolution is between 20 – 30  $\mu\text{m}$  at an imaging depth corresponding to 0.5 mm PDLLA plus 3 mm porcine skin.....121

**Figure B.8** Spectral responses of microsphere signals as well as autofluorescence noises. The microsphere signal was obtained by centering the excitation spot on a single microsphere placed on the phantom lumen. The autofluorescence noise was obtained by moving the excitation spot to a location on the lumen that was free of microspheres. The SNR is calculated as the microsphere signal divided by the autofluorescence. a) The SNR through 0.5 mm PDLLA is around 4 between 510 – 545 nm. b) The SNR through 0.5 mm PDLLA + 3 mm porcine skin is around 2 between 510 – 545 nm.....121

**Figure B.9** (a) Control image showing the actual EC distribution on scaffold lumen. (b) A fluorescence mapped image of EC distribution that corresponds to the image in (a). Comparison between the control image and the fluorescence mapped image indicates that our method can “see” through a 0.5 mm thick PDLLA scaffold with single-cell-level resolution. (c) SNR measurement for a single GFP-labeled EC on scaffold lumen. The SNR is around 2 for a 0.5 mm thick PDLLA phantom.....122

**Figure B.10** A schematic showing the potential sources for imaging system noise.....123

**Figure C.1.** Schematic of the PCL-Collagen scaffold mounted within the bioreactor. The FEP tube provides mechanical support for the scaffold and ensures its patency.....129

**Figure C.2.** (a) Schematic of the rotating blood vessel bioreactor for free-space OCT imaging. (b) Bioreactor is rotated at high angular resolution using a stepper motor.....130

**Figure C.3.** Schematic representation of TEBV wall thickness measurement protocol.....132

**Figure C.4.** Representative cross-sectional co-registered OCT images of the TEBV at different time-points, using co-registered free-space and catheter-based images. Scale bars = 1 mm...133

**Figure C.5.** Average wall thickness of the TEBV at different time points. (a) Mean wall thickness of individual cellularized TEBVs (n=10) increase over time, whereas (b) mean wall thickness (n=3) of non-cellularized/control scaffolds remain constant over time.\* =p<0.05 when compared with D1.....134

**Figure C.6.** Average scattering coefficient of the TEBVs increases over time, suggesting that the TEBVs become more scattering (n=3) in the first three weeks of culture after cell-seeding. \*=p<0.01 when compared with D1.....135

**Figure C.7.** (a) DAPI stained histology images of the tissue-engineered blood vessels. Faded background shows the scaffold structure while the red dots indicate the location of cell nuclei. (Scale bar = 250  $\mu$ m). (b) Plot shows average wall thickness of the control TEBV using the DAPI-stained histology images. \*=p<0.01 when compared with D4.....136

## List of Tables

	<b>Page</b>
<b>Table 2.1:</b> PCL/collagen electrospinning parameters for scaffolds with varying fiber diameter	36
<b>Table 2.2:</b> Electrospun fiber diameter, fiber angular standard deviation, and cell angular standard deviation for scaffolds fabricated with varying solution concentrations, electrospinning parameters, and mandrel rotation rates. ....	38
<b>Table 4.1</b> Electrospinning parameters for scaffold fabrication .....	70
<b>Table A1.</b> Fiber diameter, pore diameter, porosity and scaffold thickness for mineralized PLLA scaffolds with varying initial PEO content.....	105

## List of Equations

	<b>Page</b>
<b>Equation 2.1</b> Wrapped normal distribution.....	33
<b>Equation 2.2</b> Mean resultant length.....	33
<b>Equation 2.3</b> Mean angle.....	33
<b>Equation 2.4</b> Angular standard deviation .....	33
<b>Equation 3.1</b> Mean absolute error .....	56
<b>Equation 3.2</b> Root mean squared error.....	56
<b>Equation A.1</b> Scaffold apparent density.....	103
<b>Equation A.2</b> Scaffold porosity.....	103

## **Chapter 1 - Introduction**

### **1.1 Overview**

Cardiovascular disease is currently the leading cause of death in the United States with atherosclerosis being one of the most severe forms of this disease. Vascular bypass surgery is a common treatment for atherosclerosis and accounts for nearly 500,000 bypass graft implantations in the United States each year [1]. Current options for bypass surgeries include the use of autologous and synthetic grafts, but these grafts have a high rate of thrombosis and failure when used for small diameter (< 6 mm diameter) bypass procedures. Consequently, the need for small diameter grafts to perform bypass procedures, such as for the coronary arteries, is ever increasing. The clinical need for vascular conduits that remain open (i.e. patent) in small diameter bypass surgeries has led researchers to create bioengineered equivalents typically consisting of scaffolds that support vascular cells. A critical design requirement for bioengineered vascular grafts is the formation of an uninterrupted monolayer of endothelial cells (ECs), i.e. endothelium, on the lumen of the graft to provide a barrier between circulating blood and the vessel wall to prevent thrombosis, regulate vessel homeostasis, and platelet adhesion, among others [2]. Graft failure due to inadequate EC coverage, function and integrity under physiological fluid flow is a common limitation with bioengineered vessels and has led researchers to incorporate scaffold designs to enhance EC attachment, growth and integrity under physiological fluid flow both in vitro (during preconditioning) and in vivo (after implantation). Additionally, methods to better assess EC growth, function and response to fluid flow with high spatial and temporal resolution are severely lacking. Therefore, the goals of this research project are to design scaffolds capable of enhancing endothelium adhesion under fluid flow and to develop a noninvasive imaging method to monitor the endothelium of a bioengineered vascular graft. Sections 1.2 – 1.8 below provide an overview of the clinical relevance, vascular tissue engineering, scaffold design, and endothelialization methods. Section 1.9 provides an outline of current imaging methods and the difficulty of monitoring a bioengineered vascular graft endothelium using these methods. Finally, in Section 1.10, the objective and the experimental plan of the research is outlined.

## 1.2 Clinical Significance

Cardiovascular disease is currently the number one cause of death in the United States, accounting for approximately 25% of deaths in 2009 [1]. Atherosclerosis, or hardening of the arteries, is one of the most common forms of cardiovascular disease and causes narrowing of the vessel. Atherosclerosis occurs when cholesterol, fat and other substances build up in the vessel walls to form plaques, which can eventually restrict or completely block blood flow [3]. Current methods used to treat restricted or blocked arteries include angioplasty, vascular stenting or bypass grafting. Angioplasty is a technique in which arteries are mechanically widened using a balloon catheter. This treatment involves passing a collapsed balloon on the tip of a vascular guide wire to the site of narrowed artery and then inflating the balloon, usually with an injected liquid, thereby flattening the atherosclerotic lesion to improve blood flow. Often times, a vascular stent will be placed at the time of ballooning in order to ensure that the vessel remains patent. Vascular stents are typically composed of metal or absorbable polymer and some elute drugs, such as Avastin, to minimize lesion recurrence. However, vascular restenosis at the site of angioplasty and stenting is a common occurrence, with 25 – 50% of patient's experiencing this phenomenon within 6 months that requires additional vascular intervention [4]. Another treatment option is bypass grafting, wherein an autologous, allogeneic, xenogeneic, or synthetic vessel is used to reroute blood flow around the affected and often occluded vessel. Autologous grafts are usually taken from the patient's own saphenous vein or internal mammary artery. Although autografts are the gold standard for bypass grafting, they have a 35% failure rate and 5-30% of patients have no suitable vein or artery available due to prior vascular disease or other complications [5]. Allografts, taken from a human cadaver or living donor, and xenografts, harvested from a non-human species, have also been used as vascular grafts, however, have limited use due to lack of supply and disease transmission [6]. Synthetic grafts are typically fabricated from expanded polytetrafluoroethylene (ePTFE) or Dacron and have had relatively high success rates for bypass of large arteries (> 6 mm diameter) [7, 8]. However, synthetic grafts smaller than 6 mm in diameter, such as those required for coronary and infrapopliteal bypass, are prone to clogging due to thrombosis [9]. With current limitations in autologous and synthetic bypass grafts, an ideal alternative is development of a bioengineered small diameter vascular graft that is non-thrombogenic and exhibits long-term patency after implantation.

### **1.3 Vascular tissue engineering**

Vascular tissue engineering, or bioengineering, has emerged as a promising strategy to treat patients suffering from vascular tissue loss or damage as a result of disease or trauma [10]. Bioengineering of vascular grafts typically involves the expansion of the patient's own cells from a small biopsy, or circulating progenitor cells in the blood, followed by culturing of the cells in a 3D scaffold to form a functional replacement vessel (Figure 1.1). This approach is promising because it has several advantages of current treatment options, which include the use of vessels from autologous, allogeneic and xenogeneic sources. Autologous grafts are taken directly from a healthy site of the patient and transplanted into the wound/defect site. This method is very effective; however limitations include donor site morbidity, risk of infection from a secondary surgical site, and limited supply of tissue available for harvesting [6]. Allogeneic vascular grafts are harvested from a human cadaver or living donor and are transplanted into the patient needing the graft. Limitations of this method include bacterial or viral infection from donor to patient and an overall lack of organ donors [6]. Xenogeneic vessels are harvested from a non-human species, and while there is greater supply of these organs/tissues compared to allogeneic sources, immune response and graft rejection is often a limiting factor for this treatment option [11]. Tissue engineering is therefore a potential alternative to the aforementioned approaches because, by using scaffolding materials wherein supply is virtually unlimited in combination with the patient's own cells, this approach has the advantages of autografts without the problems associated with adequate supply, tissue rejection or infection that may arise from allogeneic or xenogeneic sources.

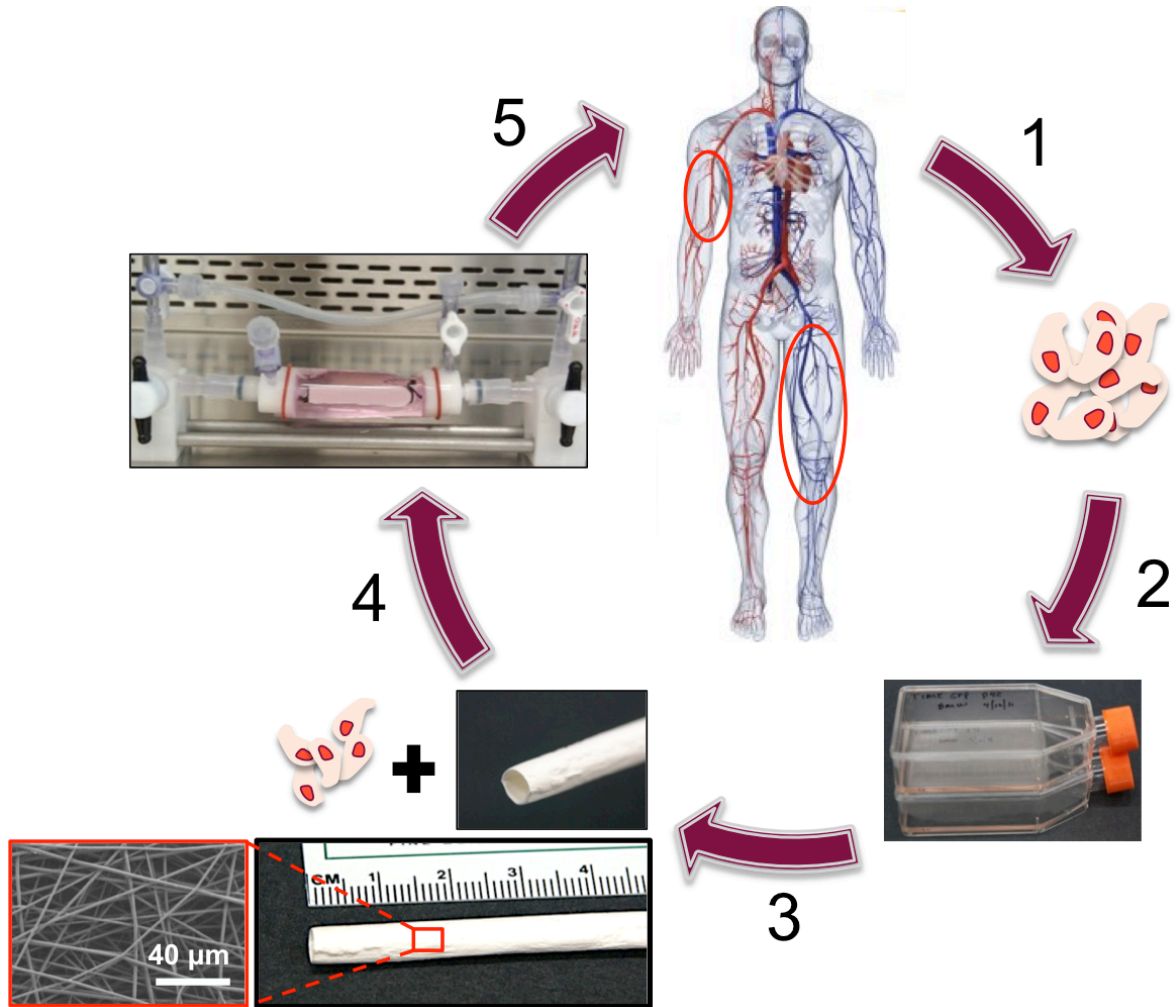


**Figure 1.1** Depiction of a common tissue engineering approach to repair/replace diseased/damaged blood vessels. 1) Vascular cells are taken from the patient in need of treatment, 2) cells are expanded *in vitro*, 3) cells are seeded into three-dimensional scaffolds, 4) the scaffolds are then incubated under physiologic conditions (i.e. fluid flow) to allow cells to proliferate, differentiate and produce extracellular matrices, and finally, 5) the cell-seeded vascular grafts are implanted into the patient to provide a functional replacement.

#### 1.4 Native arteries

Bioengineered vascular grafts must be able to withstand physiological forces associated with blood flow and must remain patent while the scaffold undergoes cell-mediated remodeling *in vivo*. Therefore, bioengineered vascular grafts should be designed to mimic those of native arteries, both in terms of structure and function. While the overall components and structure of native arteries are hierarchical, very complex, and not feasible to replicate in every aspect, many functional aspects can be replicated from a bioengineering standpoint. Some important

considerations in designing a bioengineered vascular graft include mechanical properties (suture retention, burst pressure, modulus) and maintenance of an uninterrupted endothelium under physiological flow.

Figure 1.2 shows the anatomical structure of an artery, which has three main layers. The strong outer layer, called the adventitia, consists of longitudinally arranged fibroblasts in a predominately collagen matrix. The media is the middle, and thickest layer, which consists primarily of smooth muscle cells (SMCs) that are concentrically arranged and, with autonomic control, regulate the diameter of the artery. The media also contains varying amounts of type I and type III collagen fibers, with lesser amounts of other proteins and proteoglycans secreted by the SMCs. The inner layer, or intima, consists of an uninterrupted monolayer of ECs to form an endothelium and a small amount of sub-endothelial connective tissue called the basement membrane, which is composed primarily of collagen type IV and laminin. ECs play an important role in regulation of vascular tone, tissue homeostasis, and regulation of nutrient transport across the vessel wall [12]. In addition, the endothelium forms a selectively permeable, antithrombogenic barrier between the circulating blood and vessel wall [13]. Without a durable endothelium, vascular grafts are susceptible to failure after bypass surgery as a result of neointimal hyperplasia and thrombosis, typically caused by a lack of endothelial coverage on the graft [14-16]. Bioengineered vascular grafts must be able to withstand physiological forces of blood flow while allowing blood flow to propagate and therefore must exhibit mechanical properties similar to those of native vessels. Native human coronary arteries exhibit a young's modulus of 1.8 MPa, ultimate tensile strength of 2.4 MPa, suture retention of 3.0 N, and burst pressure of 5000 mm Hg [17, 18]. Additionally, human arteries experience wall shear stresses on the lumen that range from 20 – 40 dyne/cm<sup>2</sup> [19, 20] and therefore the ECs must be able to remain adherent to the lumen under these flow conditions.

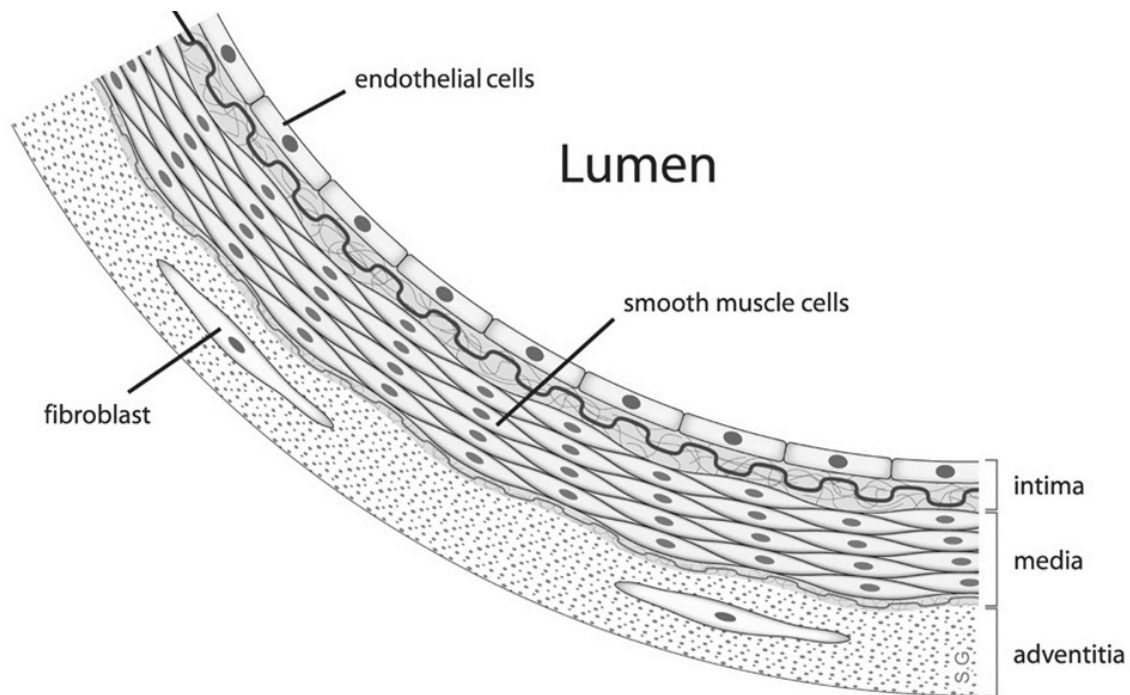


**Figure 1.2** Anatomy of an artery. ([http://en.wikipedia.org/wiki/File:Endothelial\\_cell.jpg](http://en.wikipedia.org/wiki/File:Endothelial_cell.jpg) - Creative Commons - GNU Free Documentation License)

The endothelium in native arteries is highly regulated by the constant exposure to hemodynamic shear stress caused by blood flow. It is well known that hemodynamic shear stress increases EC nitric oxide (NO) and prostacyclin production on a short time scale (minutes to hours), both of which hinder platelet activation, attenuate SMC proliferation, and inhibit neointimal formation [21]. Physiologic levels of shear stress ( $> 15 \text{ dyne/cm}^2$ ) also decrease EC turnover by both decreasing proliferation rates and apoptosis. On longer time scales (days), shear stress transforms EC morphology from a polygonal, cobblestone like shape to an elongated morphology in the direction of fluid flow [21]. Associated with this change in morphology, ECs switch from an atherogenic phenotype, susceptible to atherosclerosis, to an atherprotective phenotype with increasing levels of vasodilators, paracrine growth factors, inflammatory mediators, and adhesion molecules. Also, ECs aligned with the direction of blood are less prominent to the surface of the lumen and give rise to lower spatial variations of shear stress and stress gradients at the EC surface, essentially streamlining the endothelium surface [19]. In addition, EC cytoskeletal structure, specifically F-actin, reorganizes from the banding pattern at the periphery of ECs under low shear stress to thick bundles of F-actin that traverse the cell in the direction of high shear stress [2, 22]. These morphological characteristics of ECs under

physiologic levels of shear stress directly increase the endothelium's ability to resist deformation and detachment under shear stress [2, 19].

The endothelium not only experiences hydrodynamic shear stress as a result of blood flow, but also experiences hoop stress (substrate stretching), and hydrostatic pressure (Figure 1.3). While the majority of research has focused on how shear stress regulates the endothelium, there is an increasing body of research to support the idea that these other forces on the endothelium regulate phenotype, morphology and function as well. ECs and SMCs are subject to uniaxial stretch (hoop stress) as a result of pulsatile blood flow in the direction perpendicular to blood flow. It has been shown that ECs respond to uniaxial stretch alone, without shear stress or pressure, by aligning perpendicular to the direction of stretch, increase release of NO, and stimulate stretch activated  $\text{Ca}^{2+}$  ion channels [23]. Evaluation of pressure on ECs, in the absence of shear stress and stretch, has shown that ECs respond to pressure alone by increasing proliferation, cytoskeletal organization, synthesis of EC proteins, and  $\text{Ca}^{2+}$  transport [24-26].

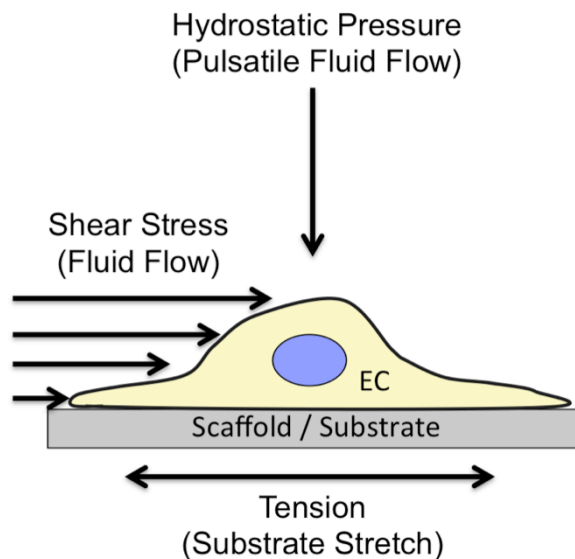


**Figure 1.3** Forces acting on an EC under pulsatile blood flow.

## 1.5 Scaffolds for bioengineered vascular grafts

A critical component for creating a functional bioengineered vascular graft, in addition to selecting the appropriate cell type and preconditioning methods, is the scaffold. Scaffolds in tissue engineering provide a temporary three-dimensional (3D) framework for new tissue growth to occur and play an important role in supporting and manipulating cell function. Isolated and expanded cells adhere to the scaffold surface, proliferate, differentiate into the appropriate

phenotype (if the cells are progenitor cells), and form extracellular matrices of the target tissue to replace the biodegradable scaffold. Ideally, vascular scaffolds should meet the following design criteria: (1) the scaffold should be biocompatible to avoid inflammation or toxicity once implanted, (2) the scaffold surface must permit cell adhesion, cell growth, and allow retention of differentiated cell function, (3) the scaffold should degrade and eventually be eliminated as tissue formation progresses, (4) the porosity and pore size must be large enough to allow for sufficient diffusion and permit uniform spatial cell distribution to facilitate homogeneous tissue formation, and (5) must be mechanically strong enough to support blood flow [27].

The earliest attempt at creating a bioengineered vascular graft was seeding ECs on the lumen of synthetic ePTFE or Dacron grafts. Synthetic grafts have not been successful as small-diameter grafts because of their thrombogenic blood-contacting surface. Initial attempts at creating a non-thrombogenic surface on synthetic grafts were to seed the lumen of the grafts *in vitro* with ECs from peripheral veins or microvasculature to form a “natural” antithrombogenic surface. The majority of these attempts failed *in vivo* due to EC detachment from the surface under physiological flow or maintenance of EC phenotype after attachment [28, 29]. While significant progress has been made in addressing EC attachment to synthetic surfaces using surface modification, synthetic grafts still pose other barriers to a long-term grafting solution. These drawbacks include the inability for synthetic grafts to be remodeled *in vivo* and inability of the graft to regulate vessel diameter in response to stimuli (i.e. vasotone) similar to native vessels.

A promising method to fabricate a small diameter bioengineered vascular graft may be through the use of cell-based ECM scaffolding. In a method developed by L’Heureux et al., bioengineered vascular grafts were assembled using a sheet-based method, where autologous fibroblasts were cultured *in vitro* under conditions necessary to promote deposition of ECM to produce a cohesive sheet that could be detached from the culture flask [16]. The sheets were then wrapped around a mandrel and cultured further to promote fusion of the sheets to create a graft without using exogenous biomaterials. Prior to implantation into a primate model, grafts were seeded with ECs and preconditioned *in vitro* for 3 days. The cell-based scaffolding had similar mechanical properties to human arteries, remained patent for 8 months *in vivo*, and explants showed complete remodeling and tissue integration.

Decellularized allogeneic and xenogeneic grafts have also been explored as potential candidates for bioengineered vascular grafting. This process involves using vessels from human

skin or vein in addition to porcine and bovine carotid arteries where the cellular components are removed produce an intact and structurally organized ECM scaffolding. Alternatively, tissues such as small intestinal submucosa (SIS) have been decellularized and used as small diameter vascular grafts. These tissues are mechanically robust, capable of withstanding arterial blood flow, and vascular cells readily attach and colonize the matrices to form cellularized constructs. In a study conducted by Badylak et al., a SIS graft was used in a canine carotid artery bypass where an EC monolayer was formed after 28 days of implantation and remained patent for 120 days [30].

Fabrication of a bioengineered vascular graft using both synthetic and natural polymers has been a major area of research in the field. The advantages of this bottom-up approach to scaffolding includes unlimited supply of materials and customization of grafts according to patient need. Some progress has been made in fabricating vascular scaffolds from natural polymers such as collagen and elastin [31]. These polymers have excellent biocompatibility profiles and are biomimetic, however, usually lack the mechanical integrity necessary to support forces associated with physiologic blood flow. Biodegradable synthetic polymers, such as aliphatic polyesters, have gained wide acceptance for vascular tissue engineering applications because of their biocompatibility, mechanical properties, resorption characteristics and ease of processing [32]. Among the polyesters, poly (lactic acid) (PLA), poly (glycolic acid) (PGA) and polycaprolactone (PCL) (and their respective copolymers, i.e. poly (lactic-co-glycolic acid)) have been used extensively to form vascular scaffolds [32]. The degradation rates of these polymers are highly tunable and can range from several weeks to years by altering the chemical composition (i.e. lactide/glycolide ratios in the PLGA copolymer), molecular weight, crystallinity, etc. In addition to providing adequate structural and cell adhesive properties as vascular scaffolds, these synthetic polymers also have the capacity to be modified to deliver agents such as drugs, proteins and DNA. Hybrid blends of synthetic and natural polymeric materials can provide an optimal combination of mechanical and biomimetic properties. In a study performed by Stitzel et al., a blend of type I collagen (45%), PLGA (40%) and elastin (15%) was used to fabricate a vascular graft via electrospinning [33]. The authors showed that addition of PLGA to the vascular graft greatly increased the ability to electrospin the graft as compared to electrospinning type I collagen and elastin alone. In addition, the burst pressure was determined to be 1425 mmHg, or nearly 12 times physiologic systolic pressure, and the vessel

diameter change under physiologic pressures was found to be similar to native vessels. Thus, by using a blend of natural and synthetic materials, the authors were able to form a scaffold possessing mechanical properties, tissue composition, and bioactivity similar to native vessels.

## **1.6 Electrospinning of bioengineered vascular grafts**

Electrospinning is a relatively simple and versatile method for producing non-woven fibrous vascular grafts. This fabrication technique has been used to produce scaffolds from a wide-range of polymeric materials (i.e. aliphatic polyesters, polyurethanes, collagen, silk, etc.) and for many different applications (i.e. bone, vascular, cartilage, tendon, ligament, muscle, etc.). Electrospinning of synthetic and natural polymers has become an effective method to fabricate vascular scaffolds because the resulting fibrous mesh mimics the natural extracellular matrix of native tissues [34]. A typical electrospinning setup consists of a capillary through which the polymer solution is forced, a pump to inject the polymer solution through the capillary, and a high voltage source to create an electric field to deposit the polymer solution onto a grounded target. Electrospun fibers have been produced with diameters ranging from approximately 100 nm to 14  $\mu\text{m}$  [34]. The fiber diameter of these scaffolds can be adjusted by modifying the electrospinning processing parameters, which include applied voltage, polymer flow rate, capillary-collector distance, and polymer concentration.

One of the first examples of using electrospinning to fabricate vascular scaffolds was a study conducted by Boland et al. [35]. In this study, the authors electrospun collagen type I and elastin onto a grounded spinning mandrel to form vascular grafts measuring 2 mm and 4 mm in inner diameter. The natural polymers used in this study were chosen to mimic the composition of native vessels. The grafts were then seeded with SMCs in the outer wall of the graft and human umbilical vein ECs (HUVECs) on the lumen of the graft. Histological sectioning and staining revealed that SMC infiltrated the wall of the vessel while HUVECs formed an intact endothelium. While the results of this study showed that natural polymers could be electrospun into a tube configuration, and the resulting scaffold could support vascular cells, the construct was weak and delaminated after just a few days in culture. More recently, electrospinning blends of synthetic and natural polymers for use as vascular grafts has shown promise both *in vitro* and *in vivo*. Lee et al. demonstrated that vascular scaffolds comprised of a 1:1 blend of PCL and type I collagen derived from calf skin had mechanical properties equivalent to those of native arteries and

supported both SMC and EC growth and maintenance in a pulsatile bioreactor. In a separate study, the same PCL/collagen scaffold was successfully implanted and remained patent for 1 month in a rabbit aortoiliac bypass model [36].

One advantage of electrospinning vascular grafts is the ability to modify scaffold properties by simply changing the electrospinning parameters. For example, an important design requirement for vascular grafts is the ability for various vascular cells (i.e. SMCs or fibroblasts) to penetrate the wall of the vessel to colonize and remodel the construct. One technique is to simply increase the fiber diameter of the electrospun scaffold to result in larger pore sizes. Ju et al. used this technique to successfully increase smooth muscle cell infiltration into the wall of an electrospun PCL/type I collagen vascular graft [37]. Their findings showed that scaffolds with average fiber diameters of 2.39 and 4.45  $\mu\text{m}$  allowed cells to infiltrate to the full-thickness of the scaffold as compared to scaffolds with average fiber diameters of 1.00 and 0.27  $\mu\text{m}$ , in which cells could not penetrate and remained on the cell-seeded side of the scaffold during the 4 week study. The mechanical properties of the scaffolds, however, decreased as a result of increasing fiber diameter.

Although small pore size is considered a hindrance for the wall of vascular scaffolds, it can actually be an advantage where cell infiltration is unwanted, such as for the endothelium. Electrospun scaffolds with pore sizes less than the size of a cell (i.e. less than 10  $\mu\text{m}$ ) are particularly useful in these barrier applications. An example would be using a nanofiber scaffold to form a lumen for vascular graft applications. The electrospun nanofiber scaffold can provide a nano-textured surface area for endothelial cell attachment while preventing smooth muscle cells, which are typically seeded into the outer wall of the graft, from penetrating into the lumen of the vessel. Although the pore size is too small to allow cell infiltration, media exchange can still take place to allow nutrient transport, waste removal, and paracrine signaling between endothelial and smooth muscle cells.

In addition to modifying scaffold pore size, vascular graft mechanical properties and morphology can be tuned by controlling fiber orientation. Electrospun fiber orientation can be controlled by electrospinning directly onto a rotating mandrel or by electrospinning between an insulating gap to produce aligned fibers. Increasing the rotational speed of the mandrel or introducing an insulating gap can increase the degree of fiber alignment. It has been shown that the resulting anisotropy of an aligned fiber scaffold can greatly increase its mechanical properties

in the direction of fiber alignment. This can certainly be advantageous for increasing the mechanical properties of a vascular graft. The mandrel onto which the graft is spun can be rotated such that the fibers align parallel to the direction of hoop stress caused by blood flow. Li et al. demonstrated that randomly oriented PCL electrospun scaffolds (33% fiber alignment) had a tensile modulus of 2.1 MPa, whereas aligned scaffolds (94% fiber alignment) had a tensile modulus of 11.6 MPa parallel to fiber alignment, in addition to a 33-fold increase in elastic modulus [38].

Not only can the anisotropic nature of the scaffold enhance mechanical properties, but it can also affect cell adhesion, proliferation, morphology, alignment and migration by introducing an aligned surface topography [34, 39-44]. Cells spread and align on an oriented surface topography through a phenomenon called contact guidance [45]. In recent years, several studies have investigated the effect of oriented topographic features on cell spreading and alignment by using oriented electrospun scaffolds. In a study by Xu et al., aligned nanofibrous poly(L-lactate-co-caprolactone) copolymer vascular scaffolds were fabricated and seeded with human smooth muscle cells [46]. They found that the cells attached and migrated along the axis of the aligned fibers with their cytoskeletal actin also parallel to the aligned fibers. SMC alignment within the wall of the vascular scaffold mimicked the configuration of SMCs in native vessels.

## **1.7 Scaffold endothelialization techniques**

As mentioned previously, the native endothelium provides a nonthrombogenic barrier between the circulating blood and the vessel wall in addition to regulating many important functions. Therefore, an ideal bioengineered vascular graft should contain an uninterrupted, mature and healthy endothelium. Common methods to create an endothelialized vascular graft include seeding the graft with ECs prior to implantation (*in vitro* endothelialization) or optimizing graft properties to enhance self-endothelialization after implantation (*in situ* endothelialization). Both approaches, with their associated advantages and disadvantages, are discussed below.

### **1.7.1 *In vitro* endothelialization**

*In vitro* endothelialization techniques involve harvesting autologous ECs from the patient, expansion of cells, and then seeding of ECs onto the lumen of the bioengineered graft. Many EC

sources have been explored for *in vitro* endothelialization of grafts including those from veins, microvasculature, and endothelial progenitor cells (EPCs). One of the first attempts at using venous ECs to form an endothelium on a vascular graft was by Herring et al. in 1984 [47]. In this study, ePTFE grafts were seeded with ECs from the saphenous vein and then implanted into human patients in the femoropopliteal position. The results showed that the patency of seeded grafts was significantly better than unseeded grafts after 30 months. Drawbacks with using veins as a source for ECs include infection and pain at the secondary surgery site and lack of a suitable vein for harvesting ECs due to prior vascular disease.

These drawbacks associated with venous ECs led researcher to explore other potential EC sources. In 1986, Jarrell et al. showed that harvesting and expansion of microvascular endothelial cells (MVECs) from fat tissue proved promising to form an endothelium on a synthetic vascular graft [48]. Baitella-Eberle et al. later showed that omental fat derived MVECs seeded on polyester vascular grafts were able to form an endothelium resembling those in native arteries [49]. Two advantages of MVECs to those derived from veins are that high amounts of MVECs can be obtained from liposuctioned fat tissue and they can be readily expanded in culture.

More recently, EPCs have gained interest to be used in seeding of bioengineered vascular grafts. EPCs, such as those derived from bone marrow, are cells that circulate in the peripheral blood of adults and can differentiate into mature ECs. EPCs have been shown to participate in neovascularization of ischemic limbs, play a crucial role in reestablishing endothelial integrity in injured vessels, and also contribute to re-endothelialization of prosthetic grafts in animals [50]. Advantages of using EPCs include simple extraction via venipuncture and ease of expansion *in vitro*.

### 1.7.2 *In situ* endothelialization

*In vitro* endothelialization of bioengineered vascular grafts requires harvesting of autologous cells from the patient and typically necessitates long culturing periods. *In situ* endothelialization of grafts is an approach that could eliminate the need for cell harvesting and expansion. This approach involves implanting the graft without prior EC seeding with the goal of attaining a fully endothelialized lumen shortly after implantation. *In situ* endothelialization requires native ECs to attach and proliferate to populate the lumen surface. Possible mechanisms for *in situ* endothelialization include (1) transanastomotic migration, where ECs migrate from the native vessel to the graft to cover the surface, (2) transmural migration through the wall of the

vessel via capillary ingrowth, and (3) recruitment of EPCs in circulation to the lumen surface [51]. Below are a few examples of how bioengineered grafts have been designed or modified to enhance *in situ* endothelialization. These scaffold designs include incorporation of topographic cues on the lumen surface, larger pores in the vessel wall, and homing molecules within the graft.

In the case of fully synthetic grafts in humans, transanastomotic migration of ECs historically has not exceed more than 1 – 2 cm from the native vessel even after years of implantation [52]. This is a major limitation for synthetic grafts because bypass grafting typically requires more than just a few centimeters, as in the case of peripheral bypass, which necessitates 40 – 60 cm lengths. However, recent work has shown that micropatterning of the graft lumen can facilitate EC migration with the goal of full anastomosis. Recent studies have shown that incorporating engineered topographical cues, such as grooves and waves, on the lumen surface can significantly enhance EC migration [53, 54]. These approaches are promising but micropatterning alone has not delivered a completely anastomosed endothelium *in vivo*. Therefore, it appears that a combinatorial approach, using transmural migration of ECs and recruitment of EPCs, may provide a promising solution.

Transmural migration of ECs requires capillary ingrowth of microvasculature into the bioengineered vascular graft wall in order to reach the lumen to deposit ECs on the lumen surface. Two main limitations to achieve transmural migration is the porosity of the vascular wall to permit cell infiltration and a driving force to elicit vasculature to penetrate the vessel wall [52]. Solutions to this problem include increasing the pore size of the vessel wall by means of many methods including the use of sacrificial fibers, particles, or processing techniques [43, 55] and inclusion of growth factor gradients, such as vascular endothelial growth factor (VEGF), in the vessel wall to enhance capillary ingrowth [56, 57].

Recruitment of EPCs to the lumen surface of a graft has been shown to be a promising method to endothelialize the graft *in situ*. This method includes presentation of EPC homing molecules on the graft surface that recognize EPC specific markers to selectively capture the cells in circulation [58]. EPCs express several surface markers such as CD34, VEGF receptor 2 (VEGFR-2) and CD133. Bioengineered vascular grafts coated with antibodies towards these markers, specifically CD34, have shown promise in capturing EPCs to form a fully confluent endothelium after 3 days *in vivo* [59].

## 1.8 Fluid flow preconditioning of vascular grafts *in vitro*

Fluid flow preconditioning of cell-seeded vascular grafts *in vitro* has become a nearly ubiquitous practice in the field of vascular tissue engineering [14, 16, 23, 26, 50-52, 60-66]. This technique involves mounting the graft in a fluid flow bioreactor and pumping cell culture media through the lumen to mimic blood flow *in vivo*. An image of a typical fluid flow bioreactor is presented in Figure 1.4 below. In addition to providing a continuous nutrient renewal, gas exchange, and waste removal, preconditioning of vascular grafts exerts mechanical stimuli upon cells seeded within the graft. Specific to the endothelium, fluid flow preconditioning provides hydrodynamic shear stress, pressure, and substrate stretch caused by hoop stress. The effects of fluid flow preconditioning on the endothelium *in vitro* are very similar to those experienced *in vivo* as explained in section 1.4 above. For example, when exposed to physiologic levels of shear stress, ECs transform from a cuboidal morphology to an elongated morphology aligned with the direction of fluid flow as shown in Figure 1.5 [21]. One of the most beneficial effects of preconditioning an EC-seeded bioengineered vascular graft prior to implantation is the enhanced retention of ECs to the lumen surface after onset of fluid flow when compared to non-preconditioned grafts. The main mechanism of enhanced EC retention under fluid flow is the reduction in shear stress at the cell surface as shown in Figure 1.6 [19]. In one of the first studies to utilize fluid flow preconditioning, Ott et al. exposed an EC-seeded polyester vascular graft to a 6 day preconditioning protocol - 3 days at 2 dynes/cm<sup>2</sup> hydrodynamic shear stress followed by 3 days at 25 dynes/cm<sup>2</sup> [67]. The authors demonstrated that EC retention on the lumen of the preconditioned graft retained nearly 40% more ECs than grafts cultured under static conditions when exposed to a pulsatile shear stress of 25 dynes/cm<sup>2</sup> to mimic blood flow after implantation. In addition, whole blood clotting time *in vitro* was significantly increased for grafts that underwent fluid flow as compared to static controls. Inoguchi et al. similarly showed that preconditioning of an endothelialized electrospun PCL vascular graft significantly enhanced EC retention under flow [62]. Specifically, the authors showed that an incremental increase in shear stress from 3.2 dynes/cm<sup>2</sup> to 19.8 dynes/cm<sup>2</sup> over a 3 day period (after 3 days static seeding) maintained a fully confluent endothelium compared to grafts, which completely lost the endothelium at 19.8 dynes/cm<sup>2</sup> when only cultured under static conditions. ECs under shear stress in the preconditioned group went from a cuboidal morphology to elongating with the direction of fluid flow. The authors also showed that F-actin reorganization occurred in the

preconditioned ECs in response to shear stress - from a banding pattern at the periphery of cells to thick bundles traversing the cells in the direction of fluid flow.

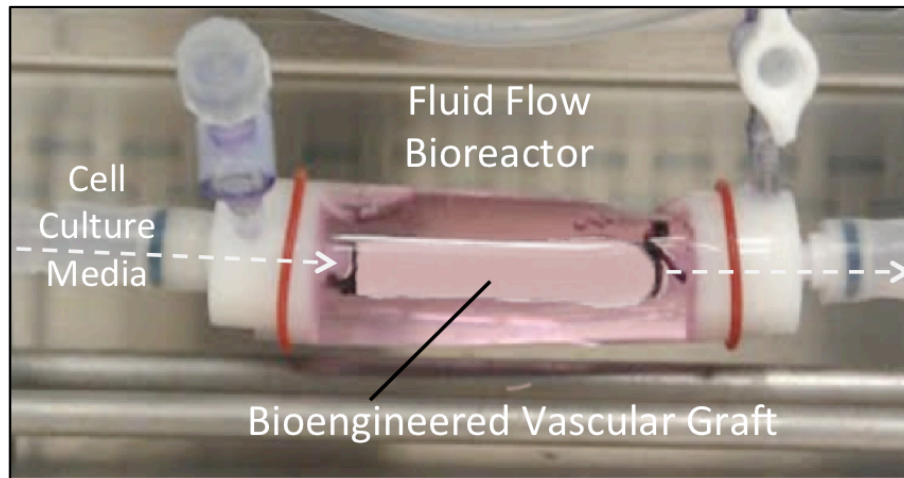


**Figure 1.4** Image of a fluid flow bioreactor used at the Wake Forest Institute for Regenerative Medicine to precondition bioengineered vascular grafts.

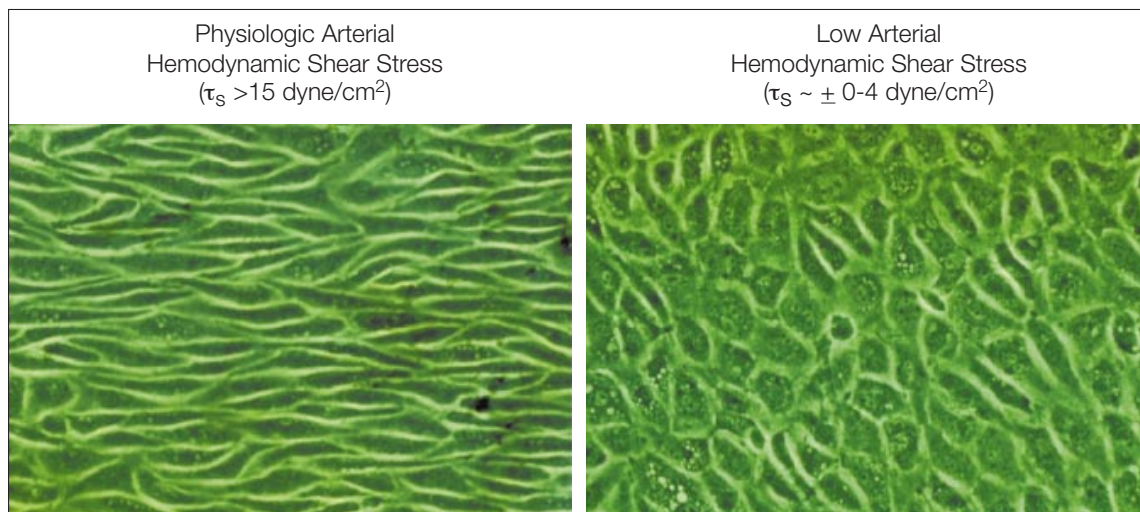


**Figure 1.5** Bovine aortic ECs elongate and align with flow under physiologic levels of hemodynamic shear stress *in vitro*, but retain a polygonal morphology under no or low shear stress. (Reprinted with permission from The American Medical Association from [21])

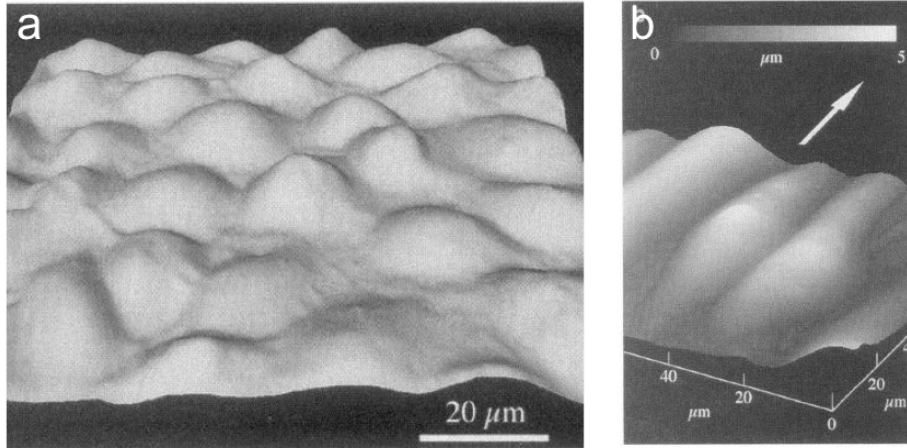


**Figure 1.6** Atomic force microscopy images of bovine aortic endothelial cells a) cultured under no flow, and b) after exposure to 12- dynes/cm<sup>2</sup> shear stress in steady laminar flow. Flattened profiles of aligned ECs give rise to smaller spatial variations of shear stress and stress gradients at the EC surface. Arrow indicates direction of flow. Gray micrometer scale in b indicates height of cell surface referenced to lowest point (at junctions between cells). (Reprinted from Davies et al. 1995 – Reprint permission not required for this use [19])

## 1.9 Methods to evaluate vascular grafts *in vitro*

A successful bioengineered vascular graft will exhibit properties (i.e. structural, organizational and morphological) of native vessels and maturation *in vitro* that can in part be identified by cellular organization and protein/gene expression by the seeded vascular cells. To evaluate the development and maturation of bioengineered vascular grafts, and tissue scaffold in general, many assays and methodologies can be employed. These methodologies can be divided into those that are destructive and nondestructive to the scaffold and cells seeded within.

### 1.9.1 Destructive methods

Conventional assessment techniques include invasive methods, such as fixation, staining, sectioning, and chemical assays to analyze specific metrics such as cell number, cell viability, protein accumulation and gene expression. These assays are used to determine cell number, such as the PicoGreen assay [68], which measures the amount of double-stranded DNA in a given sample, or the widely used 3-(4,5-dimethylthiazol-2-yl)-5-(3-carboxymethoxyphenyl)-2-(4-sulfophenyl)-2H-tetrazolium (MTS) assay to measure cell metabolic activity [69]. Western blotting can be used to measure both intercellular or matrix-bound proteins, and real-time reverse transcription polymerase chain reaction (RT-PCR) can be used to measure gene expression. While these assays provide quantitative biological information, they cannot provide spatial

information within the scaffold, i.e. cell distribution or locale of protein accumulation. Immunofluorescence imaging is a powerful tool to visualize proteins within a cell or tissue and can be used in conjunction with histological sectioning for thick tissue samples. This methodology can both provide quantitative and spatial biological information. While these methods are effective at assessing such metrics, they are destructive to the sample and cell viability, making it impossible to monitor the development of the graft in a spatial and temporal manner. In addition, these techniques do not allow collection of data that occurs on a short time scale (i.e. minutes) for processes that are critical for understanding the tissue response to physiochemical stimuli. For example, it would be difficult to monitor EC migration on the lumen of the graft, endothelial nitric oxide synthase (eNOS) expression, or platelet accumulation in response to various stimuli such as fluid flow preconditioning since these changes occur on a very short time scale. Given these limitations in destructive techniques, researchers have begun to use nondestructive techniques, usually in the form of imaging methodologies, to assess both maturation and function of tissue engineered scaffolds in a spatial and temporal manner.

### 1.9.2 Nondestructive imaging methods

As mentioned previously, optical imaging techniques utilizing stains or immunofluorescence is very useful for detecting cells and proteins they express. However, these can compromise the viability of the cells and limit the measurement to one time point. Recently, these limitations have been overcome by genetically modifying cells to express fluorescent proteins, which can be imaged without damaging the sample or compromising cell viability. For example, Blum et al. modified a fibroblast cell line to constitutively express an enhanced green fluorescent protein (EGFP) reporter to noninvasively monitor cell proliferation and distribution within a tissue-engineered scaffold [70]. In a study by Kuhn et al., osteoblasts were modified with a Collagen Type 1 promoter with an EGFP reporter to monitor the level of osteoblastic differentiation in a nondestructive manner [71]. The following sections provide more detail of conventional optical imaging methodologies used for nondestructive assessment of tissue engineered scaffolds.

### 1.9.3 Confocal Microscopy

Confocal microscopy is a widely used optical imaging technique in tissue engineering because of the high resolution obtained and also because of its ability to image through optically

thick samples [72]. The main advantage of confocal microscopy over wide-field microscopy is its ability to provide depth-resolved imaging. Standard wide-field fluorescence microscopy, shown in Figure 1.7A, uses a collimated beam of excitation light to illuminate the whole field of view, then the fluorescence signal is subsequently imaged onto a detector (either a camera or eye retina). While fluorescence emanating from the objective focal plane is optimally captured onto the detector, out-of-focus fluorescence from multiple focal planes within the sample is also detected, resulting in loss of resolution and image degradation.

In a confocal microscope, a laser excitation source is focused onto the imaging focal plane within a specimen, as illustrated in Figure 1.7B. The fluorescence emission from the focal plane is then imaged onto a pinhole and detected by the sensor. The pinhole is used to eliminate fluorescence detection below or above the focal plane and therefore can dramatically increase the imaging resolution and image quality, as illustrated in Figure 1.7 C,D. The effective working distance of objectives typically used for confocal microscopy range from up to a few millimeters for low numerical aperture objectives to only a few hundred microns for high numerical aperture objectives [72]. This working distance can limit the imaging depth obtained in 3D samples, however, the scattering and absorption that light experiences as it travels throughout the specimen is usually the determining factor for the effective depth of imaging through a thick sample. Therefore, the depth at which images can be obtained through a thick sample at the desired resolution needed depends not only on the capabilities of the microscope (i.e. working distance), but also on the optical properties of the specimen.

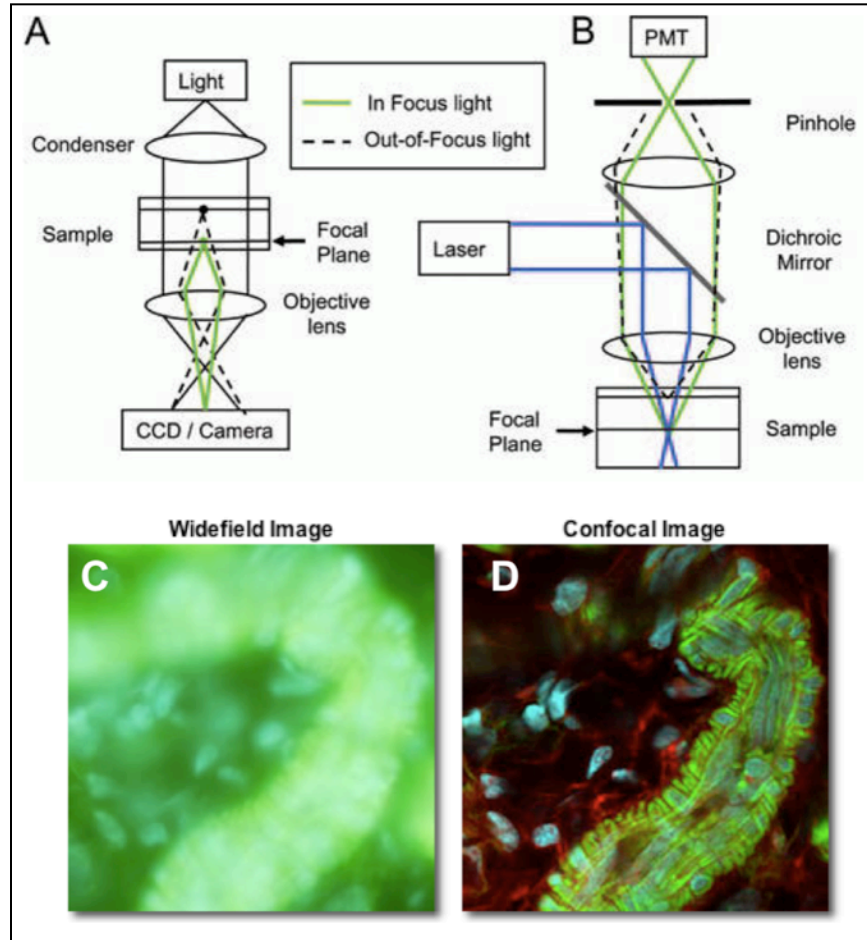


**Figure 1.7** A) A standard fluorescence microscope utilizes an optical path that provides uniform illumination of the sample. Fluorescence from the focal plane, as well as from out-of-focus planes, reaches the detector. B) A confocal microscope provides focused illumination of a point within a sample, which is then imaged through a pinhole in front of the detector. Most out-of-focus light from other imaging planes does not reach the detector because of the pinhole. C) A typical fluorescence microscope image of a thick human bladder section, and D) the same section as imaged by a confocal microscope (both 60X). (Reprinted with permission from Mary Ann Liebert, Inc. [72])

#### 1.9.4 Two-Photon Microscopy

Two-photon microscopy has the capability to image through highly scattering tissues at depths up to hundreds of microns with sub-micron resolution [73] and has been used extensively to perform noninvasive imaging in tissue engineered constructs [72]. This imaging modality is based upon simultaneous absorption of two photons in a single event, as compared to absorption of one photon, which occurs in typical fluorescence microscopy. Since the energy of a photon is inversely proportional to its wavelength, the two absorbed photons must have a wavelength

about twice that required for one-photon excitation. For example, a fluorophore that normally fluoresces under ultraviolet light (i.e. 360 nm – Figure 1.8a) can also be excited by two photons of near-infrared light (i.e. 720 nm – Figure 1.8b) if both reach the fluorophore at roughly the same time.

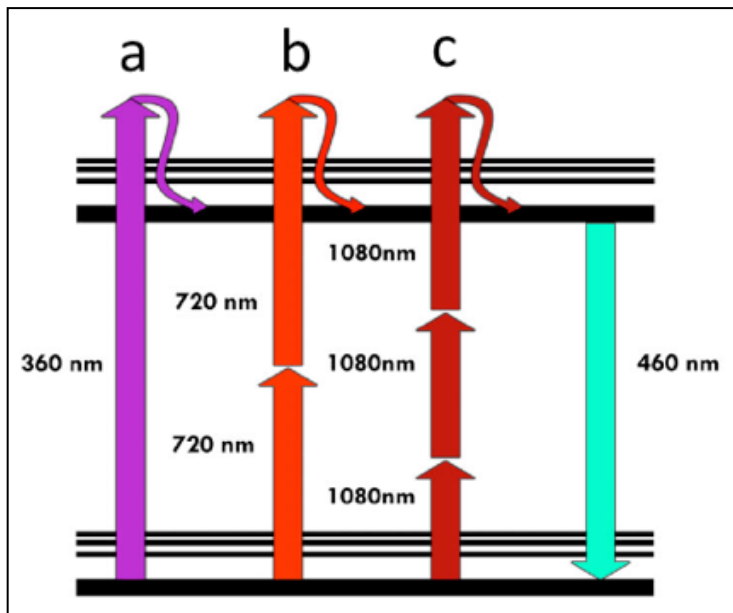


**Figure 1.8** A simplified Jablonski fluorescence diagram showing a) 1, b) 2 and c) 3 photon excitation. Once the excited state has been reached, the fluorescence emission (i.e. 460 nm) is exactly the same for all three modalities of excitation. (Creative commons attribution license – Reprinted from [74]).

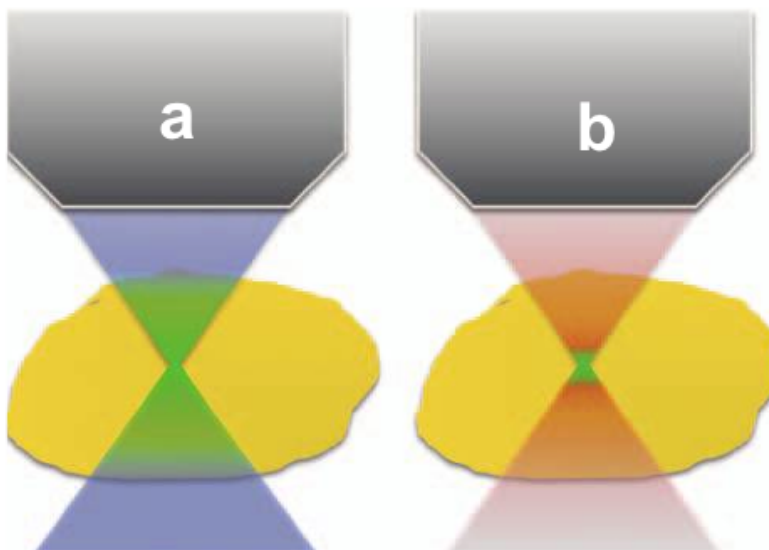


**Figure 1.9** Diagram of fluorescence excitation volume in a 3D sample (yellow), where a) fluorescence (green) is generated throughout the excitation (blue) light path in confocal

microscopy, and b) fluorescence (green) is confined to a small volume with two-photon excitation in the excitation path (red). (Reprinted with permission from Mary Ann Liebert, Inc. [72])

Two-photon microscopy typically provides better imaging resolution and penetration through highly scattering biological materials, such as tissue scaffolds, when compared to confocal microscopy [72]. This is a direct result of the unique characteristics of two-photon excitation. First, the absorption of two photons simultaneously depends on the square of the excitation intensity. As the laser excitation source is focused, the spatial density of the excitation photons is increased, and the probability that two of them are absorbed simultaneously increases. Therefore, the laser focal point can be tuned to create a small spatial volume wherein the photons are crowded enough to generate a significant occurrence of two-photon excitation (Figure 1.9). This allows selective excitation within a thick sample and makes micron-level 3D image reconstruction possible. Secondly, using near-infrared light as an excitation source is advantageous since these wavelengths experience minimal adsorption and scattering in biological tissues – allowing deeper penetration into the sample. Drawbacks associated with two-photon imaging include high laser intensities, which require pulsing to keep the average power delivered to the specimen low to avoid thermal damage, and limitations associated with short working distance objectives, similar to confocal microscopy.

#### 1.9.5 Optical Coherence Tomography

Optical coherence tomography (OCT) is a powerful nondestructive imaging methodology that is based not on fluorescence but on the concept of optical ultrasound. Low-coherence light is shone onto the sample and the morphological structure of the material is determined by how much time it takes for the incident light to travel through the sample and back to the detector. The main advantage of OCT is that it can provide information about the sample at up to 2 – 3 mm in depth at a lateral and axial resolution on the order of 10 – 15  $\mu\text{m}$  [72]. Initial studies that explored the use of OCT to nondestructively assess tissue scaffolds *in vitro* have been promising. In a study conducted by Bonnema et al., the authors used OCT to visualize the endothelial lining of a synthetic vascular graft in response to a bare metal stent [75]. They showed that OCT was capable of noninvasively measuring the endothelial lining of the graft with response to the stent with good accuracy as compared to histological images. In another study, Chen et al. used OCT to measure the structure of macroporous hydrogel scaffolds over time [76]. Specifically, the authors demonstrated that OCT was a viable method to assess scaffold porosity, pore size and

pore interconnectivity over time. However, to visualize seeded cells, the authors had to use fluorescence microscopy to image cell distribution and viability within the scaffolds to co-register with OCT. OCT has primarily been used to measure anatomical or morphological structures within tissue scaffolds, or to distinguish different layers of tissue, because individual cells are not optically scattering enough to detect using OCT.

#### 1.9.6 Bioluminescence imaging

Bioluminescence is the enzymatic generation of visible light by a living organism. In recent years, bioluminescence has been utilized in the biomedical sciences to study such mechanisms as cancer metastasis, gene expression, and cell proliferation/trafficking in small rodent models *in vivo* through bioluminescent reporters [77]. More recently, bioluminescence imaging (BLI) has been used in tissue engineering to monitor cell attachment, proliferation and gene expression in tissue-engineered constructs both *in vitro* and *in vivo* [78]. The most popular bioluminescent reporter used for bioluminescence is firefly luciferase from the North America firefly *Photinus pyralis*. The enzyme catalyzes the substrate D-luciferin into oxoluciferin, leading to the emission of photons in the visible range (between 500 and 620 nm) [78]. This wavelength of light can pass through animal tissues/tissue scaffolds and can be captured with sensitive electron multiplying charged coupled device (EMCCD) cameras to provide nondestructive, real-time information from deep within a tissue.

One of the first uses of BLI in tissue engineering was by Blum et al. where a rat fibroblastic cell line was stably transduced to express a luciferase reporter under the control of a constitutive promoter [70]. Cells were seeded into both a hydrogel and on a titanium mesh, and the level of luminescence was measured with a CCD camera *in vitro* over the course of a week to quantify cell proliferation in the constructs. Additionally, cell-seeded titanium meshes were implanted subcutaneously into rats and luminescence was successfully measured during the 28-day study. More recently, BLI has been used to monitor expression of genes associated with tissue-specific cell differentiation. Vilalta et al. stably transduced a rat bone marrow stromal cell line with a procollagen II (COL2A1) promoter driving a firefly luciferase gene reporter (PLuc) to noninvasively measure chondrogenic differentiation [79]. They showed that PLuc expression simultaneously increased with chondrogenic gene expression of COL2A1 and Sox9 both *in vitro* and *in vivo*.

### 1.9.7 Nondestructive imaging of vascular graft endothelialization

A bioengineered vascular graft presents a unique geometry for imaging cells within the vascular scaffold using conventional imaging techniques – especially for imaging the graft endothelium. The tubular shape limits access to the lumen, and using conventional imaging systems, can be reached either externally (i.e. imaging through the vessel wall) or by insertion of the optics through the lumen using an endoscope. These imaging difficulties are magnified even further when the vascular scaffold is housed within a fluid flow bioreactor, as shown in Figure 1.10a. Microscope-based imaging systems, such as confocal or two-photon as shown in Figure 1.10b, have two main limitations in imaging the vascular endothelium: 1) imaging penetration depth through the thick and highly porous vessel wall which causes photon scattering, and 2) limited working distances of the optical objectives. As mentioned previously, conventional confocal or two-photon microscopes have a maximum imaging penetration depth of a few hundred microns (depending on medium scattering) and the working distances are between a few hundred microns to 1 mm [72]. This presents a problem, as vascular grafts are typically more than a few hundred microns thick and often very optically scattering. Endoscope-based imaging systems that incorporate confocal or two-photon optics are a promising alternative to image the endothelium of a vascular graft. These endomicroscopes, which can be as small as 1 mm in diameter, can be inserted through the lumen of the graft to visualize the endothelium, as shown in Figure 1.10c. Kim et al. demonstrated that their multi-photon capable endomicroscope was capable of imaging the gastrointestinal and respiratory tracts of mice *in vivo* with single-cell level resolution and a 250  $\mu\text{m}$  x 250  $\mu\text{m}$  field of view [80]. Endomicroscopes, however, are limited in continual monitoring of the vascular lumen because they would block flow within the fluid flow bioreactor. Therefore, a completely new imaging system is presented in this dissertation to solve this problem. Our approach is to develop an integrated system by embedding micro-imaging channels within the vascular scaffold to direct fiber-optic guided excitation light to the endothelium to excite fluorescent ECs as illustrated in Figure 1.10d. The fluorescence response is then captured using a sensitive photon collector from outside the bioreactor. This new fiber optic based (FOB) imaging system is a promising alternative to conventional systems to monitor the endothelium of a vascular graft *in vitro*.

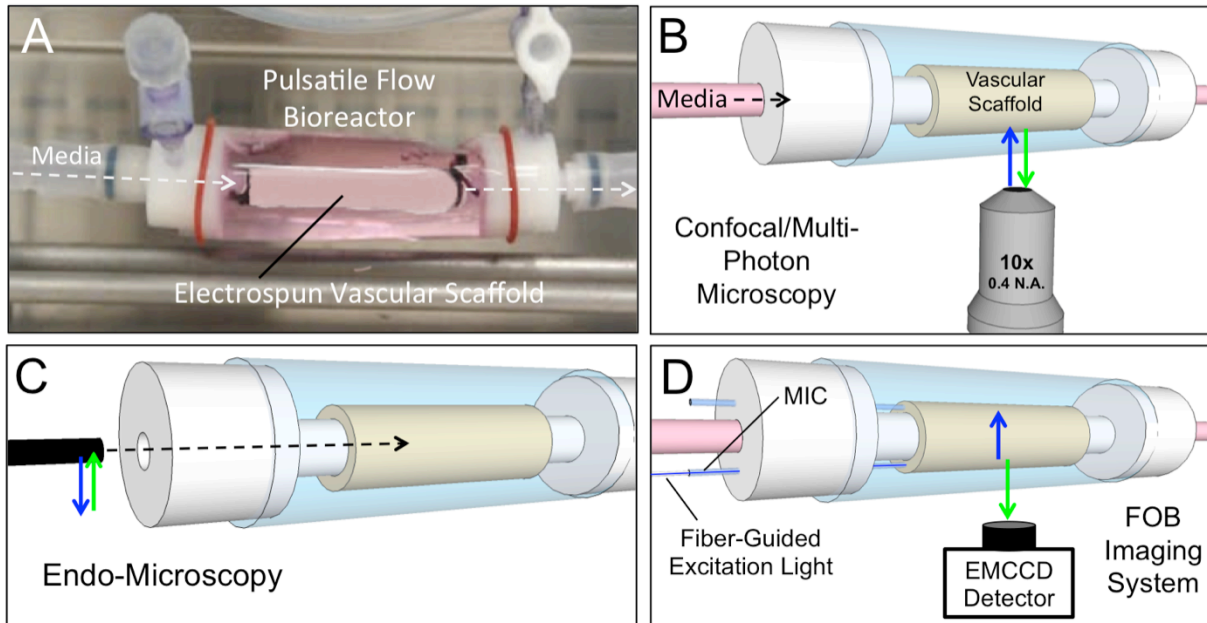


**Figure 1.10** Options for imaging a bioengineered vascular graft endothelium. A) Image of a pulsatile bioreactor used to precondition a bioengineered electrospun vascular scaffold. B) Schematic representation of imaging the endothelium of a bioengineered vascular scaffold in a pulsatile bioreactor using microscope-based imaging techniques such as confocal/multi-photon microscopy. Blue arrows represent excitation light and green arrows represent fluorescence emission. Microscope-based techniques have a limited capacity to image the endothelium of a vessel due to the highly scattering nature of the vascular scaffold wall and limited working distance of the objectives. C) Schematic representation of imaging the endothelium using endo-microscopy techniques. To accomplish this, an endo-microscope must be inserted into the lumen of the vessel, which may cause abrasion on the lumen surface, introduce sterility concerns, and occlude fluid flow. D) Schematic representation of the FOB imaging system integrated into a pulsatile bioreactor. Excitation light is guided into the scaffold wall and fluorescence emission is collected from outside the bioreactor. Using this technique, it is possible to image the endothelium through the thick vessel wall in a dynamic manner without disturbing the vessel during preconditioning in a bioreactor.

## 1.10 Objective and Experimental Plan

Tissue engineering of vascular grafts is a promising alternative to current vascular grafting options for cardiovascular disorders such as atherosclerosis. A promising approach to creating a viable bioengineered vascular graft involves fabrication of a resorbable scaffold and seeding the construct with vascular cells capable of withstanding the physiological forces of blood flow until graft remodeling is complete. Current limitations associated with bioengineered vascular grafts include the capacity to support a confluent and well-adhered endothelium under physiologic levels of shear stress and the lack of noninvasive imaging methods to assess graft endothelialization and response to fluid flow. Therefore, the objectives of this research were to develop scaffold topographies to enhance EC adherence to the scaffold surface under physiologic hydrodynamic shear stress and to develop an imaging technology capable of assessing graft endothelialization in a dynamic and noninvasive manner with the overall goal of enhancing a bioengineered vascular graft endothelium. The work completed to meet these objectives is outlined in the following chapters:

### 1.10.1 Chapter 1: The influence of nanofiber scaffold topography on endothelial cell morphology, alignment, and adhesion in response to fluid flow

Bioengineered vascular grafts require scaffold designs capable of supporting a confluent endothelium that resists EC detachment under physiologic levels of hydrodynamic shear stress. Therefore, this study examines the effects of electrospun Poly( $\epsilon$ -caprolactone) (PCL)/type I collagen nanofiber diameter and orientation on EC morphology, alignment, and structural protein organization with the goal of forming a confluent endothelium that resists detachment under fluid flow. To accomplish this, scaffold topography was tuned by adjusting electrospinning parameters to systematically vary fiber diameter and orientation. Cell morphology (cell area, aspect ratio, and length of long axis) and degree of alignment were quantified by performing image analysis of fluorescently stained cells and expression/organization of two principal structural proteins (VE-cadherin and F-actin) and a cell-substrate linker protein (vinculin) was observed by immunofluorescence imaging. EC monolayers on nanofiber scaffolds were exposed to fluid shear in a parallel plate flow chamber and cell detachment was quantified to elucidate the effect of nanofiber diameter and orientation on EC adhesion to the scaffold.

### 1.10.2 Chapter 2: A Fiber-Optic-Based (FOB) Imaging System for Non-Destructive Assessment of Cell-Seeded Tissue-Engineered Scaffolds

The main focus of this study was to develop a novel imaging method to evaluate bioengineered vascular grafts, where the assessment endothelialization on the lumen (inner surface) of bioengineered blood vessels is of significant interest. From an imaging standpoint, it is exceedingly difficult to monitor endothelialization on the lumen through a thick and optically opaque tubular vessel using conventional microscopy techniques. Furthermore, the preconditioning of such vessels in fluid flow bioreactors poses additional geometrical constraints on the objective's working distance. Therefore, the key significance of this study is the design and validation of an entirely new imaging technique that is capable of performing non-destructive imaging of endothelial cells (ECs) through a thick and optically opaque electrospun scaffold housed within a bioreactor. Our approach is based on embedding thin and flexible micro-imaging channels (MICs) directly into a fibrous scaffold. The validity of our method was demonstrated by imaging through an opaque scaffold model and visualizing GFP-labeled ECs located on the luminal surface. The accuracy of our method was quantified through direct comparison with conventional, direct-line-of-sight fluorescence microscopy.

### 1.10.3 Chapter 3: Dynamic, nondestructive imaging of a bioengineered vascular graft endothelium

The objective of this study was to use the FOB imaging system to assess the graft endothelium without disturbing the graft during incubation in a bioreactor. In this study, we evaluate the feasibility of the FOB imaging system to image and quantify endothelialization, EC detachment, and apoptosis in a dynamic and noninvasive manner. The electrospun fiber diameter of the graft lumen was systematically varied and the FOB imaging system was used to noninvasively quantify the affect of topography on graft endothelialization over a 7-day period. Additionally, the health of the endothelium was assessed by quantifying EC apoptosis on the lumen in response to varying levels of physiological insult. Finally, the imaging depth of the FOB imaging system was directly compared to that of two-photon fluorescence microscopy. The results of this study demonstrate the potential of the FOB imaging system to be utilized to nondestructively assess the maturation of a bioengineered vascular graft endothelium in real-time.

### **1.11 Material in Appendices**

The appendices contain studies that were conducted relating to tissue scaffold design and noninvasive scaffold imaging, but are not closely linked to the overall goal of this dissertation. Appendix A includes a study that assesses the effect of increasing osteoblast penetration into an electrospun scaffold by inclusion and removal of a sacrificial fiber component in addition to increasing osteoblastic differentiation by inclusion of a calcium phosphate coating. Appendix B is a study that characterized the optical properties of PDLLA scaffolds and FOB imaging penetration depth in vitro. Appendix C includes a study that measures the change in optical properties of a bioengineered blood vessel over time using OCT.

## **Chapter 2: The influence of nanofiber scaffold topography on endothelial cell morphology, alignment, and adhesion in response to fluid flow**

Bryce M. Whited<sup>a</sup> and M. Nichole Rylander<sup>a,b</sup>

<sup>a</sup> School of Biomedical Engineering and Sciences, Virginia Tech – Wake Forest University, Blacksburg, VA 24061, USA

<sup>b</sup> Department of Mechanical Engineering, Virginia Polytechnic Institute and State University, Blacksburg, VA 24061, USA

### **2.1 Abstract**

Bioengineered vascular grafts provide a promising alternative to autografts for replacing diseased or damaged arteries, but necessitate scaffold designs capable of supporting a confluent endothelium that resists endothelial cell (EC) detachment under fluid flow. To this end, we investigated whether tuning nanofiber topography (i.e. fiber diameter and orientation) could impact EC morphology, alignment, and structural protein organization with the goal of forming a confluent and well-adhered endothelium, without the need for preconditioning under fluid flow. To test this, a composite polymer blend of Poly( $\epsilon$ -caprolactone) (PCL) and type I collagen was electrospun to form scaffolds with controlled fiber diameters ranging from approximately 100 nm to 1200 nm and with varying degrees of fiber alignment. ECs were seeded onto scaffolds, and cell morphology and degree of alignment were quantified using image analysis of fluorescently stained cells. Our results show that ECs form confluent monolayers on nanofiber scaffolds, with cell alignment systematically increasing with a larger degree of fiber orientation. Additionally, cells on aligned nanofiber scaffolds display thick F-actin bundles parallel to the direction of fiber alignment and strong VE-cadherin expression at cell-cell junctions. Under fluid flow, ECs on highly aligned fiber scaffolds had greater resistance to detachment compared to cells cultured on randomly oriented and semi-aligned fiber scaffolds. These results indicate that scaffolds with aligned nanofiber topographies may be useful in forming a confluent endothelium with enhanced EC adhesion for vascular tissue engineering applications.

## 2.2 Introduction

Currently, there are more than one million vascular procedures performed each year in the US to treat various forms of cardiovascular disease such as coronary and peripheral artery disease [64]. Many of these procedures include bypass surgery, wherein autologous vessels are used to reroute blood flow around occluded or diseased arteries. While autologous vessels are considered the gold standard for bypass grafts, this procedure can result in donor site morbidity or is often not feasible since many patients lack a suitable vein or artery for bypass grafting [81, 82]. As a result, there has been significant interest in using bioengineered vascular grafts fabricated from both synthetic and natural sources as an alternative to autologous grafts.

A critical design requirement for small-diameter (<6 mm) bioengineered vascular grafts is the formation of a continuous monolayer of endothelial cells (ECs) on the lumen of the construct. This is typically accomplished by seeding autologous ECs, such as venous ECs [63, 83] or endothelial progenitor cells [84, 85] on the lumen surface of the vascular graft prior to implantation. In native vessels, ECs play an important role in regulation of vascular tone, tissue homeostasis, and regulation of nutrient transport across the vessel wall [12]. In addition, the endothelium forms a selectively permeable, antithrombogenic barrier between the circulating blood and vessel wall [13]. Without a durable and adherent endothelium, vascular grafts are susceptible to failure after bypass surgery as a result of neointimal hyperplasia and thrombosis, typically caused by a lack of endothelial coverage on the graft [14-16]. Therefore, an ideal bioengineered vascular graft should possess a continuous monolayer of ECs that functions similar to the native endothelium while remaining adherent under physiological flow conditions.

It is well known that the morphology and cytoskeleton arrangement of ECs in native arteries directly affects their ability to function and resist detachment under physiological fluid flow [86]. The endothelium in native vessels is composed of ECs that are aligned with the direction of blood flow in straight vessel segments. These morphological properties (i.e. shape and orientation) are directed by flow-mediated mechanotransduction, where mechanical forces are converted into cellular activity through cell-surface membrane protein mechanoreceptors and mechanosensitive ion channels, among others [19]. Under flow conditions, mechanotransduction induces cytoskeletal rearrangement, specifically F-actin, in ECs exposed to fluid flow [19, 86]. ECs located at sites of disturbed fluid flow *in vivo*, i.e. at vessel branches or atherosclerotic lesions, or under static conditions *in vitro*, display a polygonal morphology where F-actin is

organized at the periphery of the cells. Upon exposure to high shear stress, cells align with the direction of flow and F-actin rearranges to create thick bundles of stress fibers parallel to the direction of fluid flow. Furthermore, the reorientation and alignment of ECs, in addition to F-actin organization, substantially increases the cells ability to resist deformation and detachment under shear stress [19, 22, 86]. Therefore, in this study, we hypothesized that if ECs can be directed to adopt an *in vivo*-like morphology, alignment, and F-actin organization in the direction of fluid flow, their resistance to detachment may increase as a result.

An effective method that has been employed to achieve an endothelium with *in vivo* like morphology and alignment is *in vitro* fluid flow preconditioning prior to implantation *in vivo* [60]. This approach utilizes fluid flow bioreactors to expose the lumen of the graft to incremental increases in hydrodynamic shear stress to achieve an aligned and well-adhered endothelium. While effective, this approach is time and resource intensive, typically requiring several days to weeks to achieve a conditioned endothelium which can accept physiologic levels of shear stress without detachment [20, 65]. Alternatively, a potentially promising method to form an endothelium with *in vivo*-like morphology and alignment may be through the use of a phenomenon called contact guidance, where substratum surface topography can direct cell spreading [87]. Several groups have shown that EC morphology, orientation, and cytoskeleton can be controlled on a variety of topographic features including nanoscale silicone and polyurethane grooves [54, 88, 89], micron-diameter methacrylic terpolymer fibers [90, 91], and nanoscale poly(dimethylsiloxane) waves [92]. Despite these studies, it remains unclear how ECs respond to topographical features such as fiber diameter and orientation, specifically for fiber diameters in the sub-micron range, in an effort to control cell morphology and alignment to increase cell adhesion strength under hydrodynamic shear stress. Therefore, the main objective of the current study is to examine the effects of electrospun Poly( $\epsilon$ -caprolactone) (PCL)/type I collagen nanofiber diameter and orientation on EC morphology, alignment, and structural protein organization with the goal of forming a confluent endothelium that resists detachment under fluid flow. To accomplish this, scaffold topography was tuned by adjusting electrospinning parameters to systematically vary fiber diameter and orientation, concurrently. Cell morphology (cell area, aspect ratio, and length of long axis) and degree of alignment were quantified by performing image analysis of fluorescently stained cells and expression/organization of two principal structural proteins (VE-cadherin and F-actin) and a cell-substrate linker protein

(vinculin) was observed by immunofluorescence imaging. EC monolayers on nanofiber scaffolds were exposed to fluid shear in a parallel plate flow chamber and cell detachment was quantified to elucidate the effect of nanofiber diameter and orientation on EC adhesion to the scaffold.

## **2.3 Materials and Methods**

### **2.3.1 Scaffold Fabrication**

Scaffolds consisting of a polymer blend of type I collagen and PCL were electrospun similar to a method previously reported by Lee et al. [17]. Briefly, 1:1 (weight ratio) blends of type I collagen derived from calf skin (Elastin Products Co., Owensville, MO, USA) and PCL (Lactel Absorbable Polymers, Pelham, AL, USA) were prepared in 1,1,1,3,3,3-hexafluoro-2-propanol (HFP, Sigma Aldrich, St. Louis, MO, USA). PCL/collagen concentrations of 5%, 10%, and 15% (w/v) were used to fabricate scaffolds with varying fiber diameters. To form scaffolds with random fiber orientations, PCL/collagen solutions were electrospun onto a grounded stationary tissue culture polystyrene (TCPS) substrate. To fabricate scaffolds with varying fiber orientation, PCL/collagen solutions were electrospun onto TCPS substrates attached to a grounded rotating aluminum mandrel at 1500 and 3000 rpm (with corresponding linear velocities of 4.0 and 8.0 m/s, respectively). Approximately 1 ml of each solution was used to fabricate PCL/collagen scaffolds with varying fiber diameters and orientations by varying electrospinning parameters (refer to Table 2.1). The scaffolds were then placed in a vacuum desiccator overnight to remove all residual solvent.

### **2.3.2 Scaffold Characterization**

Scaffold morphology was investigated using field emission scanning electron microscopy (SEM) using a LEO 1550 field emission SEM (Carl Zeiss, Thornwood, NY, USA). SEM images were then analyzed using Image J software (U.S. National Institutes of Health, Bethesda, MD, USA) to determine fiber diameter and degree of fiber orientation. A total of 50 random fibers per image were manually measured to determine fiber diameter and angle of orientation ( $n = 5$  images/scaffold,  $n = 250$  fibers total). The degree of fiber orientation was characterized by the angular standard deviation for a wrapped normal distribution using the method previously

described by Bashur et al. [39]. The wrapped normal distribution is given by the following equation:

$$f(\theta) = \frac{1}{\pi} \left( 1 + 2 \sum_{p=1}^{\infty} \rho^{p^2} \cos(2p(\theta - \mu)) \right), \quad 0 \leq \theta \leq \pi, \quad (2.1)$$

where  $\rho$  is the mean resultant length, and  $\mu$  is the mean angle for a set of  $n$  measured fiber angles,  $\theta_i$ , as given by the following equations:

$$\rho = \frac{1}{n} \sqrt{\left( \sum_{i=1}^n \cos 2\theta_i \right)^2 + \left( \sum_{i=1}^n \sin 2\theta_i \right)^2}, \quad (2.2)$$

$$\mu = \tan^{-1} \left( \frac{\sum_{i=1}^n \sin 2\theta_i}{\sum_{i=1}^n \cos 2\theta_i} \right). \quad (2.3)$$

The angular standard deviation,  $\sigma$ , was then calculated from the mean resultant length:

$$\sigma = \frac{1}{2} \sqrt{-2 \ln \rho}. \quad (2.4)$$

### 2.3.3 Cell Culture and Cell Seeding

Primary human umbilical vein endothelial cells (HUVEC) were purchased from American Type Culture Collection (Manassas, VA, USA) and were used to perform cell studies. All cells were used below passage 5 and cultured in Medium 200PRF supplemented with 2% fetal bovine serum, 1  $\mu\text{g/ml}$  hydrocortisone, 10  $\text{ng/ml}$  human epidermal growth factor, 3  $\text{ng/ml}$  basic fibroblast growth factor, and 10  $\mu\text{g/ml}$  heparin (Invitrogen, Carlsbad, CA, USA) in a 37°C, 5% CO<sub>2</sub> incubator. Before cell seeding, scaffolds were sterilized by immersion in 70% ethanol for 1 hr followed by 3 washes in sterile phosphate buffered saline (PBS). HUVECs were then seeded onto the scaffolds at a density of  $1.5 \times 10^4$  cells/cm<sup>2</sup>.

### 2.3.4 Cell Morphology and Alignment

EC morphology and degree of alignment were assessed 3 days post-seeding by using image analysis of Calcein AM stained cells. This time point was chosen based on preliminary data showing cell confluence at 3 days for the seeding density used (data not shown). Briefly, scaffolds were incubated in medium containing Calcein AM (Molecular Probes, Eugene, OR, USA) at a final concentration of 5  $\mu\text{M}$  for 30 min at 37°C. Scaffolds were washed twice with sterile PBS, culture medium was added to each well, and fluorescent cells were imaged using a

Leica DMI6000-B microscope (Leica, Wetzlar, Germany). Images were then analyzed with Image J software (National Institutes of Health, Bethesda, MD) to determine cell morphological properties including 1) projected area, 2) aspect ratio, and 3) length of long axis. The degree of cell alignment was characterized by measuring the angle of cell orientation relative to the vertical axis of the image. Care was taken to ensure that cell-seeded samples were imaged with the direction of mandrel rotation parallel to the vertical axis of the image. A total of at least 10 images ( $n \geq 10$ ) per scaffold condition were analyzed using this method. The degree of cell orientation was characterized by the angular standard deviation for a wrapped normal distribution as previously described.

### 2.3.5 Immunofluorescence Staining

Expression and organization of F-actin, VE-cadherin, and vinculin were visualized by immunostaining ECs on scaffolds after 3 days post-seeding. Briefly, all samples were fixed in 3.7% paraformaldehyde (EMD chemicals, Gibbstown, NJ, USA) for 15 min and washed with PBS 3 times for 5 min each. Next, cells were permeabilized by incubation in 0.1% Triton X-100 (Sigma Aldrich) for 5 min, washed 3 times with PBS for 5 min each, then incubated in 1% bovine serum albumin (Santa Cruz Biotechnology, Inc., Santa Cruz, CA, USA) for 30 min to reduce non-specific background staining. For VE-cadherin staining, the samples were incubated for 1 hr in rabbit polyclonal anti-VE-cadherin primary antibody (1:200, Abcam, Cambridge, MA, USA). The samples were then washed with PBS and incubated for 1 hr in goat anti-rabbit secondary antibody (1:100, DyLight 488, Jackson ImmunoResearch, West Grove, PA, USA). To stain for vinculin, samples were incubated for 1 hr in mouse monoclonal anti-vinculin primary antibody (1:100, Abcam), washed with PBS, and incubated for 1 hr in goat anti-mouse secondary antibody (DyLight 594, Jackson ImmunoResearch). For F-actin staining, samples were incubated in rhodamine phalloidin (Invitrogen) for 20 min. All samples were counter-stained using Vectashield with 4',6-diamidino-2-phenylindole (DAPI, Vector Laboratories, Burlingame, CA, USA) to visualize cell nuclei and imaged using a Leica DMI6000-B microscope. Vinculin was quantified by using Image J to perform image analysis of area covered by fluorescent (red) pixels within each image.

### 2.3.6 Cell Adhesion Assays

ECs on nanofiber scaffolds were exposed to hydrodynamic shear stress to test cell adherence using a custom parallel plate flow chamber (PPFC) of similar design to that previously described [93]. After 3 days of static culture, EC-seeded scaffolds were mounted in the PPFC and exposed to shear stresses of 20 and 40 dyne/cm<sup>2</sup> for 1 hr according to the parallel plate approximation as previously described [93]. These shear stresses were chosen because they represent the average (20 dyne/cm<sup>2</sup>) and maximum (40 dyne/cm<sup>2</sup>) physiologic shear stress that ECs experience *in vivo* [94]. Samples were mounted in the PPFC such that the direction of fluid flow was parallel to the direction of electrospun fiber alignment (i.e. mandrel rotation). The PPFC was connected to a media reservoir and centrifugal pump (Ismatec BVP-Z, Cole-Parmer, Vernon Hills, IL, USA) to form a closed flow loop. Cell culture media was maintained at 37°C and under a 5% CO<sub>2</sub>. Prior to flow, cell nuclei were stained with Hoechst 33342 live cell stain (Invitrogen). The PPFC with EC-seeded scaffolds were then mounted on an imaging stage and imaged at 6 random locations on each scaffold at 0, 5, 10, 20, 30, 40, 50, 60 min after the onset of flow. Three separate flow experiments were conducted for each scaffold condition (n = 3) to yield a total of n = 18 images for each scaffold condition. Image J software was used to count cell nuclei in each image, and the strength of cell adhesion was represented by the percentage of cells remaining after the onset of flow relative to the initial images before flow (0 min).

### 2.3.7 Statistical Analysis

All values are reported as the mean ± standard deviation. Statistical analysis was performed using one-way analysis of variance (ANOVA) with a significance criterion of  $p \leq 0.05$ . For assessment of scaffold fiber diameter and alignment, 50 random fibers from n = 5 images per scaffold condition were used (250 fibers total). To determine cell morphology and alignment, a total of at least 10 images (n ≥ 10) per scaffold condition were analyzed. Cell studies were repeated to ensure reproducibility of trends.

## 2.4 Results

### 2.4.1 Scaffold Topography

Electrospinning was used in this study to fabricate fibrous PCL/collagen scaffolds with variable fiber diameters and degrees of alignment. By tuning polymer solution concentration, mandrel rotation rate, and electrospinning parameters (Table 2.1), a 3 x 3 scaffold property matrix was formed. This 3 x 3 scaffold property matrix is displayed in Figure 1, where

representative SEM images demonstrate that both fiber diameter and fiber alignment were systematically controlled using the aforementioned fabrication parameters. Quantitative analysis of the SEM images showed that fiber diameters produced from the 5%, 10%, and 15% (w/v) polymer solutions were roughly 100 nm, 300 nm, and 1200 nm, respectively (Figure 2, Table 2.2), and will be referred to hereafter as “100-nm”, “300-nm”, and “1200-nm”, respectively. Scaffold fiber alignment was controlled by electrospinning onto a stationary TCPS substrate or rotating the TCPS substrate on a mandrel at 1500 and 3000 rpm. Histograms of fiber orientation were plotted for each scaffold condition and show close agreement to the wrapped normal distribution (Supplemental Figure 1). These results indicate that the degree of fiber alignment systematically increased with greater mandrel rotation rates, while the angular standard deviation systematically decreased (Table 2.2). Scaffolds electrospun at static conditions, 1500 rpm and 3000 rpm will be referred to hereafter as “random”, “semi-aligned”, and “fully-aligned”, respectively, to describe the degree of fiber orientation. Additionally, increasing the mandrel rotation rate, and thus increasing fiber alignment, did not have a statistically significant influence on scaffold fiber diameter (Figure 2.2).

Solution Concentration (% w/v)	Flow Rate (ml/hr)	Distance (cm)	Voltage (kV)	Needle gauge (g)
5	1	10	19	30
10	2	10	16	25
15	5	10	17	18

**Table 2.1:** PCL/collagen electrospinning parameters for scaffolds with varying fiber diameter

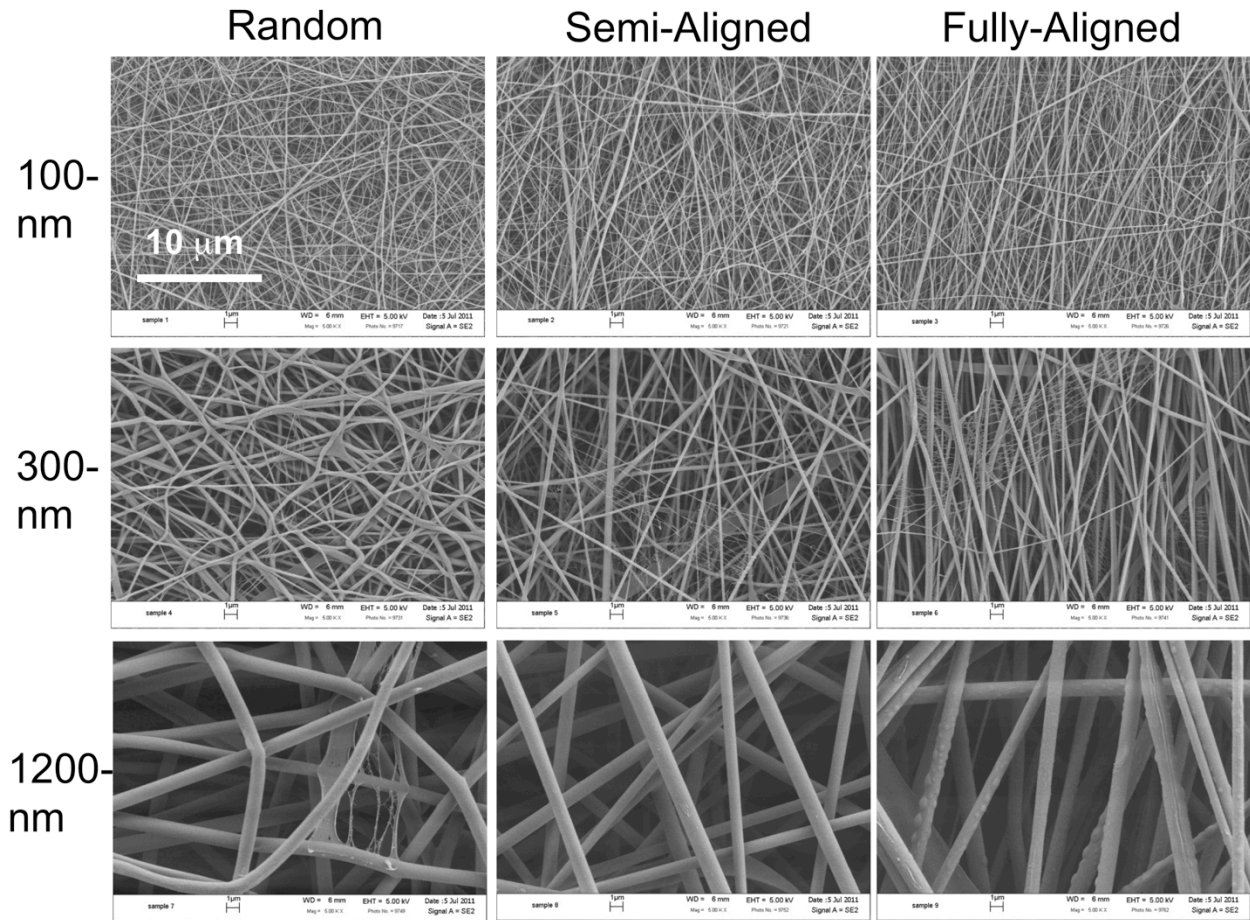


**Figure 2.1:** Representative SEM images of electrospun PCL/collagen scaffolds. A 3 x 3 scaffold property matrix was formed by systematically varying fiber diameter (100-nm, 300-nm, and 1200-nm) and degree of fiber alignment (random, semi-aligned, and fully-aligned).

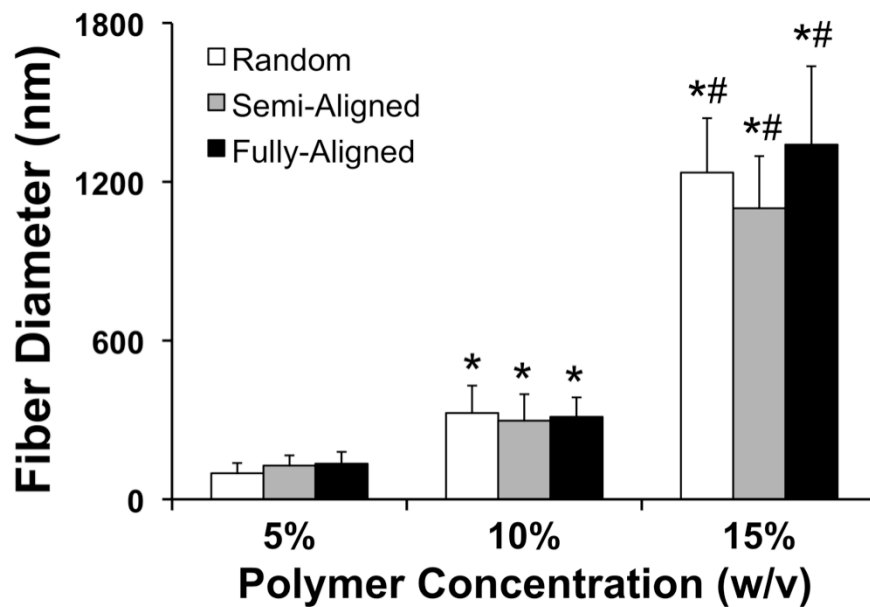


**Figure 2.2:** Fiber diameters for scaffolds electrospun from various polymer solution concentrations (5%, 10%, and 15% w/v) and fabrication parameters with varying degrees of fiber alignment. An “\*” indicates a statistical difference from the 5% (w/v) group, and a “#” indicates statistical difference from the 10% (w/v) group ( $p < 0.05$ ) ( $n = 250$  fibers for each group).

Solution Concentration (% w/v)	Rotation Speed (rpm)	Designation	Fiber Diameter (nm)	Fiber Angular Deviation (°)	Cell Angular Deviation (°)
5	0	100-nm, Random	99 ± 39	68.7	59.8
	1500	100-nm, Semi-Aligned	127 ± 39	35.9	47.2
	3000	100-nm, Fully-Aligned	135 ± 44	27.9	33.5
10	0	300-nm, Random	326 ± 103	54.6	51.8
	1500	300-nm, Semi-Aligned	297 ± 100	34.7	43.5
	3000	300-nm, Fully-Aligned	311 ± 73	19.1	24.8
15	0	1200-nm, Random	1235 ± 205	56.6	55.5
	1500	1200-nm, Semi-Aligned	1101 ± 196	43.4	58.3
	3000	1200-nm, Fully-Aligned	1341 ± 296	20.4	59.4

**Table 2.2:** Electrospun fiber diameter, fiber angular standard deviation, and cell angular standard deviation for scaffolds fabricated with varying solution concentrations, electrospinning parameters, and mandrel rotation rates.

#### 2.4.2 Cell Morphology and Alignment

To assess the effect of scaffold topography on cell morphology and alignment, ECs were seeded onto the scaffolds and visualized using a live-cell stain (Calcein AM). Three days post-seeding, the cells were attached to the PCL/collagen scaffold and remained viable. Figure 2.3 shows representative images of ECs attached to each scaffold group. The cells formed a confluent monolayer on the surface of the 100-nm and 300-nm scaffolds; however, cells on the 1200-nm scaffolds appeared to have infiltrated into the constructs (white arrows, Figure 2.3) evidenced by fibers traversing over the fluorescent cells, which were located at an imaging focal plane within the scaffold. Furthermore, cells on 100-nm and 300-nm aligned scaffolds displayed an elongated morphology, whereas cells on random scaffolds exhibited a polygonal, cobblestone-like appearance. Quantitative analysis of the images indicated that projected cell area on the 1200-nm scaffolds was significantly diminished compared to the 100-nm and 300-nm scaffolds, whereas cell area was not significantly affected by degree of fiber alignment (Figure 2.4a). Although fiber alignment did not have a statistically significant impact on projected cell area, it did have a dramatic effect on cell elongation, as measured by cell aspect ratio and length of long axis. Figures 4b,c show that cells on the 100-nm and 300-nm aligned scaffolds had significantly greater aspect ratios and long axis lengths as compared to those on 1200-nm and random scaffolds.

Figure 2.3 shows that fiber orientation had a strong impact on guiding cell alignment on 100-nm and 300-nm scaffolds, whereas cells on 1200-nm scaffolds were unaffected. Normalized histograms of cell orientation on 100-nm and 300-nm scaffolds provided quantitative evidence that cell alignment increased with greater fiber alignment (Supplemental Figure 2.2). Furthermore, cell angular deviation systematically decreased with diminishing fiber angular standard deviation for these scaffold groups (Table 2.2). In contrast, the analysis demonstrated that fiber alignment did not impact cell orientation on the 1200-nm scaffolds.

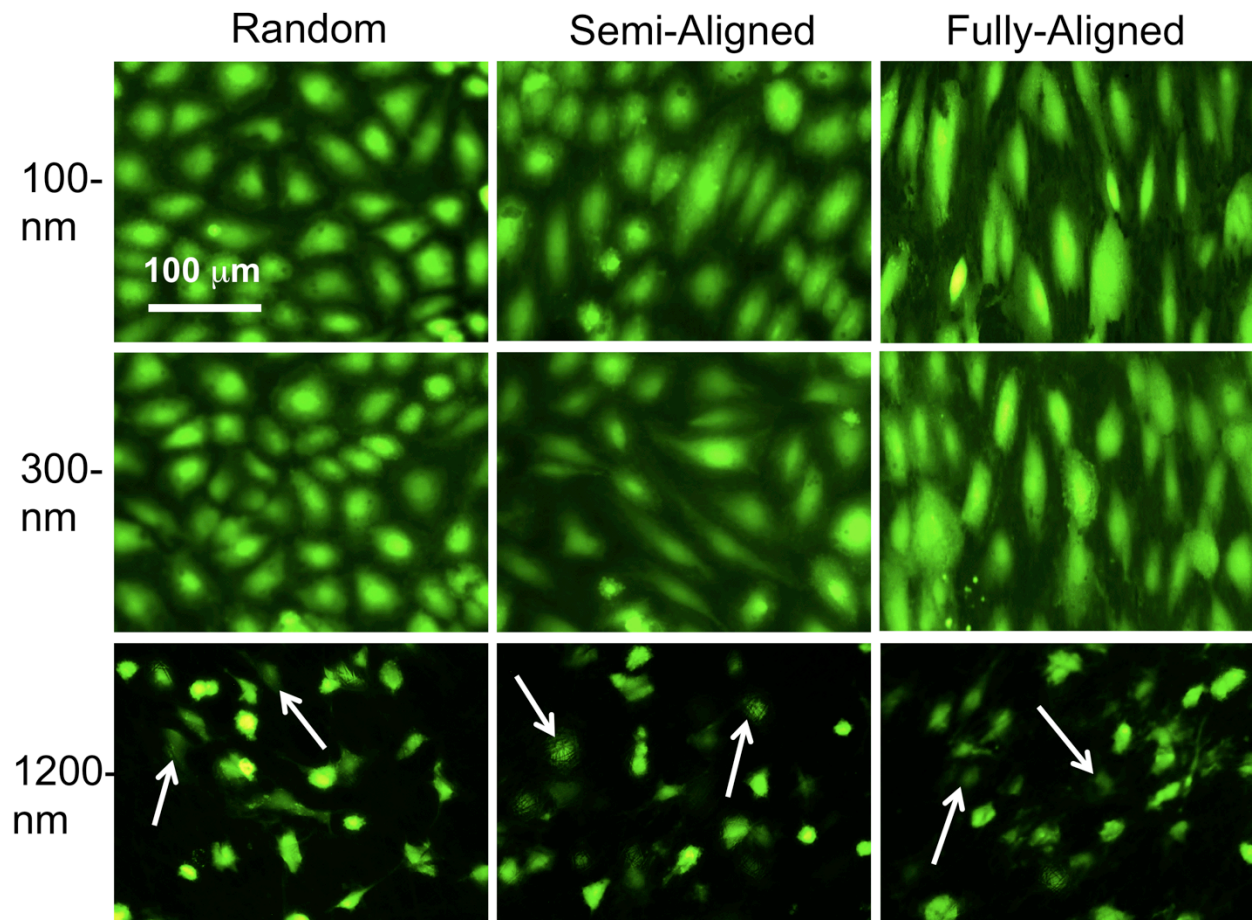


**Figure 2.3:** Representative images of Calcein AM stained ECs on electrospun scaffolds. Cells displayed a more cuboidal morphology on random nanofiber scaffolds as compared to scaffolds with defined fiber alignment, where cells were elongated and aligned with the direction of fiber orientation. Cells on 1200-nm scaffolds displayed a rounded morphology, no preferred orientation, and appear to have infiltrated into the scaffold (white arrows).

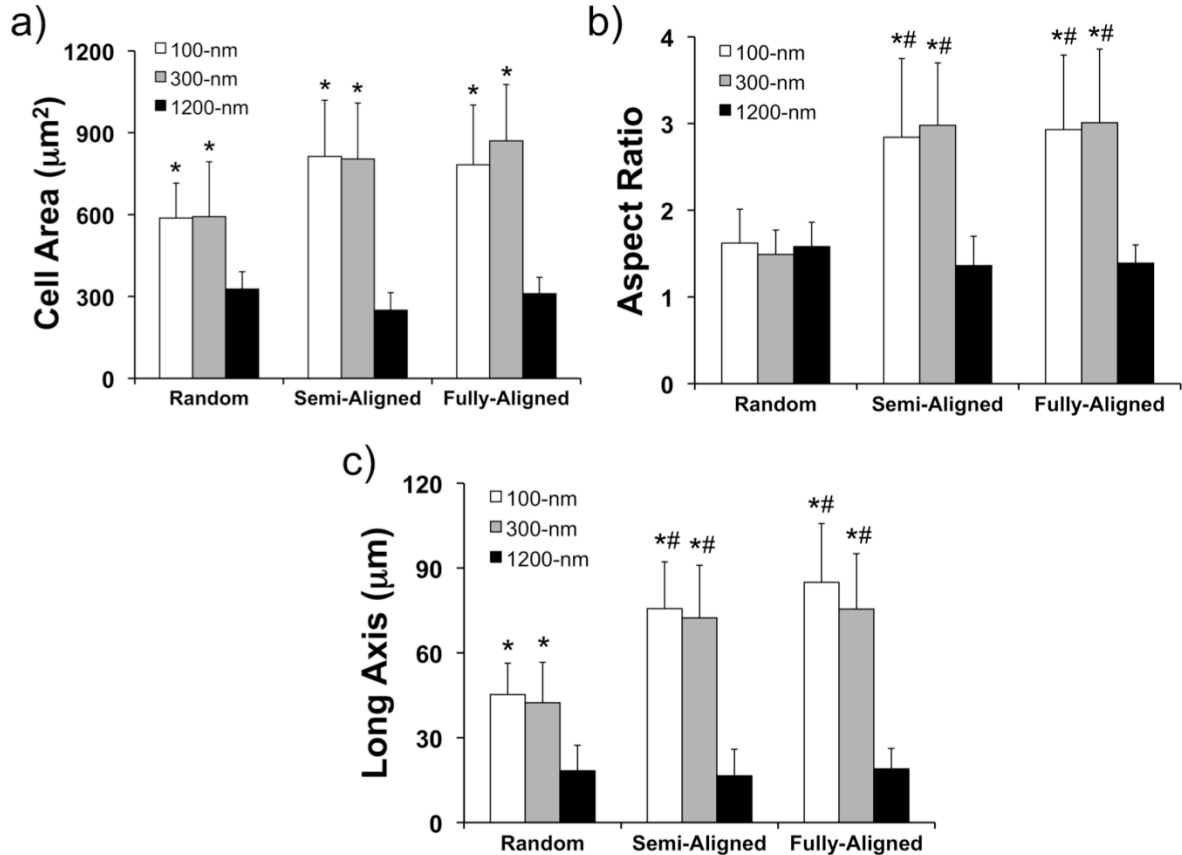


**Figure 2.4:** Quantitative analysis of a) cell area, b) aspect ratio, and c) length of long axis of Calcein AM stained ECs on electrospun scaffolds. Cell area was significantly greater on 100-nm and 300-nm scaffolds when compared to 1200-nm scaffolds. Cell aspect ratio and length of long axis were significantly increased on aligned 100-nm and 300-nm scaffolds as compared to random and 1200-nm scaffolds. An “\*” indicates a statistical difference from the 1200-nm scaffold group, and a “#” indicates statistical difference from the random scaffold group ( $p < 0.05$ ) ( $n \geq 10$  images per group).

### 2.4.3 Structural and cell-substrate protein expression and organization

Immunofluorescence staining of cells on electrospun scaffolds was performed to determine the effect of scaffold topography on expression and organization of two principal structural proteins (F-actin and VE-cadherin) and a cell-substrate linker protein (vinculin). Staining for F-actin showed that cells on 100-nm and 300-nm random scaffolds had randomly oriented actin filaments that appeared to line the periphery of the cells (Figure 2.5). In contrast, cells on 100-nm and 300-nm fully-aligned scaffolds exhibited thick actin filaments traversing the full length of the cell parallel to fiber alignment. Cells on the 1200-nm scaffolds also stained positive for F-actin, however, the actin appeared to be weakly expressed. All 100-nm and 300-nm scaffolds showed strong staining for VE-cadherin at cell-to-cell contact regions, whereas this

protein was not expressed in cells on 1200-nm scaffolds (Figure 2.6). To determine the effect of scaffold topography on cell-scaffold interactions, ECs were stained for vinculin, an important protein complex for cell adhesion. Figure 2.7 shows that cells on semi-aligned and fully-aligned scaffolds displayed higher levels of vinculin as compared to those on random scaffolds. The total area occupied by vinculin in the images was quantified using image analysis and results are shown in Figure 2.8 ( $n = 3$  scaffolds per condition). Cells on semi-aligned and fully-aligned scaffolds exhibited 2-3 times the amount of vinculin expression of those cells on random scaffolds; however, no statistically significant difference in amount of vinculin was observed between cells on semi-aligned versus fully-aligned scaffolds.

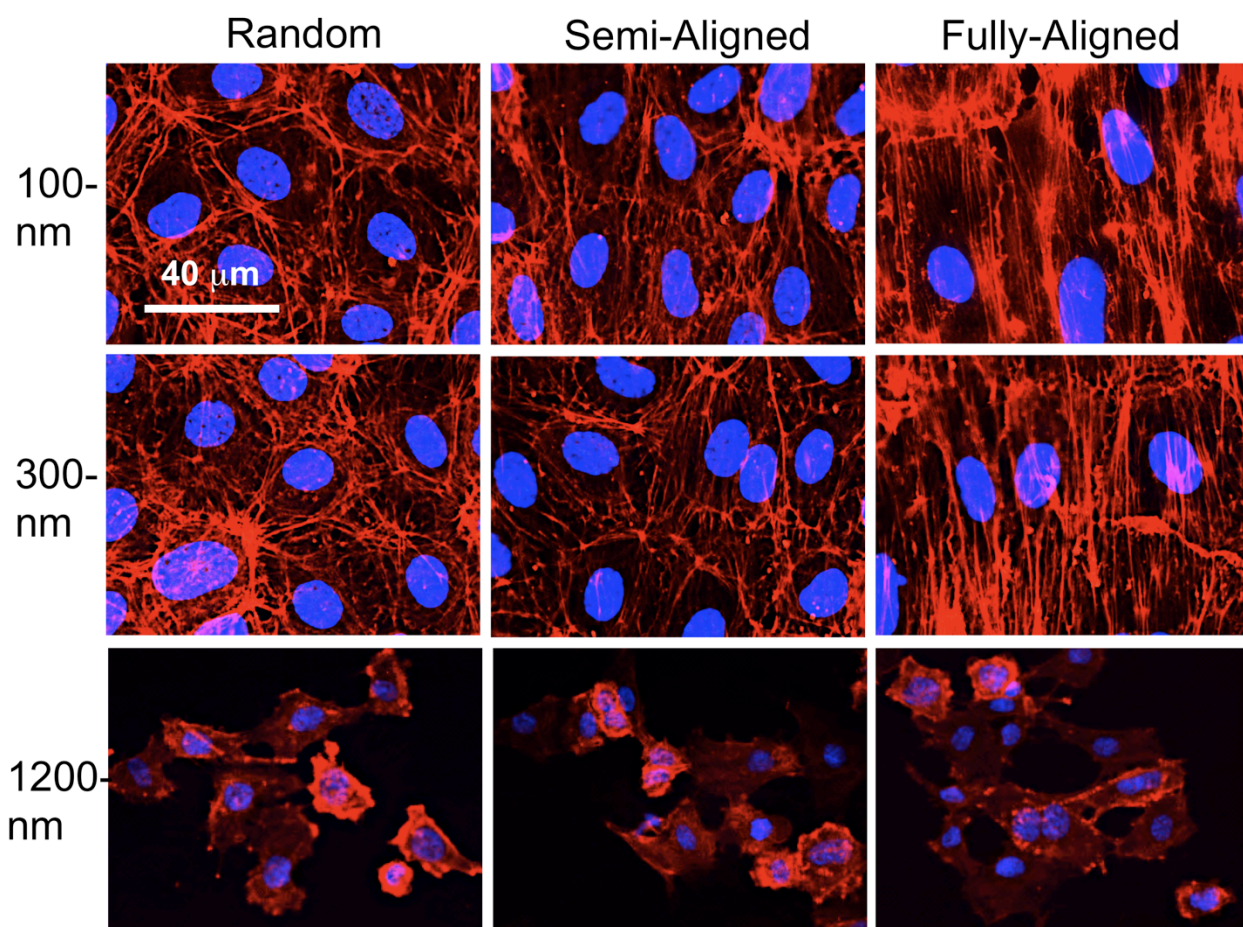


**Figure 2.5:** Representative fluorescent images of cytoskeletal F-actin organization for ECs on scaffolds with varying fiber diameters and orientations. F-actin (red) was organized at the periphery of cells on random 100-nm and 300-nm scaffolds, but was located throughout the cells in thick bundles parallel to nanofiber orientation on 100-nm and 300-nm fully-aligned scaffolds.

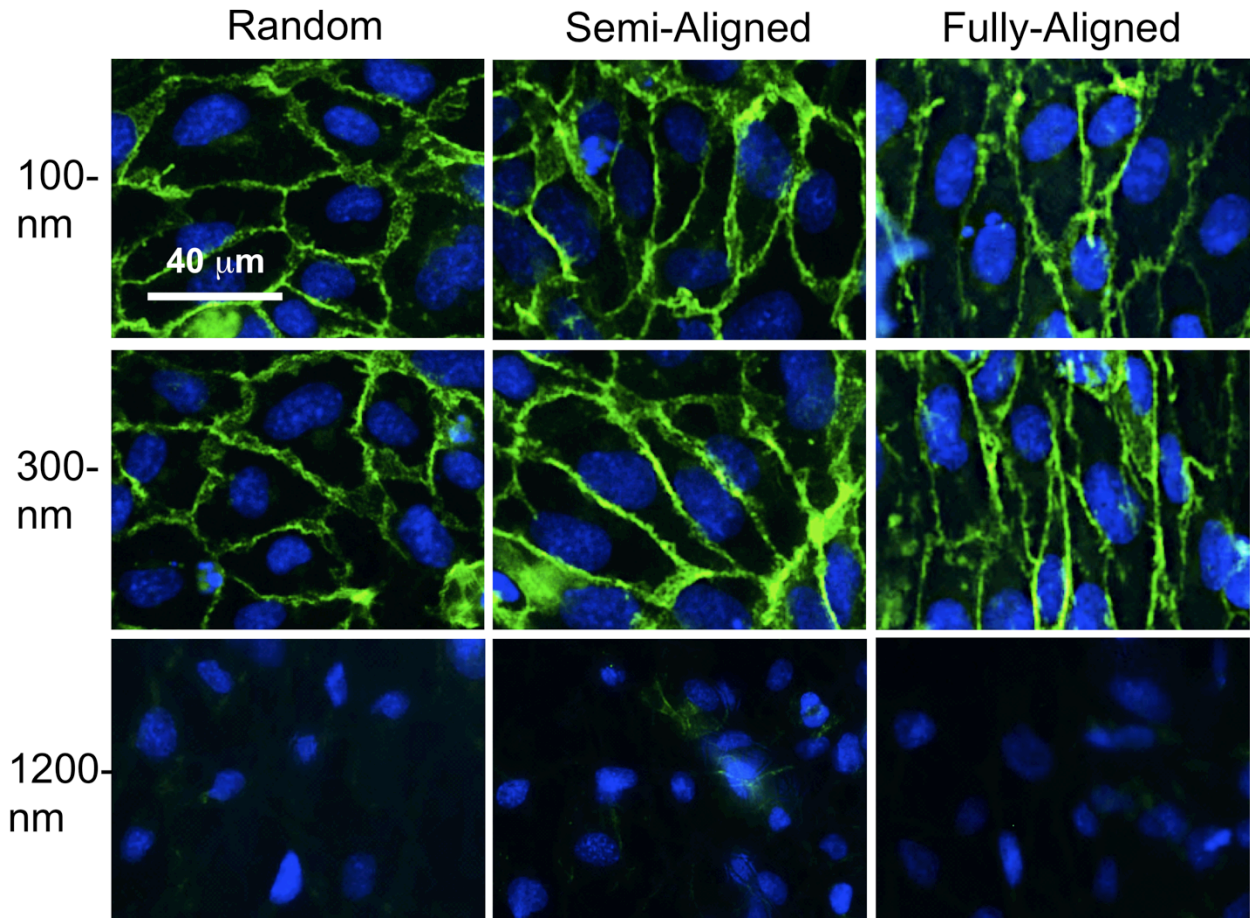


**Figure 2.6:** Representative fluorescent images of VE-cadherin (green), showing that the cell-cell adhesion protein was strongly expressed at the periphery of cells where cell-cell contact occurred on 100-nm and 300-nm scaffolds. VE-cadherin was not, however, expressed in cells on 1200-nm scaffolds.

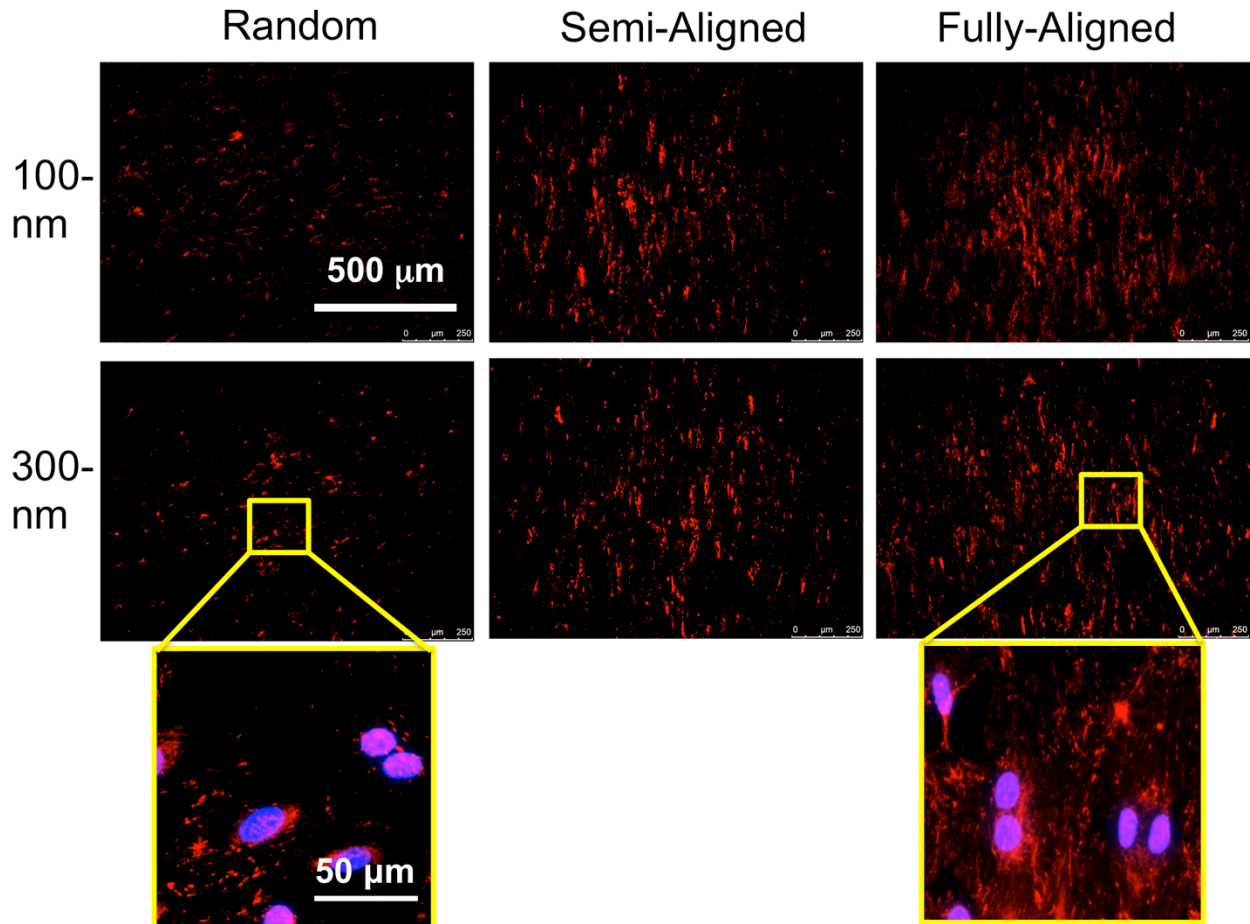


**Figure 2.7:** Staining for vinculin revealed that cells on aligned scaffolds displayed a considerably higher level of vinculin than cells on random scaffolds.

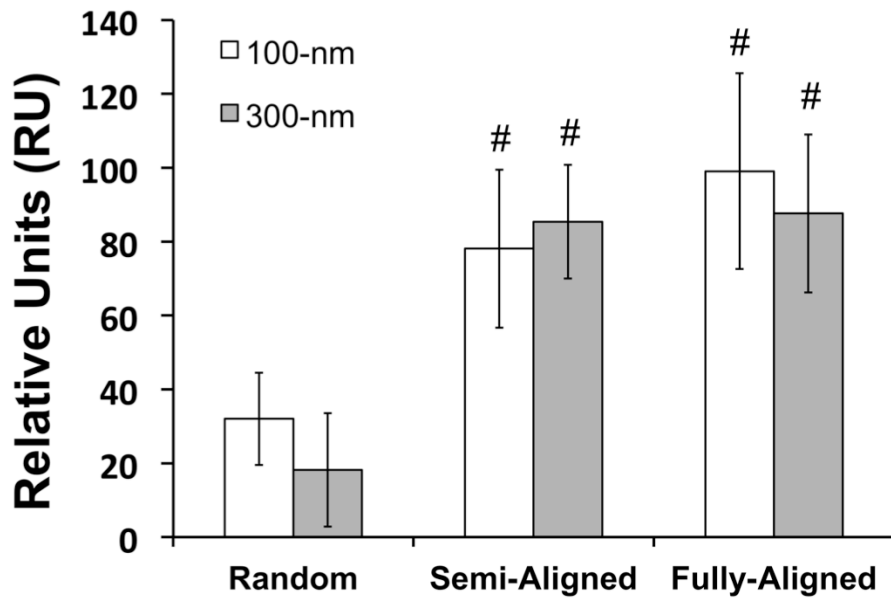


**Figure 2.8:** The total area covered by vinculin in each image was quantified using image analysis. The results show that cells on aligned scaffolds expressed 2-3 times the amount of vinculin than cells on random scaffolds. A “#” indicates a statistical difference from the random scaffold group ( $p < 0.05$ ) ( $n = 9$  images per group).

#### 2.4.4 EC Adhesion Under Fluid Flow

Confluent monolayers of ECs on both 100-nm and 300-nm scaffolds were exposed to continuous hydrodynamic shear stresses of 20 and 40 dyne/cm<sup>2</sup> using a PPFC to test the adhesion strength of ECs on different scaffold topographies. Cells on 1200-nm scaffolds were not exposed to flow since confluent monolayers had not formed and therefore were not considered as viable for use as a vascular graft lumen. Cell adhesion was dynamically measured by counting cell nuclei on the scaffolds for a duration of 60 min under flow. Figure 2.9a shows the percentage of cells attached to the 100-nm and 300-nm scaffolds at a shear stress of 20 dyne/cm<sup>2</sup> as a function of time. The rate of cellular detachment was the greatest for cells on the random scaffolds as compared to those on the aligned scaffolds. When cells were exposed to 40 dyne/cm<sup>2</sup> (Figure 2.9b), the rate of cellular detachment increased for cells on all scaffolds as compared to those exposed to 20 dyne/cm<sup>2</sup> (Figure 2.9a), however the trends remained the same between scaffold groups. Figures 9a and 9b show that cell detachment from all scaffolds at both shear stresses normalize after about 40 min. Figure 2.9c shows the percentage of cells attached on all scaffolds after 60 min flow at both shear stresses. These results demonstrate that ECs exposed to 20 dyne/cm<sup>2</sup> on fully-aligned scaffolds display roughly 95% cell adherence, whereas only ~80% and ~60% of cells remained adherent on semi-aligned and random scaffolds, respectively. At a shear stress of 40 dyne/cm<sup>2</sup>, roughly 62% of cells remained adherent on fully-aligned scaffolds, whereas 46% and 27% of cells were adherent to semi-aligned and random scaffolds, respectively. The results also demonstrate that scaffold fiber diameter did not have a statistically significant impact on cell attachment after 60 min of fluid flow.

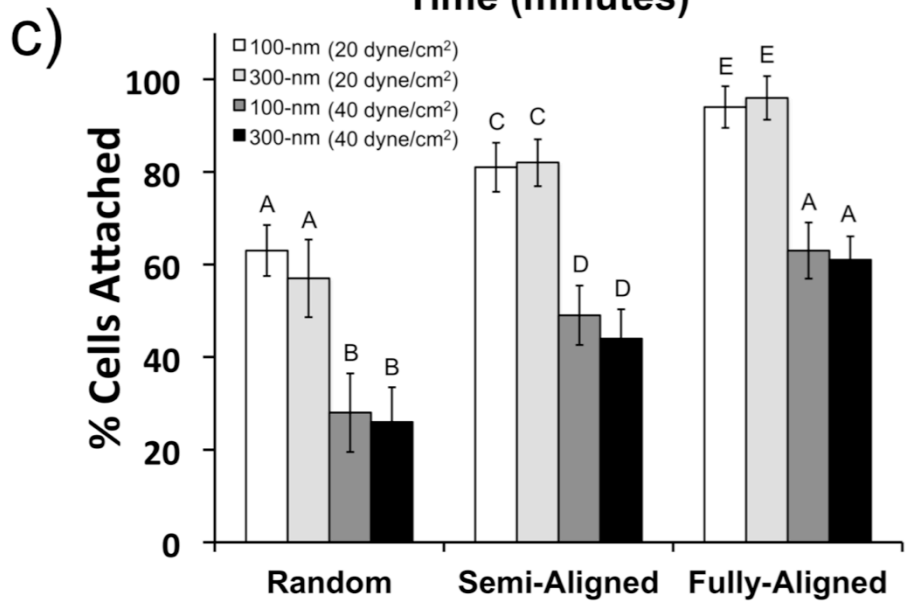
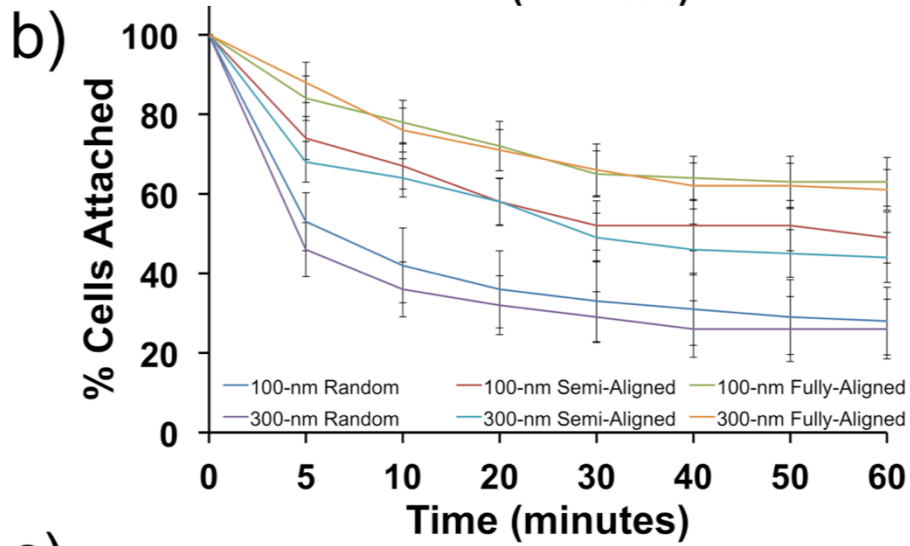
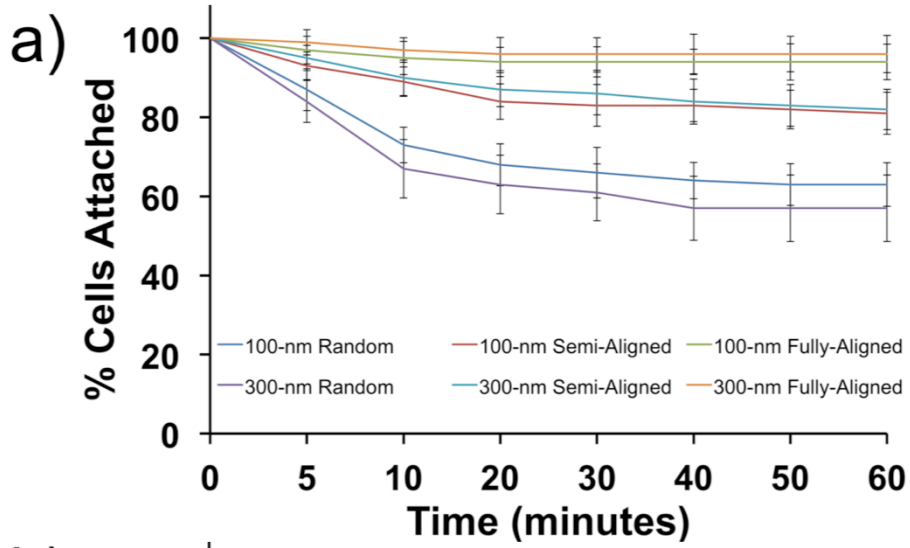


**Figure 2.9:** Percentage of cells that remained adherent to the 100-nm and 300-nm scaffolds during 60 min of a) 20 dyne/cm<sup>2</sup> and b) 40 dyne/cm<sup>2</sup> continuous hydrodynamic shear stress. c) Percentage of cells adherent to the scaffolds after 60 min of continuous hydrodynamic shear stress. Values marked with the same letter are not significantly different ( $p < 0.05$ )

## 2.5 Discussion

Due to the prevalence of vascular disorders, such as coronary and peripheral artery disease, there exists a great need for viable conduits for bypass grafting that overcome the drawbacks associated with the use of autologous grafts. Vascular tissue engineering has provided a promising approach for creation of such grafts, commonly in the form of tubular scaffolds composed of natural or synthetic materials wherein viable vascular cells are seeded to allow construct remodeling once implanted *in vivo* [16, 17, 37, 63, 95]. A critical factor for the success of these bioengineered vessels is the formation of a well-functioning endothelium on the lumen portion of the construct that provides the graft with a non-thrombogenic layer between circulating blood and the arterial wall. The endothelium should be well adhered to the surface of the construct and exhibit native EC morphology, specifically, ECs aligned with the direction of blood flow to permit high shear stress resistance and minimal flow disturbance [2, 22, 62, 96]. We hypothesized, therefore, that if ECs can be directed to adopt morphology, alignment, and F-actin organization similar to those *in vivo* using scaffold topographical cues, then resistance to deformation and detachment under shear stress may be enhanced as a result. Therefore, the main objective of this study was to examine the effect of scaffold design parameters, such as fiber diameter and orientation, on EC morphology, alignment, and adherence to the surface under fluid flow. The overarching goal was to investigate the potential of these nanofiber substrates to direct ECs to form a confluent endothelium with morphological and structural protein properties similar to ECs *in vivo* in an effort to increase adherence to the scaffold surface.

To test this hypothesis, PCL/type I collagen scaffold topography was varied by tuning electrospinning parameters and mandrel rotation rates to systematically produce a 3 x 3 scaffold property matrix consisting of 3 different fiber diameters (roughly 100 nm, 300 nm, and 1200 nm) each with varying degrees of fiber alignment. PCL/collagen was specifically chosen for this study because of its promising characteristics as a vascular graft that include excellent mechanical properties [17], capacity to facilitate EC attachment/growth [37], and patency when implanted *in vivo* [36]. Quantitative analysis of SEM images show that the degree of fiber alignment systematically increased with greater mandrel rotation rate (Figure 2.3), while the

angular standard deviation systematically decreased (Table 2.2), indicating a more aligned structure. Scaffold topography had a large impact on EC morphology as visualized by fluorescence microscopy of Calcein AM stained cells. Cells had a well-spread morphology and were able to form confluent monolayers on 100-nm and 300-nm scaffolds, whereas cells on 1200-nm scaffolds were rounded and appeared to have infiltrated into the scaffold (Figure 2.4). In addition, ECs on 100-nm and 300-nm scaffolds expressed VE-cadherin in a continuous and linear manner at the periphery of cells where cell-cell contacts occurred, regardless of fiber orientation, indicating a confluent endothelium (Figure 2.8). Quantitative analysis of the fluorescent images indicated that cell area and length of long axis were significantly greater for cells on 100-nm and 300-nm scaffolds as compared to 1200-nm scaffolds (Figures 5b and c). These findings are consistent with a study by Ju *et al.*, in which ECs displayed a well-spread morphology only on 270 nm diameter PCL/collagen fibers when compared to cells on micron diameter fibers [37]. One possible explanation is that an increase in pore size, which is known to substantially increase with larger electrospun fiber diameter [37, 55], may lead to a lack of sites available for focal adhesions to form on the underlying substrate and thus prevent adequate cell spreading. Nonetheless, nanofiber meshes fabricated in this study (i.e. 100-nm and 300-nm) allowed EC spreading and formation of an uninterrupted endothelial layer, as evidenced by VE-cadherin expression at cell-cell junctions, after 3 days post-seeding.

Our results show that fiber orientation had a significant impact on directing the degree of EC alignment and elongation – consistent with the phenomenon of contact guidance. Similar studies have shown that various cell types, such as fibroblasts [39], neural stem cells [97], tendon progenitor cells [98], and smooth muscle cells [41], respond to aligned fiber matrices in a similar manner by elongating and aligning parallel to fiber orientation. For this study, a systematic increase in EC alignment coincided with a greater degree of nanofiber alignment (Figure 2.6), while the angular standard deviation for both cells and fibers systematically decreased (Table 2.2). Additionally, ECs were elongated in the direction of fiber orientation for 100-nm and 300-nm aligned scaffolds quantified by a significant increase in cell aspect ratio and long axis (Figures 5b and c). Concurrent with variations in cell alignment and elongation, ECs displayed drastically different cytoskeletal arrangements in response to scaffold topography. ECs on 100-nm and 300-nm random scaffolds exhibit a banding pattern of F-actin at the periphery of the cells, whereas cells on fully-aligned 100-nm and 300-nm scaffolds display F-actin bundles that

traverse the entire length of the cell parallel to fiber orientation (Figure 2.7). These results are strikingly similar to those in a study by Inoguchi *et al* [62], where HUVECs were seeded on the lumen portion of an electrospun vascular graft and exposed to gradually graded shear stress over a 3 day period. In that study, HUVECs exposed to incremental shear stress aligned with the direction of flow and expressed thick bundles of F-actin parallel to shear stress, whereas cells under static conditions retained a cuboidal morphology and expressed banding patterns of F-actin at their periphery. When exposed to fluid flow, ECs displaying a cuboidal morphology detached in response to shear stress less than 3.2 dyne/cm<sup>2</sup>, whereas cells that had gradually undergone a regimen of gradual increase in shear stress over a 3 day period displayed an aligned morphology and remained adherent under a shear stress of 19.2 dyne/cm<sup>2</sup> [62]. This is one example of how EC adherence to a scaffold can be improved *in vitro* by using dynamic culturing conditions such as exposing EC-seeded vascular grafts to physiological fluid flow through bioreactor preconditioning [60, 99]. Previous work has shown that preconditioning grafts before implantation increases EC retention, functionality, and graft patency once implanted *in vivo* as compared to non-conditioned grafts [61, 66]. As a result of shear stress preconditioning, ECs adopt an elongated morphology, align with the direction of fluid flow, and display cytoskeletal (F-actin) and adherens junction protein (vascular endothelial (VE) cadherin) organization similar to the native endothelium [62, 66]. These morphological and structural protein properties directly contribute to an endothelium with minimal flow disturbance and high adherence to the graft [2, 22, 62, 96] – both of which are required for a successful vascular graft. While shear-stress preconditioning is an effective method to increase the attachment and shear resistance of seeded ECs, this process is resource intensive and time consuming, often taking several days or weeks for the ECs to reorganize sufficiently to resist detachment under physiological shear stresses (20 – 40 dynes/cm<sup>2</sup>) [20, 65].

In contrast, the method used in this study to influence endothelial cell morphology did not require the use of fluid flow preconditioning to increase EC adherence to the scaffolds under physiological shear stress. We found that topographical guidance of ECs into an elongated morphology and organized cytoskeleton in the direction of fluid flow was an effective means to increase EC resistance to detachment under fluid flow. Specifically, we demonstrated that ECs cultured on fully-aligned scaffolds had roughly 35% more cells adherent to the scaffold as compared to ECs on random scaffolds after 60 min of flow at both shear stresses of 20 and 40

dyne/cm<sup>2</sup>. In addition, ECs cultured on aligned scaffolds had a much lower rate of detachment compared to those cultured on random scaffolds (Figure 2.9b, c). With the increase in cell elongation, our results demonstrated that ECs also expressed higher levels of vinculin – an adaptor protein that is recruited from the cytoplasm to regulate focal adhesion complexes in anchorage dependent cells [100]. Quantification of vinculin expression showed that ECs on semi-aligned and fully-aligned scaffolds had roughly 2-3 times the amount of vinculin as compared to ECs on random scaffolds. An interesting finding of this work is that even though ECs cultured on semi-aligned and fully-aligned scaffolds displayed statistically insignificant differences in morphologies (Figure 2.4) and vinculin expression (Figure 2.8), ECs on fully-aligned scaffolds had roughly 15% more cells attached after 60 min of flow at both shear stresses when compared to ECs on semi-aligned scaffolds. We propose that the difference in EC attachment between the semi-aligned and fully-aligned scaffolds arose from differences in cell alignment and F-actin organization with the direction of flow. In a study conducted by Barbee *et al* [101], ECs cultured under flow conditions showed that cells had a significant decrease in height profile and were streamlined with the direction of flow as compared to those cultured under static conditions. The authors showed that cell alignment and elongation in the direction of flow decreased the shear stress and gradients of shear stress at the cell surface. We believe that a similar phenomenon occurred with cells on the fully-aligned scaffolds in the present study, where topography-induced elongation and alignment in the direction of fluid flow diminished shear stress at the cell surface, thereby decreasing detachment as compared ECs on random and semi-aligned scaffolds. Therefore, our findings indicate that not only can EC elongation, alignment, and F-actin organization be directed by tuning nanofiber orientation through contact guidance, but also the resulting changes in F-actin organization and increased adherence to the scaffold surface are similar to those of ECs exposed to hydrodynamic shear stress without the use of dynamic culturing conditions using fluid flow systems.

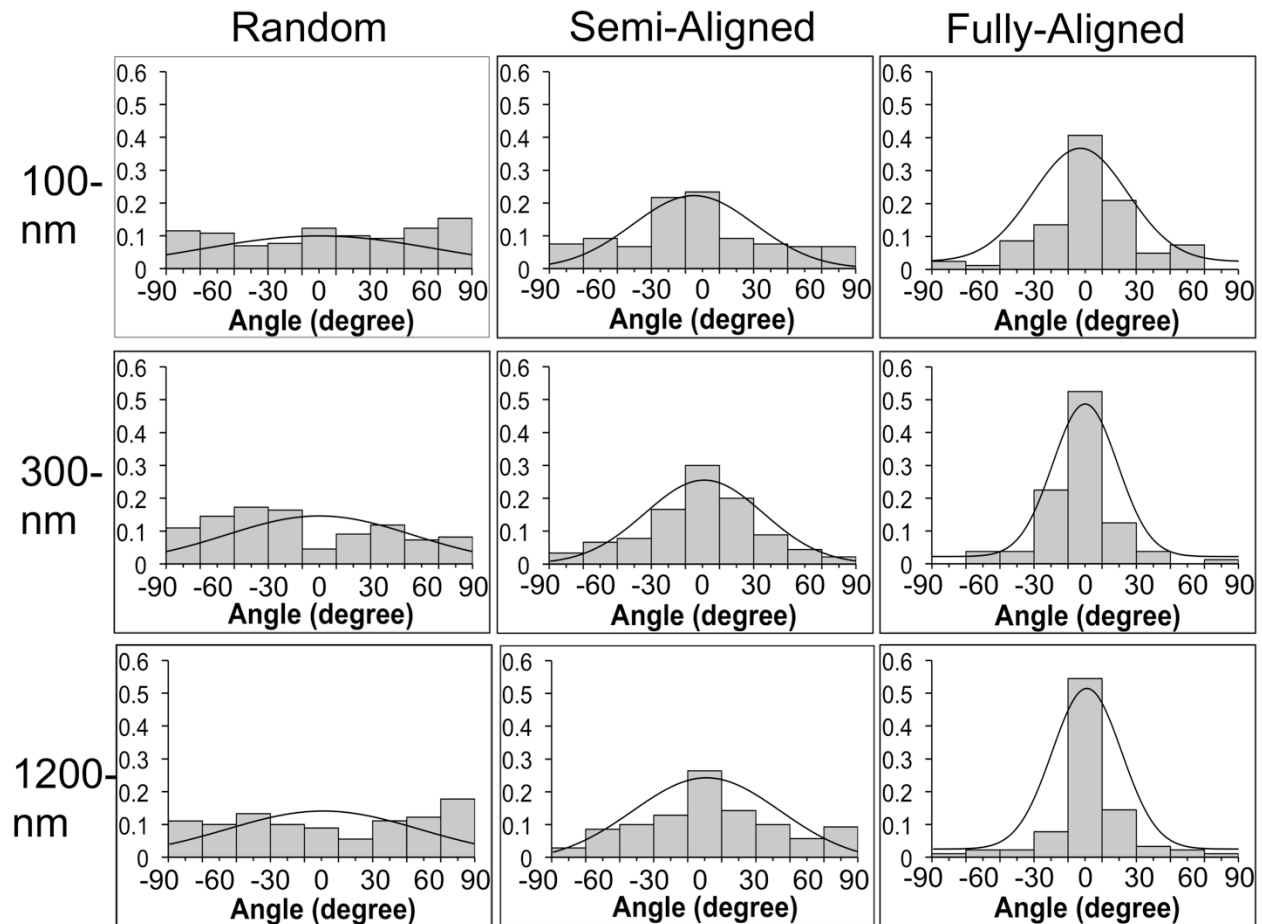
## 2.6 Conclusion

In this study, we varied the fiber diameter and orientation of electrospun fibers in an effort to elucidate the impact of scaffold topography on EC morphology, alignment, structural protein expression/organization and adherence under fluid flow. We found that ECs on nanofiber scaffolds formed confluent monolayers and alignment of cells was found to systematically

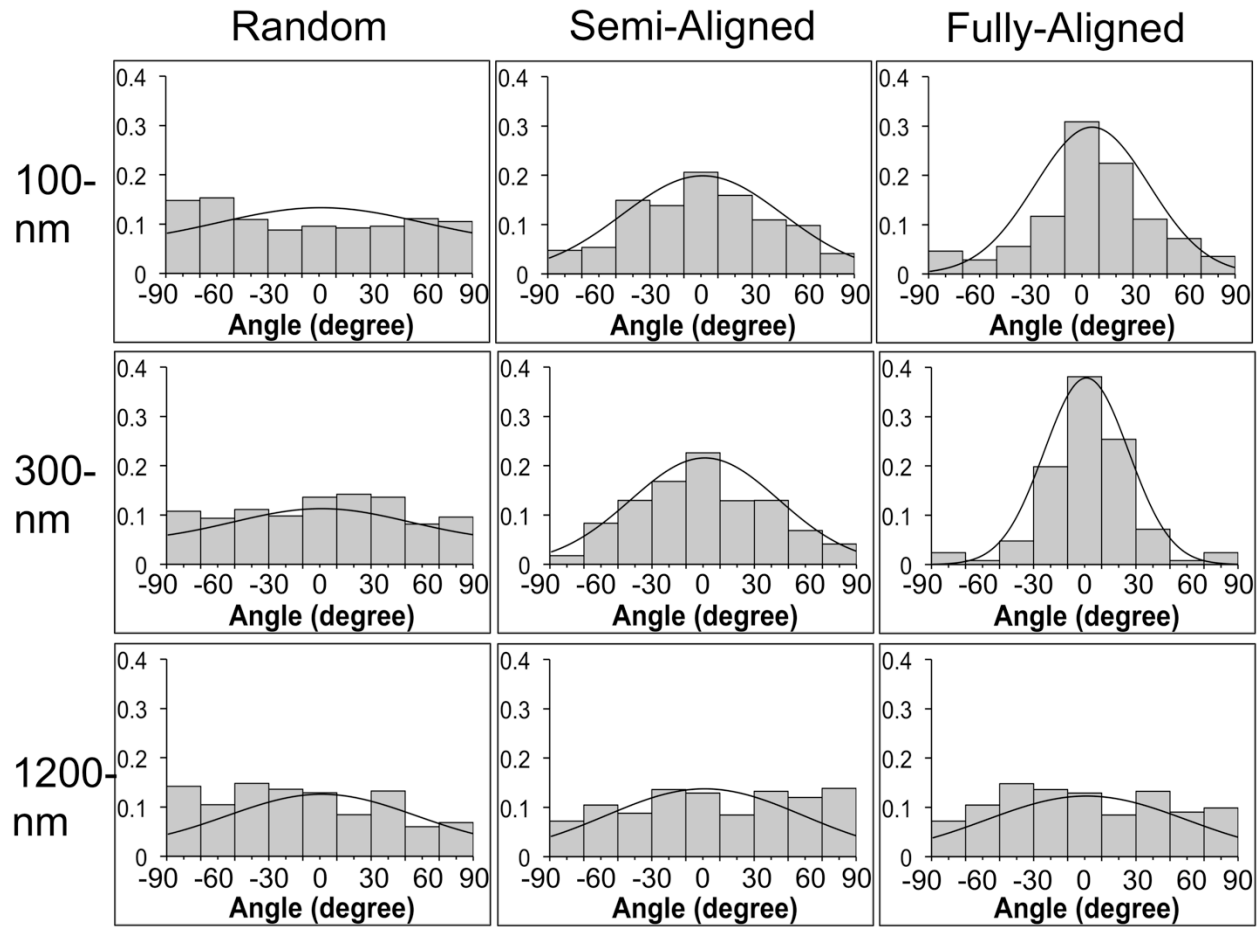
increase as a function of increased fiber orientation, leading to a fully aligned endothelium on the most aligned scaffolds. Concurrent with cell alignment, ECs exhibited thick bundles of oriented F-actin parallel to the direction of fiber alignment, mimicking F-actin organization of native ECs in straight artery segments that are exposed to high shear stress. ECs on fully-aligned scaffolds displayed higher levels of adherence to the scaffolds under physiological shear stress as compared to those on random and semi-aligned scaffolds. These findings indicate that EC morphology and alignment can be directed through tuning nanofiber topography and could be used to form an uninterrupted, fully aligned and shear resistant endothelium for vascular tissue engineering applications.

## 2.7 Acknowledgements

Funding for this project was provided by the National Institutes of Health/National Heart, Lung, and Blood Institute R01HL098912, National Science Foundation CAREER Award CBET 0955072, and Institute for Critical Technology and Applied Science Grant at Virginia Tech.



**Supplemental Figure 2.1:** Normalized histograms of fiber angle for scaffolds electrospun with varying fiber diameters and fiber orientations (grey bars) ( $n = 250$  fibers for each group). Degree of fiber alignment systematically increased with an increase in mandrel rotation rate. Curves represent the wrapped normal distribution (Equation 2.1).



**Supplemental Figure 2.2:** Normalized histograms of cell angle for ECs seeded on scaffolds with varying fiber diameters and fiber orientations (grey bars) ( $n \geq 10$  images per group). Cell alignment systematically increased with fiber alignment on 100-nm and 300-nm scaffolds. Curves represent the wrapped normal distribution (Equation 2.1).

### **Chapter 3: A Fiber-Optic-Based Imaging System for Non-Destructive Assessment of Cell-Seeded Tissue-Engineered Scaffolds**

Hofmann MC<sup>1,\*</sup>, Whited BM<sup>2,\*</sup>, Criswell T<sup>3</sup>, Rylander MN<sup>2,4</sup>, Rylander CG<sup>2,4</sup>, Soker S<sup>3</sup>, Wang G<sup>2</sup>, and Xu Y<sup>1</sup>

<sup>1</sup> Department of Electrical Engineering, Virginia Polytechnic Institute and State University, Blacksburg, VA 24061, USA

<sup>2</sup> School of Biomedical Engineering and Sciences, Virginia Tech – Wake Forest University, Blacksburg, VA 24061, USA

<sup>3</sup> Wake Forest Institute for Regenerative Medicine, Virginia Polytechnic Institute and State University, Blacksburg, VA 24061, USA

<sup>4</sup> Department of Mechanical Engineering, Virginia Polytechnic Institute and State University, Blacksburg, VA 24061, USA

\* These authors contributed equally to this work

# A Fiber-Optic-Based Imaging System for Nondestructive Assessment of Cell-Seeded Tissue-Engineered Scaffolds

Matthias C. Hofmann, M.S.,<sup>1,\*</sup> Bryce M. Whited, M.S.,<sup>2,\*</sup> Tracy Criswell, Ph.D.,<sup>3</sup>  
Marissa Nichole Rylander, Ph.D.,<sup>2,4</sup> Christopher G. Rylander, Ph.D.,<sup>2,4</sup> Shay Soker, Ph.D.,<sup>3</sup>  
Ge Wang, Ph.D.,<sup>2</sup> and Yong Xu, Ph.D.<sup>1</sup>

A major limitation in tissue engineering is the lack of nondestructive methods that assess the development of tissue scaffolds undergoing preconditioning in bioreactors. Due to significant optical scattering in most scaffolding materials, current microscope-based imaging methods cannot “see” through thick and optically opaque tissue constructs. To address this deficiency, we developed a fiber-optic-based imaging method that is capable of nondestructive imaging of fluorescently labeled cells through a thick and optically opaque scaffold, contained in a bioreactor. This imaging modality is based on the local excitation of fluorescent cells, the acquisition of fluorescence through the scaffold, and fluorescence mapping based on the position of the excitation light. To evaluate the capability and accuracy of the imaging system, human endothelial cells (ECs), stably expressing green fluorescent protein (GFP), were imaged through a fibrous scaffold. Without sacrificing the scaffolds, we nondestructively visualized the distribution of GFP-labeled cells through a ~500  $\mu\text{m}$  thick scaffold with cell-level resolution and distinct localization. These results were similar to control images obtained using an optical microscope with direct line-of-sight access. Through a detailed quantitative analysis, we demonstrated that this method achieved a resolution on the order of 20–30  $\mu\text{m}$ , with 10% or less deviation from standard optical microscopy. Furthermore, we demonstrated that the penetration depth of the imaging method exceeded that of confocal laser scanning microscopy by more than a factor of 2. Our imaging method also possesses a working distance (up to 8 cm) much longer than that of a standard confocal microscopy system, which can significantly facilitate bioreactor integration. This method will enable the nondestructive monitoring of ECs seeded on the lumen of a tissue-engineered vascular graft during preconditioning *in vitro*, as well as for other tissue-engineered constructs in the future.

## Introduction

**T**ISSUE ENGINEERING aims at developing functional tissues and organs that replace or restore those damaged by disease and trauma.<sup>1–4</sup> In recent years, a bottom-up approach to tissue design has become increasingly popular, where custom-fabricated scaffolds are combined with appropriate cells and bioactive molecules to emulate the structure and function of the target tissue.<sup>5,6</sup> The *in vivo* success or failure of such engineered tissues depends on the critical *in vitro* preconditioning phase during which seeded cells can proliferate, differentiate toward a specific phenotype, and deposit native extracellular matrices. Specialized bioreactors are often utilized during preconditioning to provide the necessary mechanical and biochemical stimuli to

cell-seeded constructs that enhance tissue development (i.e., cellularity, cell differentiation, protein expression, and organization, etc.) before implantation.<sup>7–9</sup>

Optimizing the preconditioning phase is often a challenging and time-consuming process during which a cell-seeded construct should be periodically assessed with regard to the progress of tissue development. Conventional scaffold assessment methods typically require removal of the sample from the bioreactor followed by fixation, histological sectioning, and staining at a given time point. This method, however, destroys the sample and can only provide “snapshots” of tissue development at a limited number of time points.<sup>10,11</sup> This inefficiency severely limits our understanding of the biological processes associated with tissue growth during the *in vitro* preconditioning phase and is resource and time intensive.

<sup>1</sup>Department of Electrical and Computer Engineering, Virginia Tech, Blacksburg, Virginia.

<sup>2</sup>School of Biomedical Engineering and Sciences, Virginia Tech–Wake Forest University, Blacksburg, Virginia.

<sup>3</sup>WakeForest Institute for Regenerative Medicine, Wake Forest University School of Medicine, Winston-Salem, North Carolina.

<sup>4</sup>Department of Mechanical Engineering, Virginia Tech, Blacksburg, Virginia.

\*These authors contributed equally to this work.

Due to the aforementioned limitations, researchers have begun developing alternative nondestructive methods for assessing tissue development. For example, methods based on confocal or nonlinear microscopy have been employed to nondestructively monitor cells in their microenvironment.<sup>12–17</sup> Of particular relevance are two recently reported microscope-based methods that can monitor tissue development during preconditioning in bioreactors.<sup>18,19</sup> Despite these advances, current microscope-based methods for non-destructive tissue assessment remain constrained by two major drawbacks: a limited imaging depth and a short working distance.

The main focus of this study is to develop a fiber-optic-based (FOB) imaging method that can significantly extend the depth of cell-level resolution imaging as well as greatly improve the working distance of the imaging system. In particular, we focus on developing a novel imaging method that evaluates bioengineered vascular grafts, where the assessment endothelialization on the lumen (inner surface) of synthetic bioengineered blood vessels is of significant interest.<sup>20</sup> From an imaging standpoint, it is exceedingly difficult to monitor endothelialization on the lumen through a thick and optically opaque tubular vessel using conventional microscopy techniques. Furthermore, the preconditioning of such vessels in pulsatile-flow bioreactors poses additional geometrical constraints on the objective's working distance. Therefore, the key significance of this study is the design and validation of an entirely new imaging technique that is capable of performing nondestructive imaging of endothelial cells (ECs) through a thick and optically opaque electrospun scaffold housed within a bioreactor.

Our approach is based on embedding thin and flexible microimaging channels (MICs) directly into a fibrous scaffold. The validity of our method was demonstrated by imaging through an opaque scaffold model and visualizing green fluorescent protein (GFP)-labeled ECs located on the luminal surface. The accuracy of our method was quantified through a direct comparison with conventional, direct-line-of-sight fluorescence microscopy. To further illustrate the advantage of this method, we compared its performance with a confocal laser scanning microscope (CLSM) and demonstrated that the imaging depth of this method exceeded that of the CLSM by at least a factor of 2. To demonstrate future potential of our imaging method, we nondestructively tracked the migration and cytokinesis of ECs through the opaque scaffold by capturing several consecutive images at 30-min time intervals. Another practical yet important advantage of this imaging method is the dramatically increased working distance (up to 8 cm), which significantly facilitated the integration of our imaging platform with a parallel-plate bioreactor for nondestructive cell tracking. Given the advantages offered by a significantly enhanced imaging depth and working distance, this imaging method may find numerous *in vitro* or *in vivo* applications in other tissue-engineered constructs that contain epithelial tissues.

## Materials and Methods

### Design principle

The basic principle of our imaging system is illustrated in Figure 1. Through each MIC, a fiber micromirror is inserted

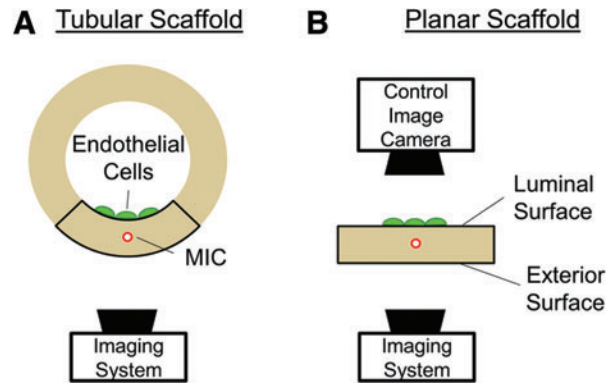


**FIG. 1.** Experimental design. **(A)** A thin and flexible microimaging channel (MIC) is embedded into the scaffold wall, allowing controlled local delivery of fluorescence excitation light. By scanning the excitation light across the lumen of the vessel and capturing the cell-emitted fluorescence responses from the exterior surface, the original cell distribution of the luminal surface can be reconstructed via signal processing. All imaging hardware for fiber-optic-based (FOB) imaging is denoted “imaging system” in the figure and is located outside the exterior surface. **(B)** For a quantitative comparison with the control images, a planar scaffold was fabricated to allow direct-line-of-sight access to the luminal surface using a conventional optical microscope (control image camera). Both before and after unwrapping, the imaging system for FOB imaging remains the same. The control image camera captured images of cell distribution using conventional, direct-line-of-sight, fluorescence microscopy. Such images were denoted as control images and used to validate our FOB imaging method. The model scaffold in **(B)** can be regarded as the result of “unwrapping” the tubular scaffold in **(A)**. Color images available online at [www.liebertonline.com/tec](http://www.liebertonline.com/tec)

to locally deliver pump light for fluorescence excitation across a region of interest (ROI) on the lumen. By collecting the cell-emitted fluorescent signals from the scaffold's exterior and mapping them to the scanning position, the distribution of ECs on the scaffold lumen can be reconstructed through signal processing. The system shown in Figure 1A is sufficient for the purpose of vascular studies. However, in order to quantify the resolution of our imaging system, the imaging results need to be compared with a current gold standard such as conventional, direct line-of-sight, fluorescence microscopy.

To facilitate a direct comparison with conventional fluorescence microscopy, the imaging study was carried out using the planar scaffold model shown in Figure 1B. After “unwrapping” the tubular scaffold in Figure 1A, all GFP-labeled ECs are located on one side of the model scaffold—the luminal surface. As a result, their distributions can be directly imaged using standard, direct-line-of-sight, fluorescence microscopy to obtain control images. The opposite of the luminal surface is referred to as the exterior surface. As indicated in Figure 1, both before and after “unwrapping,” the imaging system required to perform FOB imaging remains on the side of the exterior surface. The results obtained through FOB imaging are referred to as fluorescence-mapped images, or simply, mapped images. By comparing the difference between the control and the mapped images, both the resolution and the accuracy of the imaging method

could be quantitatively determined. We emphasize that the main purpose of the system design in Figure 1B is to ensure that after validation using the planar scaffold model, the FOB imaging method can be directly applied to the investigation of tubular scaffolds.

#### Scaffold fabrication

The scaffolds used in this study were fabricated by electrospinning bioabsorbable poly(D,L-lactide) (PDLLA).<sup>21</sup> Briefly, a 22% w/v PDLLA ( $M_w = 80,000$  g/mol) (Sur Modics Pharmaceuticals) solution was prepared in a 3:1 ratio of tetrahydrofuran:dimethylformamide (Fisher Scientific) under gentle stirring for 4 h. Next, a 5-mL syringe with a 18G blunt-tip needle was filled with the solution and delivered at a flow rate of 5 mL/h. A 16-kV voltage difference provided by a DC power supply (Gamma High Voltage Research) was applied between the needle tip and a 2" diameter aluminum mandrel rotating at 60 rpm. The distance between the needle and the mandrel was set at 15 cm. Electrospun scaffold mats with an approximate thickness of 300  $\mu$ m were fabricated and placed in a desiccator overnight to remove the residual solvent. An SEM image of the scaffold is shown in Figure 2A.

#### MIC integration

A transparent MIC for excitation light delivery was embedded into a PDLLA scaffold via heat sintering.<sup>22</sup> The MIC is a flexible silica glass capillary (Polymicro Technologies) with an inner and outer diameter of 150 and 245  $\mu$ m, respectively. The scaffold composite was fabricated by placing the MIC between two 3  $\times$  2 cm rectangular sections that were cut from the electrospun PDLLA mats, as illustrated in Figure 2B. Next, the scaffold sections with the MIC were placed between two glass slides and compressed with a 32 g weight in an oven at 54°C for 15 min. This technique effectively sintered the scaffold sections together to produce a one-piece planar scaffold with an MIC securely embedded, as shown in Figure 2C.

For this study, a total of 3 MIC-embedded planar scaffolds were fabricated with an average thickness of  $513 \pm 21$   $\mu$ m. These scaffolds were used to conduct the imaging study illustrated in Figure 1B. The top surface of the scaffold represents the luminal surface of a blood vessel. As previously discussed, the planar configuration allowed a direct-line-of-sight access to the luminal surface for quantitative image comparison and validation.

#### Cell culture and scaffold seeding

A human microvascular EC line was used for this experiment (hTIME; American Type Culture Collection), and cells were cultured in endothelial growth medium-2 (Lonza Biomedical). The cells were genetically modified by a lentivirus vector to stably express eGFP. The EC-GFP cells were sorted by fluorescence-activated cell sorting (FACS Aria; BD Biosciences) for the highest  $\sim 5\%$  GFP expressing cells. ECs were grown in a 95% relative humidity atmosphere of 5% CO<sub>2</sub> at 37°C, and culture media were changed every 3 days.

Before cell seeding, the scaffolds were sterilized using 70% ethanol for 30 min, followed by three sterile phosphate-buffered saline (PBS) washes for 10 min each. A 300  $\mu$ L aliquot of media containing 100  $\mu$ g/mL fibronectin (Sigma Aldrich) was then added to the scaffold for 30 min to en-

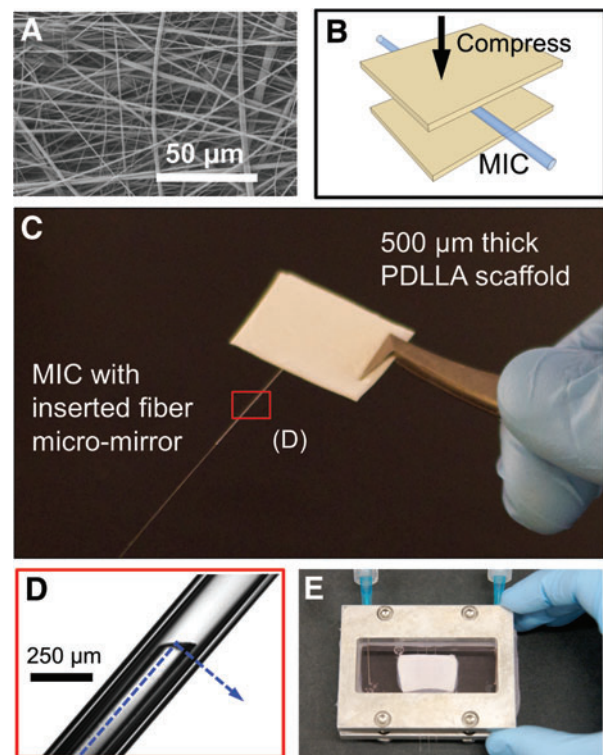


**FIG. 2.** Vascular scaffold model fabrication and bioreactor design. (A) poly(D,L-lactide) (PDLLA) was electrospun into a 300- $\mu$ m-thick scaffold mat. (B) A MIC was embedded into PDLLA by heat sintering two 3  $\times$  2 cm rectangular scaffold mats together. (C) Through heat sintering, a planar scaffold was fabricated with a luminal surface simulating blood vessel lumen and an exterior surface where diffused photons are collected to form fluorescence-mapped images using the FOB imaging method. (D) Microscope image of a fiber micro-mirror inserted into a MIC. The blue arrow indicates the direction of the excitation light. Through movement of the fiber, the excitation light was selectively delivered into the scaffold. (E) A photograph of the custom bioreactor designed to house the scaffold while simultaneously enabling external access to the MIC. Color images available online at [www.liebertonline.com/tec](http://www.liebertonline.com/tec)

hance cell adhesion. ECs were trypsinized, and cell viability was determined using trypan blue staining (Vi-cell; Beckman Coulter). Cells were then re-suspended in 100  $\mu$ L of media and seeded onto the luminal surface of the scaffold at a density of  $1 \times 10^4$  viable cells/cm<sup>2</sup>. The scaffolds were placed in the incubator for 2 h to allow cell attachment and were then washed gently with PBS to remove any unattached cells. The scaffolds were then placed in the bioreactor with cell culture media for imaging experiments.

#### Excitation light delivery

The delivery of fluorescence excitation light was achieved by inserting an optical fiber with a micromirror tip into the MIC. The fiber micromirror was fabricated by angle polishing a standard single mode optical fiber (SMF430; Nuferr, Inc.). The polishing angle was selected to be 45° so that the incidence angle of the excitation light exceeded the critical angle for total internal reflection at the polished air-silica

interface. This created an optical fiber mirror through which excitation light could be launched at a 90° angle relative to the fiber (Fig. 2D). By inserting the fiber mirror within the MIC, a highly localized beam of excitation light can be generated on the luminal surface of the scaffold.

#### *Spectral measurements and signal-to-noise ratio*

To investigate the signal-to-noise ratio (SNR) of cell fluorescence versus the background noise produced by scaffold autofluorescence, the spectral response of the cells and the scaffold were measured from 450 to 750 nm using a spectrometer (S2000; Ocean Optics). To quantify the background autofluorescence noise, the excitation spot was aimed toward a location on the scaffold that was void of cells. Conversely, the excitation spot was aimed directly at a cell to collect GFP fluorescence from the cells. The response signal was then collected through the scaffold by an EM-CCD camera (iXon+; Andor), and the excitation light was filtered out with a long-pass filter with a cutoff at 490 nm (BLP01-488R; Semrock). By using a long-pass filter, the spectral band with the largest SNR could be determined.

#### *Confocal laser scanning microscopy*

Three PDLLA scaffolds of varying thicknesses (100, 230, and 460 μm) were fabricated using the same electrospinning and sintering technique as previously described. GFP-labeled ECs were seeded onto one side (luminal surface) of the scaffolds at a density of  $1 \times 10^4$  viable cells/cm<sup>2</sup>, incubated for 2 h to allow cell attachment, and then placed into a culture dish with a 170 μm glass coverslip bottom on which the scaffold rested. The CLSM (Zeiss LSM510 META; Carl Zeiss, Inc.) equipped with a 10× Plan-Apochromat 0.45 NA objective (Carl Zeiss, Inc.) was then used to obtain a direct-line-of-sight image of cells on each scaffold and, subsequently, used in an attempt at “looking” through each scaffold to resolve the cells on the luminal surface.

#### *Statistical analysis of mapping results*

To quantify the accuracy and reliability of the imaging method, both the mean absolute error (MAE) and the root mean squared error (RMSE) were calculated between 25 pairs of fluorescence-mapped images and their corresponding control images for all three scaffold samples. Both the MAE and RMSE estimation method are widely accepted for comparing two sets of data obtained by intrinsically different methods.<sup>23</sup> The MAE is defined as follows:

$$MAE_i = \frac{1}{N} \sum_{n=1}^N |P_{i,n} - C_{i,n}| \quad (1)$$

The RMSE is defined as,

$$RMSE_i = \sqrt{\frac{1}{N} \sum_{n=1}^N (P_{i,n} - C_{i,n})^2} \quad (2)$$

In these equations,  $i$  is the trial number that ranges from 1 to 25,  $n$  is a specific pixel in each image,  $C_{i,n}$  are the control images,  $P_{i,n}$  are the fluorescence-mapped images, and  $N$  is the total number of pixels in the control as well as mapped images. Before error estimation, each  $C_{i,n}/P_{i,n}$  image pair was

normalized to values between 0 and 100 such that MAE and RMSE represented percent error. It is critical that the fluorescence-mapped image and the control image pairs overlap precisely to allow accurate error estimation. Therefore, a custom MATLAB image registration script was written to calculate the best spatial fit between  $C_i$  and  $P_i$  before error estimation.<sup>24</sup>

## **Results**

### *Bioreactor*

A custom bioreactor was designed to house the scaffold while simultaneously enabling FOB imaging via the MIC. The bioreactor was based on a parallel-plate flow chamber as previously reported in Ref.<sup>25</sup> The major difference was the use of a biocompatible silicone adhesive (Dow Corning, Midland, MI) to seal the portion of MIC that extended beyond the scaffold between a series of polydimethylsiloxane (PDMS) (Specialty Manufacturing, Inc., Saginaw, MI) gaskets and glass slides. The cavity created by the PDMS gaskets formed a sterile growth chamber, while the glass slides provided viewing access to both the luminal and exterior surface of the scaffold. A photograph of the bioreactor is shown in Figure 2E.

### *Procedure for fiber scanning and fluorescence mapping*

The imaging procedure is summarized in Figure 3A–C. First, a ROI is designated on the luminal surface, and then, the ROI is divided into a two-dimensional (2D) grid of imaging pixels (Fig. 3A). By adjusting the position and the angle of the fiber micromirror inside the MIC, a localized beam of excitation light can be delivered toward any given imaging pixel on the luminal surface, as indicated in Figure 3B. The light spot formed on the luminal surface is referred to as the excitation spot. The position and the angle of the fiber micromirror is carefully chosen such that the center of the excitation spot always coincides with its corresponding imaging pixel on the luminal surface. By repeating this process for each imaging pixel, a one-to-one correspondence is established between a specific set of fiber micromirror locations and the 2D grid of imaging pixels.

After linking the 2D imaging pixels with the fiber micromirror locations, the principle of the FOB imaging method can be explained as follows. If a GFP-labeled EC overlaps with the chosen imaging pixel, then the portion of the luminal surface illuminated by the excitation spot can generate significant green fluorescence. A part of the green fluorescence then travels through the scaffold to the exterior surface, and its intensity is measured using a sensitive detector. On the other hand, if the particular imaging pixel is void of GFP-labeled ECs, then the resultant fluorescence intensity captured by the detector would be noticeably weaker. Consequently, the fluorescence intensity measured by the detector provides a quantitative indication of the “amount” of GFP-labeled ECs within the specific imaging pixel on the luminal surface.

With this capability, the fiber micromirror can be moved such that the center of the excitation spot is sequentially scanned across all imaging pixels within the ROI, as indicated in Figure 3A. At each illuminated imaging pixel, the detector is used to record the amount of green fluorescence

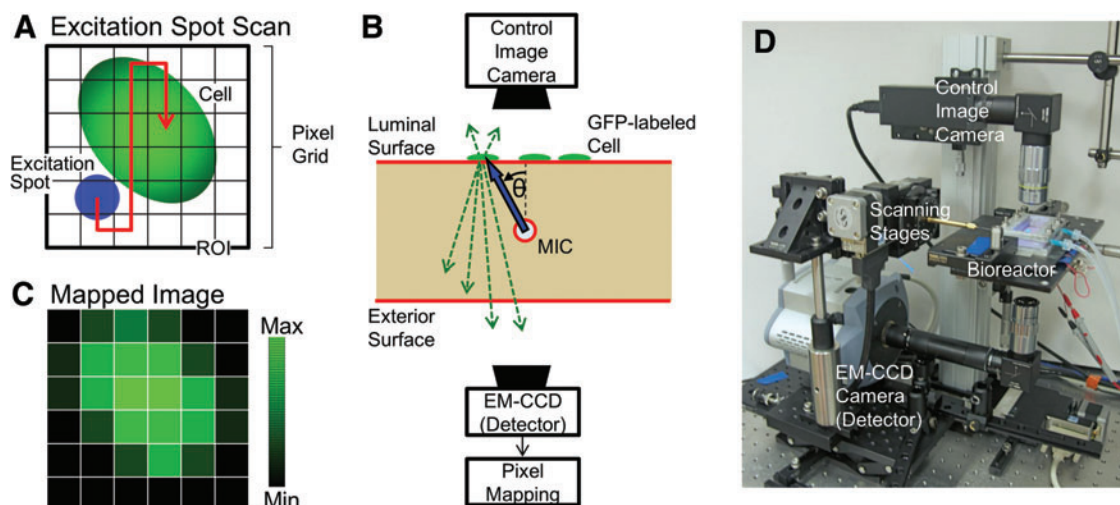


**FIG. 3.** Image mapping procedure and scanning system. **(A)** Illustration of a 2D pixel grid on the luminal surface of the scaffold containing a green fluorescent protein (GFP)-labeled EC (represented by the green oval) and the excitation spot (represented by the blue circle). **(B)** A schematic drawing illustrating the principle of the FOB imaging method. Through fiber micromirror delivery via an MIC, a micron-scale excitation spot is generated on the luminal surface. Within any given excitation spot, a different amount of green fluorescence is generated, depending on whether a GFP-labeled EC overlaps with the local excitation spot. An EM-CCD camera is used as a sensitive detector that captures the portion of fluorescence light which is transmitted through the scaffold to the exterior surface. The amount of fluorescence detected by the EM-CCD camera is then assigned to the corresponding imaging pixel. After sequentially scanning the excitation spot over all imaging pixels within the region of interest (ROI) followed by assigning fluorescence intensity measured by EM-CCD camera to each imaging pixel, a fluorescence-mapped image is obtained that depicts the distribution of GFP-labeled ECs on the luminal surface. Note that all imaging instruments required for this process are located on the side of the exterior surface. **(C)** An illustration of a fluorescence-mapped image that corresponds to the configuration shown in **(A)**. **(D)** A photograph of the imaging system showing the bioreactor on the heated platform. The micromirror position inside the MIC is controlled by the scanning stages in the figure. Color images available online at [www.lieberonline.com/tec](http://www.lieberonline.com/tec)

transmitted through the exterior surface of the scaffold. Finally, the measured values are assigned to each imaging pixel to generate the pseudo-color map, as shown in Figure 3C. This image is referred to as a fluorescence-mapped image. In Figure 3C, the pixels associated with low GFP intensity are plotted black, whereas the pixels with high GFP intensity are plotted green. As shown later in the Results section, such fluorescence-mapped images provide an accurate depiction of EC distributions on the luminal surface.

To implement the fiber scanning and fluorescence mapping procedure, we built a custom imaging system, as shown in Figure 3D. A heated platform was designed to firmly support the bioreactor containing the cell-seeded scaffold in place and to maintain a constant 37°C environment inside. Fluorescence excitation light was provided by a 473 nm continuous wave solid-state laser (BLM-100; Extreme Lasers, Inc.) operated at 0.5 mW and coupled into the optical fiber with the micromirror tip. The micromirror's position inside the MIC was controlled using a fiber chuck that was clamped to a motorized translation stage (UTM100PP.1; Newport) and a 0.01°-precision motorized rotation stage (UR-M100APP; Newport). Both motorized stages were controlled by a program developed in LabView (National Instruments). The fluorescence excitation light traveling through the scaffold to the exterior surface was measured using a high-sensitivity EM-CCD camera (iXon+; Andor) with a 2× long working distance objective attached (M-Plan; Mitutoyo). The distance from the objective to the bioreactor was 8 cm. Bandpass filters (525/45 BrightLine; Semrock, Rochester,

NY) were used to block the excitation light while letting GFP fluorescence emission light pass to the EM-CCD camera. The 500–545 nm band pass region was selected after selecting the spectral region with the highest SNR.

#### Control image capture

To evaluate the accuracy of the fluorescence-mapped images, a CCD camera (XCD-X710; Sony) with a GFP band-pass filter in front was mounted above the bioreactor to capture control images. In Figure 3B, this CCD camera is represented by the “control image camera.” An external 473 nm light source (not shown in Fig. 3B) was used to illuminate the entire luminal surface and provided excitation light for the control images. The control images were obtained using conventional, direct-line-of-sight fluorescence microscopy, and can, therefore, be used as the gold standard for image comparison and analysis. By quantitatively comparing the fluorescence-mapped images to the control images, the quality and reliability of the imaging system was calculated using a custom image comparison script written in MATLAB (MathWorks). It should be emphasized that such control images were only available using the “unwrapped” planar scaffold instead of the original tubular scaffold.

#### Imaging results and image analysis

The goal of this research is to develop a method that images “through” an optically thick and opaque scaffold. For

all fiber-scanned images, a  $300 \times 300 \mu\text{m}$  ROI was selected on the scaffold's luminal surface, where the ECs were seeded. Afterward, fiber scanning and fluorescence mapping was performed to image the GFP-labeled ECs, as previously described. After each fluorescence mapping, we used direct-line-of-sight access to take a control image of the same ROI to quantify the experimental error. Both the mapped and the control images were plotted in a false-color black-green, where the brightness of the green color represents the intensity of GFP fluorescence (Fig. 4). When comparing the mapped images with the control images, we observe that the spatial distribution of the GFP-labeled ECs are in good agreement between the corresponding image sets. Furthermore, from the mapped images, it is evident that individual cells could be resolved through the  $\sim 500 \mu\text{m}$  thick scaffolds.

To quantify the overall accuracy of the imaging method, the MAE and RMSE were calculated for 25 pairs of fluorescence-mapped and control images. The MAE and RMSE results for each scaffold were plotted as histograms in Figure 5, showing overall error deviation for both image comparison methods. The mean  $\pm$  SD of the MAE and RMSE between the three scaffolds was found to be  $5.83\% \pm 0.88\%$  and  $10.26\% \pm 1.14\%$ , respectively.

#### Comparison with confocal microscopy

The penetration depth of the FOB imaging method through the PDLLA scaffold was compared with that of confocal laser scanning microscopy, which is widely used in tissue engineering to image through biologically thick tissues and scaffolds.<sup>15</sup> We used the experimental configuration shown in Figure 6A and B to quantify the quality of the optical image when we attempt to image "through" the scaffold.

First, the CLSM was used to obtain a direct-line-of-sight image of cells in each scaffold sample (Fig. 6A). Next, the scaffolds were reversed, and the CLSM was used in an attempt to image the cells "looking" through the scaffold (Fig.

6B). To obtain the sharpest possible image of cells on the luminal surface when imaging through the scaffold, a z-stack was performed at  $5\text{-}\mu\text{m}$  increments until the luminal surface reached the imaging focal plane. This measurement is analogous to placing the confocal microscope outside a blood vessel (i.e., exterior surface) and trying to image through the scaffold to capture EC distributions on the luminal surface.

GFP-ECs can easily be imaged if placed in the direct line of sight to the CLSM objective (Fig. 6C); however, the resolution of confocal images is greatly diminished when "seen" through the  $100\text{-}\mu\text{m}$ -thick PDLLA scaffold (Fig. 6D). Furthermore, confocal microscopy failed to visualize individual cells through the thicker  $230$  and  $460\text{-}\mu\text{m}$  PDLLA scaffolds (Fig. 6E and F, respectively). In contrast, the FOB imaging method was able to detect and accurately identify individual EC distribution through the  $\sim 500\text{-}\mu\text{m}$ -thick PDLLA scaffold (Fig. 6H). The corresponding direct-line-of-sight image in Figure 6G confirmed the accuracy of the fluorescence-mapped image in Figure 6H.

#### Mapping resolution

Based on the mapping procedure and image processing theory, the resolution of this imaging method is directly determined by the size of the excitation spot. For quantitative analysis, the size of the excitation spot is defined as the full-width-half-maximum (FWHM) of the excitation light intensity profile on the luminal surface. Mathematically, the scanning process is equivalent to performing a discrete convolution of the features inside the ROI with the excitation spot profile.<sup>26</sup> Hence, the mapped image can be regarded as the convolution between a given control image and a kernel defined by the corresponding excitation spot profiles.

To measure the size of the excitation spot, the filters on the control image camera were removed, and images of the luminal surface were captured while varying the fiber launching angle  $\theta$  from  $-45^\circ$  to  $45^\circ$  in five-degree increments. This was

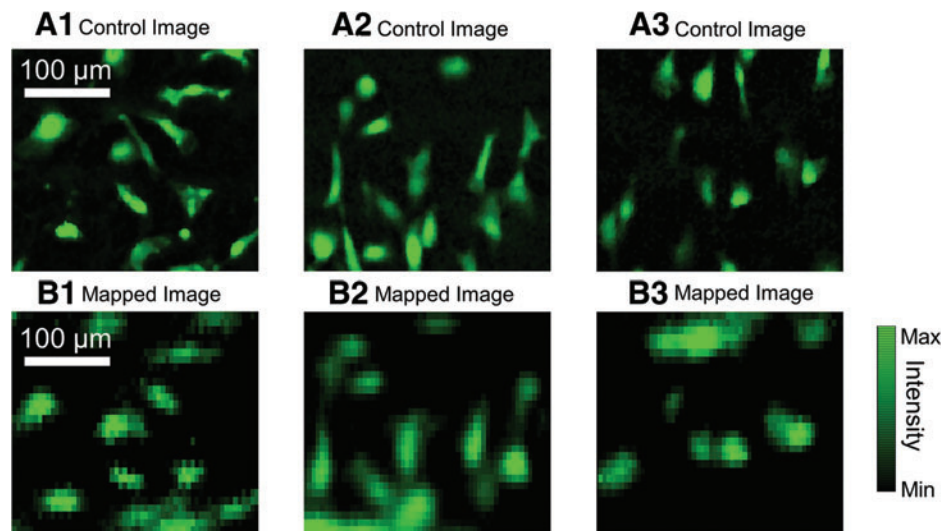


**FIG. 4.** Fluorescence mapping results and comparison. (A.1–3) Control images obtained through direct line-of-sight image acquisition. (B.1–3) An ROI measuring  $300 \times 300 \mu\text{m}$  above the MIC was selected on each scaffold, and a fluorescence-mapped image was obtained using the fiber-scanning algorithm. The fluorescence signals were captured on the exterior surface of the scaffold to demonstrate the capability of mapping cells through  $\sim 500 \mu\text{m}$ -thick PDLLA scaffolds. A total of 75 image pairs (25 pairs per scaffold) were obtained and evaluated for this experiment. Color images available online at [www.liebertonline.com/tec](http://www.liebertonline.com/tec)

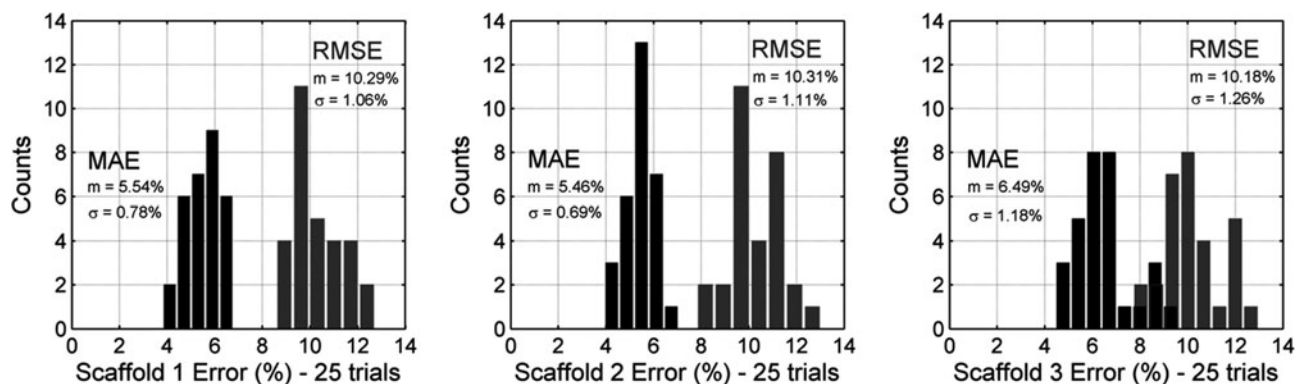


FIG. 5. Statistical validation of the fluorescence-mapping method. Mean absolute error (MAE) and root mean squared error (RMSE) histograms for comparison between pairs of fluorescence-mapped and control images for each scaffold. The mean  $\pm$  SD of the MAE and RMSE between the three scaffolds was  $5.83\% \pm 0.88\%$  and  $10.26\% \pm 1.14\%$ , respectively.

repeated at five random locations on a scaffold in the absence of cells. The FWHM was then extracted from each successive image and plotted as a function of launching angle  $\theta$  (Fig. 7). The angle  $\theta=0^\circ$  denotes the case where the excitation light was launched directly toward the luminal surface and produced an FWHM of  $16.5 \pm 0.5 \mu\text{m}$ . At  $\pm 45^\circ$ , the FWHM roughly doubled to  $31.6 \pm 3.7 \mu\text{m}$ . Since the spatial profile of the excitation spot directly determines the resolution of the imaging method, the imaging system can achieve an effective resolution in the order of 16.5 to  $31.6 \mu\text{m}$ . The plot in Figure 7 indicates that the resolution of the imaging system was highest at  $0^\circ$  and decreased with fiber micromirror rotation.

#### Spectral emission response and SNR

First, the optical spectrum of the fluorescent signals generated by the ECs, and the autofluorescence (noise) produced by the scaffold was measured (Fig. 8A). To ensure that the

measured fluorescence can be accurately attributed to either GFP-labeled ECs or scaffold autofluorescence, the control camera was used to identify the fluorescent source on the luminal surface. Figure 8B shows the exterior surface image captured by the EM-CCD camera when (1) an EC was illuminated by the excitation spot on the luminal surface, and (2) the excitation spot did not encounter a GFP-labeled cell. The two images are clearly distinct in both spatial distribution as well as fluorescence intensity, which further corroborates the difference in spectral responses identified in Figure 8A.

#### Dynamic assessment of cell growth and distribution

After sealing the scaffolds in a bioreactor, the cells were provided with the appropriate environment for cell migration and growth. To illustrate the dynamic capability of the FOB imaging method, the same ROI was scanned on the cell-seeded scaffold at an interval of 30 min over 1.5 h, producing a

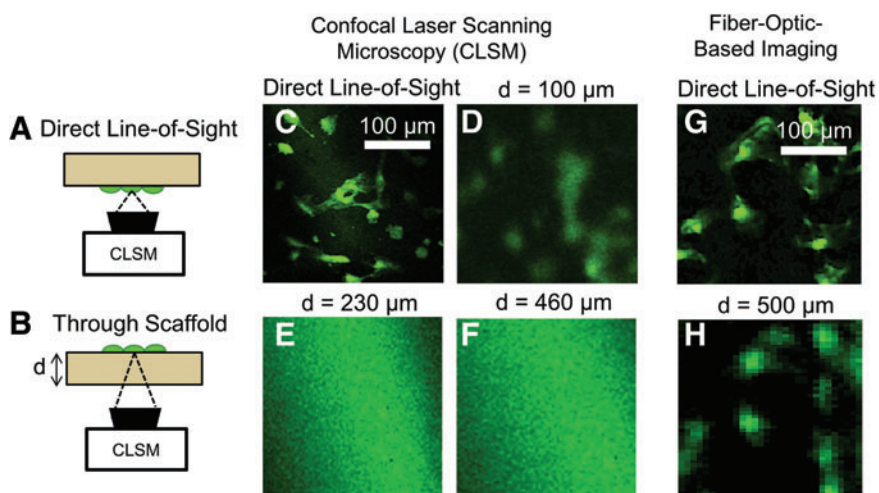
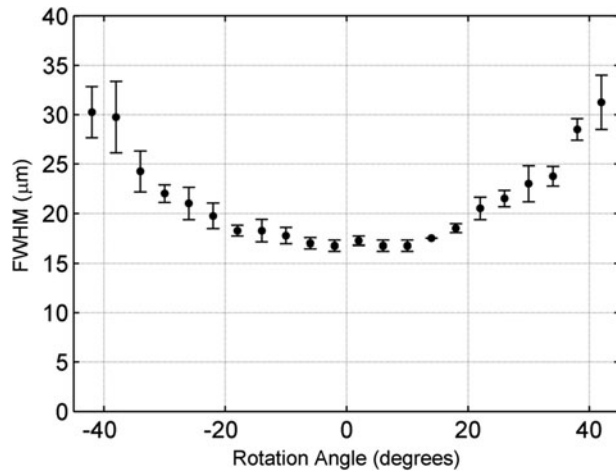


FIG. 6. Imaging depth comparison of confocal laser scanning microscope (CLSM). (A) Diagram of direct-line-of-sight CLSM image that visualizes “actual” GFP EC distribution. (B) The sample is then reversed to image the luminal surface through the electrospun PDLLA scaffold with the CLSM. Three scaffolds with a thickness  $d=100$ , 230, and  $460 \mu\text{m}$  were used. (C) Direct-line-of-sight CLSM image of GFP ECs on the luminal surface. (D) ECs on the luminal surface when imaged through the thickness of a  $100 \mu\text{m}$ -thick scaffold. Individual ECs could not be identified when imaging through (E)  $230 \mu\text{m}$  and (F)  $460 \mu\text{m}$ -thick scaffolds. The FOB method could, however, detect ECs on the luminal surface through a  $\sim 500 \mu\text{m}$ -thick scaffold (H). Comparison with a direct-line-of-sight image (G) confirms the accuracy of the fluorescence-mapped image. Color images available online at [www.liebertonline.com/tec](http://www.liebertonline.com/tec)



**FIG. 7.** Image mapping resolution. Full-width-half-maximum (FWHM) of the excitation spot on the luminal surface for micromirror launching angles  $\theta = -45^\circ$  to  $+45^\circ$  (mean  $\pm$  SD of  $n=5$  trials). This plot indicates that the resolution of the system is best when the excitation light is launched directly toward the luminal surface ( $\theta=0$ ) and deteriorates by  $\sim 1/2$  when the fiber micromirror is rotated to  $\theta = \pm 45^\circ$ .

collection of time-lapsed, fluorescence-mapped images. By comparing successive images, we were able to track the relative cell movement in the ROI. Figure 9 shows four mapped images 30 min apart. These results demonstrate the ability to continuously and nondestructively track single cells in their scaffold microenvironment. Observing a different ROI (Fig. 9E–G) at a 30 min interval, we were able to detect a single, localized fluorescent feature (red arrow) progressively separating into two spatially distinct fluorescent “spots” (double-headed red arrow). This behavior strongly suggests that the cell indicated by the red arrow had undergone cytokinesis.

## Discussion

A major challenge in tissue engineering is the inability to accurately and nondestructively monitor and evaluate the progress of a bioengineered tissue *in vitro*. To address this need, we presented here a new FOB imaging method and quantitatively evaluated its performance through a comparison with standard optical microscopy. In particular, we demonstrated that the FOB imaging method could “see” through a 500  $\mu\text{m}$ -

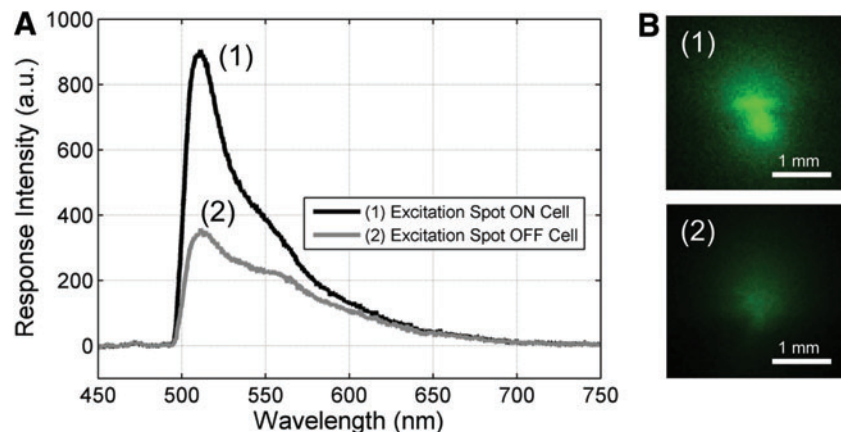
thick scaffold with a single-cell-level resolution. After a quantitative image comparison, we confirmed that the fluorescence-mapped images obtained using the FOB method matched very well with the control images obtained using standard fluorescence microscopy. Furthermore, we have shown that the imaging depth of the FOB method exceeded that of confocal laser scanning microscopy by at least a factor of 2. We further discuss the performance of the imaging system in the following contexts: the need for nondestructive imaging in tissue engineering, the comparison of the FOB imaging method with other optical microscopy techniques, and the implications of this study for tissue-engineering research.

### *The need for nondestructive imaging in tissue engineering*

It is critical for tissue engineers to assess the neo-tissue’s maturation progress in response to external stimuli such as mechanical stimulation, specific growth factors, and overall culturing conditions. These parameters have a major effect on tissue maturation, viability, and function after *in vivo* implantation. Similarly, tuning scaffold properties such as porosity, topography, mechanical properties, and chemistry can have a significant impact on cell attachment, viability, differentiation potential, and ECM production.<sup>27–29</sup> Therefore, the evaluation of cell-seeded tissue-engineered constructs in response to these conditions and scaffold properties *in vitro* can provide valuable information on the suitability of scaffold design and predict the overall regenerative capacity of the construct *in vivo*. Evaluating the specific parameters of engineered tissue maturation is equally important for the optimization of tissue-engineering techniques.

Current methodologies that are used to evaluate tissue development *in vitro* employ either destructive or nondestructive techniques. However, there are significant limitations with both approaches. Destructive techniques such as fixation, staining, and/or histological sectioning can provide valuable information on cellular interactions within the scaffold, albeit at a limited number of time points. Perhaps more importantly, destructive methods do not permit real-time monitoring of cells under physiological conditions within their intact microenvironment. As an example, it would be impossible to apply standard histological methods to continuously monitor cell proliferation and differentiation within an intact scaffold housed in a bioreactor. Nondestructive techniques, such as microscopy-based optical methods, can be used to image

**FIG. 8.** Signal-to-noise ratio (SNR) characterization. **(A)** Comparison of the spectral emission response signal of the ECs and background noise caused by scaffold autofluorescence from 450 to 750 nm. Comparison of the cell response to the background noise gives the SNR. **(B)** Representative EM-CCD camera images taken from the exterior surface when (1) the excitation spot is on a cell or (2) placed in an area void of cells (scaffold autofluorescence). Color images available online at [www.liebertonline.com/tec](http://www.liebertonline.com/tec)



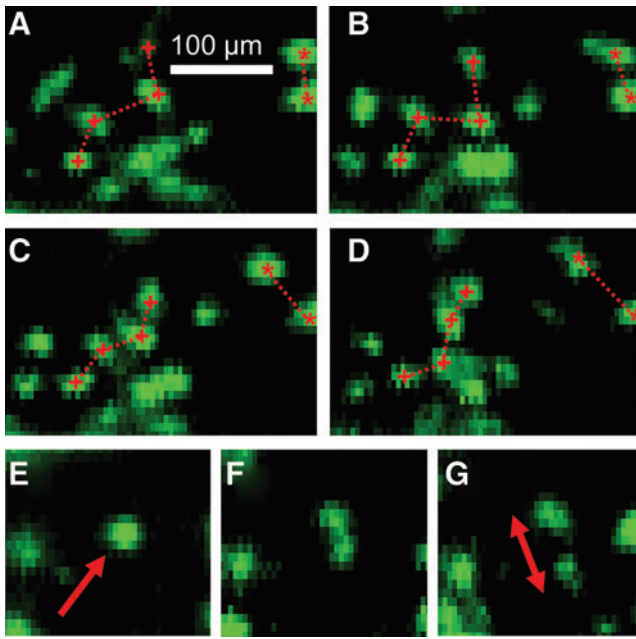


**FIG. 9.** Dynamic imaging. (A–D) Four fluorescence-mapped images were taken in the same ROI at a 30 min interval to demonstrate the dynamic imaging capability. The dashed lines in (A–D) serve as a visual aid that tracks the relative movement of cells between successive images. Images in (E–G), which are taken at a 30 min time interval in another ROI, suggest that we can use our imaging method to monitor cell cytokinesis. In particular, (E–G) suggest that the cell indicated by the red arrow in (E) had undergone cytokinesis and became two separate cells, as indicated by the double-headed arrow in (G). Color images available online at [www.liebertonline.com/tec](http://www.liebertonline.com/tec)

individual cells by labeling them with fluorescent markers, including fluorescent proteins, fluorescent dyes, or quantum dots.<sup>14</sup> However, optical waves in the visible or near-infrared spectrum experience significant scattering and absorption in most tissues and scaffolding materials. Consequently, most optical imaging systems have a limited penetration depth and cannot fully capture the underlying biological processes that occur deep within the tissue scaffold.<sup>15</sup>

#### Comparison with other optical imaging modalities

Current optical imaging modalities that are used to assess tissue-engineered constructs include confocal and nonlinear microscopy.<sup>12–17</sup> These techniques have become ubiquitous in the field due to their ability to nondestructively image cells and their surrounding matrices through biologically thick tissues. While these techniques are typically applied to cells or scaffolds under standard culturing conditions, several research groups are currently using these methods to perform nondestructive *in situ* imaging of scaffolds undergoing preconditioning in bioreactors. Kluge *et al.* recently introduced a bioreactor system capable of applying mechanical stretch to a porous silk fibroin sponge while allowing access to nondestructively image GFP-tagged fibroblasts with a penetration depth of approximately 162  $\mu\text{m}$  in the scaffold using confocal microscopy and collagen deposition at a penetration depth of approximately 200  $\mu\text{m}$  using nonlinear microscopy.<sup>18</sup> In a similar manner, Niklason *et al.* used a

nonlinear optical microscope that assesses collagen deposition at penetration depths of approximately 135  $\mu\text{m}$  within smooth muscle cell-seeded poly (glycolic acid) vessel scaffolds housed within a specialized pulsatile bioreactor undergoing preconditioning.<sup>19</sup> These studies demonstrate that while various advanced microscopy methods can be used for nondestructive scaffold assessment, such imaging modalities cannot maintain single-cell-level resolution beyond the limit of 100–200  $\mu\text{m}$  in turbid biological tissues and scaffolds. Fundamentally, this constraint is due to the fact that engineered tissue scaffolds typically require very high porosities (i.e., electrospun scaffolds<sup>27,30–32</sup>) for cell migration and overall colonization of the scaffold. As a result, scaffolds tend to induce very strong optical scattering and are consequently highly opaque. With a limited imaging depth, the methods reported in Refs. 18 and 19 may not be suitable for the evaluation of a clinically relevant vascular graft, where the graft should possess sufficient thickness to maintain structural integrity in the presence of pulsatile blood flow.

The FOB imaging method presented in the current study demonstrates the potential of using fiber-guided light to locally excite fluorescent cells to produce mapped images in highly scattering scaffolds. Our study using GFP-tagged ECs on electrospun PDLA scaffolds showed that the penetration depth and the imaging resolution of the FOB method compared favorably with confocal microscopy. More specifically, the confocal microscopy results in Figure 6B displayed a greatly diminished resolution at a scaffold thickness of 100  $\mu\text{m}$ . Furthermore, at imaging depths of 230 and 460  $\mu\text{m}$ , the confocal microscope was unable to identify fluorescent cells through the scaffold and failed to generate the spatial distribution of GFP-labeled ECs on scaffold lumen (Fig. 6C, D). Therefore, in terms of imaging depth, the FOB imaging method is superior to confocal laser scanning microscopy, which is one of the state-of-the-art imaging methods for tissue-engineering research.

Current optical imaging methodologies are limited not only by penetration depth, but also by the short working distances of their optical objectives, which typically range from hundreds of microns to a few millimeters. Such short working distances require a specialized bioreactor design in order to place a tissue scaffold close enough to the objective to perform imaging.<sup>18,19</sup> The FOB imaging method has a very large working distance that can reach up to 8 cm. This distance can be easily extended using commercially available long distance objectives, as the method is based on collecting diffused fluorescence light emitted from the scaffold. This practical advantage can be particularly useful for preconditioning studies that require a larger distance between the objective and the tissue scaffold. In contrast, advanced imaging methods such as confocal and nonlinear microscopy critically depend on using high numerical aperture objectives with very short working distances. For example, the 10 $\times$  objective we used for confocal imaging in this study has a short working distance of 2 mm and could not be used to image the PDLA scaffold sealed within the parallel plate bioreactor. Consequently, the results of imaging studies in Figure 6 had to be carried out in a Petri dish with a 170  $\mu\text{m}$  glass slide. Only in this configuration could the sample be placed close enough to the objective for imaging.

The data presented here show that currently, the imaging method can monitor fluorescent-labeled cells only in a 2D

configuration. This technique is appropriate for endothelium and epithelium monolayers, seen in a large number of tissues and organs, and critical for their proper functions. Consequently, our method is uniquely suited for the study of hollow cavity organs and structures such as blood vessels, intestine, urogenital tract, and so on. However, this limitation is not a fundamental constraint and can potentially be circumvented by using more sophisticated signal processing and tomographical reconstruction techniques. For example, we have developed several fluorescence tomography techniques that are capable of reconstructing three-dimensional (3D) distributions of fluorophores in various scaffolds and animal models. Such methods can potentially be combined with signal processing reported in Ref. 33 to achieve 3D tomographical reconstruction. For tissues and scaffolds that possess significant heterogeneity, we may account for complex scaffold geometry and nonuniform optical parameters by using the tomographical technique discussed in Ref. 34.

### Study results and implications

With an “unwrapped” configuration in Figure 1B, the planar scaffold enabled us to directly compare the FOB imaging method with standard fluorescence microscopy. In order to validate the imaging method, we performed a statistical comparison between the fluorescence-mapped images and control images using the  $\sim 500\ \mu\text{m}$  thick PDLLA scaffolds. In particular, the MAE and RMSE were calculated using 75 pairs of fluorescence-mapped images and their corresponding control images (25 pairs per scaffold). The MAE indicates that the mapped images are within 6% error compared with the control images, and the RMSE shows that deviations are roughly around 10%. It should be noted that the RMSE comparison method is more sensitive to statistical outliers than the MAE and, thus, the preferred indicator of mapping accuracy.<sup>23</sup> Overall, both methods show that the error is consistent between scaffold groups and that the standard error within scaffold groups is small, thereby validating that the fluorescence-mapped images are a reliable estimation of the actual cell distribution.

Characterization of the excitation spot on the scaffold surface allowed an estimation of the spatial resolution of the FOB imaging method. Once excitation light was delivered into the scaffold through the MIC, it experienced optical scattering as it traveled to the surface. Since the MIC-to-surface distance varied with regard to the launching angle, the FWHM of the excitation spot at the scaffold surface varied accordingly. As a result, the system resolution decreased as the launching angle increased. According to the results in Figure 7, the FOB imaging method has a spatial resolution in the range of 20–30  $\mu\text{m}$ . Furthermore, the results in Figure 4 showed that the imaging system can spatially resolve single GFP-labeled ECs on the scaffold’s surface, which is consistent with 20–30  $\mu\text{m}$  imaging resolution. Although the increasing FWHM presents a limitation along the field of view that is perpendicular to the MIC, the range is at least 300  $\mu\text{m}$  according to Figure 4. If a higher resolution is desired in a larger field of view, then we can always incorporate more MICs within the scaffold. Furthermore, we also note that the field of view along the MIC direction is essentially unlimited.

Similar to other imaging methods, the results of the fiber-based imaging method are only accurate if the cell fluorescence

signal is stronger than the scaffold autofluorescence noise. Given the spectral response in Figure 8A, the SNR of the imaging system is found by dividing the signal curve (1) by the noise curve (2), which is equal to or greater than 2 at the peak GFP emission (510–530 nm). As observed in Figure 4, an SNR of 2 is sufficient to separate the signal from the noise to obtain cell-level resolution images. In future, we can further improve the SNR by ensuring the fluorescently labeled ECs have a minimal spectral overlap with scaffold autofluorescence.

We emphasize that the imaging method is dynamic and nondestructive, which means that we can scan the same ROI multiple times over any desired time period. In fact, in Figure 9, we have demonstrated that we can continuously monitor the movement of single GFP-labeled ECs through the  $\sim 500\text{-}\mu\text{m}$ -thick scaffold. The substantial increase in imaging penetration depth and flexibility in the placement of camera and objective lens enables us to address the pressing need for the nondestructive, dynamic imaging of engineered tissue constructs in geometrically constrained configurations. The example we used in the current study was intended to visualize fluorescent ECs through a relatively thick and optically opaque scaffold contained in a bioreactor. However, due to the constraint imposed by the enclosed tubular geometry of a blood vessel, and the design of fluid flow bioreactors, it is exceedingly difficult to monitor the cells in a nondestructive and dynamic manner with conventional microscope-based methods.<sup>10</sup> A major motivation of the current work was to design an imaging method that can circumvent these geometrical constraints. Given the advantages offered by a significantly enhanced imaging depth and working distance, this imaging method is perfectly suited to evaluate the endothelialization of tissue-engineered vascular grafts (i.e., EC proliferation, coverage, and response to flow) and may find numerous *in vitro* or *in vivo* applications in other tissue-engineered constructs that contain epithelial tissues.

### Conclusion

In this study, we developed a novel imaging method that is capable of nondestructive and dynamic imaging of fluorescent cells through an optically opaque scaffold housed within a bioreactor. The FOB imaging modality is based on the targeted excitation of individual cells, capturing the emitted fluorescence through the scaffold and producing a mapped image based on the position of the excitation light. A comparison of the fluorescence-mapped images to the control images confirmed that the system can accurately provide a cellular distribution through the optically opaque scaffold. Furthermore, the method demonstrated an imaging penetration depth of greater than 500  $\mu\text{m}$  through the electrospun PDLLA scaffold, which significantly exceeded what can be achieved using confocal microscopy. We envision that this imaging modality will advance our understanding of the complex process of neo-tissue development and remodeling *in vitro* in a nondestructive manner. Building on the dynamic imaging capabilities, we intend to further develop this technology to assess bioengineered vascular grafts *in vitro* and potentially for *in vivo* tissue engineering studies.

### Acknowledgments

The authors thank Dr. Aaron Goldstein in the Department of Chemical Engineering at Virginia Tech for his insight in

the bioreactor design and Dr. Joseph Freeman in the Department of Biomedical Engineering at Virginia Tech for his advice in scaffold sintering. This research was funded by a grant from the National Institutes of Health (NIBIB, HL098912), the National Science Foundation (CBET 0955072), and the Institute for Critical Technology and Applied Science (Holey Scaffolds, Virginia Tech).

### Disclosure Statement

No competing financial interests exist.

### References

- Nerem, R.M., and Sambanis A. Tissue engineering: from biology to biological substitutes. *Tissue Eng* **1**, 3, 1995.
- Atala, A., Bauer, S.B., Soker, S., Yoo, J.J., and Retik, A.B. Tissue-engineered autologous bladders for patients needing cystoplasty. *Lancet* **367**, 1241, 2006.
- Laurencin, C.T., and Freeman, J.W. Ligament tissue engineering: an evolutionary materials science approach. *Biomaterials* **26**, 7530, 2005.
- Raya-Rivera, A., Esquiliano, D.R., Yoo, J.J., Lopez-Bayghen, E., Soker, S., and Atala, A. Tissue-engineered autologous urethras for patients who need reconstruction: an observational study. *Lancet* **377**, 1175, 2011.
- Elbert, D.L. Bottom-up tissue engineering. *Curr Opin Biotechnol* **22**, 674, 2011.
- Yang, S., Leong, K.F., Du, Z., and Chua, C.K. The design of scaffolds for use in tissue engineering. Part II. Rapid prototyping techniques. *Tissue Eng* **8**, 1, 2002.
- Martin, I., Wendt, D., and Heberer, M. The role of bioreactors in tissue engineering. *Trends Biotechnol* **22**, 80, 2004.
- Sodian, R., Lemke, T., Fritsche, C., Hoerstrup, S.P., Fu, P., Potapov, E.V., Hausmann, H., and Hetzer, R. Tissue-engineering bioreactors: a new combined cell-seeding and perfusion system for vascular tissue engineering. *Tissue Eng* **8**, 863, 2002.
- Goldstein, A.S., and Christ, G. Functional tissue engineering requires bioreactor strategies. *Tissue Eng Part A* **15**, 739, 2009.
- Angela, H. and Huang, L.E.N. Engineering biological-based vascular grafts using a pulsatile bioreactor. *J Vis Exp* **52**, pii 2646, 2011.
- Thevenot, P., Nair, A., Dey, J., Yang, J., and Tang, L. Method to analyze three-dimensional cell distribution and infiltration in degradable scaffolds. *Tissue Eng Part C Methods* **14**, 319, 2008.
- Keyes, J.T., Haskett, D.G., Utzinger, U., Azhar, M., and Geest, J.P.V. Adaptation of a planar microbiaxial optomechanical device for the tubular biaxial microstructural and macroscopic characterization of small vascular tissues. *J Biomech Eng* **133**, 075001, 2011.
- Georgakoudi, I., Rice, W.L., Hronik-Tupaj, M., and Kaplan, D.L. Optical spectroscopy and imaging for the noninvasive evaluation of engineered tissues. *Tissue Eng Part B Reviews* **14**, 321, 2008.
- Ntziachristos, V. Fluorescence molecular imaging. *Annu Rev Biomed Eng* **8**, 1, 2006.
- Ntziachristos, V. Going deeper than microscopy: the optical imaging frontier in biology. *Nat Methods* **7**, 603, 2010.
- König, K., Schenke-Layland, K., Riemann, I., and Stock, U.A. Multiphoton autofluorescence imaging of intratissue elastic fibers. *Biomaterials* **26**, 495, 2005.
- Schenke-Layland, K., Riemann, I., Stock, U.A., and König, K. Imaging of cardiovascular structures using near-infrared femtosecond multiphoton laser scanning microscopy. *J Biomed Opt* **10**, 024017, 2005.
- Kluge, J.A., Leisk, G.G., Cardwell, R.D., Fernandes, A.P., House, M., Ward, A., Dorfmann, A.L., and Kaplan, D.L. Bioreactor system using noninvasive imaging and mechanical stretch for biomaterial screening. *Ann Biomed Eng* **39**, 1390, 2011.
- Niklason, L.E., Yeh, A.T., Calle, E.A., Bai, Y., Valentin A., and Humphrey, J.D. Enabling tools for engineering collagenous tissues integrating bioreactors, intravital imaging, and biomechanical modeling. *Proc Natl Acad Sci U S A* **107**, 3335, 2010.
- Yazdani, S.K., Tillman, B.W., Berry, J.L., Soker, S., and Geary, R.L. The fate of an endothelium layer after preconditioning. *J Vasc Surg* **51**, 174, 2010.
- Pham, Q.P., Sharma, U., and Mikos, A.G. Electrospinning of polymeric nanofibers for tissue engineering applications: a review. *Tissue Eng* **12**, 1197, 2006.
- Wright, L., Young, R., Andric, T., and Freeman, J. Fabrication and mechanical characterization of 3D electrospun scaffolds for tissue engineering. *Biomed Mater* **5**, 055006, 2010.
- Ji, L., and Gallo, K. An agreement coefficient for image comparison. *Photogramm Eng Remote Sensing* **72**, 823, 2006.
- MathWorks. Image Registration. Image Processing Toolbox, MATLAB R2011a Documentation: Natick, MA: The MathWorks, Inc., 2011.
- Kreke, M.R., and Goldstein, A.S. Hydrodynamic shear stimulates osteocalcin expression but not proliferation of bone marrow stromal cells. *Tissue Eng* **10**, 780, 2004.
- Solomon, C., and Breckon, T. Fundamentals of Digital Image Processing: A Practical Approach with Examples in Matlab. New York: Wiley, 2011, pp. 28–31.
- Lutolf, M., and Hubbell, J. Synthetic biomaterials as instructive extracellular microenvironments for morphogenesis in tissue engineering. *Nat Biotechnol* **23**, 47, 2005.
- Griffith, L.G. Emerging design principles in biomaterials and scaffolds for tissue engineering. *Ann N Y Acad Sci* **961**, 83, 2002.
- Hubbell, J.A. Biomaterials in tissue engineering. *Nat Biotechnol* **13**, 565, 1995.
- Li, W.J., Laurencin, C.T., Caterson, E.J., Tuan, R.S., and Ko, F.K. Electrospun nanofibrous structure: a novel scaffold for tissue engineering. *J Biomed Mater Res* **60**, 613, 2002.
- Ma, Z., Kotaki, M., Inai, R., and Ramakrishna, S. Potential of nanofiber matrix as tissue-engineering scaffolds. *Tissue Eng* **11**, 101, 2005.
- Whited, B.M., Whitney, J.R., Hofmann, M.C., Xu, Y., and Rylander, M.N. Pre-osteoblast infiltration and differentiation in highly porous apatite-coated PLLA electrospun scaffolds. *Biomaterials* **32**, 2294, 2011.
- Cong, A.X., Hofmann, M.C., Cong, W., Xu, Y., and Wang, G. Monte Carlo fluorescence microtomography. *J Biomed Opt* **16**, 070501, 2011.
- Cong, A., and Wang, G. A finite-element-based reconstruction method for 3D fluorescence tomography. *Opt Expr* **13**, 9847, 2005.

Address correspondence to:  
Yong Xu, Ph.D.

Department of Electrical & Computer Engineering  
Virginia Tech  
467 Whittemore Hall  
Blacksburg, VA 24061

E-mail: yong@vt.edu

Received: August 28, 2011

Accepted: March 14, 2012

Online Publication Date: May 10, 2012

## **Chapter 4: Dynamic, nondestructive imaging of a bioengineered vascular graft endothelium**

Bryce M. Whited<sup>1,#</sup>, Matthias C. Hofmann<sup>2,#</sup>, Peng Lu<sup>2</sup>, Yong Xu<sup>2</sup>, Christopher Rylander<sup>1,3</sup>, Ge Wang<sup>1</sup>, Etai Sapoznik<sup>4</sup>, Tracy Criswell<sup>4</sup>, Sang Jin Lee, Ph.D.<sup>4</sup>, Shay Soker<sup>4</sup>, Marissa Nichole Rylander<sup>1,3</sup>

<sup>1</sup>School of Biomedical Engineering and Sciences, Virginia Tech, Blacksburg, VA 24061, USA <sup>2</sup>

<sup>2</sup>Department of Electrical and Computer Engineering, Virginia Tech, Blacksburg, VA 24061, USA

<sup>3</sup>Department of Mechanical Engineering, Virginia Tech, Blacksburg, VA 24061, USA

<sup>4</sup>Wake Forest Institute for Regenerative Medicine, Wake Forest University School of Medicine, Medical Center Boulevard, Winston-Salem, NC, 27157, USA

<sup>#</sup>These authors contributed equally to this work

### **4.1 Abstract**

Bioengineering of vascular grafts holds great potential to address the shortcomings associated with autologous and conventional synthetic vascular grafts used for small diameter grafting procedures. Lumen endothelialization of bioengineered vascular grafts is essential to provide an antithrombogenic graft surface to ensure long-term patency after implantation. Conventional methods used to assess endothelialization typically involve periodic harvesting of the graft for histological sectioning and staining of the lumen. Endpoint testing methods such as these are effective but do not provide real-time information of endothelial cells in their intact microenvironment, rather only a single time point measurement of endothelium development. Therefore, nondestructive methods are needed to provide dynamic information of graft endothelialization and endothelium maturation. To address this need, we have developed a nondestructive fiber optic based (FOB) imaging method that is capable of dynamic assessment of graft endothelialization without disturbing the graft housed in a bioreactor. In this study we demonstrate the capability of the FOB imaging method to quantify graft endothelialization, EC

detachment, and apoptosis in a nondestructive manner. This imaging method can be further adapted to monitor endothelium maturation and response to fluid flow preconditioning *in vitro*.

## 4.2 Introduction

Cardiovascular disease is currently the leading cause of death in the U.S., accounting for nearly 600,000 deaths in 2008 [1]. Atherosclerosis, i.e. fatty plaque buildup causing narrowing of the artery and restricting blood flow, is one of the most common and severe forms of cardiovascular disease. A common surgical intervention to treat atherosclerosis is bypass surgery, wherein blood flow is re-directed around the atherosclerotic plaque to improve blood supply to ischemic areas. The most widely used and reliable conduits for bypass surgery are autologous vessels, such as the saphenous vein and internal mammary artery [102]. Autologous vessels, however, still have a 35% failure rate and 5-30% of patients have no suitable vein or artery available due to vascular disease or other complications [5]. Fully synthetic grafts made from Dacron and expanded polytetrafluoroethylene have been successfully used for over 50 years for large diameter ( $> 5$  mm) bypass conduits, however, these grafts are susceptible to intimal hyperplasia and surface thrombogenicity when used for small diameter bypass ( $< 5$  mm) [52]. Therefore, small diameter vascular graft alternatives are greatly needed to address the shortcomings associated with autologous and fully synthetic grafts.

Tissue engineering of small diameter vascular grafts holds great potential to address the shortage of bypass grafts. This approach often involves the combination of natural and/or synthetic scaffolds and autologous vascular cells to create a functional conduit that is remodeled after implantation [103-106]. Bioengineered vascular grafts must be able to withstand physiological forces associated with blood flow, possess good suture retention, and maintain structural integrity during neotissue formation [36]. Additionally, the bioengineered graft must possess a lumen surface that inhibits thrombus formation, unwanted inflammatory responses, and limits proliferation of smooth muscle cells that may cause neointimal hyperplasia. In native vessels, endothelial cells (ECs) lining the lumen of blood vessels provide a nonthrombogenic barrier between circulating blood and the blood vessel wall, and play a key role in regulating dynamic mechanisms that protect blood vessels from the aforementioned detriments [107]. Previous studies have shown that incorporation of an EC monolayer on the graft lumen prevents thrombogenic events and contributes to long-term patency and function [108-111]. It is therefore

broadly accepted that bioengineered vascular grafts must possess a confluent, healthy, and mature endothelium on the lumen surface of the graft to maintain graft patency and function [50].

A promising approach to obtain a bioengineered vascular graft with a functional endothelium is to seed the lumen with autologous ECs *in vitro*, harvested from a variety of sources such as veins [109], arteries [112], and circulating endothelial progenitor cells [113], prior to implantation. Successful graft endothelialization *in vitro* relies heavily on the ECs being able to attach, proliferate, and form a confluent endothelium on the graft lumen surface. Factors that affect graft endothelialization include the inherent material properties of the graft including biomaterial surface topography, chemistry, elasticity, and the ability to adsorb proteins [114]. Significant work has been done to modify the graft surface via physiochemical modification and biofunctionalization to promote complete endothelialization and strong adherence of ECs to grafts [115]. The ability of ECs to strongly adhere to the surface of the graft surface is important because the hydrodynamic shear stress that they will experience by blood flow *in vivo* increases the chance of detachment and subsequent thrombus formation and vessel occlusion [50]. Several groups have shown that preconditioning the graft with a gradual increase in shear stress via fluid flow *in vitro* enhances overall EC retention under physiological flow [65, 116, 117]. Flow preconditioning of grafts in a well-controlled environment, such as fluid flow bioreactors, allows ECs to gradually adapt to the shear stress through reorganization of their cytoskeleton, presence of focal adhesions, and cell alignment with the direction of fluid flow to increase EC adhesion strength [62, 67, 118].

Experimental approaches to promote a confluent, adherent, and shear resistant endothelium in bioengineered vascular grafts, such as biomaterial surface modification and flow preconditioning, must be rigorously tested *in vitro* prior to implantation *in vivo*. Critical parameters that need to be measured to assess graft endothelialization include EC attachment, proliferation, and coverage of the lumen surface. Additionally, ensuring that ECs remain adherent to the lumen surface (resisting detachment) and determining their response to physiological fluid flow is of great importance to creating successful *in vitro* flow preconditioning methods and protocols. Current approaches used to assess these parameters include techniques such as histological sectioning and staining, which, aside from being time and labor intensive, destroys the graft and only provides a single time point measurement. However, endothelialization and EC response to flow mediated shear stress are dynamic processes and

would be best understood if continuous observation of the lumen within an intact vessel were possible. Therefore, the ability to noninvasively image the growth, health, and integrity of a vascular graft endothelium during preconditioning in real-time is greatly needed and will aid in identification and optimization of scaffold properties and preconditioning protocols to enhance EC function and ultimately graft success once implanted.

The necessity to monitor vascular graft endothelialization and maturation in real time during preconditioning has led our group to develop a fiber optic based (FOB) imaging system to accomplish this task [119, 120]. The imaging system is designed to noninvasively assess the graft endothelium without disturbing the graft during preconditioning in a bioreactor. In this study, we evaluate the feasibility of the FOB imaging system to image and quantify endothelialization and EC detachment from an electrospun vascular graft in a dynamic and noninvasive manner. The graft scaffold topography was systematically varied by modifying electrospinning parameters and the FOB imaging system was used to noninvasively quantify the affect of topography on graft endothelialization over a 7-day period. Additionally, the health of the endothelium was assessed by quantifying EC apoptosis on the lumen in response to varying levels of insult. Finally, the imaging depth of the FOB imaging system was directly compared to that of two-photon fluorescence microscopy. The results of this study demonstrate the potential of the FOB imaging system to be utilized to nondestructively assess the maturation of a bioengineered vascular graft endothelium in real-time and possible extension for use in other bioengineered tissues.

### **4.3 Materials and Methods**

#### **4.3.1 Vascular scaffold fabrication and micro-imaging channel (MIC) integration**

Vascular scaffolds were fabricated by using a layer-by-layer electrospinning approach to integrate micro-imaging channels (MICs) directly into the wall of the scaffold. The MICs are silica glass capillaries with inner diameter of 150  $\mu\text{m}$  and outer diameter of 245  $\mu\text{m}$  (Polymicro Technologies, Phoenix, AZ) that facilitate insertion of fiber optics into the scaffold wall. To fabricate the scaffolds, solutions of poly (D,L-lactide) (PDLLA) (SurModics Pharmaceuticals, Birmingham, AL) with 5%, 10%, and 20% w/v concentrations were prepared in 1,1,1,3,3,3-hexafluoro-2-propanol (HFP, Sigma Aldrich, St. Louis, MO). Next, 150  $\mu\text{L}$  of PDLLA was electrospun onto a rotating grounded mandrel (4.75 mm diameter) to form the scaffold lumen

layer, as illustrated in Figure 4.1A. The 3 different concentrations of PDLLA were electrospun separately for the lumen layers, with varied electrospinning parameters (Table 4.1), to produce 3 different scaffolds with varying scaffold fiber diameter and surface topography. Two MICs were then placed on opposite sides of the mandrel, as illustrated in Figure 4.1B. Next, 850  $\mu\text{L}$  20% w/v PDLLA was electrospun over the MICs to produce a composite vascular scaffold with MICs tightly embedded within the scaffold wall (Figure 4.1C). Figure 4.1D shows an entire vascular graft with 2 MICs firmly embedded into the vessel, and Figure 4.1E shows the MIC integrated within and extending from the vessel wall. A total of 13 vascular scaffolds exhibiting an average wall thickness of  $510 \pm 55 \mu\text{m}$  were fabricated for this study. Vascular scaffold thicknesses were measured using a digital micrometer (Mitutoyo Corporation, Japan) before scaffold seeding.

Both full-vessel scaffolds (Figure 4.1D) and half-vessel scaffolds (Figure 4.1F) were fabricated and used for imaging in this experiment. Some vascular grafts were sectioned in half lengthwise (i.e. half-vessel scaffolds) before cell seeding to provide direct direct-line-of-sight viewing to the lumen portion of the graft for “control image” acquisition (Figure 4.1F). By taking direct-line-of-sight control images of the lumen with a conventional fluorescence microscope setup, we were able to validate the accuracy of the FOB imaging system by comparing the FOB images to their corresponding control image. It should be emphasized that these control images would otherwise be impossible to obtain unless the vessel were cut in half to allow direct-line-of-sight viewing of the lumen with the microscope. The half-vessel scaffolds were used to verify the accuracy of the FOB imaging system in quantifying EC coverage, cell detachment, and apoptosis (Section 4.5, 4.6 and 4.7; respectively). To acquire a control image, the lumen of a half-vessel scaffold was imaged with a CCD camera (XCD-X710, Sony, Japan) coupled with a 10x objective to obtain a corresponding direct-line-of-sight fluorescent image of the cells on the scaffold surface. After FOB imaging validation, we progressed to imaging full-vessel grafts to test the feasibility of nondestructively imaging and quantifying the effect of varied lumen topography on vascular graft endothelialization over time (Section 4.8 below).

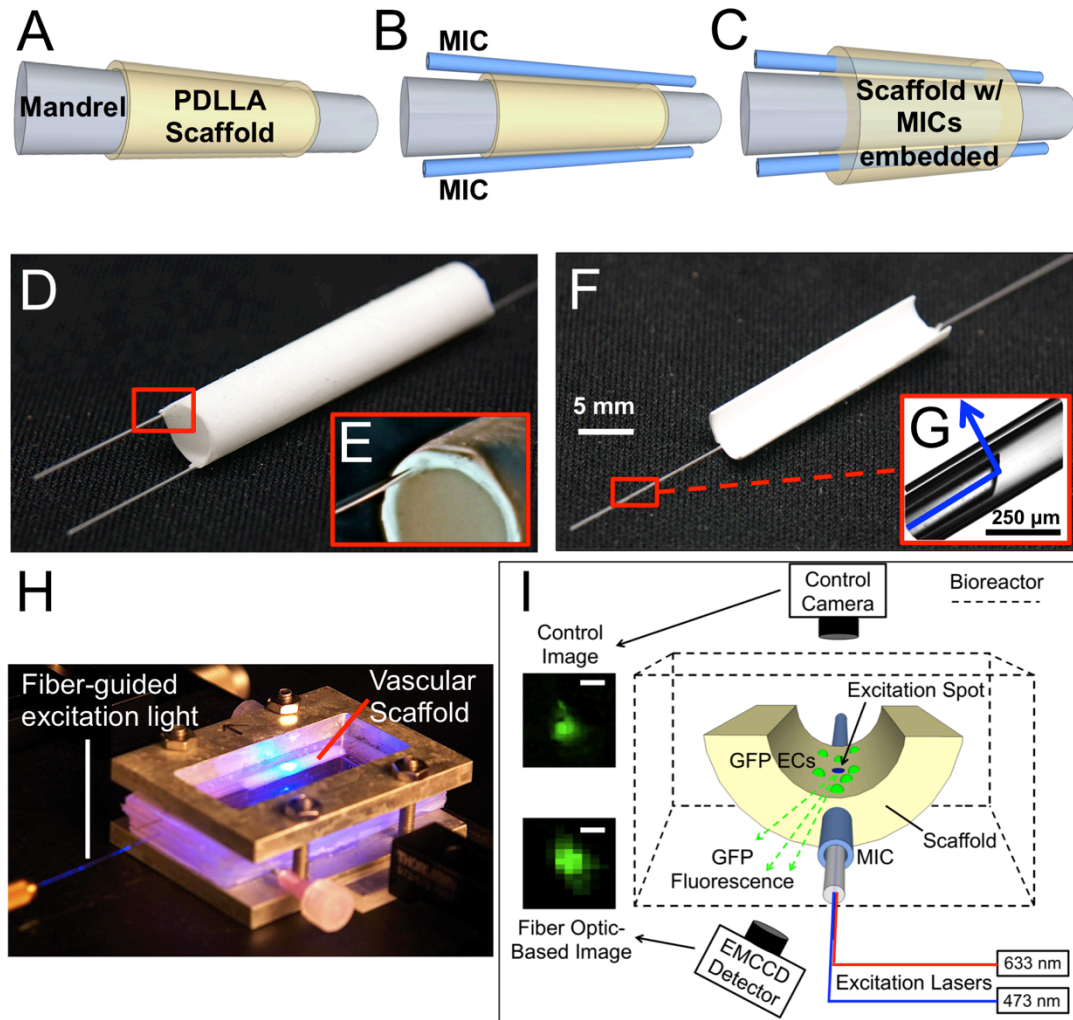


**Figure 4.1. Vascular scaffold fabrication, MIC integration, and FOB imaging method.** A-C) Illustration of the layer-by-layer electrospinning fabrication technique used to embed MICs within the wall of the vascular scaffold to facilitate imaging. D,E) Images of a vascular scaffold with MICs embedded within the wall. F) Image of a vascular scaffold sectioned lengthwise to validate endothelium imaging (half-vessel scaffold). G) Image of the fiber optic micro-mirror inserted within an MIC. Light is directed at a 90° angle relative to the fiber optic to allow excitation of ECs on the lumen of the vascular graft. H) Photograph of the vascular scaffold during an imaging experiment with the fiber-guided excitation light on. I) Schematic of the fiber optic imaging method used to create FOB images through the scaffold wall. Excitation laser light was guided to the fiber optic micro-mirror to excite GFP-ECs on the lumen of the vascular scaffold. The excitation spot created by the laser light was incrementally rastered on the lumen surface and GFP fluorescence was measured through the scaffold wall using an EMCCD detector. Linking the excitation spot to the GFP fluorescence values enabled fluorescence mapping to create a fiber optic-based (FOB) image. A corresponding control image was obtained by a direct-line-of-sight control camera to validate the imaging method on half-vessel scaffolds.

	Polymer Concentration (% w/v)	Flow Rate (ml/hr)	Throw Distance (cm)	Voltage (kV)	Needle Gauge (g)	Electrospun Fiber Diameter ( $\mu\text{m}$ )
Condition 1	5	1	7	20	30	$0.36 \pm 0.07$
Condition 2	10	2	10	15	25	$1.00 \pm 0.31$
Condition 3	20	5	15	12	18	$3.32 \pm 0.63$

**Table 4.1** Electrospinning parameters for scaffold fabrication

#### 4.3.2 Scaffold morphology

Scanning electron microscopy (SEM) was used to characterize electrospun scaffold morphology using a LEO 1550 field emission SEM (Carl Zeiss, Thornwood, NY). SEM images were analyzed with Image J software (U.S. National Institutes of Health, Bethesda, MD) to quantify scaffold fiber diameter. A total of 60 random fibers were selected from each image and measured to determine mean fiber diameter for each scaffold ( $n = 3$  images/scaffold,  $n = 180$  fibers total).

#### 4.3.3 Cell culture and scaffold seeding

A human dermal microvascular endothelial cell line (American Type Culture Collection, Manassas, VA) was infected with a lentivirus expressing green fluorescent protein (GFP) to stably express GFP, as previously described [119]. GFP-ECs were maintained in an incubator at  $37^{\circ}\text{C}$ , 5%  $\text{CO}_2$  and cultured in EGM-2 media (Lonza Biomedical, Walkersville, MD). Before cell seeding, the scaffolds were immersed in 70% ethanol for 5 min for sterilization and then washed 3 times for 5 min in sterile PBS to remove residual ethanol. GFP-ECs were then seeded onto the scaffolds at a density of  $1.5 \times 10^4$  cells/ $\text{cm}^2$ , allowed to attach for 1 hr in the incubator, and rinsed once with PBS to remove unattached cells. Before imaging, the sample was placed in a custom bioreactor and filled with EGM-2 prior to imaging experiments. The bioreactor formed a hermetically sealed chamber for scaffold incubation while allowing fiber optic access through the MICs.

#### 4.3.4 Excitation light delivery and FOB image acquisition

Nondestructive imaging of the vascular lumen was carried out using the FOB imaging system, which enabled continuous image acquisition through the scaffold wall during construct maturation in the bioreactor. A detailed description of the system and scanning/fluorescence mapping method can be found elsewhere [119, 120]. Briefly, after the scaffold was seeded and the bioreactor assembled, the construct was placed on a heated imaging stage to maintain a  $37^{\circ}\text{C}$  environment (Figure 4.1H). Fluorescence excitation light was delivered to the scaffold lumen by

inserting a 45° angle polished single-mode optical fiber (SMF430, Nufern Inc., East Granby, CT) into the MIC (Figure 4.1G). The angled fiber formed an optical micro-mirror by which excitation light could be launched at a 90° angle relative to the fiber longitudinal axis to illuminate GFP-ECs on the lumen of the vascular scaffold. A continuous wave solid-state laser with a wavelength of 473 nm (BLM-100, Extreme Lasers Inc., Seabrook, TX) was operated at 0.5 mW and coupled into the optical fiber with the micro-mirror tip to excite the cells on the vessel lumen.

To obtain an image of GFP-ECs seeded on the lumen surface, a fiber scanning and fluorescence mapping procedure was performed, as illustrated in Figure 4.1I. Briefly, the laser light introduced into the scaffold wall formed a localized beam of excitation light on the lumen surface, which will be referred to as the “excitation spot”. The excitation spot was then sequentially raster-scanned on the luminal surface by controlling the position and angle of the fiber micro-mirror within the MIC using two motion stages: a motorized translation stage (UTM100PP.1, Newport, Irvine, CA) and rotation stage (URM100APP, Newport). When the excitation spot reached a GFP-EC, the GFP was excited and subsequently emitted green fluorescence light, part of which traveled through the scaffold wall. The intensity of the fluorescence light leaving the scaffold was measured using an EM-CCD detector (iXon+, Andor, Belfast, Ireland) with a 2x long working distance objective attached (M-Plan, Mitutoyo). Bandpass filters (525/45 BrightLine, Semrock, Rochester, NY) were used to block excitation light while allowing GFP fluorescence to reach the EM-CCD detector. By coupling the fluorescence intensity to the excitation spot location, it was possible to create a fluorescence intensity map representing EC distribution on the lumen surface via signal processing using a custom MATLAB script (Mathworks, Cambridge, MA). This fluorescence intensity map will hereafter be referred to as the fiber optic based image, or FOB image. Custom LabView (National Instruments, Austin, TX) programs were written and utilized to control the motion stages and cameras for image acquisition.

#### 4.3.5 Nondestructive quantification of EC lumen coverage

The half-vessel scaffold was used to provide initial verification of the capability of the integrated FOB system to nondestructively image GFP-EC coverage of the vascular scaffold lumen during maturation in the bioreactor. Using the half-vessel configuration, we could simultaneously acquire a direct-line-of-sight “control” image of the lumen using conventional fluorescence microscopy (i.e. control camera) for comparison. After cell seeding, a 1 mm x 250

$\mu\text{m}$  area of the vascular lumen was scanned with the 473 nm laser excitation spot and GFP fluorescence intensities were recorded at each excitation spot location. The excitation spot was translated at 5  $\mu\text{m}$  intervals and rotationally scanned at a step size of  $1.33^\circ$  to cover the aforementioned area. Three separate 1 mm x 250  $\mu\text{m}$  areas of the lumen were imaged daily using this method to follow the progression of endothelialization of the surface until confluency was achieved. For each FOB image obtained, a corresponding direct-line-of-sight control image was acquired with the control camera, to provide  $n = 3$  FOB/control image pairs of the lumen at each time point, to assess the accuracy of the FOB imaging method. Both control and FOB images were then evaluated for area of EC coverage using Image J software. Images were imported into ImageJ, thresholded to the same value, a binary image was created, and then the area of cell coverage on the scaffold surface (fluorescence coverage) was measured.

#### 4.3.6 Nondestructive quantification of EC detachment

EC detachment from the lumen of vascular grafts was imaged and quantified after the scaffolds reached confluency. Half-vessel scaffolds were used for this study to expose the lumen to the control camera. At day 4 after seeding, the media in the bioreactor was replaced with a 1  $\mu\text{M}$  trypsin EDTA solution in phosphate buffered saline (PBS) to induce EC detachment. A 250  $\mu\text{m}$  x 250  $\mu\text{m}$  area of each scaffold lumen was then continuously imaged using the FOB imaging system at 20 minute intervals for 1 hour ( $n = 3$  scaffolds total). Control images were also obtained for comparison to the FOB images. Control and FOB images were then analyzed, as explained previously, to nondestructively measure area of cell coverage through the scaffold wall over time.

#### 4.3.7 Nondestructive quantification of EC apoptosis

The FOB imaging method was used to nondestructively detect EC apoptosis on the vascular scaffold lumen. To induce varying degrees of EC apoptosis, concentrations of 1 and 5  $\mu\text{M}$  camptothecin (MP Biomedicals, Solon, OH) were prepared in EBM-2 media and applied to confluent monolayers of GFP-ECs on the vessel lumen 4 days post-seeding. Separate scaffolds were incubated in the camptothecin solutions for 4 hr at  $37^\circ\text{C}$  followed by 2 rinses with PBS. Next, an Alexa Fluor<sup>®</sup> 647 annexin V conjugate (Invitrogen, Carlsbad, CA) solution was prepared in 1X annexin-binding buffer (Invitrogen, Carlsbad, CA) to a final concentration of 5% v/v. Annexin V specifically binds apoptotic cells only, with no binding associated with non-

apoptotic cells. The scaffolds treated with camptothecin, and a non-camptothecin treated control scaffold, were then incubated in the annexin V solution for 15 minutes, after which the vessel lumens were imaged.

A 500  $\mu\text{m}$  x 250  $\mu\text{m}$  area of the vascular lumen was scanned with the 473 nm laser to obtain a FOB image of GFP-EC distribution on the scaffold lumen. Next, to detect GFP-ECs that bound the far-red fluorescent annexin V conjugate, a 633 nm laser (05-LHR-121, CVI Melles Griot, Albuquerque, NM) was used to excite the apoptotic cells. A 647 nm longpass filter (Semrock, Rochester, NY) was used to block excitation light while allowing red fluorescence to reach the EM-CCD detector. The area previously imaged for GFP-ECs was then scanned with the 633 nm laser to obtain a FOB image of annexin V bound to apoptotic cells.

#### 4.3.8 Nondestructive quantification of graft endothelialization in response to scaffold fiber diameter

GFP-EC proliferation and coverage on full-vessel graft lumens was quantified in response to varying luminal electrospun fiber diameter. Full-vessel scaffolds with 3 different luminal electrospun fiber diameters (0.36  $\mu\text{m}$ , 1.00  $\mu\text{m}$ , and 3.32  $\mu\text{m}$ ) were fabricated by varying electrospinning parameters as outlined in Table 4.1. After cell seeding, three different 500  $\mu\text{m}$  x 250  $\mu\text{m}$  areas of each scaffold were imaged daily and GFP-EC coverage was quantified for each scaffold group ( $n = 3$  total per group) for 7 days. After imaging on day 7, the scaffolds were sectioned lengthwise and stained for F-actin and nuclei to compare to the FOB images at day 7. To accomplish this, the following steps were performed with PBS washes in between: samples were fixed in 3.7% paraformaldehyde (EMD chemicals, Gibbstown, NJ) for 20 min, permeabilized with 0.1% Triton X-100 (Sigma Aldrich) for 5 min, incubated in 1% bovine serum albumin (Santa Cruz Biotechnology, Inc., Santa Cruz, CA) for 30 min, incubated for 20 min in rhodamine phalloidin (Invitrogen) to stain for F-actin, and nuclei were counter stained with DAPI (Invitrogen). Cells were imaged using a conventional fluorescence microscope (Leica DMI6000-B, Wetzlar, Germany).

#### 4.3.9 Two-photon microscopy

The imaging depth of the FOB imaging system was directly compared to that of two-photon microscopy. Three electrospun PDLLA full-vessel scaffolds of varying thicknesses (95, 230, and 520  $\mu\text{m}$ ) were fabricated as described in section 2.1. The grafts were then sectioned

lengthwise to allow direct access to image the lumen. GFP-ECs were then seeded onto the lumen of the vascular grafts at a density of  $1.5 \times 10^4$  cells/cm<sup>2</sup>. Cell seeded grafts were then allowed to incubate for 1 day before imaging. To image, sectioned grafts were placed into a culture dish with a 170  $\mu$ m coverslip on which the scaffold rested. A two-photon microscope (Zeiss LSM 510, Carl Zeiss Inc., Germany) equipped with a 20 x Plan-Apochromat objective (20x/0.8 N.A., Zeiss M27, Carl Zeiss Inc.) operating at 960 nm was then used to obtain images of GFP-ECs on the lumen surface by imaging through the electrospun vessel wall to resolve the GFP-ECs on the lumen surface. Additionally, images were obtained by placing the objective in direct-line-of-sight to the lumen surface to serve as control images.

#### 4.3.10 Statistical analysis

All values are expressed as mean  $\pm$  one standard deviation. Statistical analysis was performed using one-way analysis of variance (ANOVA) and significance was considered at  $p < 0.05$ .

## 4.4 Results and Discussion

### 4.4.1 Nondestructive quantification of EC lumen coverage

Obtaining a confluent endothelium on the lumen of a vascular graft before implantation is vital to the success of the implant because thrombus formation is extremely sensitive to exposed surfaces [108]. Therefore, measurement of graft endothelialization is an important metric to determine the functionality and antithrombogenicity of the graft prior to implantation. The first set of experiments aimed to assess the feasibility of the FOB imaging method to noninvasively monitor endothelialization of the lumen surface of the vascular graft during incubation in a bioreactor. A half-vessel scaffold was seeded with GFP-ECs, placed in a bioreactor, and imaged over a 4-day period. Using the half-vessel configuration, we could simultaneously acquire a direct-line-of-sight control image of the lumen using conventional fluorescence microscopy (i.e. control camera). Figure 4.2A shows representative FOB and corresponding control images of the graft lumen for the duration of the study. The GFP-ECs have proliferated to cover the surface of the graft, and in 4 days have formed a nearly confluent endothelium with very few denuded regions. The FOB images closely resemble the control images in terms of overall cell distribution. To quantify the degree of lumen confluency, each image was analyzed for area of cell coverage (Figure 4.2B). The area of cell coverage for corresponding FOB and control

images are not statistically different at each time point ( $p < 0.05$ ), demonstrating that the FOB imaging method provides an accurate assessment of endothelial coverage. Furthermore, the resolution of the FOB imaging method is sufficient to detect statistically different levels of endothelial coverage over time, even when the graft lumen becomes nearly confluent from day 3 to 4 (increase from ~75% to ~95% coverage).

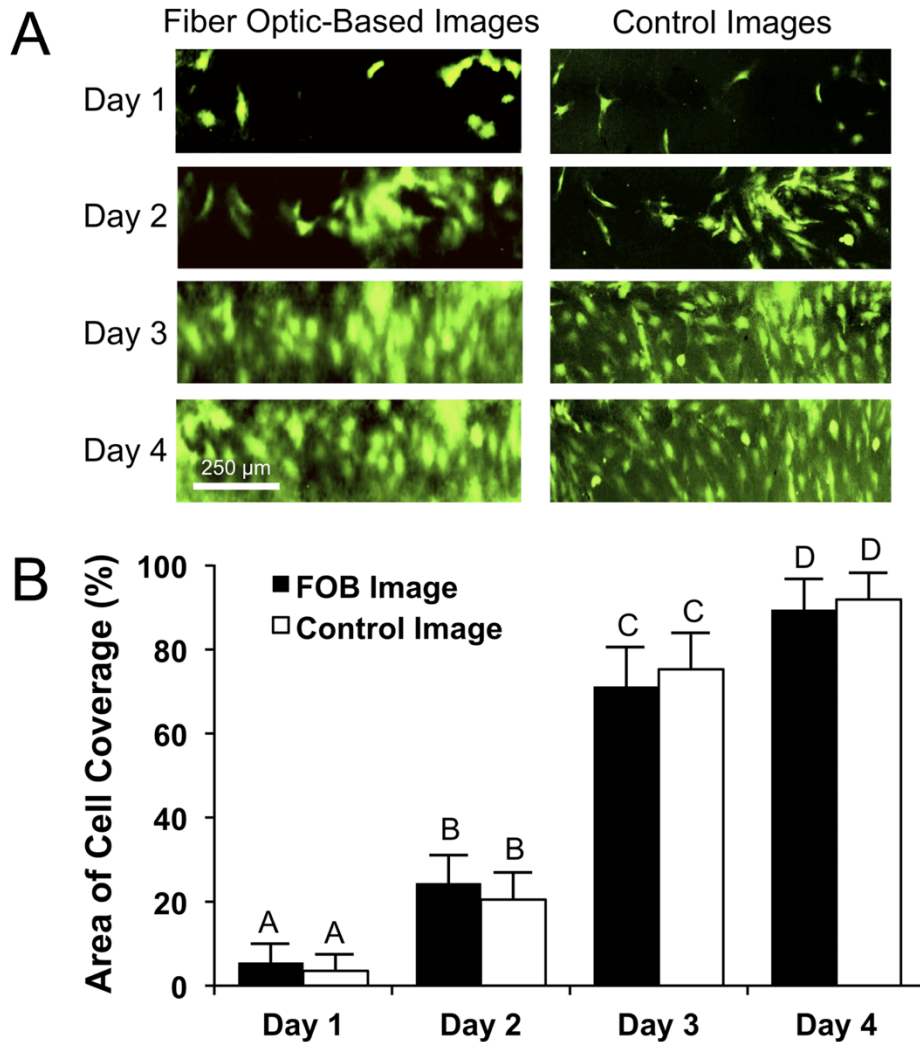


**Figure 4.2. Quantification of GFP-EC proliferation and lumen coverage.** A) A vascular scaffold sectioned lengthwise was seeded with GFP-ECs and 3 separate 1 mm x 250  $\mu$ m areas of the graft were imaged daily until the lumen reached confluency at Day 4 (representative images shown). B) Images were analyzed to quantify the amount of cell coverage on the vascular lumen ( $n = 3$  images/time point). The results show that there is good agreement between amount of cell coverage for the FOB images, obtained through scaffold wall, and direct-line-of-sight control images at each time point. Data are presented as mean  $\pm$  one standard deviation and values marked with the same letter are not significantly different ( $p < 0.05$ ).

#### 4.4.2 Nondestructive quantification of EC detachment

In this study, we tested if the FOB imaging method could successfully image and quantify EC detachment from the vessel lumen. Figure 4.3A shows a 250  $\mu\text{m}$  x 250  $\mu\text{m}$  section of the vascular graft that was continuously imaged at 20 minute intervals after the onset of cell detachment. At 0 min, the lumen surface is nearly confluent, and after trypsin addition, the ECs gradually detach from the surface. Similar to Figure 4.2A, there is close agreement between the FOB and control images, demonstrating that the FOB images accurately represent cell distribution on the lumen surface. These results were quantified by analyzing the images for area of cell coverage (Figure 4.3B) and show that the amounts of cell coverage between the corresponding FOB and control images are not statistically different at each time point ( $p < 0.05$ ). The high temporal resolution of the FOB imaging system allowed for dynamic assessment of EC detachment over time. Endothelial cell retention on the lumen of a bioengineered vascular graft is a key requirement to maintain long-term patency of the graft. EC detachment from the lumen surface of a vascular graft *in vivo* can potentially cause thrombus formation, leading to graft obstruction or embolism [107]. *In vitro*, EC detachment from the graft can be caused by a deficiency in adequate cell/biomaterial adherence, high shear stress, or as a result of shear induced apoptosis [19, 121]. The ability to noninvasively monitor EC detachment *in vitro*, especially for grafts undergoing fluid flow preconditioning, can provide real-time feedback on the integrity, confluency, and adhesiveness of the endothelium.

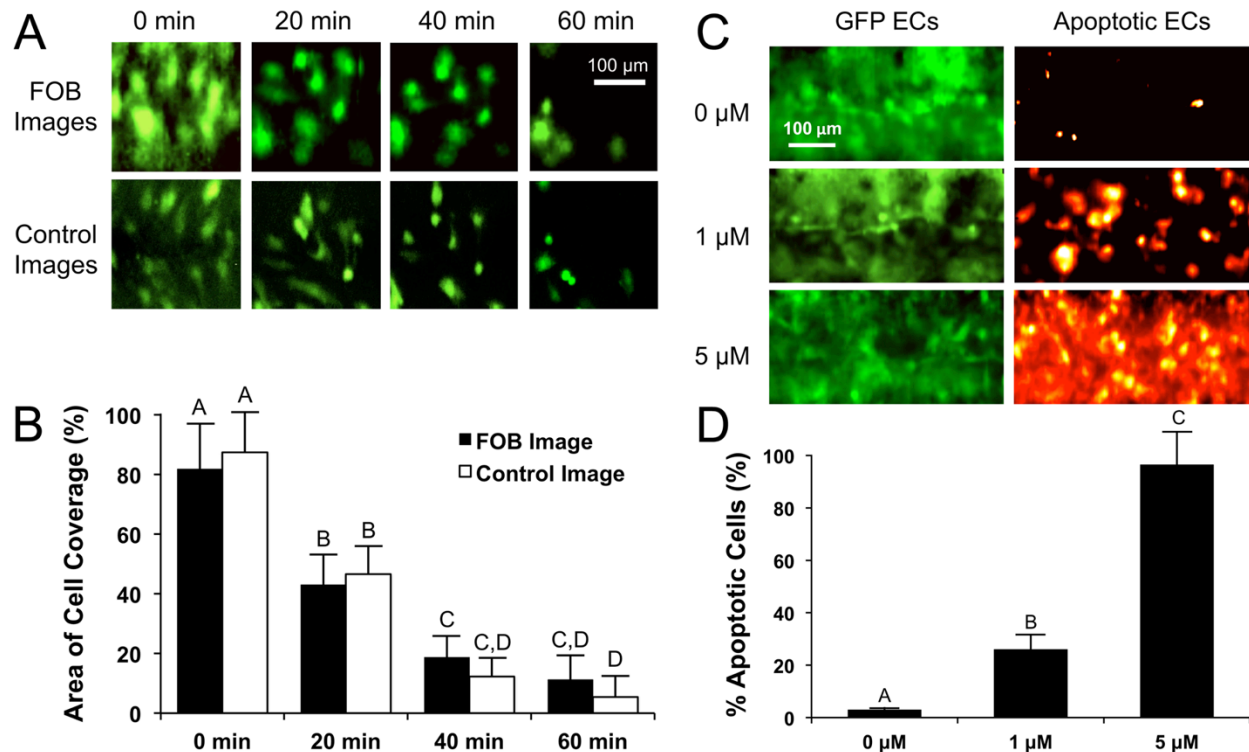


**Figure 4.3. Quantification of GFP-EC detachment and apoptosis.** A) Representative images of a near confluent endothelium that was subjected to a dilute concentration (1  $\mu\text{M}$ ) of trypsin EDTA to induce cell detachment from the lumen. An area of  $250 \mu\text{m} \times 250 \mu\text{m}$  was continuously scanned to image GFP-EC detachment from the lumen over time. B) Extent of GFP-EC detachment from the lumen was quantified by analyzing the area of cell coverage from the fluorescent images ( $n = 3$  images/time point). The FOB and corresponding control images had equivalent amounts of cell coverage at each time point. C) A near confluent endothelium was exposed to varying concentrations of camptothecin to induce GFP-EC apoptosis. A red fluorescent annexin-V conjugate was then added to visualize the extent of EC apoptosis on the vascular scaffold lumen. Three different  $500 \mu\text{m} \times 250 \mu\text{m}$  areas were imaged to detect both GFP and red fluorescent annexin-V (apoptotic cells) on each scaffold for each condition. Results showed that varying levels of GFP-EC apoptosis could be noninvasively imaged and B) the fraction of apoptotic cells could be quantified through the scaffold wall using the FOB imaging method ( $n = 3$  images/condition). Data are presented as mean  $\pm$  one standard deviation and values marked with the same letter are not significantly different ( $p < 0.05$ ).

In addition to monitoring EC detachment, we are interested in determining the effect of fluid flow on vascular endothelialization and EC morphology. Traditional methods used to study the effect of fluid flow on ECs include the use of parallel plate flow chambers wherein cell culture media is perfused between two parallel substrates upon which the cells are cultured. These chambers deliver mechanical shear stress to the cultured cells by facilitating uniform laminar flow to develop across the cultured surface [122]. While useful for studying the effects

of shear stress alone, these systems do not allow for combinatorial mechanical stimulation (i.e. shear stress, hoop stress, and hydrodynamic pressure) that is known to occur in native arterial vessels. There is increasing data to support the hypothesis that not only does shear stress modulate endothelial development and function, but also hoop stress that is caused by vessel stretch and hydrostatic pressure caused by pulsating blood flow [123, 124]. By incorporating the FOB imaging system in an intact vessel undergoing pulsatile flow *in vitro* to mimic vascular flow *in vivo*, we believe that the endothelium could be studied under a more physiological loading scenario where the lumen is subjected to all three modes of mechanical stimulation.

#### 4.4.3 Nondestructive quantification of EC apoptosis

Apoptosis, or programmed cell death, is a naturally occurring cell-death pathway that occurs in ECs and plays an important part in vascular tissue homeostasis. In this study, we induced various levels of EC apoptosis by exposing a near confluent endothelium to different concentrations of camptothecin, a well-known apoptosis-inducing agent [125]. To detect apoptotic cells, red fluorescent annexin-V conjugate was added, and the graft lumen was imaged for both GFP and far-red fluorescent annexin-V. Figure 4.3C (left column) shows that each graft had a near-confluent endothelium for each condition as evidenced by near complete GFP coverage. The control sample that was not exposed to camptothecin (0  $\mu\text{M}$ ) showed very little EC apoptosis, whereas the grafts exposed to 1 and 5  $\mu\text{M}$  solutions experienced a dose dependent increase in cell apoptosis. Three sections of each vascular graft were imaged for both GFP and annexin-V and the resulting images were analyzed to quantify the fraction of apoptotic cells on the vessel lumen (Figure 4.3D). While EC apoptosis is a naturally occurring event in native vessels, premature or extensive apoptosis in engineered vascular grafts can be an indication of non-optimal culture or preconditioning methods [126, 127]. Recently, it has been shown that endothelial cell apoptosis, and subsequent cell death, can occur by biomaterial-induced toxicity [128, 129]. This phenomenon is caused by an inflammatory reaction due to the lack of, or inappropriate, contact of ECs with the biomaterial surface. Therefore, the ability to noninvasively detect apoptosis in engineered tissues during preconditioning is an important measure of tissue homeostasis and overall tissue health in response to preconditioning and cell/biomaterial interactions.

While we demonstrate here the capability to noninvasively assess EC apoptosis on the lumen of a vascular graft, the ability to image two distinct fluorophores could have multiple

applications in monitoring the maturation of a bioengineered vascular graft. In this study, we show that it is possible to image two fluorophores using the FOB imaging system, namely co-localized GFP and far-red annexin-V conjugate. With this two-color imaging capability, it could be possible to detect two different color fluorescent proteins in the same cell simultaneously. For example, a cell could be co-transfected first with a constitutive fluorescent protein, such as GFP, for continuous visualization, and second with a red fluorescent protein (RFP) under control of a promoter for endothelial nitric oxide synthase (eNOS) – an enzyme that plays a critical role in nitric oxide production in response to shear stress. With this example, it would be possible to noninvasively monitor and quantify the effect of fluid flow preconditioning not only on endothelialization and endothelium integrity, but also on specific EC functions that are important for normal vascular function under fluid flow.

#### 4.4.4 Nondestructive quantification of graft endothelialization in response to scaffold fiber diameter

After validating the FOB imaging method using a half-vessel construct, we next tested the capacity of the FOB imaging system to measure the effect of varying surface topographies on lumen endothelialization of a full-vessel construct. Scaffold topography and architecture has been shown to affect EC proliferation, morphology, and formation of focal adhesions on the biomaterials surface [130, 131]. We therefore sought to determine if electrospun fiber diameter, and the resulting change in scaffold topography, would affect EC proliferation and the formation of an intact endothelium on the lumen surface. In these experiments, 3 different full-vessel scaffolds with varying lumen fiber diameter were fabricated to vary the lumen topography. Figure 4.4A shows SEM images of scaffolds for each fabrication condition (Table 4.1), which produced scaffolds with mean fiber diameters of  $0.36 \pm 0.07 \mu\text{m}$ ,  $1.00 \pm 0.31 \mu\text{m}$ , and  $3.32 \pm 0.63 \mu\text{m}$ . ECs were seeded onto the grafts and imaged at daily intervals for a 7-day period. For each fiber diameter, 3 scaffolds were fabricated and imaged at 3 different locations on each graft to produce  $n = 9$  images for each condition per time point. Figures 4B, C, and D show representative images of each vascular graft condition at days 0, 3, and 7; respectively. EC lumen coverage appeared to be similar for each condition immediately after cell seeding on Day 0. After 3 days of incubation in the bioreactor, the graft lumen with the smallest fiber diameter ( $0.36 \mu\text{m}$ ) appeared to have a greater extent of cell coverage than the other conditions, and at Day 7 these grafts had a near-confluent endothelium with very few void regions. Conversely, the

grafts with the largest fiber diameter (3.32  $\mu\text{m}$ ) had minimal cell coverage even after 7 days of incubation. These images were analyzed to quantify the extent of cell proliferation and coverage on the surface of the vascular grafts in response to varying the surface topography. Each vascular graft lumen was noninvasively imaged daily with the FOB imaging system to provide a continuous trend of graft endothelialization over time (Figure 4.4F). The data shows that while coverage of the graft lumen increases over time for each condition, the graft with a 0.36  $\mu\text{m}$  fiber diameter has the greatest proliferation rate and nearly encompasses ( $\sim 95\%$ ) the entire luminal surface by day 7. In comparison, the grafts with 1  $\mu\text{m}$  and 3.32  $\mu\text{m}$  fiber diameters show that the lumens achieve only approximately  $\sim 70\%$  and  $\sim 30\%$  coverage at day 7; respectively. These results are consistent with those of Ju *et al.* [37], who showed that human aortic endothelial cells could only form a confluent monolayer on PCL/collagen type 1 scaffolds with fiber diameters smaller than 1  $\mu\text{m}$  in diameter. In the current study, grafts at day 7 were sectioned lengthwise and stained for F-actin and DAPI to compare to the FOB images at day 7. Figure 4.4D shows that the FOB images appear to be very similar to the stained images obtained with direct-line-of-sight fluorescence microscopy (Figure 4.4E). This data demonstrates that the FOB imaging system is sufficiently sensitive to accurately determine the rate of graft endothelialization and degree of EC confluency in response to varied scaffold properties during graft incubation in a bioreactor.

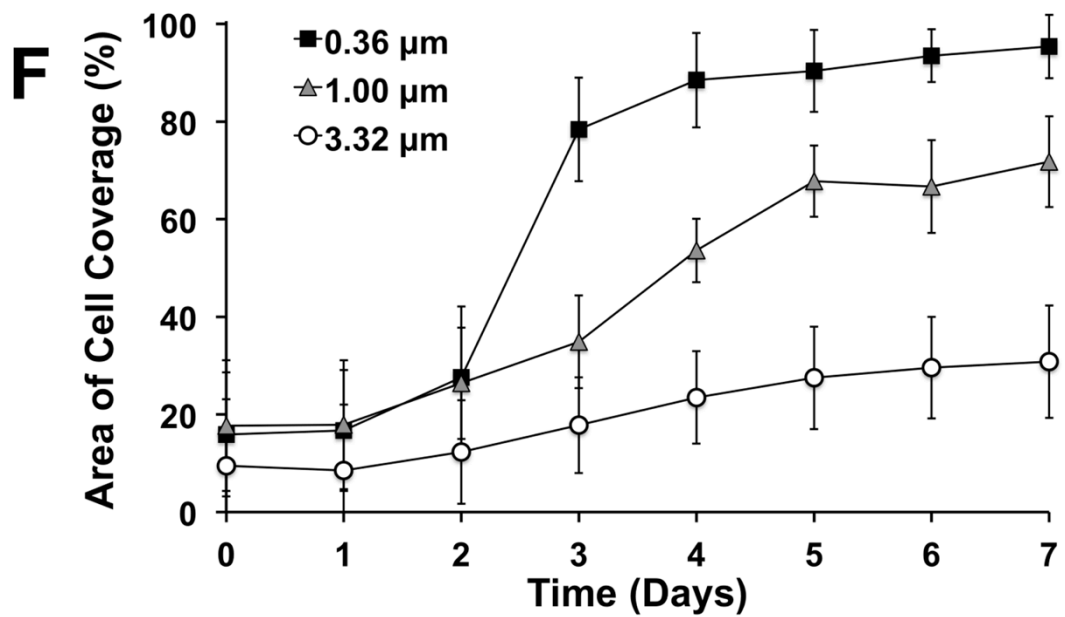
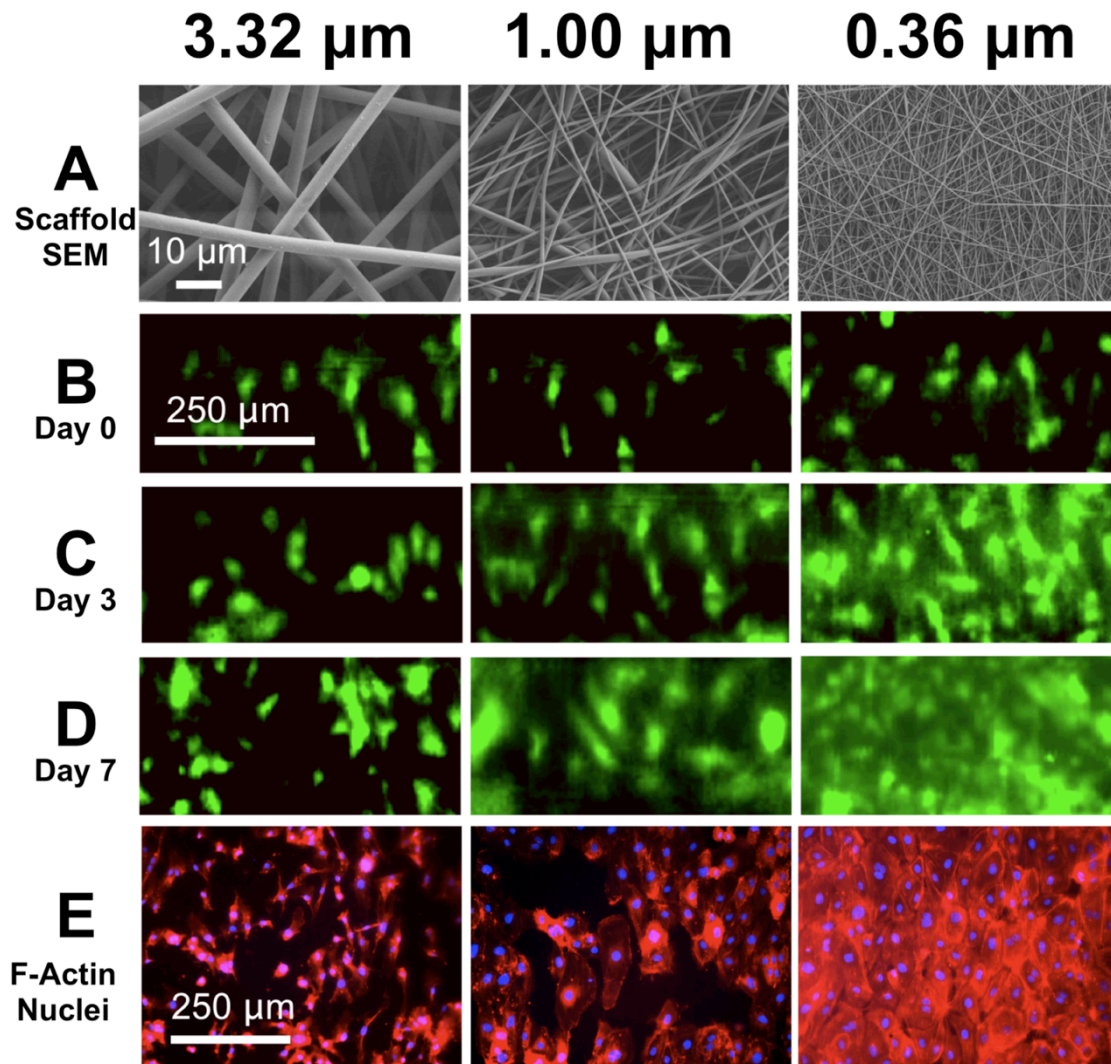


**Figure 4.4. Effect of lumen topography on graft endothelialization.** Full-vessel grafts with varied electrospun fiber diameters were fabricated to study the effect of lumen fiber diameter and varying topography on EC proliferation and endothelialization. A) Mean fiber diameters of 3.32  $\mu\text{m}$ , 1.00  $\mu\text{m}$  and 0.36  $\mu\text{m}$  were electrospun by varying electrospinning parameters as shown in Table 4.1. After cell seeding, three separate 500  $\mu\text{m}$  x 250  $\mu\text{m}$  areas of each vascular graft were imaged daily to assess luminal coverage and EC growth over time. Representative FOB images of GFP-EC coverage are shown for each scaffold fiber diameter at B) Day 0, C) Day 3, and D) Day 7. E) After FOB imaging on Day 7, scaffolds were removed from the bioreactor, sectioned in half, stained for F-actin (red) and cell nuclei (blue), and imaged using a conventional fluorescence microscope to provide a comparison to the FOB images at Day 7. F) A total of  $n = 3$  scaffolds for each fiber diameter were imaged, and  $n = 3$  areas (500  $\mu\text{m}$  x 250  $\mu\text{m}$ ) for each scaffold, yielding a total of  $n = 9$  images for each scaffold group every day. The FOB imaging method provided a noninvasive, accurate measurement of vascular graft lumen endothelialization over time. Data are presented as mean  $\pm$  one standard deviation.

An important aspect is that the FOB imaging method has the capacity to assess EC distribution through a relatively thick wall of the vessel, and can therefore collect data on the lumen of the vessel without removal from the bioreactor or destruction of the sample. To collect the same information of lumen coverage as shown in Figure 2B in a tubular vascular graft using conventional fluorescence microscopy, 4 different scaffolds (one at each time point) would need to be seeded, incubated, and histologically sectioned to obtain identical information as we acquired with a single vessel using the FOB imaging system. Similarly, the data obtained in Figure 4.4F would require a total of 72 scaffolds ( $n = 9$  different scaffolds at each time point) using conventional microscopy as compared to repeatedly imaging the same 9 scaffolds at each time point using the FOB imaging system. Conventional fluorescence microscopic techniques would require different samples at each time point since the vessel would have to be histologically sectioned to image the lumen, thus destroying the scaffold. Direct-line-of-sight imaging such as this is necessary since the wall of the vascular graft is far too thick and optically scattering to obtain an image of the endothelium through the vessel wall using microscopic techniques such as confocal laser scanning microscopy [119].

#### 4.4.5 Two photon microscopy and comparison to conventional imaging methods

Two-photon microscopy, or multi-photon microscopy, is a powerful imaging technique used to image deep within biological tissues or scaffolds with high resolution [72]. Currently, there is no other diffraction-limited optical imaging system that can reach the imaging penetration depth of multi-photon microscopy at a given resolution [132]. We therefore compared the imaging penetration depth of the FOB imaging system to that of two-photon

microscopy. To accomplish this, 3 different PDLLA vascular scaffolds with varying wall thickness (95, 230, and 520  $\mu\text{m}$ ) were fabricated using the electrospinning approach as described earlier. The scaffolds were sectioned lengthwise, seeded on one side of the scaffold with GFP-ECs, and then imaged using a two-photon microscope. The scaffolds were placed in a cell culture dish with glass coverslip bottom to allow imaging access within the working distance of the objective. First, the scaffold lumens were imaged in direct-line-of-sight to the lumen to ensure that ECs were on the lumen surface (Figure 4.5A,B). Next, the scaffolds were positioned such that the exterior surface of the scaffold wall faced the optical objective to mimic a situation in which a two-photon microscope would be used to image through the vascular scaffold wall to view GFP-ECs on the lumen (Figure 4.5C). Figure 4.5D shows an image obtained through a 95  $\mu\text{m}$  thick PDLLA electrospun scaffold to view the GFP-ECs on the lumen surface. In this image, the resolution of the cells is diminished as compared to the direct-line-of-sight view in Figure 4.5B. This reduction in imaging resolution is likely due to the highly scattering nature of the electrospun material. Figure 4.5E shows that the cells could not be resolved when imaging through the 230  $\mu\text{m}$  or 520  $\mu\text{m}$  electrospun PDLLA scaffolds (520  $\mu\text{m}$  scaffold image not shown) using two-photon microscopy. The FOB imaging system, however, was capable of imaging through the  $\sim 500$   $\mu\text{m}$  thick PDLLA scaffold with sufficient resolution to accurately identify the distribution of GFP-ECs (Figures 5F,G).

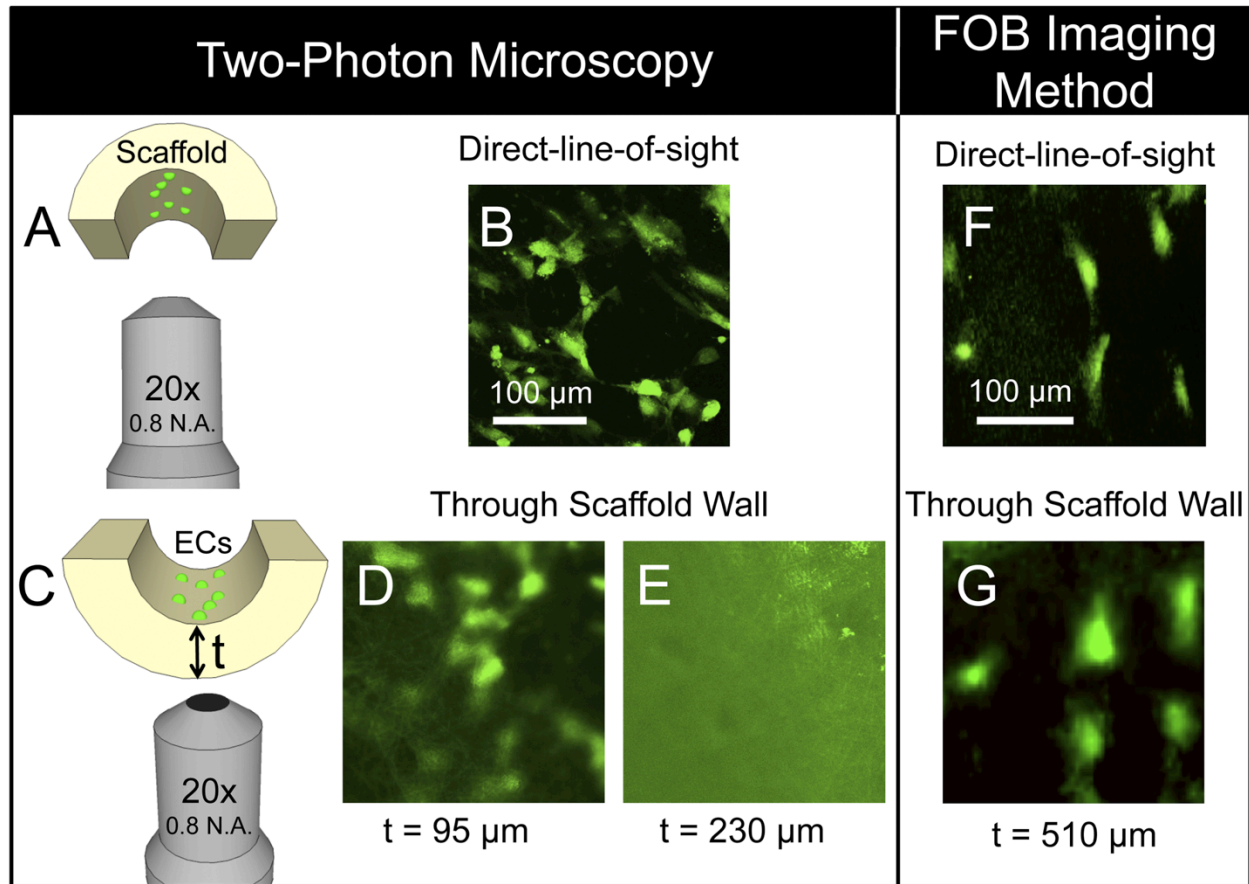


**Figure 4.5. Imaging penetration depth: comparison of FOB imaging method to Two-photon microscopy.** A) EC-seeded half-vessel scaffolds were imaged with a two-photon microscope in direct-line-of-sight to the lumen. B) Representative image of GFP-ECs in direct-line-of-sight to the vessel lumen. C) The two-photon microscope was then used to image GFP-ECs on the lumen through the wall of vascular scaffolds of varying thicknesses ( $t = 95, 230$  and  $520 \mu\text{m}$ ). Images of GFP-ECs on the vessel lumen through a D)  $95 \mu\text{m}$  and E)  $230 \mu\text{m}$  thick scaffold. Although cells were visible through the  $95 \mu\text{m}$  thick scaffold, GFP-ECs could not be resolved through the  $230$  and  $520 \mu\text{m}$  thick scaffolds. The FOB imaging method, however, was capable of resolving individual GFP-ECs through a  $\sim 510 \mu\text{m}$  thick scaffold wall (G) and the overall cell distribution of the same region of interest matched very closely to the direct-line-of-sight fluorescence image (F).

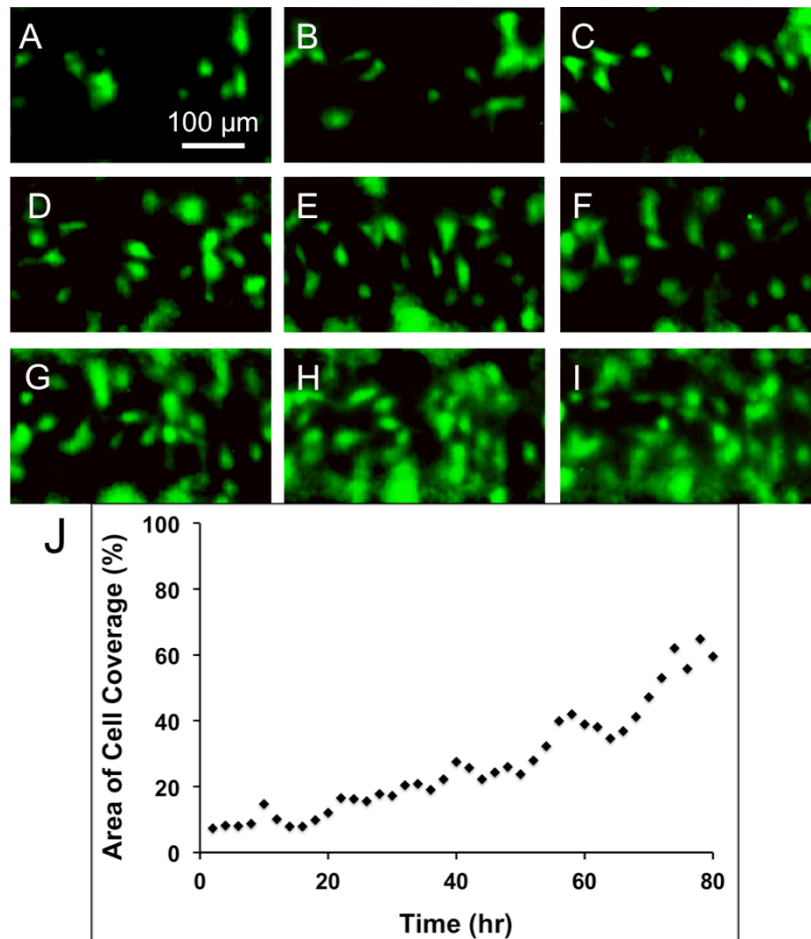
This experiment illustrates the difficulty of performing nondestructive imaging of a bioengineered vascular graft endothelium while housed in a bioreactor using conventional microscopy techniques. Confocal or two-photon microscopy are options to image the endothelium, however, due to the photon-scattering nature of the highly porous scaffold, it is exceedingly difficult to image through the thick vessel wall. In the present study, we demonstrated that two-photon microscopy only had an effective imaging depth of approximately  $95 \mu\text{m}$  through the highly opaque electrospun PDLLA scaffold. Electrospun vascular grafts used

for bypass grafting typically range from 300  $\mu\text{m}$  to 1 mm in thickness to sustain the physiological forces associated with blood pressure [17, 36, 37]. It is therefore impossible to use conventional microscope imaging techniques to penetrate through the wall of these vessels to noninvasively image the endothelium.

A potential alternative to using conventional microscope-based systems to image the endothelium are endomicroscope-based probes. In this approach, the endomicroscope could be inserted into the lumen of the vessel through the bioreactor flow chamber. Several groups have recently used endomicroscopes on the order of 1 mm in diameter to image cells and tissues both *in vitro* and *in vivo*. One notable example is a rotational side-view endomicroscope developed by Kim *et al* that is capable of imaging the gastrointestinal and respiratory tracts of mice *in vivo* with single-cell level resolution and a 250  $\mu\text{m}$  x 250  $\mu\text{m}$  field of view [80]. This imaging technique could potentially be used to assess the endothelium of a bioengineered vascular graft *in vitro*, however issues with sterility may limit its use due to repeated insertion into the bioreactor at evaluation intervals. Moreover, insertion of the endomicroscope into the lumen will likely disrupt the flow profile during fluid flow preconditioning. Therefore, this imaging method may not be suitable for dynamic assessment of a preconditioning vessel housed within a fluid flow bioreactor.

The FOB imaging system, alternatively, uses a micro-imaging channel embedded in the wall of the scaffold through which the excitation fiber optic is inserted and GFP-EC fluorescence is captured from outside the bioreactor using an EM-CCD detector. This allows for nondestructive, dynamic imaging of the endothelium of the vascular graft with no impact on the vascular scaffold or biological system in the bioreactor. Additionally, the FOB imaging method is capable of continuous scanning and subsequent image acquisition. This provides real-time data that could not otherwise be obtained using conventional, static fluorescence imaging using conventional microscopes. In Figures 2 and 4, the vascular grafts were imaged at daily intervals to assess graft endothelialization; however, it is possible to provide continuous scanning and image acquisition with the FOB imaging system. To demonstrate this capability, a 500  $\mu\text{m}$  x 250  $\mu\text{m}$  section of a full-vessel scaffold was sequentially imaged at 2 hr intervals for a 3-day period. Supplemental Figure 4.1 shows the GFP-ECs on the scaffold lumen and corresponding plot of GFP-EC coverage over time. In this video, GFP-ECs are actively migrating along the surface of the lumen and each image was analyzed to provide a real-time assessment of EC coverage,

which in this case increases with incubation time. It should be noted that the FOB imaging system is fully automated and does not require any manual adjustments during semi-continuous imaging. This capability of the FOB imaging system could be used as a “hands-off” approach to study EC proliferation rates and endothelialization with greater temporal resolution than could be obtained using conventional fluorescence microscopy. Additionally, the FOB imaging system could potentially be used to monitor EC migration along the vascular graft lumen in response to various stimuli, such as varied fluid flow regimes – an impossible task using conventional fluorescence microscopy and a difficult task for endomicroscopy techniques.



**Supplemental Figure 4.1. Dynamic imaging of graft endothelialization.** A full-vessel scaffold was seeded with GFP-ECs and a 500 μm x 250 μm section of the lumen was sequentially imaged at 2 hr intervals for a 3-day period. The figure shows the scaffold lumen at A) 2 hr, B) 10 hr, C) 20 hr, D) 30 hr, E) 40 hr, F) 50 hr, G) 60 hr, H) 70 hr, and I) 80 hr after seeding and J) corresponding plot of GFP-EC coverage over time. In this Figure, GFP-ECs are actively migrating along the surface of the lumen and each image can be analyzed to provide a real-time assessment of EC coverage.

#### **4.5 Conclusion**

In this study, we demonstrated the capability of the FOB imaging system to provide nondestructive, real-time data regarding endothelialization of a bioengineered vascular graft. The dynamic capabilities of this method allowed visualization and quantification of endothelial cell proliferation, coverage, detachment, and apoptosis. Additionally, we showed that the FOB imaging method is sufficiently sensitive to detect varied endothelialization rates in response to varied biomaterial topographies. Finally, we demonstrated that the FOB imaging system had a much greater imaging depth than that of two-photon microscopy. This method has clear advantages over endpoint testing to assess bioengineered vascular graft endothelium maturation and has the potential to be used to assess other endothelialized bioengineered tissues as well.

#### **4.6 Acknowledgements**

We would like to thank Dr. Hans Robinson in the Department of Physics at Virginia Tech for assistance with two-photon microscopy and Mr. Steve McCartney in the Nano Characterization and Fabrication Laboratory (NCFL) for his assistance with scanning electron microscopy. This research was funded by a grant from the National Institutes of Health (NIBIB HL098912), the National Science Foundation CAREER Award (CBET 0955072), and a grant from the Institute for Critical Technology and Applied Science (Virginia Tech).

## **Conclusions and Future Work**

### **5.1 Conclusions**

The objectives of this research were to develop scaffolds to enhance EC adherence to the surface under physiologic hydrodynamic shear stress and to develop an imaging methodology capable of assessing graft endothelialization in a dynamic and noninvasive manner with the overall goal of enhancing a bioengineered vascular graft endothelium. To meet these objectives, three studies were performed: 1) creation and evaluation of scaffold topographies that enhance EC adhesion under physiologic levels of shear stress, 2) development and validation of a noninvasive fiber optic based imaging system capable of resolving fluorescent ECs through a thick and opaque scaffold, and 3) incorporation of the FOB imaging system into vascular scaffolds to measure endothelialization in response to scaffold topography, EC detachment and EC apoptosis in a dynamic and nondestructive manner.

In the first study, ECs were seeded onto scaffolds with varying fiber diameter and orientation to determine their effect on EC shape, alignment, cytoskeleton organization and focal adhesions with the goal of increasing EC adhesion to the scaffold in response to shear stress. The results demonstrated that ECs became more elongated and aligned with the direction of nanofiber orientation. A confluent endothelium was formed on 100 nm and 300 nm scaffolds, whereas cells on 1200 nm scaffold did not form a confluent endothelium. Under physiologic levels of hydrodynamic shear stress, ECs on aligned nanofiber scaffolds displayed increased adherence to the scaffold as compared to those cells on randomly oriented nanofibers. These results suggest that aligned nanofiber scaffold topographies are capable of producing an aligned endothelium that is capable of resisting shear stress to create a more adherent endothelium for bioengineered vascular grafts applications.

In the second study, a FOB imaging system was developed and validated to image fluorescent ECs through thick and optically opaque electrospun scaffolds. To test the system, a planar vascular scaffold model was fabricated by sintering electrospun PDLA scaffold sheets with a micro-imaging channel embedded within. Fluorescent ECs constitutively expressing GFP were then seeded on the scaffolds and the FOB imaging system was used to map cells on the scaffold surface. Results demonstrated that the FOB imaging system was able to accurately

image fluorescent ECs in a noninvasive manner with spatial resolutions ranging from approximately 15 – 30  $\mu\text{m}$  at a SNR of approximately 2. Comparison between FOB images and control direct-line-of-sight images revealed that the FOB imaging system could produce images with 10% or less deviation from standard optical microscopy. Furthermore, the FOB imaging system was able to produce continuous images to visualize EC migration and cytokinesis in real-time.

In the third study, the FOB imaging system was used to quantify vascular scaffold endothelialization, EC detachment and apoptosis in a noninvasive manner. To perform this study, micro-imaging channels were incorporated into tubular scaffolds by utilizing a layer-by-layer electrospinning approach. GFP-ECs were then seeded onto the vascular lumen and imaged to provide an assessment of graft endothelialization over a 4-day period. Results showed that EC coverage as assessed by FOB and direct-line-of-sight images were not statistically different, thus demonstrating that the method can provide an accurate measure of EC coverage even as grafts near confluency. Furthermore, the FOB imaging system was capable of accurately detecting EC detachment and apoptosis through the vessel wall. Additionally, it was demonstrated that the FOB imaging method is sufficiently sensitive to detect varied endothelialization rates in response to varied scaffold topographies. Finally, it was shown that the FOB imaging system had a much greater imaging depth than that of two-photon microscopy and is a promising tool to provide online monitoring of a vascular graft endothelium.

By performing these studies, three significant results were achieved: 1) EC adhesion to scaffold surfaces under shear stress was enhanced by modifying the surface topography, 2) a fiber optic based imaging system was developed to noninvasively image cells through thick scaffolds, and 3) the fiber optic based imaging system was used to accurately measure vascular graft endothelialization with better spatial and temporal resolution than current optical imaging systems available.

## **5.2 Future Work**

While the findings and progress made in this research are promising advances in developing and monitoring vascular graft maturation *in vitro*, they also highlight several areas where further research is needed. These areas include 1) incorporation of aligned nanofibers on the lumen of a bioengineered vascular graft, 2) integration of the FOB imaging system into a fluid flow bioreactor to allow imaging during fluid flow preconditioning and 3) use of the FOB

imaging system to monitor cellularization and formation of an ECM in the vessel wall in response to preconditioning.

### 5.2.1 Incorporation of an aligned nanofiber lumen in a bioengineered vascular graft

In the study performed in chapter 2, PCL/collagen scaffolds were electrospun onto plastic substrates. This was sufficient for testing the effects of electrospun scaffold topography on EC morphology and alignment, however, this aligned topography needs to be incorporated into a tubular structure to fabricate a viable vascular graft. The axially aligned nanofibers on the vessel lumen would be incorporated to enhance EC alignment and adhesion to the graft under flow. To accomplish this task, the rotating mandrel upon which the vascular grafts are electrospun need to be modified to incorporate an insulating gap between the negatively charged mandrel holders as shown in Figure 5.1. This method is adapted from Zhu et al. that fabricate axially aligned fibers on the lumen and randomly oriented fibers in the wall of the tubular construct to produce an electrospun nerve conduit [133]. The insulating gap significantly alters the electric field between the positively charged polymer dispenser tip and the grounded collector. Uniaxial alignment of fibers is achieved through oppositely charged attraction between the positively charged fiber and negatively charged conductive mandrel. The fiber is subsequently aligned and stretched across the insulating gap due to the electrostatic attraction [134]. Once the aligned nanofiber lumen has been established, the mandrels can be pushed together to form a negative continuous charge across the graft length to produce randomly oriented fibers for the vessel wall. This electrospinning fabrication process will result in axially aligned nanofibers on the vessel lumen to enhance EC alignment and adhesion in the direction of fluid flow and randomly oriented nanofibers for the vessel wall to support blood flow.

The results in Chapter 2 demonstrated that ECs on aligned nanofibers significantly increased EC adhesion strength to the scaffold under physiological levels of shear stress *in vitro*. To determine if the scaffold design provides improved EC adhesion and improved patency *in vivo*, the vascular grafts with aligned and random nanofiber lumens should be implanted into an animal model. Future work with the vascular grafts containing axially aligned nanofiber lumens can be implanted in a rabbit aortoiliac bypass model and compared to vascular grafts lumens with randomly aligned nanofibers. This can be accomplished by isolating progenitor ECs from rabbits using a CD133 affinity-based blood pheresis purification system as previously described [17], seeding the grafts, then implanting the grafts as previously described [36]. Noninvasive

measurements of graft patency could be obtained by using Doppler ultrasound and contrast computed tomography angiography. To assess EC adhesion to the graft and EC morphology over time, explants could be extracted at days 1, 14 and 28 after implantation and imaged using scanning electron microscopy. The future work is expected to show that vascular grafts with axially aligned nanofiber lumens will retain a larger portion of seeded ECs and therefore remain patent after implantation as compared to randomly aligned nanofiber lumens, which should have lower EC retention.

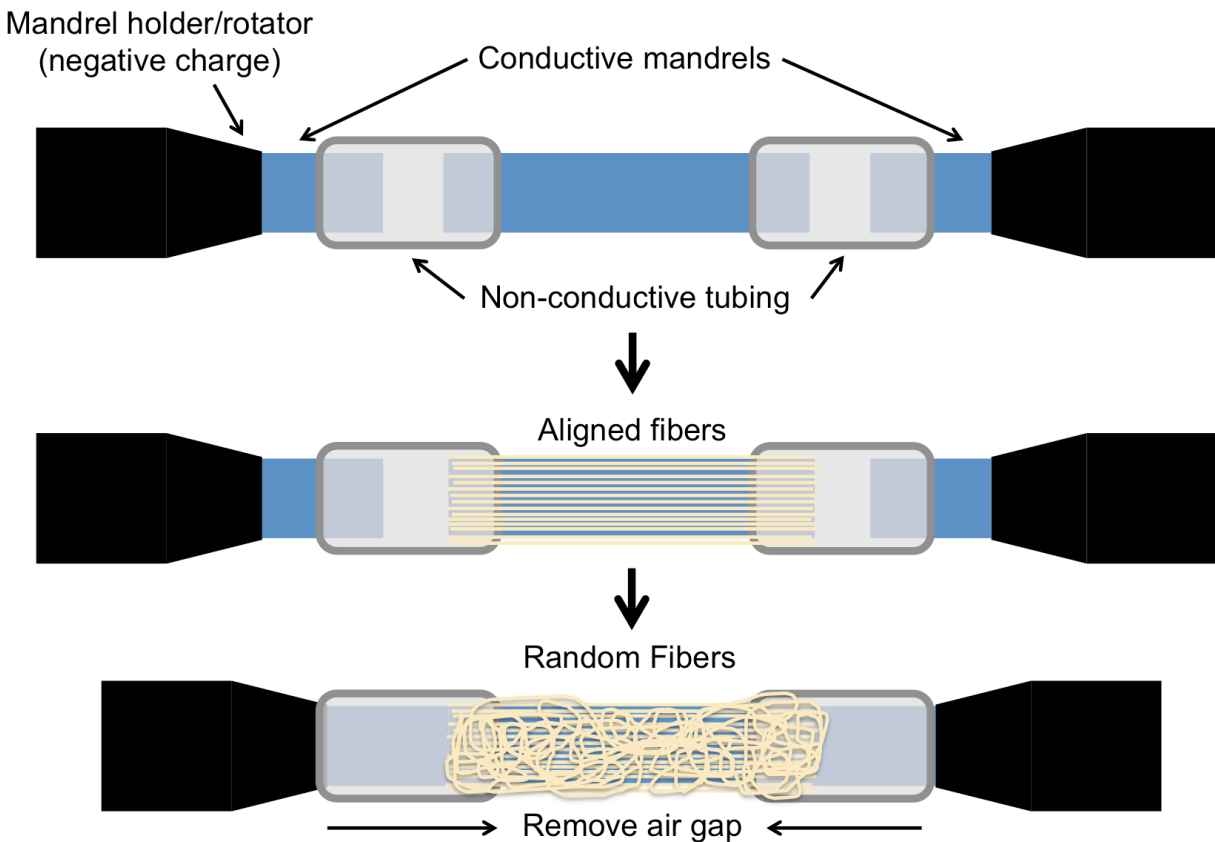


**Figure 5.1** A negatively charged mandrel with insulating gaps will alter the electric field between the positively charged polymer jet and negatively charged mandrel to produce axially aligned nanofibers for the vascular graft lumen. Once the aligned lumen has been established, the mandrel will be pushed together to remove the insulating gap to produce randomly oriented nanofibers for the vessel wall (adapted from zhu et al. [133]).

### 5.2.2 Integration of FOB imaging into a fluid flow bioreactor

Experiments conducted with the FOB imaging system in chapters 2 and 3 were carried out under static conditions and grafts were not exposed to fluid flow. A current goal is to design and test a fluid flow bioreactor that is compatible with integration of the FOB imaging system. We have begun designing and testing such a bioreactor with the following specifications: 1) the

fluid flow bioreactor must be modified to accommodate the MIC without leakage under fluid flow, 2) the MIC must not break during bioreactor construction or during imaging, 3) the fiber optic within the MIC must be free to translate and rotate freely during preconditioning, and 4) the fluid flow bioreactor must be compatible with OCT imaging method. A schematic of the fluid flow bioreactor is shown in Figure 5.2a. Bioreactor components include 1) quartz glass chamber, 2) silicone skirt stopper, 3) stainless steel dispensing needle, 4) 90° elbow fitting, and 5) PTFE slip bearings. Central to the design of the bioreactor is the quartz chamber that allows OCT imaging from the exterior of the bioreactor with minimal signal attenuation. The silicone skirt stoppers allow chamber sealing while permitting MIC extension from the vascular graft. The 90° elbow allows flow to be directed away from the MIC to permit fiber optic insertion into the MIC and the PTFE slip bearings allow the bioreactor to be rotated freely while mounted on the bioreactor stand. Rotation of the vessel is necessary to allow OCT imaging from the exterior as demonstrated in Appendix C. Construction of the bioreactor is shown in Figure 5.2b. First, the vessel with MICs embedded is mounted onto the stainless steel dispensing needles using dow corning medical grade silicone adhesive. Next, the vessel is slid through the quartz chamber and the proximal end is secured with a silicone stopper. Once the vessel is seated securely in the chamber, a 90° elbow fitting is placed on the proximal end of the dispensing needle. Silicone adhesive is then placed around the MIC to ensure that leakage does not occur. To ensure that the MIC does not break during bioreactor construction or imaging, only a small section of the polymer coating on the MIC is selectively removed such that the “imaging window” lies within the vessel for a length necessary for imaging region of interest (ROI) within the scaffold (i.e. 1 cm). This keeps the MIC mechanically flexible to reduce the chance of breakage during bioreactor construction and handling during imaging experiments. Another consideration in the design of the bioreactor is the mechanical instability of the fiberoptic used to deliver excitation light. The fiberoptic is made of silica and is very thin (145  $\mu$ m diameter), resulting in torsional instability when long sections of the fiber are rotated. This can result in the fiber lagging during imaging experiments, which causes aberrations in the resulting images. To alleviate this problem, the bioreactor was designed such that the fiberoptic only needs to be inserted a total length of approximately 5 cm to reach the imaging ROI within the vessel.

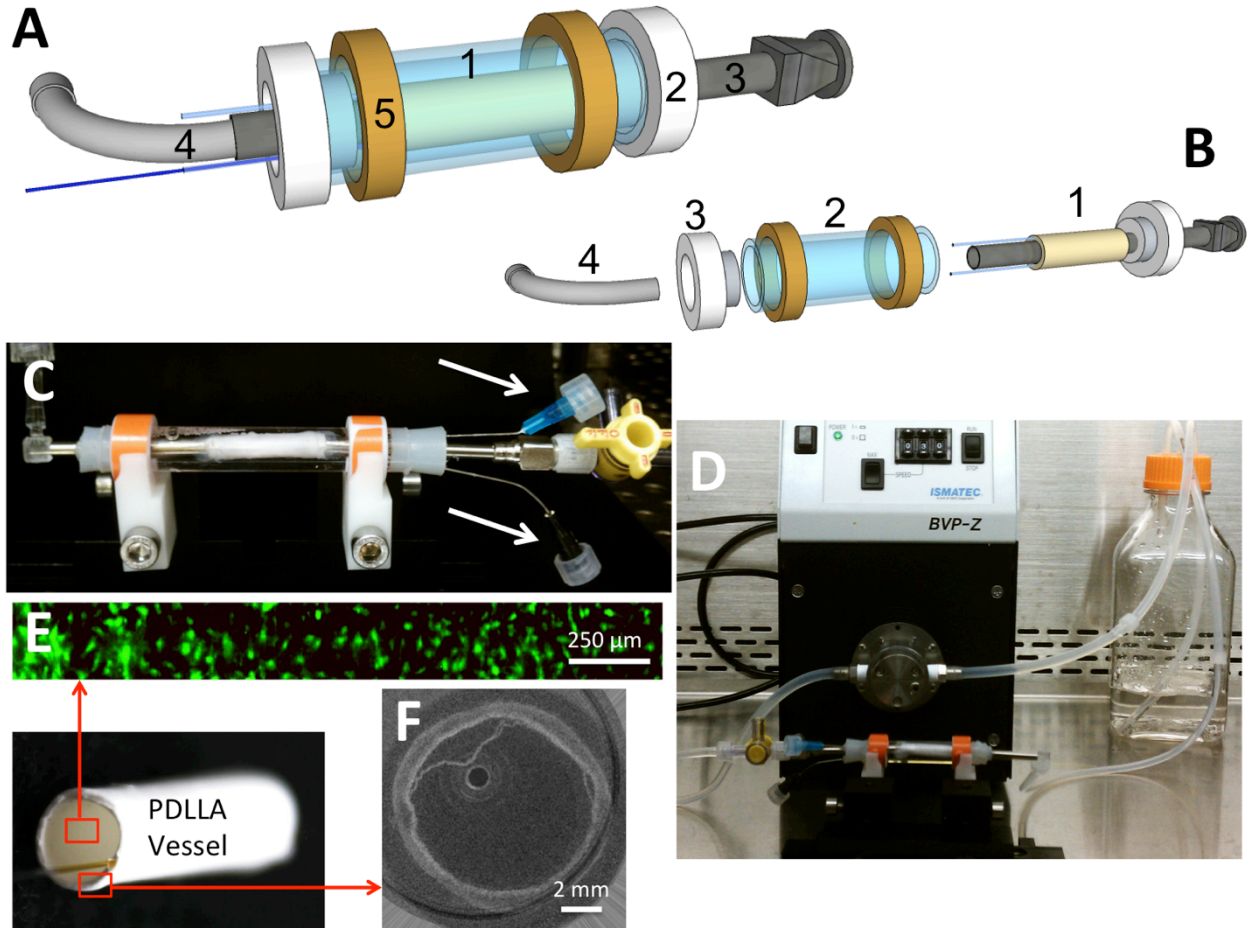


**Figure 5.2** Design and fabrication of an imaging-compatible fluid flow bioreactor. A) Schematic of the fluid flow bioreactor, B) construction of the bioreactor, C) Image of the constructed fluid flow bioreactor, D) bioreactor connected to the media reservoir and centrifugal pump, E) FOB image of GFP-ECs on the lumen after seeding, and F) OCT cross-section image of the vessel wall.

An image of the fully constructed bioreactor with vessel housed within is shown in Figure 5.2c. Two – 22 gauge needles (white arrows) were inserted into one of the silicone stoppers to allow access to the exterior portion of the vessel. The bioreactor was then filled with PBS and connected to a centrifugal pump as shown in Figure 5.2d. Flow rates of up to 1000 ml/min were achieved without bioreactor leakage. To test the imaging compatibility of the fluid flow bioreactor, the 500  $\mu\text{m}$  thick PDLLA vessel was seeded with GFP-ECs at a density of  $2 \times 10^4$  cells/ $\text{cm}^2$  and imaged using the FOB method. As shown in Figure 5.2e, a 2 cm length of the vessel was successfully imaged using the FOB imaging method. Additionally, it was possible to perform OCT imaging to obtain a cross-sectional image of the vessel wall as shown in Figure 5.2f. This bioreactor design allows noninvasive fluorescence imaging of the endothelium using

the FOB method and imaging of morphological changes in the vessel wall using OCT. Incorporation of these imaging capabilities in a fluid flow bioreactor will provide a better understanding of cell dynamics and tissue remodeling in response to various fluid flow preconditioning protocols with better temporal and spatial resolution than conventional *in vitro* assessment techniques.

### 5.2.3 FOB imaging system to measure scaffold wall maturation

The research conducted in this project demonstrates that the FOB imaging method is a powerful tool to monitor and assess the endothelium of a vascular graft. The *in vivo* success of a bioengineered vascular graft, however, not only relies on a functioning endothelium, but also on a functioning vessel wall that mimics a native artery in terms of cell composition and structure. The current paradigm in tissue engineering of vascular grafts not only include endothelialization of the lumen, but also seeding of the vascular wall with fibroblasts or SMCs to colonize and remodel the wall with cell-mediated ECM deposition [20, 36, 37, 135]. Since this component is necessary for a functioning vascular graft, it would be beneficial to image 1) the process of vascular wall cell proliferation and 2) ECM formation during preconditioning using the FOB imaging system. Additionally, being able to monitor the interplay between EC and SMC/fibroblasts (i.e. paracrine signaling) in real-time during preconditioning would aid in better understanding tissue maturation and response to preconditioning. Therefore, the following proof of concept work is proposed to utilize and validate the FOB imaging method in assessing SMC/fibroblast colonization and ECM deposition in the wall of a bioengineered vascular graft. The experimental plan proposed to complete this goal is outlined below.

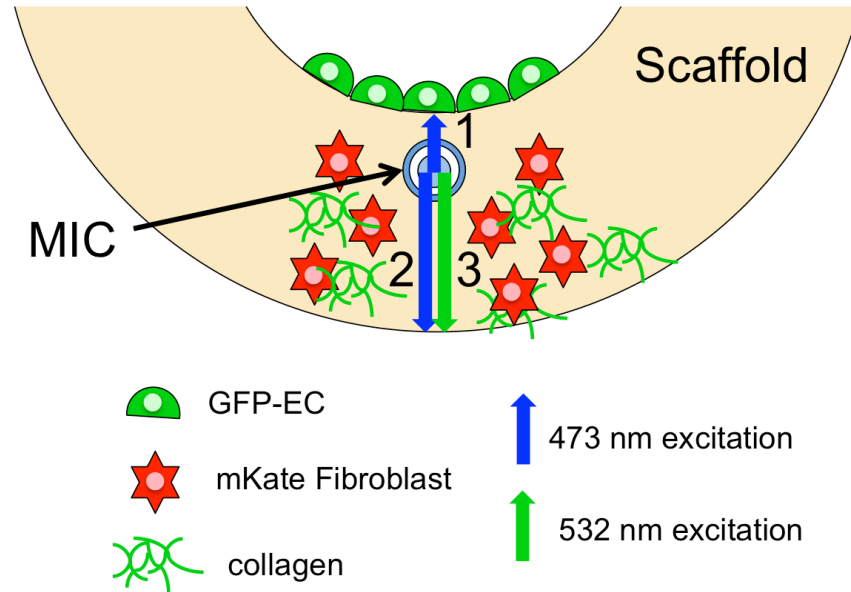


**Figure 5.3** Schematic representation of imaging both the endothelium and maturation of the vessel wall using the FOB imaging system.

A schematic representation of the proposed experimental setup for the study is shown in Figure 5.4. Scaffolds comprised of PDLGA or PCL would be fabricated with MIC embedded according to the method established in Chapter 3. ECs constitutively expressing GFP are seeded on the graft lumen and imaged using the FOB method, as previously demonstrated in Chapter 3. An excitation source of 473 nm can be used to excite the GFP-ECs on the lumen surface and a 525/45 bandpass filter would be used to allow green fluorescence to pass through to the EMCCD. SMCs or fibroblasts expressing a red fluorescent protein, such as mKate, can be seeded on the exterior of the scaffold wall. Cells expressing mKate fluorescent protein are shown in Figure 5.4. The fiber optic micro-mirror would then be rotated 180° relative to the lumen surface to excite mKate cells using 532 nm excitation and a 600 nm longpass emission collection filter according to excitation/emission characteristics of mKate (excitation/emission max 585/635 nm [136]). The fiber can then be translated along the vessel length to measure the total fluorescence emission from the mKate cells over time. It is expected that as cells proliferate and colonize the scaffold, the fluorescence emission would likewise increase as a result. Cells would be seeded, and the FOB imaging system would be used to capture total fluorescence at days 1, 3, 7, 14 and 21. The FOB imaging results would then be compared to histological sectioning and dapi stained sections. While this will not provide a measure of penetration depth of cells into the vessel wall, it can provide a relative measure of cell number. Additionally, deposition of cell-mediated ECM

production in the vessel wall can be measured in a similar manner. One of the main ECM components that SMCs and fibroblasts produce is collagen type I [137, 138]. Collagen type I possesses a high autofluorescence when excited at the UV or blue wavelengths [139]. A fluorescence image of collagen type I derived from calf skin as obtained by fluorescence microscopy can be seen in Figure 5.4 (excitation:  $488 \pm 20$  nm Emission:  $510 \pm 20$  nm). To measure cell-mediated collagen deposition in the vessel wall, 473 nm fiber optic excitation can be translated through the vessel wall and total fluorescence emission can be measured over time using the same filters for GFP.

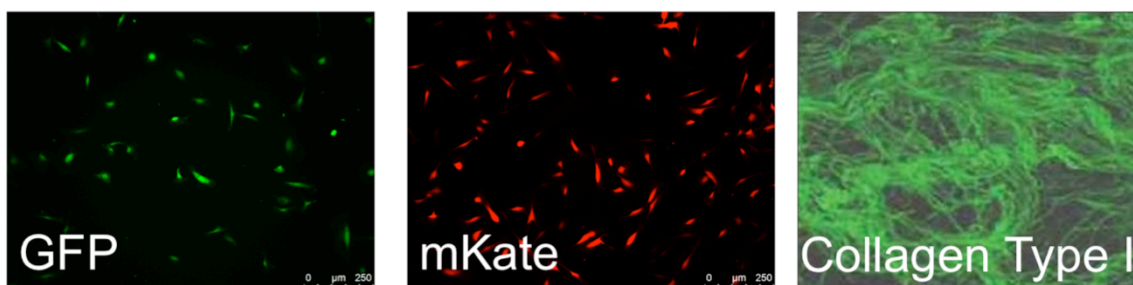


**Figure 5.4** Fluorescence images of GFP-ECs, mKate-ECs and Collagen Type 1.

To demonstrate the feasibility of using the FOB imaging method to measure collagen content in the vessel wall, a preliminary experiment was conducted with electrospun PCL vessels containing varying concentrations of type I collagen. PCL/collagen scaffolds ranging from 0.7 – 50 % w/w type I collagen were electrospun from 15% w/v PCL/collagen mixtures in HFIP. To fabricate scaffolds, polymer solutions were delivered at 5 ml/hr with a 18 g stainless steel needle with 10 cm throw distance onto a 5 mm aluminum mandrel. First, 100  $\mu$ l solution was electrospun to establish the lumen, the MIC was placed on top, then an additional 900  $\mu$ l solution was electrospun to form the vessel wall. The thickness of each vessel was measured with a micrometer and the average thickness was  $432 \pm 42$   $\mu$ m. The vessels were then mounted in a parallel plate chamber, filled with EBM-2 cell culture media, and the vessel wall was imaged. The fiber optic micro mirror with 473 nm excitation light was translated for a 1 cm length on all vessels and the resulting fluorescence emission was summed. The results, shown in Figure 5.5, demonstrate that the fluorescence response from the collagen type I in the vessels was measurable and the fluorescence response due to collagen concentration was nearly linear.

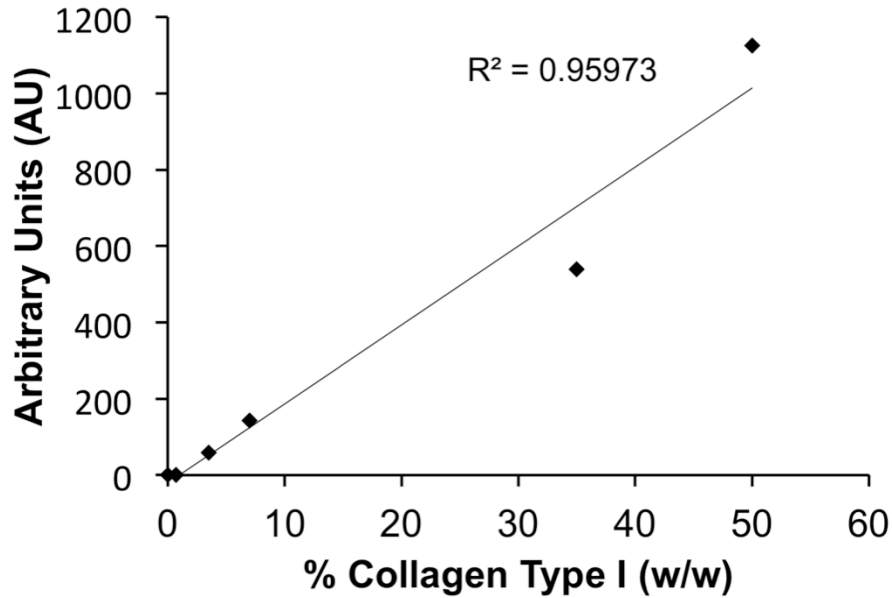


**Figure 5.5** Total fluorescence measured by the FOB imaging system as a result of varied concentration of collagen type I in PCL vessels

The results obtained from utilizing the FOB imaging method to measure cell number and collagen deposition in the vessel wall can be validated with histological section and staining at certain time points. To demonstrate, a PCL vessel was fabricated and the exterior vessel wall was seeded with CH310T1/2 mouse fibroblasts to show proliferation and cell-mediated ECM collagen production in the electrospun scaffolds. Cells were seeded onto the electrospun PCL vessel wall at day 0 and a section was taken from the cultured vessel at days 1, 14 and 28 to perform histology and staining for cell nuclei and collagen production. Scaffold biopsies were cryosectioned to 12  $\mu\text{m}$  and stained using aniline blue to detect collagen and dapi to detect cell nuclei. The results in Figure 5.6 demonstrate that fibroblasts proliferate and migrate through the scaffold wall, towards the lumen (left side of images), over time and produce a collagen matrix. The preliminary results above demonstrate that the FOB imaging system could potentially be used to measure cell proliferation and collagen type I deposition in the scaffold wall.

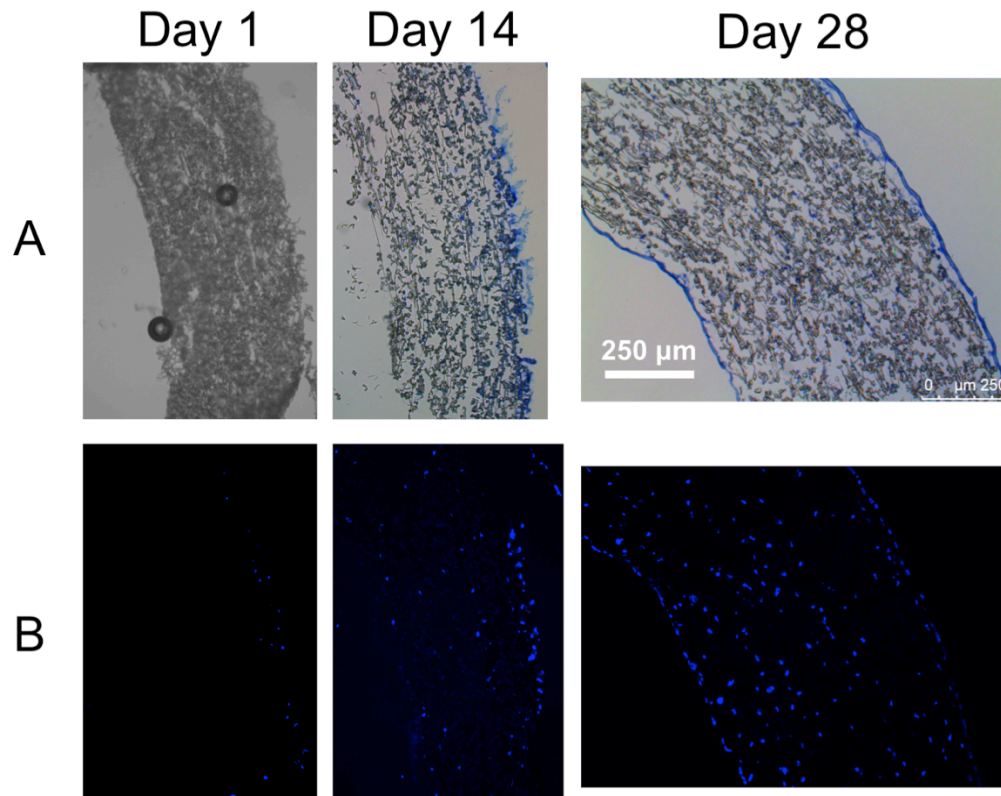


**Figure 5.6** Histological sections of PCL vessels seeded with CH310T1/2 cells over time reveal that A) cell-mediated collagen deposition (blue) increases over time in conjunction with B) cell colonization of the vessel wall towards the lumen of the vessel.

#### 5.2.4 Conclusions

The goal of this dissertation research was to advance the field of vascular tissue engineering by 1) creating methodologies to enhance EC adherence to a vascular graft and 2) development of a noninvasive and real-time imaging system capable of assessing the graft endothelium. To achieve these objectives, scaffold topographies were varied to enhance EC adhesion to the scaffold under fluid flow, and a FOB imaging system was developed to image endothelialization of a vascular graft in a noninvasive and real-time manner. Important areas of future research include incorporation of aligned nanofiber topographies in vascular grafts to enhance EC retention and patency *in vivo*, developing a fluid flow bioreactor with optics integrated to measure the effects of flow preconditioning in real-time, and use of the FOB imaging system to noninvasively measure cell proliferation and ECM deposition in the vessel wall. Completion of the proposed future work is envisioned to result in enhanced modalities to

assess maturation of bioengineered vascular grafts *in vitro* and creation of suitable grafts for *in vivo* implantation and testing.

**Appendix A: Pre-osteoblast infiltration and differentiation in highly porous apatite-coated PLLA electrospun scaffolds**

Bryce M. Whited <sup>a</sup>, Jon R. Whitney <sup>b</sup>, Matthias C. Hofmann <sup>c</sup>, Yong Xu <sup>c</sup>, Marissa Nichole Rylander <sup>a,b</sup>

<sup>a</sup> School of Biomedical Engineering and Sciences, Virginia Tech – Wake Forest University, Blacksburg, VA 24061, USA

<sup>b</sup> Department of Mechanical Engineering, Virginia Polytechnic Institute and State University, Blacksburg, VA 24061, USA

<sup>c</sup> Department of Electrical and Computer Engineering, Virginia Polytechnic Institute and State University, Blacksburg, VA 24061, USA



## Pre-osteoblast infiltration and differentiation in highly porous apatite-coated PLLA electrospun scaffolds

Bryce M. Whited<sup>a,\*</sup>, Jon R. Whitney<sup>b</sup>, Matthias C. Hofmann<sup>c</sup>, Yong Xu<sup>c</sup>, Marissa N. Rylander<sup>a,b</sup>

<sup>a</sup> School of Biomedical Engineering and Sciences, Virginia Tech – Wake Forest University, Blacksburg, VA 24061, USA

<sup>b</sup> Department of Mechanical Engineering, Virginia Polytechnic Institute and State University, Blacksburg, VA 24061, USA

<sup>c</sup> Department of Electrical and Computer Engineering, Virginia Polytechnic Institute and State University, Blacksburg, VA 24061, USA

### ARTICLE INFO

#### Article history:

Received 28 September 2010

Accepted 1 December 2010

Available online 30 December 2010

#### Keywords:

Electrospinning

Scaffold

Tissue engineering

Osteoblast

Bone

### ABSTRACT

Electrospun polymer/apatite composite scaffolds are promising candidates as functional bone substitutes because of their ability to allow pre-osteoblast attachment, proliferation, and differentiation. However these structures usually lack an adequate pore size to permit sufficient cell migration and colonization of the scaffold. To overcome this limitation, we developed an apatite-coated electrospun PLLA scaffold with varying pore size and porosity by utilizing a three-step water-soluble PEO fiber inclusion, dissolution, and mineralization process. The temporal and spatial dynamics of cell migration into the scaffolds were quantified to determine the effects of enhanced pore size and porosity on cell infiltration. MC3T3-E1 pre-osteoblast migration into the scaffolds was found to be a function of both initial PEO content and time. Scaffolds with greater initial PEO content (50% and 75% PEO) had drastically accelerated cell infiltration in addition to enhanced cell distribution throughout the scaffold when compared to scaffolds with lower PEO content (0% and 25% PEO). Furthermore, scaffolds with an apatite substrate significantly upregulated MC3T3-E1 alkaline phosphatase activity, osteocalcin content, and cell-mediated mineralization as compared to PLLA alone. These findings suggest that such a scaffold enhances pre-osteoblast infiltration, colonization, and maturation *in vitro* and may lead to overall improved bone formation when implanted *in vivo*.

© 2010 Elsevier Ltd. All rights reserved.

### 1. Introduction

The clinical need for viable bone substitutes to heal skeletal defects has been steadily increasing, while key obstacles associated with successful bone grafting remain unsolved [1]. Current methods for bone replacement include the use of both autologous and allogenic grafts, however these options possess significant drawbacks including donor site morbidity, insufficient supply, and disease transmission, which limit their clinical utility. Tissue engineering of bone grafts, on the other hand, offers a new paradigm for treatment of skeletal defects and therefore has the potential to alleviate the demand arising from the shortage of adequate autografts and allografts. The combinatorial use of bone scaffolds and progenitor cells from multiple sources has permitted engineering of viable bone substitutes [1–5]. Bone scaffolds have played a central role in providing the framework for development of tissue engineered constructs. Ideally, a bone scaffold should be

biocompatible, osteoconductive, and resorb over time as tissue remodeling progresses [6,7]. Bone scaffolds also require an interconnecting microarchitecture exhibiting sufficient pore sizes to promote osteoprogenitor and endothelial cell infiltration, colonization, and development of bone extracellular matrix (ECM) and vascular beds [8,9]. It has been shown that optimal pore sizes for bone tissue engineered scaffolds range between 100 and 300  $\mu\text{m}$  to allow sufficient cell infiltration and tissue ingrowth [9]. Therefore, cell migration into the bone scaffold is a key component for survival of the implanted bone construct and healing of the bone defect.

Significant advancements have transpired in engineering three-dimensional bone tissue scaffolds composed of both synthetic and natural polymers via a wide array of fabrication techniques such as solvent casting, phase inversion and rapid prototyping to name a few [10]. Electrospun polymers and polymer composites, in particular, have been extensively investigated for use as bone tissue scaffolds because of their similarity to the extracellular matrix (ECM), large surface area to volume ratio, and their ability to guide cells to attach and proliferate over the surface of the scaffold [11]. It has also been shown that nano-fiber scaffolds can direct osteoblastic differentiation and mineralization of osteoprogenitor cells more effectively

\* Corresponding author. Tel.: +1 540 230 5981; fax: +1 540 231 9738.  
E-mail address: [bwhited@vt.edu](mailto:bwhited@vt.edu) (B.M. Whited).

than a solid wall scaffold [12]. Recently, there has been much interest in tailoring electrospun scaffold architecture, functionalizing the scaffold surface, and encapsulating bioactive agents in the fibers in an effort to further enhance the osteoconductivity and osteoinductivity of the scaffold [13]. One such approach involves incorporating calcium phosphate (CaP) bioceramics (i.e. hydroxyapatite and  $\beta$ -tricalcium phosphate) within synthetic polymeric electrospun matrices by mineralization of these components on the surface to create composite scaffolds [14–17]. Several *in vitro* studies have shown that CaP minerals, when incorporated with electrospun scaffolds, dramatically improve cell attachment, allow osteoblastic differentiation, and bone ECM synthesis [16–21]. Thus, electrospun polymeric/CaP composites are promising candidates for use as bone tissue scaffolds.

While these scaffolds show promise for use as bone tissue engineered constructs, several limitations remain – such as poor cell infiltration and tissue ingrowth. Although electrospun scaffolds exhibit an architecture with a very high percentage porosity, their pore sizes are usually only a few times larger than the fiber diameter [22] – typically ranging from nanometers to tens of microns. Sufficient cell infiltration into electrospun scaffolds is therefore limited as the pores sizes are well below the target range of 100–300  $\mu\text{m}$ . Therefore small pore sizes and dense fiber packing have been identified as factors that limit cell migration and colonization of electrospun scaffolds thereby limiting their potential for three-dimensional applications [23,24]. Furthermore, it has also been shown that small pore sizes inhibit vascular ingrowth when implanted *in vivo*, thus creating hypoxic regions and limiting nutrient and waste transfer [9,25]. Thus, the dense meshwork of micro and nano-fibrous features that make electrospun scaffolds attractive for cell attachment and ECM formation can severely limit cell infiltration and tissue ingrowth.

To overcome the limitation of poor cell infiltration in electrospun scaffolds, many methods have been proposed and employed with varying results. In a study by Stankus et al., cells were uniformly dispersed throughout an electrospun scaffold by simultaneously electrospinning cells onto the scaffold as it was being formed, however sterility and cell survival were concerns [26,27]. In a study by Pham et al., fiber diameter was increased to enlarge pore size while flow perfusion was used to further enhance cell infiltration [28]. It was observed that increasing fiber diameter only had a modest effect on cell infiltration – leading to maximum cell infiltration of 200  $\mu\text{m}$  in the approximately 1 mm thick scaffolds under static culture conditions as compared to complete infiltration under flow perfusion. Methods such as cryogenic electrospinning and salt leaching have also been used to successfully improve cell infiltration, but at the expense of macroscopic delamination and compromised structural integrity [29,30]. Alternatively, fast-dissolving fiber fractions have been co-electrospun with slow-degrading structural polymers to create micropores after aqueous submersion [31–33].

Our goal in the present study was to engineer an electrospun Poly(L-Lactic Acid) (PLLA) scaffold with enhanced pre-osteoblast infiltration and differentiation for bone tissue engineering applications. We employed a three-step water-soluble Poly(ethylene oxide) (PEO) fiber inclusion, dissolution, and mineralization process to effectively increase scaffold pore size and porosity while coating the surface with a biomimetic apatite substrate. We hypothesized that cell migration into the scaffold would be enhanced due to increased pore size and porosity of the scaffold. We also hypothesized that inclusion of the biomimetic apatite substrate would increase pre-osteoblast differentiation as compared to PLLA alone. The temporal and spatial dynamics of cell migration into the scaffolds were quantified in addition to investigating pre-osteoblast proliferation, differentiation, and maturation in the bone scaffolds.

## 2. Materials and methods

### 2.1. Materials

Poly(L-lactide) ( $M_w \sim 152,000$ ) and Poly(ethylene oxide) ( $M_w \sim 200,000$ ) were both purchased from Sigma Aldrich, St. Louis, MO. Dichloromethane, N,N-dimethylformamide, Absolute Ethanol, Paraformaldehyde, Sodium Chloride, Potassium Chloride, Calcium Chloride Dihydrate, Magnesium Chloride Heptahydrate, Sodium Phosphate Monobasic Monohydrate, and Sodium Bicarbonate – all reagent grade – were purchased from Fisher Scientific, Fair Lawn, NJ.

### 2.2. Composite scaffold fabrication

Dual polymer composite scaffolds were fabricated by co-electrospinning PLLA and PEO from opposite sides of a rotating grounded aluminum mandrel, similar to the method previously reported by Baker et al. [8]. A 12% w/v solution of PLLA ( $M_w \sim 80,000$ ) was prepared in a 3:1 mixture of dichloromethane and N,N-dimethylformamide by gentle rocking at room temperature for 16 h. PEO was solubilized in ethanol and deionized (DI) water at a ratio of 9:1 by gentle rocking for 16 h at room temperature to form a 10% w/v solution. The two polymers were electrospun simultaneously using a custom dual-electrospinning setup. To fabricate composite scaffolds, 5 ml of each solution was placed in 5 ml syringes with 18G blunt-tip needles attached. Similarly, pure PLLA scaffolds were electrospun by using the single PLLA solution at one end of the apparatus. A high voltage power supply (Gamma High Voltage Research, Ormond Beach, FL) was used to apply a +16 kV potential difference between the charged needle tips and the 2" diameter grounded aluminum mandrel, which was rotated by an attached AC motor (Dayton Electric, Niles, IL) to achieve an approximate linear velocity of 5 m/s. The flow rate of each solution was held constant at 5 ml/h via 2 syringe pumps (New Era Pump Systems, Inc., Farmingdale, NY). The PLLA and PEO fibers were collected on the grounded mandrel at a needle-mandrel distance of 20 and 17 cm, respectively. Ten milliliters of each solution was electrospun to achieve the composite electrospun mat. The electrospun mats were then placed in a vacuum desiccator overnight to remove residual solvent.

Two different types of scaffolds were fabricated using this electrospinning technique: pure PLLA scaffolds and PLLA/PEO composite scaffolds. The PLLA/PEO composite scaffolds were formed by electrospinning both solutions with needles offset at a distance of 8 cm along the mandrel length. This electrospinning setup produced a PLLA scaffold with a PEO component gradient along the mandrel length, which ranged from pure PLLA at one end to pure PEO at the opposite end.

### 2.3. PEO fiber removal

The electrospun mats were then sectioned into 30 mm  $\times$  10 mm strips along the mandrel rotation direction, weighed, and submerged in 70% ethanol for 3 h and in DI water for 1 h to remove the soluble PEO fibers. PLLA scaffolds were then dried in a vacuum desiccator overnight to remove residual water and re-weighed to determine mass loss. Since the mass of the pure PLLA scaffolds did not change after submersion, percent mass loss was taken as an indicator of PEO content in the composite scaffolds. Scaffold samples for scanning electron microscopy (SEM), mechanical testing, and cell studies were indexed to mandrel position and excised from the same electrospun mats. Samples for mechanical testing (30 mm  $\times$  10 mm) were excised in the mandrel rotation direction and samples for SEM and cell studies were punched out with a 12 mm diameter circular die. For this study, scaffolds with 0%, 25%, 50%, and 75% PEO content were chosen for mechanical testing and cell infiltration. Scaffolds with 50% PEO content were used for cell proliferation and differentiation studies.

### 2.4. Scaffold surface mineralization

Scaffolds to be mineralized for later testing were not dried in the vacuum desiccator, but were immediately surface mineralized after PEO removal by submersion in 10 $\times$  simulated body fluid (SBF) as previously reported by Mavis et al. [8]. The 10 $\times$  SBF, which has ion concentrations that are ten times higher than those in human plasma, was prepared by sequentially dissolving the following ingredients in 900 ml ultrapure DI water that was being stirred at room temperature: NaCl (1000 mM), KCl (5 mM), CaCl $_2$ ·2H $_2$ O (25 mM), MgCl $_2$ ·6H $_2$ O (5 mM) and NaH $_2$ PO $_4$ ·H $_2$ O (3.62 mM). Care was taken to ensure that each ingredient was fully dissolved before the next was added. Upon dissolution of the fifth reagent, DI water was added to bring the final solution volume up to 1000 ml. Before coating the scaffolds, 0.084 g of NaHCO $_3$  (10 mM equivalent) was added during stirring. After complete dissolution, the electrospun scaffolds were submerged in the 10 $\times$  SBF solution for 6 h and then rinsed with copious amounts of DI water to remove the salt residues.

### 2.5. Scaffold characterization

Scaffold morphology before and after PEO removal and surface mineralization was investigated by field emission SEM (Leo Zeiss 1550, Carl Zeiss, Thornwood, NY). To aid in surface conductivity, the scaffolds were sputter coated with Gold–Palladium

to a thickness of 12 nm. The calcium to phosphate ratio of the mineralized surface was evaluated with an energy-dispersive X-ray spectroscopy (EDXS) system attached to the SEM. The SEM images at 2000 $\times$  were analyzed with Image J (U.S. National Institutes of Health, Bethesda, MD) to determine the fiber and pore diameter of the mineralized PLLA scaffolds. Briefly, a total of 20 fibers were randomly selected from each SEM image and measured to calculate the average and standard deviation of fiber diameters ( $n = 5$  images/scaffold;  $n = 3$  scaffolds/condition). To determine scaffold pore diameter, the contrast and brightness of each SEM image was adjusted to the same level and thresholding was performed at a set value. The thresholded image was then qualitatively compared to the original image to validate that thresholding yielded similar contrast. If the thresholded image did not match the original image, thresholding was repeated until a better match between the original and thresholded image was obtained. Each pore was labeled and measured after calibrating with a known scale. Pore diameter was determined by taking the average of the major and minor axes as output by the program ( $n = 5$  images/scaffold;  $n = 3$  scaffolds/condition). The porosity of the scaffolds after PEO fiber removal and surface mineralization were evaluated as previously reported by Chong et al. [8]. The dimensions of the electrospun scaffolds ( $n = 5$  scaffolds/condition) were carefully measured with a digital micrometer (Mitutoyo, Japan) and their apparent densities and porosities were determined using the following equations:

$$\text{Scaffold apparent density (g/cm}^3\text{)} = \text{Mass of scaffold (g) / Scaffold volume (cm}^3\text{)}$$

$$\text{Scaffold porosity (\%)} = \left( 1 - \left[ \frac{\text{Scaffold apparent density (g/cm}^3\text{)}}{\text{Bulk density of PLLA (g/cm}^3\text{)}} \right] \right) \times 100\%$$

## 2.6. Mechanical testing of scaffolds

Tensile properties of the PLLA and surface mineralized PLLA scaffolds were determined using an Instron 5869 (Instron, Norwood, MA) with a 10 N load cell. Prior to testing, the thickness and width of the samples were carefully measured in three locations along the sample length using a digital micrometer (Mitutoyo, Japan). Samples were tested under uniaxial tension until failure at a crosshead speed of 1 mm min<sup>-1</sup>. Tensile modulus was calculated over a 4% strain range from the linear portion of the stress-strain curve and maximum tensile strength was determined from the maximum load achieved by the sample normalized to its original cross-sectional area. Five samples per group were tested.

## 2.7. MC3T3-E1 cell culture and cell seeding

MC3T3-E1 subclone 4 pre-osteoblasts were purchased from American Type Culture Collection (Manassas, VA) and were used to perform the cell proliferation, differentiation, and infiltration studies. All cells used were within passage 21 and were cultured in  $\alpha$ -MEM supplemented with 10% FBS and 1% antibiotic/antimycotic (Cellgro, Herndon, VA). Cells were grown in a 95% relative humidity atmosphere of 5% CO<sub>2</sub> at 37 °C and culture media was changed every 3 days. Osteogenic media consisted of  $\alpha$ -MEM with 10 mM  $\beta$ -glycerol phosphate and 50  $\mu$ g/ml L-ascorbic acid (Sigma, St. Louis, MO).

Before cells were seeded onto the scaffolds, the scaffolds (approximately 12 mm diameter) were placed in 48-well plates and sterilized with 700  $\mu$ l of 70% ethanol for 1 h. The scaffolds were then washed three times for 5 min each with sterile PBS to remove the residual ethanol. Cells were trypsinized upon subconfluence and viable cells were determined using trypan blue stain (Vi-cell, Beckman Coulter, Brea, CA). Cells were then re-suspended in 250  $\mu$ l osteogenic media and seeded onto the scaffolds or in a 48-well plate (TCPS control).  $2 \times 10^5$  and  $3 \times 10^4$  cells were seeded onto the scaffolds for the cell infiltration and proliferation/differentiation studies, respectively. Media was changed every 3 days and samples were removed after 3, 7, 14, and 21 days, rinsed with sterile PBS, and stored in 1.5 mL of sterile filtered Millipore water at -20 °C to evaluate cell proliferation/differentiation. For the cell infiltration study, scaffolds were removed at days 1, 10, and 21, rinsed with sterile PBS, fixed in 4% phosphate-buffered paraformaldehyde, and embedded in optimal cutting temperature compound (Tissue Tek, Sakura Finetek USA, Inc., Torrance, CA). For the cell proliferation/differentiation studies, four scaffolds or control samples with cells were cultured for each condition (PLLA, mineralized PLLA, and TCPS control) and three were cultured for the infiltration studies (mineralized PLLA only).

## 2.8. Assessment of cell infiltration

After fixing the mineralized scaffolds in paraformaldehyde and embedding in OCT, 8  $\mu$ m thick histological cross-sections were cut with a Microm HM 550 (Microm, Waldorf, Germany) and stained with DAPI (Vector Laboratories, Burlingame, CA) to visualize cell nuclei. A Leica MI6000-B microscope (Leica, Wetzlar, Germany) with 10 $\times$  objective was used to obtain both polarized bright field and

fluorescent images of the scaffolds. The brightness, gain, and exposure were held constant for all images. The polarized bright field images were used to demarcate the edges of the electrospun scaffold and to determine the thickness of the scaffolds. For each image, three measurements of scaffold thickness were obtained across the cross-section to determine scaffold thickness. The scaffold edge as found by the polarized bright field image was then applied to the fluorescent image to define the boundaries of the scaffold edges. A custom LabView program (LabView 8.6, National Instruments, Austin, TX) developed by our group was then used to quantify cells in each fluorescent image and linear distance from the edge of the scaffold on which the cells were seeded. Briefly, the program located the user-defined edges of the scaffold and rotated the image so that the image was vertically aligned. Next, two thresholds were applied to the fluorescence image. The first was a pixel threshold range, such that pixels having the correct color value (blue pixel values between 90 and 255 and a pixel value of zero for each of the other colors) were set to one, and pixels residing outside the range were set to zero, creating a binary image. These clusters of pixels set to one were measured by area. Groups of pixels less than 50 pixels in area were set to zero, eliminating small pixels which were likely to be the result of noise present in the imaging. The result of these techniques was a binary image, such that only groups of pixels that meet the color and size requirements are output as cells. Then, the program determined the distance between the two edges of the scaffold and exported the location of the cell relative to the two edges. These distances, originally in pixels, were linearly scaled to microns. Three scaffolds for each mineralized PLLA/PEO condition at each time point were sectioned, imaged, and processed. At least 3 images were obtained from each cross-section and 2 cross-sections from each scaffold – yielding approximately 18 images analyzed for each PLLA/PEO condition at each time point.

## 2.9. Cell number

The PicoGreen assay kit (Molecular Probes Inc., Eugene, OR) was used to measure the double stranded DNA (dsDNA) content in each scaffold or control sample. Briefly, each sample underwent 3 freeze-thaw cycles, sonication for 20 min, and vortexing for 15 s as previously described [34]. Samples were diluted 10 $\times$  with sterile, distilled DNase-free water to obtain sample concentrations within the detection range of the assay. Bacteriophage lambda dsDNA standards were diluted to concentrations of 0–1000 ng/ml in sterile, distilled DNase-free water and 100  $\mu$ l of standard or sample were added to individual wells of a 96-well plate. The PicoGreen reagent and Trisethylenediaminetetraacetic acid buffer were prepared per the manufacturers instructions and 100  $\mu$ l was added to each well. The 96-well plate was then incubated in the dark at room temperature for 10 min, whereafter the fluorescence was measured on a SpectraMax M2 plate reader (Molecular Devices, Sunnyvale, CA) using an excitation wavelength of 480 nm and an emission wavelength of 520 nm. The number of cells in each scaffold was determined by correlating the amount of DNA with a known amount of MC3T3-E1 cells (8.95 pg DNA/cell – data not shown). Analysis of each sample was performed in triplicate.

## 2.10. Alkaline phosphatase activity

Alkaline Phosphatase (ALP) Activity – an early indicator of osteoblastic differentiation – was determined by using the ALP substrate kit by Bio-Rad (Bio-Rad Laboratories, Hercules, CA). Samples used to determine ALP activity were obtained from the same cell lysate solution used for DNA quantification. Samples were diluted 20 $\times$  with sterile filtered Millipore water to achieve concentrations within the detection range of the assay. Standards were prepared by diluting 10 mM p-nitrophenol (Sigma) stock solution in DI water to final concentrations of 0–250  $\mu$ M and 100  $\mu$ l of standard or sample was added to individual wells in a 96-well plate. Finally, 20 mg p-nitrophenylphosphate (Sigma Aldrich, St. Louis, MO) was completely dissolved in 20 ml diethanolamine buffer and 100  $\mu$ l of the resulting solution was added to each well. The 96-well plate was then incubated at 37 °C for 30 min, whereafter the reaction was halted by adding 100  $\mu$ l of 0.4 M NaOH. The absorbance was then measured at 405 nm on the plate reader. Analysis of each sample was performed in triplicate and activity is expressed per cell as determined by the DNA assay.

## 2.11. Osteocalcin content

Osteocalcin (OCN), a non-collagenous protein produced by mature osteoblasts during late stage osteodifferentiation, was measured in the media using an ELISA kit from Biomedical Technologies, Inc. (Stoughton, MA). Media samples were taken over the culture period and stored at -20 °C until analysis could be performed. Samples were diluted 100 $\times$  with sterile filtered Millipore water to reside within the detection range of the assay. Mouse OCN standards were diluted in sterile filtered Millipore water to final concentrations of 0–50 ng/ml and 25  $\mu$ l of standard or sample was added to the 96-well plate. The assay was performed per the manufacturer's instructions and the absorbance at 450 nm was measured on the plate reader. Osteocalcin content is expressed as a ratio of OCN/cell (ng/cell). Analysis of each sample was performed in triplicate.

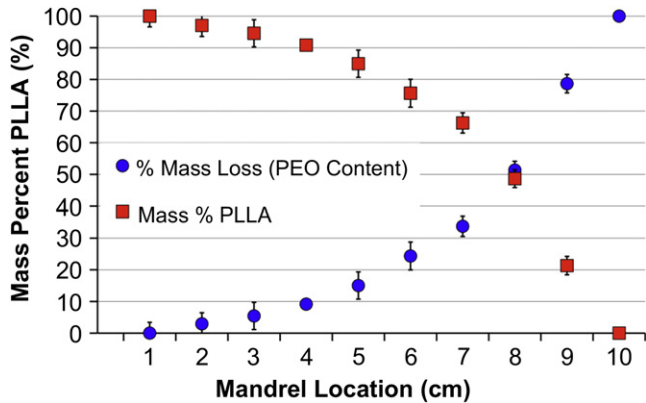


**Fig. 1.** Offsetting syringes resulted in a graded fiber sheet ranging from 0 to 100 mass % PLLA along the mandrel length as determined by PEO mass loss ( $n = 3$  scaffolds per mandrel location).

### 2.12. Calcium content

In the late stages of osteoblastic differentiation, osteoblasts produce a mineralized matrix which consists of extracellular proteins and CaP minerals [8]. To determine the amount of mineralized matrix produced by the cells in this study, a colorimetric endpoint assay from Genzyme Diagnostics (Genzyme Diagnostics P.E.I. Inc., PE Canada) was used to quantify the calcium content in each scaffold or control sample. To account for additional calcium on the mineralized PLLA scaffolds, calcium levels of mineralized scaffolds without cells (control scaffolds) were assayed at each time point and subtracted from the background on PLLA mineralized scaffolds with cells. To dissolve the calcium into solution, a volume of 1 N acetic acid equal to the volume remaining in each sample tube was added and the samples were placed on a shaker table at 80 rpm for 48 h. Standards of calcium were prepared from a 250 mM calcium stock solution in concentrations ranging from 0 to 250 mM and 20  $\mu$ L of standard or sample was added to individual wells of a 96-well plate. The Arsenazo III calcium assay reagent was then added to each well at a volume of 300  $\mu$ L, incubated at room temperature for 10 min, and absorbance at 650 nm was measured on the plate reader. Analysis of each sample was performed in triplicate and calcium content is expressed as a ratio of calcium/cell.

### 2.13. Statistical analysis

All values are expressed as mean  $\pm$  standard deviation. Statistical analysis was performed using one-way analysis of variance (ANOVA) and significance was considered at  $p \leq 0.05$ . For assessment of tensile properties, five samples per group were analyzed. Four samples per group were evaluated in the cell proliferation/differentiation studies and three samples per group for the cell infiltration studies.

## 3. Results

### 3.1. Scaffold fabrication and characterization

Both composite PLLA/PEO scaffolds and pure PLLA scaffolds were fabricated using the dual-electrospinning setup. Electrospinning only PLLA produced pure PLLA scaffolds and co-electrospinning PLLA with PEO produced composite scaffolds with 0–100% PEO fiber content along the mandrel length. The fraction of PEO in the composite scaffold was determined by mass loss after dissolving the PEO fibers in an aqueous environment (Fig. 1) ( $n = 3$  samples per mandrel location). Representative SEM images of pure PLLA scaffolds (Fig. 2A) and scaffolds containing a 3:1 ratio of PEO:PLLA (Fig. 2C) show the randomly oriented fibrous morphology before submersion and mineralization. Fig. 2B, D, and E show the apatite coating on the fiber surface after the PEO fibers were removed and mineralized. It is apparent that the scaffold containing 75% PEO has increased pore size and appears less dense after removal of the PEO fiber content (Fig. 2D vs. C). The semi-quantitative EDXS analysis showed that the biological apatite deposited on the scaffolds consisted of a Ca/P ratio of about 1.4 – indicating an amorphous calcium phosphate [17].

The SEM images were analyzed to determine average fiber and pore diameter. Because porosity and pore size are important features of a scaffold that influence the behavior of seeded cells, the scaffolds were characterized with respect to these properties. We selected four different scaffolds with varying PEO content to use in the experiment (0%, 25%, 50%, and 75% PEO). While fiber diameter remained relatively constant for all scaffold types (Table 1), increasing the PEO content in the scaffolds significantly increased the porosity (Fig. 3A) and pore diameter of the scaffolds (Fig. 3B). Average pore diameters of 27  $\mu$ m and 89  $\mu$ m were achieved for scaffolds with 50% and 75% PEO, respectively, as compared to less than 10  $\mu$ m for scaffolds with lower PEO content (Table 1). As shown in Table 1, average scaffold thickness, as determined by analyzing histological sections, varied slightly with PEO content.

### 3.2. Mechanical testing

Uniaxial tensile testing was conducted to determine the effects of mineralization and PEO fiber removal on scaffold elastic modulus and ultimate tensile strength (UTS). The data showed that mineralization of the PLLA scaffolds resulted in a decreased elastic modulus for the 0% PEO scaffolds, while significantly increasing the modulus of the 50% PEO scaffolds ( $p < 0.05$ ) (Fig. 4). A significant increase in ultimate tensile strength was also seen for the 0% PEO mineralized PLLA scaffold as compared to PLLA alone ( $p < 0.05$ ). As expected, an increase in initial PEO content led to overall decreased mechanical properties in both the pure PLLA and mineralized PLLA scaffolds. As initial PEO content increased, the elastic modulus of the mineralized PLLA scaffolds significantly decreased for each group ( $p < 0.05$ ), whereas the ultimate tensile strength of the mineralized PLLA scaffolds was only affected at higher initial PEO contents (50% and 75%). The same trend of decreased mechanical properties with increased PEO content was observed for the pure PLLA scaffolds.

### 3.3. Cell infiltration into mineralized PLLA scaffolds

To assess MC3T3-E1 pre-osteoblast migration into the mineralized PLLA scaffolds as a function of initial PEO content, cells were seeded onto scaffolds, collected at days 1, 10, and 21, and then fixed in paraformaldehyde for later evaluation. Histological cross-sections of the scaffolds were then obtained by sectioning. The cell nuclei were stained with DAPI and the cross-sections were imaged for cell position within the scaffold. A custom LabView program then analyzed each fluorescent image for both the number and position of cells within the scaffold relative to the scaffold edge as defined by the polarized bright field image shown in Fig. 5. This method was useful in evaluating the impact of initial PEO content and the effect of increased porosity and pore size on the temporal and spatial dynamics of cell migration into the composite scaffolds.

The fluorescent images showed that cell migration into the scaffolds improved with increasing initial PEO content (Fig. 6). For example, at day 1, cells were present only at the periphery of the scaffolds with 0%, 25%, and 50% PEO, whereas scaffolds with 75% PEO exhibited cell infiltration into the centermost regions of the scaffold. Also, it is evident that cell migration increased for each scaffold group over time with cell infiltration more pronounced for scaffolds with greater porosity and pore diameters (50% and 75% PEO).

To further study the dynamics of cell migration into the scaffolds with varying initial PEO content, data obtained from the image analysis was used to quantify the cellular distribution in each scaffold (Fig. 7) and average cell infiltration depth into the scaffolds over time (Fig. 8). Cellular distribution was assessed by measuring the migration distance of each cell from the edge of the scaffold that was seeded, counting the number of cells that were within the

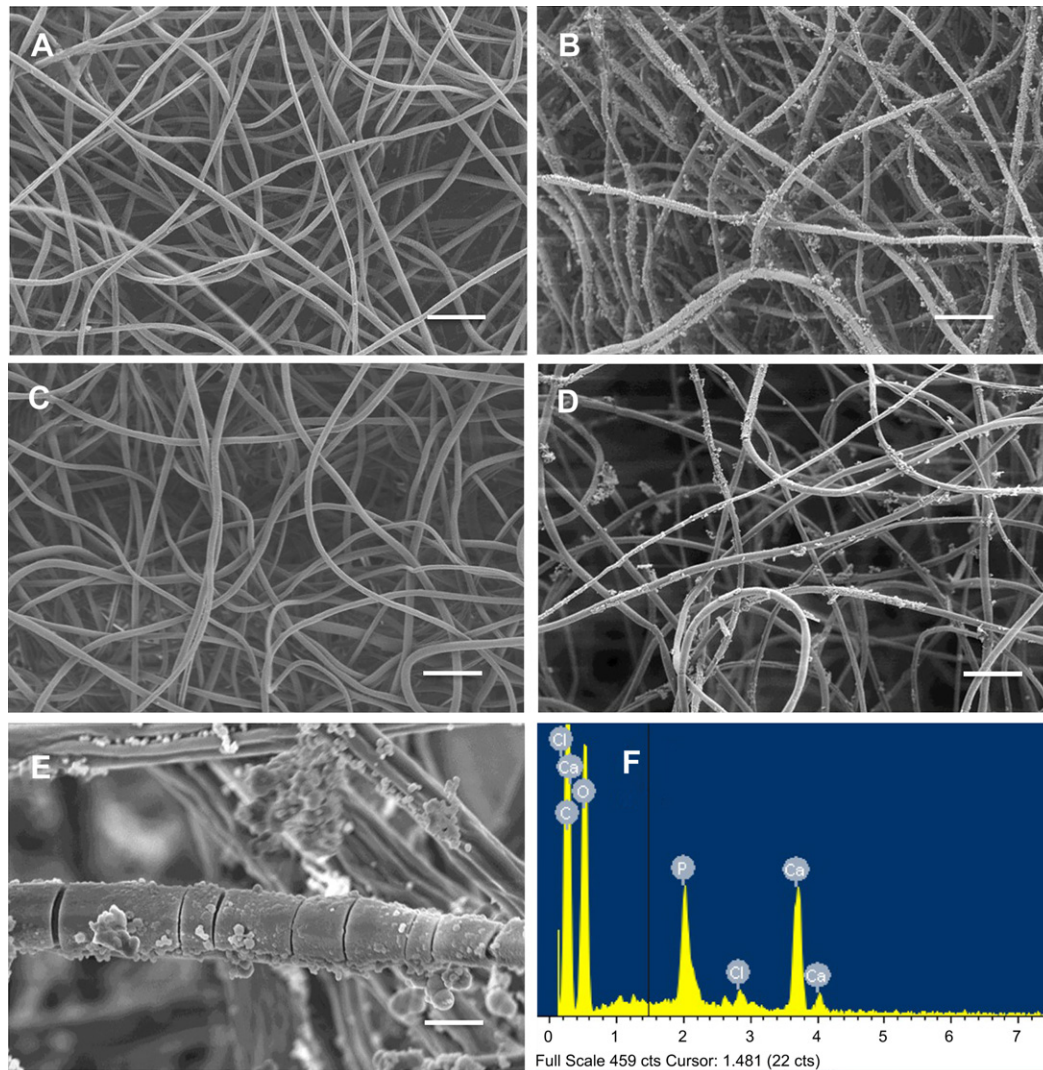


**Fig. 2.** Representative SEM images of (A) a pure PLLA scaffold (0% PEO), (B) pure mineralized PLLA scaffold (0% PEO), (C) 3:1 blend of PEO:PLLA before PEO fiber removal (75% PEO), (D) 3:1 blend of PEO:PLLA after PEO fiber removal and mineralization, (E) close-up SEM image of apatite surface on a PLLA fiber, and (F) EDXS confirms that the biomimetic apatite contains calcium and phosphorous at a Ca/P ratio of approximately 1.4. Inset bars represent 20  $\mu\text{m}$  in images A, B, C, D and 2  $\mu\text{m}$  in image E.

ranges of 0–200  $\mu\text{m}$ , 200–400  $\mu\text{m}$ , 400–600 and >600  $\mu\text{m}$ , and normalizing the number of cells in each range to the total number of cells within each scaffold to obtain a percentage of total cells in each range (Fig. 7). The results of this analysis show that cell distribution throughout the scaffolds widen as time progresses. The fraction of cells in the outermost region of the scaffolds (0–200  $\mu\text{m}$ ) was significantly lower for each group at day 21 compared to day 1 after seeding, demonstrating cell migration towards the center of the scaffolds ( $p < 0.05$ ). Likewise, the fraction of cells in the innermost regions (200–600  $\mu\text{m}$ ) of the scaffolds significantly increased as time progressed ( $p < 0.05$ ). This trend is observed for all scaffold groups with varying initial PEO contents. Similarly,

**Table 1**

Fiber diameter, pore diameter, porosity and scaffold thickness for mineralized PLLA scaffolds with varying initial PEO content.

% PEO.	Fiber diameter ( $\mu\text{m}$ )	Pore diameter ( $\mu\text{m}$ ).	Porosity (%)	Scaffold thickness ( $\mu\text{m}$ ).
0%	2.70 $\pm$ 0.55	7.87 $\pm$ 3.47	82.05 $\pm$ 0.29	822 $\pm$ 48
25%	2.71 $\pm$ 0.41	9.86 $\pm$ 5.39	85.08 $\pm$ 0.18	874 $\pm$ 73
50%	2.47 $\pm$ 0.67	27.73 $\pm$ 10.39	86.29 $\pm$ 0.35	684 $\pm$ 64
75%	2.62 $\pm$ 0.55	89.29 $\pm$ 24.32	87.50 $\pm$ 0.53	676 $\pm$ 108

increasing the initial PEO content significantly accelerated cell infiltration into the scaffolds. At day 1, nearly 99% of cells in the 0% and 25% PEO scaffolds remained in the outermost region of the scaffold (0–200  $\mu\text{m}$ ), whereas only  $\sim$ 91% and  $\sim$ 69% of cells were observed in the same region of the 50% and 75% PEO scaffolds, respectively (Fig. 7A). The remainder of the cells infiltrated to more central regions of the scaffold (200–600  $\mu\text{m}$ ). By day 21, nearly 46% of cells in the 50% and 75% PEO scaffolds had migrated further than 200  $\mu\text{m}$  into the scaffolds as compared to only  $\sim$ 21% and  $\sim$ 13% of cells in the 0% and 25% PEO scaffolds, respectively (Fig. 7C). The average cell infiltration distance into the scaffolds was also found to increase with both time and initial PEO content. Fig. 8 shows cells in the 50% and 75% PEO scaffolds possessed average infiltration depths of 240 and 320  $\mu\text{m}$ , respectively. These infiltration depths were significantly greater than those achieved in the 0% and 25% PEO scaffolds, which were 120  $\mu\text{m}$  and 140  $\mu\text{m}$ , respectively ( $p < 0.05$ ).

### 3.4. Cell number

Cell number for the scaffolds with 50% initial PEO content and TCPS control samples was quantified at days 3, 7, 14, and 21 to

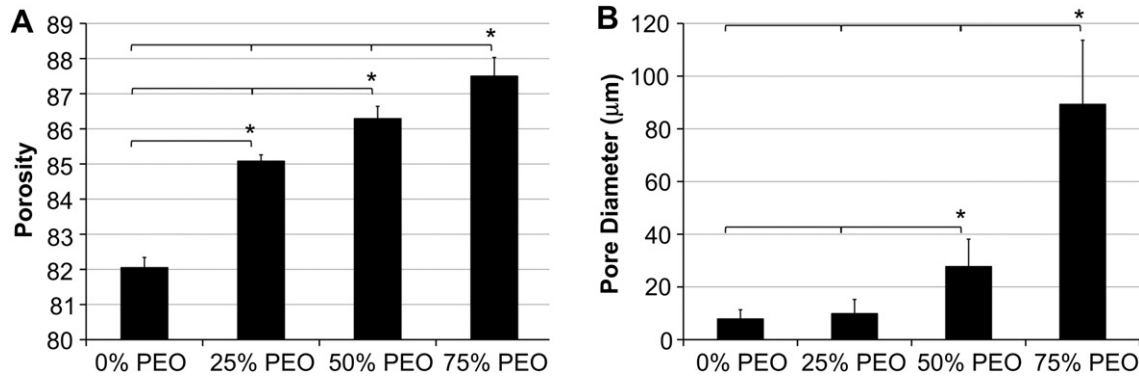


Fig. 3. (A) Porosity and (B) pore diameter of mineralized PLLA scaffolds with varying initial PEO content. An “\*\*” indicates a significant difference ( $p < 0.05$ ) between groups ( $n = 5$ ).

assess cell proliferation during the early (0–7 days), mid (7–14 days), and late (>14 days) stages of MC3T3-E1 development [35]. Fig. 9 shows the general trend for all experimental groups in which there was an increase in cell number for the duration of the experiment. The TCPS control samples exhibited a significant increase in cell number from day 0 (initial seeding density of  $3 \times 10^4$  cells/well), whereas the scaffold samples showed minimal change in proliferation ( $p < 0.05$ ). There was significantly higher cell number for the TCPS control when compared to both scaffolds at all time points except at day 21 for the PLLA scaffold ( $p < 0.05$ ). There was, however, no statistically significant difference in cell number between the pure PLLA and mineralized PLLA scaffolds at all time points ( $p < 0.05$ ).

### 3.5. ALP activity

ALP activity, an early marker of osteoblast phenotype, is upregulated at the onset of osteoblastic differentiation and subsides after differentiation progresses [35]. In this experiment, ALP activity was assayed to determine MC3T3-E1 progression towards the osteoblast phenotype for cells on scaffold constructs or TCPS controls (Fig. 10). Maximal ALP activity for scaffold constructs was expressed at day 3 with a corresponding approximate 4-fold increase compared to TCPS control levels ( $p < 0.05$ ). Maximal ALP expression for the TCPS control, however, occurred at day 7. The ALP activity for the scaffold constructs was significantly higher than the TCPS control at all time points, except for the mineralized PLLA group at day 7 ( $p < 0.05$ ).

### 3.6. Osteocalcin content

Fig. 11 shows the amount of OCN protein detected in cell culture media for each treatment group as measured by ELISA. Data is expressed as the ratio of OCN/cell (pg/cell). For this experiment, OCN secretion in cell culture media was measured between days 0–3, 3–7, 10–14, and 17–21. As seen in Fig. 11, there was a marked increase in OCN secretion from all treatment groups during days 10–14 and 17–21. Most notably the cells in the mineralized PLLA scaffolds produced more than twice as much OCN as TCPS control samples for days 10–14 and 17–21 (significant at  $p < 0.05$ ). The cells in the mineralized PLLA samples also produced roughly 1.4 times more OCN than the cells in the pure PLLA samples for these same time periods ( $p < 0.05$ ).

### 3.7. Calcium content

The calcium content in each cell/scaffold construct or TCPS control sample was measured to determine the amount of mineralization present in the extracellular matrix. This was accomplished by dissolving the calcium within the extracellular matrix in 0.5 N acetic acid and measuring the concentration of calcium ions in the resulting solution. To account for extra calcium in the mineralized PLLA samples, calcium levels of mineralized scaffolds without cells (control scaffolds) were assayed at each time point and subtracted from the background ( $n = 4$ ). Fig. 12 shows that cell-mediated mineralization increased for each treatment group with time. There was significantly more calcium on both scaffold groups than for the TCPS control at days 3 and 7 ( $p < 0.05$ ). At days 14 and 21, accreted

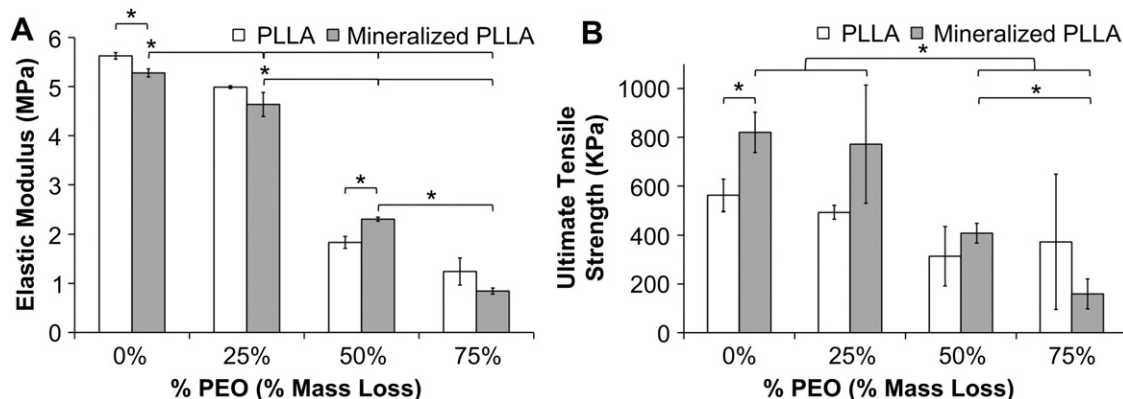
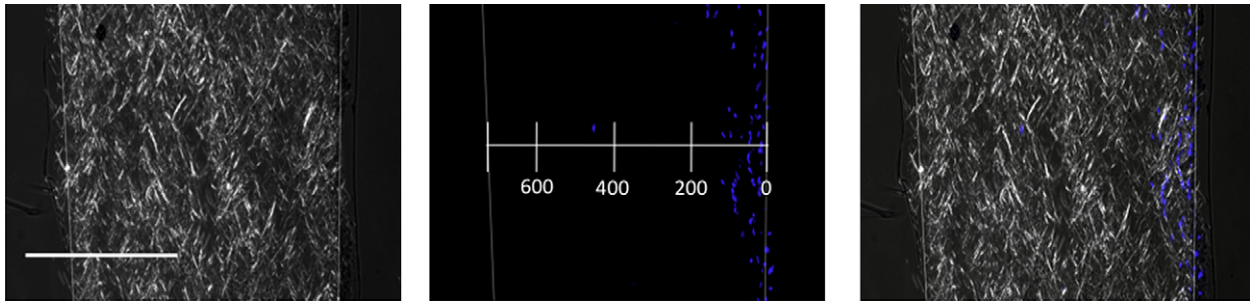


Fig. 4. (A) Elastic modulus and (B) ultimate tensile strength for pure PLLA and mineralized PLLA scaffolds with varying PEO content (% mass loss) after PEO fiber removal. A “\*\*” indicates a significant difference ( $p < 0.05$ ) between groups ( $n = 5$ ).



**Fig. 5.** Polarized bright field images of the DAPI-stained cell-seeded scaffold cross-sections (left) were used to demarcate the scaffold edges and measure scaffold thickness. The corresponding fluorescent image (center) was used to evaluate cell infiltration depth into the mineralized PLLA scaffolds. The image to the right is a combined bright field polarized and fluorescent image overlay. Scale bar = 400  $\mu\text{m}$ .

calcium on the mineralized PLLA scaffolds was significantly higher than the TCPS control and PLLA samples with roughly 3 and 4 times the amount of calcium as compared to these groups at days 14 and 21, respectively ( $p < 0.05$ ).

#### 4. Discussion

In orthopedic medicine there exists an increasing need for bone grafts with regenerative capabilities to treat bone defects arising from disease and trauma, especially with an ageing population [36]. Tissue engineering offers a promising solution for development of synthetic and/or natural scaffolds upon which osteoprogenitor cells can be seeded and cultured under optimal conditions and ultimately implanted to promote osteogenesis *in vivo*. This well-known approach has potential to provide suitable alternatives to allografts and autografts because of their unlimited supply and lack of immune response. Recently, CaP composite electrospun scaffolds have shown promise as functional bone tissue replacements because of their ability to allow osteoblast precursor cells to attach, proliferate, and differentiate towards the osteoblast phenotype [13]. However dense fiber packing and small pore size of these

fibrous structures can severely limit cell migration and colonization of the scaffold *in vitro* and inhibit tissue ingrowth and vascularization of the scaffold *in vivo* [23–25]. Therefore, the ability for cells to migrate through and colonize the bone scaffold is a critical feature for successful bone regeneration at the site of implantation.

To address this issue, we fabricated a scaffold with the intent of creating larger pores and increasing porosity by co-electrospinning a slow-degrading structural polymer (PLLA) with a water-soluble polymer (PEO) and subsequently removing the PEO by submersion in an aqueous environment. Similar fabrication techniques using PEO as a leaching polymer have previously been demonstrated with segmented polyurethane [32] and poly( $\epsilon$ -caprolactone) (PCL) [33]. The PLLA scaffolds were then mineralized by soaking in a 10 $\times$  SBF solution, thereby coating the surface with a biological apatite similar to amorphous calcium phosphate (Ca/P ratio of approximately 1.4). We hypothesized that cell infiltration into the electrospun scaffold could be enhanced by increasing the pore size and porosity, while inclusion of the biomimetic apatite substrate would increase the osteogenic capacity of the construct as compared to PLLA alone. Our fabrication technique produced surface mineralized electrospun PLLA scaffolds with varying pore sizes and

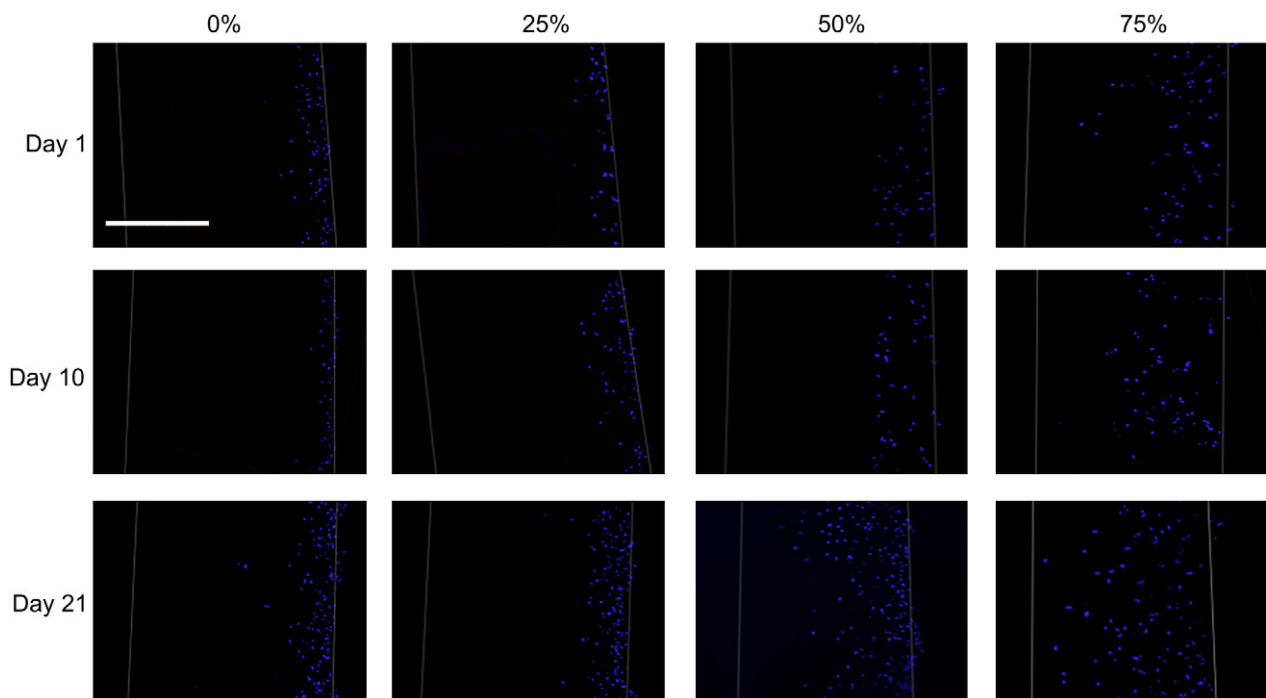


**Fig. 6.** Representative fluorescent images of mineralized PLLA cell-seeded scaffolds with 0–75% initial PEO content at days 1, 10, and 21 showing increased cell infiltration with both increased time and initial PEO content. Scale bar = 400  $\mu\text{m}$ .

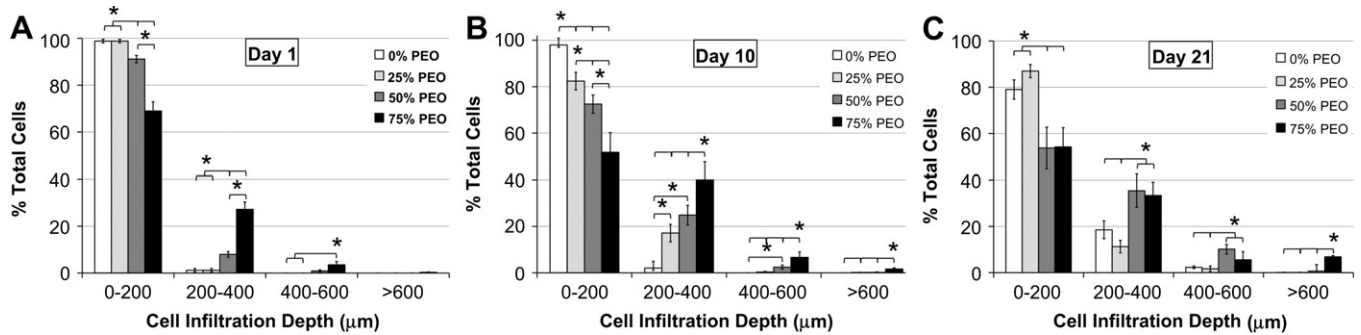


**Fig. 7.** Cell infiltration into mineralized PLLA scaffolds as a function of PEO content at (A) 1, (B) 10, and (C) 21 days after cell seeding. Cell number and cell migration distance from the edge of the scaffold are displayed as % total cells that are in measured regions through the thickness of the scaffold. A “\*” indicates a significant difference ( $p < 0.05$ ) between groups.

porosities, which were observed to be a function of initial PEO fiber content. We have demonstrated that scaffold pore size and porosity can be significantly enlarged by PEO inclusion and removal (Fig. 3). Our goal was to create a scaffold with pore sizes above the 100  $\mu\text{m}$  threshold which has been suggested to allow cell infiltration and tissue ingrowth into bone scaffolds [9]. In this study, a maximal average pore diameter of 89.3  $\mu\text{m}$  and porosity of 87.5% were obtained for mineralized PLLA scaffolds with 75% initial PEO content. This average pore diameter and porosity is considerably larger than the mineralized PLLA scaffolds without PEO (7.87  $\mu\text{m}$  and 82.1%) and the pore size is close to the target 100–300  $\mu\text{m}$  range. The fabricated pore size is also significantly greater than previously characterized electrospun PLLA [37] and PCL [38] scaffolds which exhibited average pore diameters of 21.5  $\mu\text{m}$  and 19.5  $\mu\text{m}$ , respectively.

The mechanical properties of the constructs in this study were also affected by the amount of PEO utilized. The elastic modulus and ultimate tensile strength of the mineralized PLLA scaffolds with 75% initial PEO were decreased approximately 6 fold and 5 fold, respectively, when compared to scaffolds without PEO. These findings are similar to those of Baker et al. [33], who showed that the elastic modulus of their PCL scaffolds decreased nearly 60% for scaffolds with 70% PEO as compared to those without PEO. We postulate that this is largely due to increased porosity and pore size, and decreased inter-fiber bonding. With an elastic modulus ranging from 0.8 to 5.3 MPa in tension, our highly porous mineralized PLLA scaffold, similar to most electrospun scaffolds, indicate that they

may not be suitable for load bearing applications such as for replacement of cortical bone (50–151 MPa modulus in tension) [39]. Rather, these scaffolds may be suitable for filling bony voids or gaps that are not intrinsic to the stability of the bony structure.

To elucidate the spatial and temporal effects of increasing the scaffold pore size via increased PEO content in the present study, MC3T3-E1 pre-osteoblasts were seeded onto scaffolds with 0%, 25%, 50%, and 75% initial PEO content and cell nuclear position was quantified in scaffold cross-sections at days 1, 10, and 21. In a similar study conducted by Baker et al., PCL was co-electrospun with increasing percentages of PEO (5–80%), dissolved and then seeded with mesenchymal stem cells to quantify cell infiltration at 21 days of culture. Although information was gained in Baker’s study about cell penetration into the scaffolds at the 3 week time point, the effects of increased PEO content on the temporal dynamics of cell infiltration were not presented. In a study conducted by Ju et al. [40], electrospinning parameters were varied to create electrospun PCL–collagen scaffolds with increased fiber diameters and resulting increased pore area. After seeding with smooth muscle cells, the authors assessed cell infiltration into the scaffolds for varying fiber diameters at days 1, 3, 7, 14 and 28, albeit qualitatively. Therefore, the present study is the first to our knowledge that has quantified both the spatial and temporal aspects of cell infiltration into electrospun scaffolds. Our results show that cell migration was greatly enhanced at all time points for scaffolds with 50% and 75% initial PEO content as compared to scaffolds with lower PEO fractions (Fig. 6). At day 21, nearly 11% and 12% of cells in the 50% and 75%

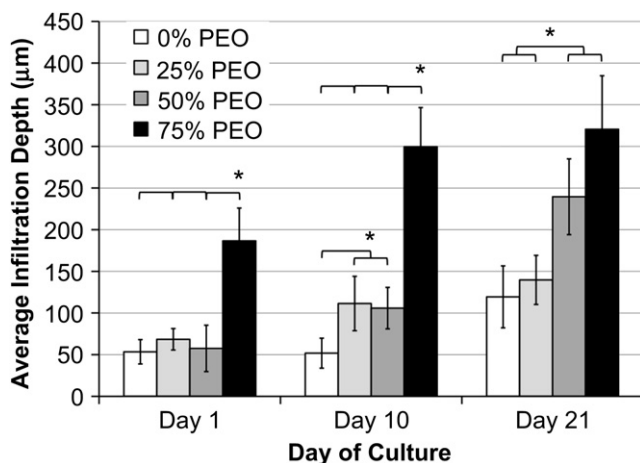


**Fig. 8.** Average cell infiltration depth into the mineralized PLLA scaffolds at 1, 10, and 21 days after cell seeding. Cell infiltration was found to increase as a function of both time and PEO content. A “\*” indicates a significant difference ( $p < 0.05$ ) between groups.

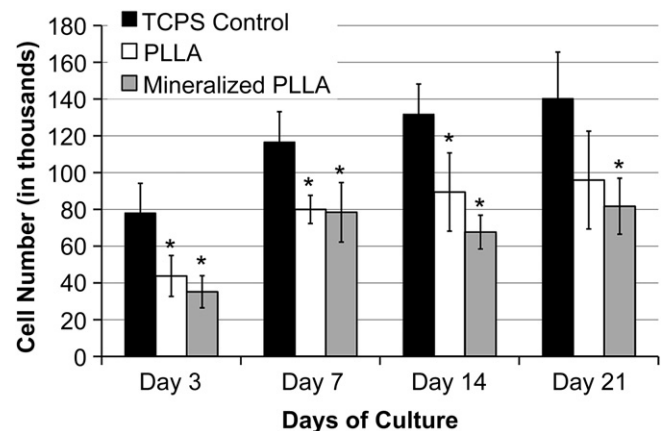


**Fig. 9.** Amount of cells per scaffold construct or TCPS control sample at days 3, 7, 14 and 21 after cell seeding as determined by the PicoGreen assay kit ( $n = 4$ ).  $3 \times 10^4$  cells were seeded onto the scaffolds or TCPS control wells at day 0. A “\*” indicates a significant difference ( $p < 0.05$ ) from the TCPS control.

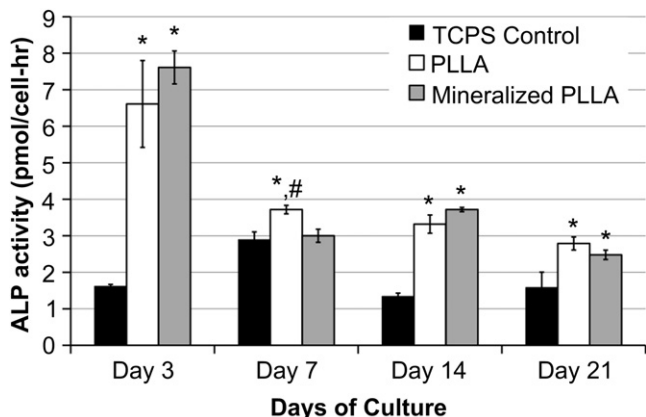


**Fig. 10.** Intracellular ALP activity of scaffold/cell constructs or TCPS control samples over time ( $n = 4$ ). Results are normalized per cell as determined by the DNA assay. A "\*" indicates a significant difference ( $p < 0.05$ ) from the TCPS control; a "#" indicates a significant difference ( $p < 0.05$ ) from the mineralized PLLA scaffold.

PEO scaffold groups, respectively, were found to have infiltrated greater than 400  $\mu\text{m}$  into the scaffold thickness, as compared to only approximately 2% of cells for the 0% and 25% PEO scaffolds. Furthermore, by day 21, 7% of cells in the 75% PEO scaffolds migrated more than 600  $\mu\text{m}$  – essentially to the opposite side of the scaffold (Fig. 7C). We postulate that enhanced cell migration in the 50% and 75% PEO scaffolds is largely due to the increased pore size and porosity between groups, as exhibited in Fig. 3. It was also observed that cell infiltration into the scaffolds was time dependent, with infiltration increasing over the duration of the experiment. The time points used in this study were chosen to evaluate the effect of initial PEO content and resultant changes in pore size and porosity, on the early (day 1) and late (days 10 and 21) stages of cell migration into the scaffolds. It was presumed that cell migration into the scaffold one day after seeding was primarily due to unhindered cell penetration, as cell migration due to proliferation and cell motility would be unlikely at such early stages in cell culture [41,42]. At day 1, nearly 31% of cells had migrated further than 200  $\mu\text{m}$  into the 75% PEO scaffold, as compared to only ~1% in the 0% and 25% PEO scaffolds – demonstrating the effect of large pore size on immediate cell infiltration. These findings indicate that cell migration into electrospun mineralized PLLA scaffolds and overall cell distribution can be enhanced by increasing the pore size

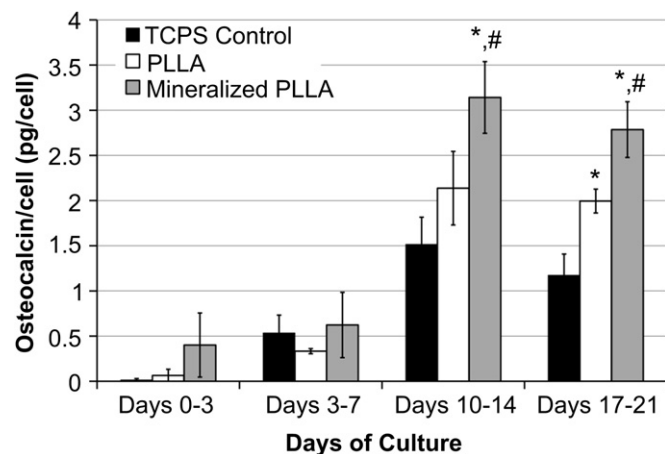


**Fig. 11.** Secreted OCN protein from scaffold/cell constructs or TCPS control samples ( $n = 4$ ). Results are normalized per cell as determined by the DNA assay. A "\*" indicates a significant difference ( $p < 0.05$ ) from the TCPS control; a "#" indicates a significant difference ( $p < 0.05$ ) from the pure PLLA scaffold.

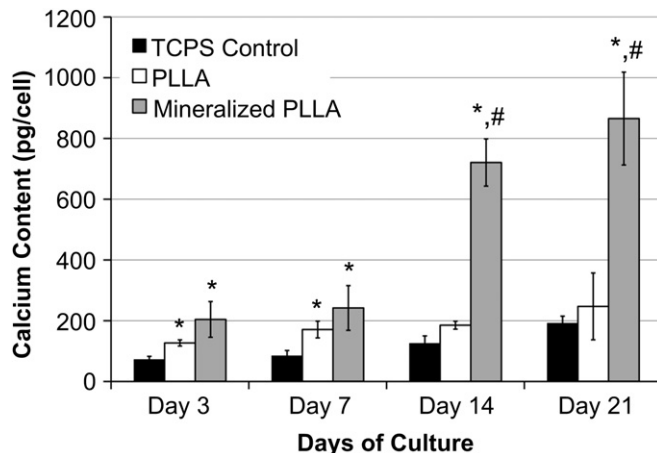


**Fig. 12.** Total calcium content for each cell/scaffold construct and TCPS control sample ( $n = 4$ ). Calcium levels of mineralized scaffolds without cells (control scaffolds) were assayed at each time point and subtracted from the background ( $n = 4$ ). Results are normalized per cell as determined by the DNA assay. A "\*" indicates a significant difference ( $p < 0.05$ ) from the TCPS control; a "#" indicates a significant difference ( $p < 0.05$ ) from the pure PLLA scaffold.

and porosity via incorporation and removal of a fast-dissolving fiber component.

In addition to providing a three-dimensional microarchitecture that allows adequate cell attachment and infiltration, a suitable bone scaffold must also support cell proliferation and direct osteoblastic differentiation. To evaluate our scaffold with respect to these parameters, MC3T3-E1 pre-osteoblast proliferation, ALP activity, osteocalcin protein expression, and ECM mineralization were assessed *in vitro* for 21 days on apatite-coated PLLA and non-coated PLLA scaffolds, in addition to TCPS as a control. The primary stage of osteoblast development is proliferation of undifferentiated cells [35]. In this study, DNA quantification revealed that cell numbers on the TCPS control were greater than both scaffolds at all time points, however, cell proliferation for all groups was observed throughout the experiment. Previous studies have shown that electrospun scaffolds can hinder osteoblast proliferation as compared to cells cultured on TCPS [16,21]. This is thought to be mediated by fiber microtopography, which can decrease cytoskeleton spreading, lead to a cuboidal cellular morphology, and result in decreased proliferation [11,24,43]. Moreover, proliferation and differentiation behaviors of osteoblasts are competing properties, e.g. the rate of cell proliferation decreases as differentiation initiates [44]. Our results indicate that ALP activity, an early biochemical marker of osteoblast phenotype, was approximately four times greater on scaffold/cell constructs than TCPS controls at day 3 ( $p < 0.05$ ). Therefore, cells in scaffold constructs appear to have begun differentiating shortly after cell seeding, whereas differentiation of cells on TCPS was delayed. Taken together, low cell numbers on scaffold/cell constructs as compared to the TCPS control at early time points can be explained at least in part by the initiation of cell differentiation as evidenced by statistically significant upregulation of ALP activity.

Both ALP activity and active cell replication are early stage markers of osteoblast differentiation [35], and our data suggest that there was a positive effect on osteodifferentiation for cells cultured in scaffolds as evidenced by upregulated ALP activity. However, since these markers are non-specific to osteoblast differentiation, other late stage indicators should be evaluated to confirm the actual cell phenotype. Therefore, OCN protein expression and ECM mineralization were measured. Osteocalcin, also known as bone Gla protein, is the most abundant non-collagenous protein found in bone and is

expressed by terminally differentiated osteoblasts during ECM mineralization [45]. OCN secretion for mineralized PLLA scaffolds was approximately 1.4 times greater than the PLLA scaffolds during days 10–14 and 17–21 ( $p < 0.05$ ), suggesting possible apatite mediated osteoblastic maturation. This finding is consistent with a study conducted by Chou et al. where OCN expression for MC3T3-E1 cells cultured on an apatite-coated poly(lactic-co-glycolic acid) (PLGA) scaffold was 2-fold greater compared to cells cultured on PLGA scaffolds at 4 weeks in culture [46]. OCN is an abundant calcium binding protein commonly found in bone and is thought to play an integral role in ECM mineralization by its ability to bind to both calcium and hydroxyapatite [45,47]. In this experiment, cell-mediated ECM mineralization for the mineralized PLLA group was roughly 3 and 4 times the amount of calcium as compared to TCPS control and PLLA groups at days 14 and 21, respectively, correlating with significantly higher OCN expression at identical time points (significant at  $p < 0.05$ ). These results indicate that the apatite surface had a significant effect on directing the MC3T3-E1 cells towards the osteoblast phenotype, thus demonstrating the osteogenic stimulating capacity of the mineralized PLLA scaffold. These findings are consistent with other studies in which polymer/CaP composite scaffolds increased bone ECM formation and mineralization of pre-osteoblasts when compared to scaffolds without a biomimetic apatite component [12–18,20,21].

## 5. Conclusions

In this study, we developed an electrospun bone tissue scaffold with a mineralized surface and enhanced pore size and porosity. This was accomplished by using a novel 3-step water-soluble fiber inclusion, removal and mineralization fabrication technique. The resulting scaffold supported MC3T3-E1 proliferation and osteogenic differentiation while accelerating cell infiltration into the scaffold and enhancing overall cell distribution. These findings indicate that such a scaffold may facilitate enhanced osteoprogenitor maturation and colonization *in vitro* that may translate to improved bone formation when implanted *in vivo*.

## Acknowledgement

This research was funded by a National Science Foundation Early CAREER award CBET 0955072 and a grant from the Institute for Critical Technology and Applied Science (ICTAS, Virginia Tech).

## Appendix

Figures with essential color discrimination. Figs. 1, 2, 5 and 6 of this article may be difficult to interpret in black and white. The full color images can be found in the online version at doi:10.1016/j.biomaterials.2010.12.003.

## References

- [1] Frohlich M, Grayson WL, Wan LQ, Marolt D, Drobic M, Vunjak-Novakovic G. Tissue engineered bone grafts: biological requirements, tissue culture and clinical relevance. *Curr Stem Cell Res Ther* 2008;3:254–64.
- [2] Ishaug SL, Crane GM, Miller MJ, Yasko AW, Yaszemski MJ, Mikos AG. Bone formation by three-dimensional stromal osteoblast culture in biodegradable polymer scaffolds. *J Biomed Mater Res* 1997;36:17–28.
- [3] Gopferich A, Peter SJ, Lucke A, Lu L, Mikos AG. Modulation of marrow stromal cell function using poly(d,l-lactic acid)-block-poly(ethylene glycol)-monomethyl ether surfaces. *J Biomed Mater Res* 1999;46:390–8.
- [4] Ishaug SL, Payne RG, Yaszemski MJ, Aufdemorte TB, Bizios R, Mikos AG. Osteoblast migration on poly(alpha-hydroxy esters). *Biotechnol Bioeng* 1996;50:443–51.
- [5] Yaszemski MJ, Payne RG, Hayes WC, Langer R, Mikos AG. Evolution of bone transplantation: molecular, cellular and tissue strategies to engineer human bone. *Biomaterials* 1996;17:175–85.
- [6] Peter SJ, Miller MJ, Yasko AW, Yaszemski MJ, Mikos AG. Polymer concepts in tissue engineering. *J Biomed Mater Res* 1998;43:422–7.
- [7] Oreffo RO, Triffitt JT. Future potentials for using osteogenic stem cells and biomaterials in orthopedics. *Bone* 1999;25:5S–9S.
- [8] Kanczler JM, Oreffo RO. Osteogenesis and angiogenesis: the potential for engineering bone. *Eur Cell Mater* 2008;15:100–14.
- [9] Karageorgiou V, Kaplan D. Porosity of 3D biomaterial scaffolds and osteogenesis. *Biomaterials* 2005;26:5474–91.
- [10] Salgado AJ, Coutinho OP, Reis RL. Bone tissue engineering: state of the art and future trends. *Macromol Biosci* 2004;4:743–65.
- [11] Pham QP, Sharma U, Mikos AG. Electrospinning of polymeric nanofibers for tissue engineering applications: a review. *Tissue Eng* 2006;12:1197–211.
- [12] Woo KM, Jun JH, Chen VJ, Seo J, Baek JH, Ryoo HM, et al. Nano-fibrous scaffolding promotes osteoblast differentiation and biomineralization. *Biomaterials* 2007;28:335–43.
- [13] Jang JH, Castano O, Kim HW. Electrospun materials as potential platforms for bone tissue engineering. *Adv Drug Deliv Rev* 2009;61:1065–83.
- [14] Yu HS, Jang JH, Kim TI, Lee HH, Kim HW. Apatite-mineralized polycaprolactone nanofibrous web as a bone tissue regeneration substrate. *J Biomed Mater Res A* 2009;88:747–54.
- [15] Erisken C, Kalyon DM, Wang H. Functionally graded electrospun polycaprolactone and beta-tricalcium phosphate nanocomposites for tissue engineering applications. *Biomaterials* 2008;29:4065–73.
- [16] Wutticharoenmongkol P, Pavasent P, Supaphol P. Osteoblastic phenotype expression of MC3T3-E1 cultured on electrospun polycaprolactone fiber mats filled with hydroxyapatite nanoparticles. *Biomacromolecules* 2007;8:2602–10.
- [17] Mavis B, Demirtas TT, Gumusderelioglu M, Gunduz G, Colak U. Synthesis, characterization and osteoblastic activity of polycaprolactone nanofibers coated with biomimetic calcium phosphate. *Acta Biomater* 2009;5:3098–111.
- [18] Ko EK, Jeong SI, Rim NG, Lee YM, Shin H, Lee BK. In vitro osteogenic differentiation of human mesenchymal stem cells and in vivo bone formation in composite nanofiber meshes. *Tissue Eng Part A* 2008;14:2105–19.
- [19] Venugopal JR, Low S, Choon AT, Kumar AB, Ramakrishna S. Nano-bioengineered electrospun composite nanofibers and osteoblasts for bone regeneration. *Artif Organs* 2008;32:388–97.
- [20] McCullen SD, Zhu Y, Bernacki SH, Narayan RJ, Pourdeyehimi B, Gorga RE, et al. Electrospun composite poly(l-lactic acid)/tricalcium phosphate scaffolds induce proliferation and osteogenic differentiation of human adipose-derived stem cells. *Biomed Mater* 2009;4:035002.
- [21] Prabhakaran MP, Venugopal J, Ramakrishna S. Electrospun nanostructured scaffolds for bone tissue engineering. *Acta Biomater* 2009;5:2884–93.
- [22] Wright LD, Andric T, Freeman JW. Utilizing NaCl to increase the porosity of electrospun materials. *Materials Science and Engineering C* 2011;31:30–6.
- [23] Boland ED, Matthews JA, Pawlowski KJ, Simpson DG, Wnek GE, Bowlin GL. Electrospinning collagen and elastin: preliminary vascular tissue engineering. *Front Biosci* 2004;9:1422–32.
- [24] Badami AS, Kreke MR, Thompson MS, Riffle JS, Goldstein AS. Effect of fiber diameter on spreading, proliferation, and differentiation of osteoblastic cells on electrospun poly(lactic acid) substrates. *Biomaterials* 2006;27:596–606.
- [25] Brauker JH, Carr-Brendel VE, Martinson LA, Crudele J, Johnston WD, Johnson RC. Neovascularization of synthetic membranes directed by membrane microarchitecture. *J Biomed Mater Res* 1995;29:1517–24.
- [26] Stankus JJ, Guan J, Fujimoto K, Wagner WR. Microintegrating smooth muscle cells into a biodegradable, elastomeric fiber matrix. *Biomaterials* 2006;27:735–44.
- [27] Stankus JJ, Soletti L, Fujimoto K, Hong Y, Vorp DA, Wagner WR. Fabrication of cell microintegrated blood vessel constructs through electrohydrodynamic atomization. *Biomaterials* 2007;28:2738–46.
- [28] Pham QP, Sharma U, Mikos AG. Electrospun poly(epsilon-caprolactone) microfiber and multilayer nanofiber/microfiber scaffolds: characterization of scaffolds and measurement of cellular infiltration. *Biomacromolecules* 2006;7:2796–805.
- [29] Leong MF, Rasheed MZ, Lim TC, Chian KS. In vitro cell infiltration and in vivo cell infiltration and vascularization in a fibrous, highly porous poly(d,l-lactide) scaffold fabricated by cryogenic electrospinning technique. *J Biomed Mater Res A* 2009;91:231–40.
- [30] Nam J, Huang Y, Agarwal S, Lannutti J. Improved cellular infiltration in electrospun fiber via engineered porosity. *Tissue Eng* 2007;13:2249–57.
- [31] Zhang Y, Ouyang H, Lim CT, Ramakrishna S, Huang ZM. Electrospinning of gelatin fibers and gelatin/PCL composite fibrous scaffolds. *J Biomed Mater Res B Appl Biomater* 2005;72:156–65.
- [32] Kidoaki S, Kwon IK, Matsuda T. Mesoscopic spatial designs of nano- and microfiber meshes for tissue-engineering matrix and scaffold based on newly devised multilayering and mixing electrospinning techniques. *Biomaterials* 2005;26:37–46.
- [33] Baker BM, Gee AO, Metter RB, Nathan AS, Marklein RA, Burdick JA, et al. The potential to improve cell infiltration in composite fiber-aligned electrospun scaffolds by the selective removal of sacrificial fibers. *Biomaterials* 2008;29:2348–58.
- [34] Thibault RA, Scott Baggett L, Mikos AG, Kasper FK. Osteogenic differentiation of mesenchymal stem cells on pregenerated extracellular matrix scaffolds in the absence of osteogenic cell culture supplements. *Tissue Eng Part A* 2010;16:431–40.

- [35] Quarles LD, Yohay DA, Lever LW, Caton R, Wenstrup RJ. Distinct proliferative and differentiated stages of murine MC3T3-E1 cells in culture: an in vitro model of osteoblast development. *J Bone Miner Res* 1992;7:683–92.
- [36] Panetta NJ, Gupta DM, Longaker MT. Bone regeneration and repair. *Curr Stem Cell Res Ther* 2010;5:122–8.
- [37] Yang F, Xu CY, Kotaki M, Wang S, Ramakrishna S. Characterization of neural stem cells on electrospun poly(l-lactic acid) nanofibrous scaffold. *J Biomater Sci Polym Ed* 2004;15:1483–97.
- [38] Lowery JL, Datta N, Rutledge GC. Effect of fiber diameter, pore size and seeding method on growth of human dermal fibroblasts in electrospun poly(epsilon-caprolactone) fibrous mats. *Biomaterials* 2010;31:491–504.
- [39] Wagoner Johnson AJ, Herschler BA. A review of the mechanical behavior of CaP and CaP/polymer composites for applications in bone replacement and repair. *Acta Biomater* 2011;7:16–30.
- [40] Ju YM, Choi JS, Atala A, Yoo JJ, Lee SJ. Bilayered scaffold for engineering cellularized blood vessels. *Biomaterials* 2010;31:4313–21.
- [41] Payer M, Lohberger B, Stadelmeyer E, Bartmann C, Windhager R, Jakse N. Behaviour of multipotent maxillary bone-derived cells on beta-tricalcium phosphate and highly porous bovine bone mineral. *Clin Oral Implants Res* 2010;7:699–708.
- [42] Liu Y, Franco A, Huang L, Gersappe D, Clark RA, Rafailovich MH. Control of cell migration in two and three dimensions using substrate morphology. *Exp Cell Res* 2009;315:2544–57.
- [43] Chou YF, Huang W, Dunn JC, Miller TA, Wu BM. The effect of biomimetic apatite structure on osteoblast viability, proliferation, and gene expression. *Biomaterials* 2005;26:285–95.
- [44] Owen TA, Aronow M, Shalhoub V, Barone LM, Wilming L, Tassinari MS, et al. Progressive development of the rat osteoblast phenotype in vitro: reciprocal relationships in expression of genes associated with osteoblast proliferation and differentiation during formation of the bone extracellular matrix. *J Cell Physiol* 1990;143:420–30.
- [45] Hauschka PV, Lian JB, Cole DE, Gundberg CM. Osteocalcin and matrix Gla protein: vitamin K-dependent proteins in bone. *Physiol Rev* 1989;69:990–1047.
- [46] Chou YF, Dunn JCY, Wu BM. In vitro response of MC3T3-E1 preosteoblasts within three-dimensional apatite-coated PLGA scaffolds. *J Biomed Mater Res B* 2005;75B:81–90.
- [47] Hauschka PV, Wians Jr FH. Osteocalcin-hydroxyapatite interaction in the extracellular organic matrix of bone. *Anat Rec* 1989;224:180–8.

## **Appendix B: A Scanning-fiber-based Imaging Method for Tissue Engineering**

Matthias C. Hofmann,<sup>1</sup> Bryce M. White,<sup>2</sup> Josh Mitchell,<sup>1</sup> William C. Vogt,<sup>2</sup> Tracy Criswell,<sup>4</sup>  
Christopher Rylander,<sup>2,3</sup> Marissa Nichole Rylander,<sup>2,3</sup> Shay Soker,<sup>4</sup> Ge Wang,<sup>2</sup> Yong Xu<sup>1</sup>

<sup>1</sup>Bradley Department of Electrical and Computer Engineering, Virginia Tech, Blacksburg, VA 24061, USA

<sup>2</sup>School of Biomedical Engineering and Sciences, Virginia Tech, Blacksburg, VA 24061, USA

<sup>3</sup>Department of Mechanical Engineering, Virginia Tech, Blacksburg, VA 24061, USA

<sup>4</sup>Wake Forest Institute for Regenerative Medicine, Wake Forest University School of Medicine, Medical Center Boulevard, Winston-Salem, NC, 27157, USA

## Scanning-fiber-based imaging method for tissue engineering

Matthias C. Hofmann  
Bryce M. Whited  
Josh Mitchell  
William C. Vogt  
Tracy Criswell  
Christopher Rylander  
Marissa Nichole Rylander  
Shay Soker  
Ge Wang  
Yong Xu

# Scanning-fiber-based imaging method for tissue engineering

Matthias C. Hofmann,<sup>a</sup> Bryce M. Whited,<sup>b</sup> Josh Mitchell,<sup>a</sup> William C. Vogt,<sup>b</sup> Tracy Criswell,<sup>d</sup> Christopher Rylander,<sup>b,c</sup> Marissa Nichole Rylander,<sup>b,c</sup> Shay Soker,<sup>d</sup> Ge Wang,<sup>b</sup> and Yong Xu<sup>a</sup>

<sup>a</sup>Virginia Tech, Bradley Department of Electrical and Computer Engineering, Blacksburg, Virginia 24061

<sup>b</sup>Virginia Tech, School of Biomedical Engineering and Sciences, Blacksburg, Virginia 24061

<sup>c</sup>Virginia Tech, Department of Mechanical Engineering, Blacksburg, Virginia 24061

<sup>d</sup>Wake Forest University School of Medicine, Wake Forest Institute for Regenerative Medicine, Medical Center Boulevard, Winston-Salem, North Carolina 27157

**Abstract** A scanning-fiber-based method developed for imaging bioengineered tissue constructs such as synthetic carotid arteries is reported. Our approach is based on directly embedding one or more hollow-core silica fibers within the tissue scaffold to function as micro-imaging channels (MIC). The imaging process is carried out by translating and rotating an angle-polished fiber micro-mirror within the MIC to scan excitation light across the tissue scaffold. The locally emitted fluorescent signals are captured using an electron multiplying CCD camera and then mapped into fluorophore distributions according to fiber micro-mirror positions. Using an optical phantom composed of fluorescent microspheres, tissue scaffolds, and porcine skin, we demonstrated single-cell-level imaging resolution (20 to 30  $\mu\text{m}$ ) at an imaging depth that exceeds the photon transport mean free path by one order of magnitude. This result suggests that the imaging depth is no longer constrained by photon scattering, but rather by the requirement that the fluorophore signal overcomes the background “noise” generated by processes such as scaffold autofluorescence. Finally, we demonstrated the compatibility of our imaging method with tissue engineering by visualizing endothelial cells labeled with green fluorescent protein through a  $\sim 500 \mu\text{m}$  thick and highly scattering electrospun scaffold. © 2012 Society of Photo-Optical Instrumentation Engineers (SPIE). [DOI: 10.1117/1.JBO.17.6.066010]

Keywords: molecular imaging; fiber optics; deep tissue imaging; tissue engineering; fluorescence imaging; endothelial cells; blood vessel; image processing.

Paper 12006 received Jan. 4, 2012; revised manuscript received Apr. 15, 2012; accepted for publication Apr. 17, 2012; published online Jun. 4, 2012.

## 1 Introduction

The field of tissue engineering has emerged as an important area of biomedical research, where its goal is to create functional tissues and organs in the laboratory in order to replace or restore those damaged by disease and trauma.<sup>1-4</sup> Typically, studies in tissue engineering are carried out in separate steps that involve fabricating a biocompatible scaffold capable of supporting cell growth (i.e., an artificial extracellular matrix), seeding living cells onto the scaffold, culturing the cell-seeded scaffold in a bioreactor, and then surgically implanting the preconditioned construct into a living animal to replace the damaged tissue or organ.<sup>5-7</sup>

Successful maturation of bioengineered tissues is a highly complex and dynamic process that involves extensive interactions among multiple cell types and their surrounding extracellular environment. Given its biological complexity, the process of tissue regeneration must be frequently monitored and evaluated in order to optimize tissue construct design and to improve the clinical outcome.<sup>8</sup> However, it is very difficult to achieve single-cell-level-resolution imaging at a depth beyond one photon transport mean free path (TMFP).<sup>9,10</sup> As a result, the current “gold standard” for evaluating tissue constructs remains histological analysis, which requires sacrificing separate specimens at different time points by dissecting them into thin slices and

then examining the slices under an optical microscope. These destructive methods are time consuming, labor intensive, and cannot reveal cell behaviors and interactions in their natural microenvironments. Consequently, the inability to perform deep-tissue imaging at single cell resolution has become a major barrier in tissue engineering research.

Accomplishing high-resolution deep-tissue imaging is a difficult challenge that goes far beyond tissue engineering. In fact, a major problem in biophotonics is the conflict between imaging depth and imaging resolution. Fundamentally, the difficulty in simultaneously achieving a high imaging resolution and a large imaging depth can be traced to this observation: Most biological tissues are turbid media and therefore strongly scatter light. Even for recently developed modalities such as photoacoustic imaging, the spatial resolution is approximately  $>50 \mu\text{m}$  at the imaging depth of three photon TMFP.<sup>11,12</sup> On the other extreme, there are various tomographical techniques such as fluorescence molecular tomography, where one can achieve a large imaging depth ( $\sim 2 \text{ mm}$ ) by sacrificing imaging resolution to the level of  $>500 \mu\text{m}$ .<sup>9</sup>

The inability to non-destructively monitor tissue development, which often requires deep-tissue, single-cell-level resolution imaging, poses a significant hindrance for tissue engineering research. A specific example is the bioengineering of synthetic vascular grafts.<sup>13,14</sup> In this case, successful clinical outcome depends critically on the coordinated endothelial cell

Address all correspondence to: Yong Xu, 467 Whittemore Hall, Virginia Tech, Blacksburg, Virginia 24060. Tel: +540 231 2464; Fax: +540 231 3362; E-mail: [yong@vt.edu](mailto:yong@vt.edu)

(EC) coverage on the lumen (inner surface) of the blood vessel graft.<sup>15</sup> However, since the thickness of the blood vessel scaffold must significantly exceed one photon TMFP in order to withstand normal blood pressure, it is difficult to apply existing imaging methods to “see” through the optically opaque scaffold and monitor EC behaviors on the scaffold lumen.

This manuscript reports a novel imaging method that can overcome the aforementioned challenge. Our approach is based on embedding flexible micro-imaging channels (MICs) directly into a vascular scaffold. Each MIC serves as a guiding channel through which we can insert a fiber micro-mirror and locally scan excitation light across a region of interest (ROI) on the scaffold lumen. After collecting fluorescent signals generated during fiber scanning, we can map the values of these signals onto a digital grid and reconstruct the spatial distributions of the fluorescently labeled ECs. A major advantage of our method is that the link between imaging resolution and imaging depth is “decoupled,” making it possible to greatly increase imaging depth without significantly sacrificing imaging resolution. Using a tissue scaffold phantom, we demonstrated that our imaging system could deliver 20 to 30  $\mu\text{m}$  imaging resolution at an imaging depth of approximately three photon TMFPs. Furthermore, the resolution of our imaging system remained essentially the same even if the total imaging depth was increased by an additional eight photon TMFPs. Given the results of this phantom study, our imaging method has the potential to find a wide range of tissue engineering applications that involve epithelial tissues.

## 2 Materials and Methods

### 2.1 Phantom Design and Fabrication

#### 2.1.1 Experimental design

In Fig. 1(a), we show a pulsatile flow bioreactor developed for the preconditioning of a synthesized vascular graft.<sup>16</sup> As shown in the figure, the vascular graft is enclosed in a sealed bioreactor and cannot be easily imaged using traditional optical imaging methods. Ultimately, we intend to use the scanning-fiber-based imaging method to assess lumen endothelialization, where a MIC is directly embedded into the scaffold wall as shown in Fig. 1(b). However, before applying this novel imaging method for any *in vitro* or *in vivo* studies, we need to first validate system performance through optical phantom studies.

As illustrated in Fig. 1(c), fluorescent labeled ECs exist only on the innermost layer (i.e., lumen) of the tubular scaffold. Consequently, it is difficult to apply direct-line-of-sight optical microscopy to visualize luminal fluorophore distributions through the optically opaque scaffold. Yet in order to validate our imaging method, we need to compare the results obtained through fiber scanning with a common standard such as direct-line-of-sight microscopy. To resolve this quandary, we created an equivalent phantom by “flattening” the tubular vessel and converting it to a planar structure, as illustrated in Fig. 1(d). Because ECs cover only the innermost surface of a blood vessel, they will exist only on one side of the “flat” vessel surface, which is referred to as the “luminal” surface. Note that the objective lens and all other instruments required for scanning-fiber-based imaging should be placed outside of the animal body as indicated by the “detector” in Fig. 1(c) and 1(d). Hence we denote the surface opposite of the luminal surface as the “exterior” surface. With these considerations, the

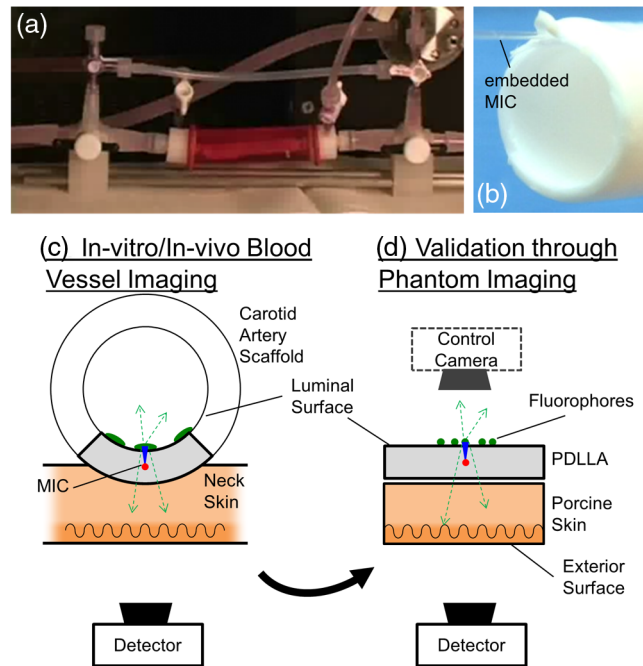


**Fig. 1** (a) A pulsatile flow bioreactor for *in vitro* incubation of bioengineered carotid artery scaffolds developed by one of the authors. Bioreactors often require a hermetically enclosed chamber that is incompatible with standard optical imaging methods. (b) A vascular scaffold embedded with a micro-imaging channel (MIC) for non-destructive, scanning-fiber-based imaging. (c) and (d) Depict design of a planar optical phantom that imitates a tubular carotid artery scaffold graft for future *in vitro* (no neck skin) or *in vivo* (with neck skin) studies. As shown in (c), an MIC is directly embedded within the wall of the scaffold. Through the MIC, we can deliver highly localized excitation light to a region of interest on scaffold lumen and generate a fluorescent signal. Part of the fluorescent signal is captured by an external detector for image reconstruction. (d) An optical phantom model was designed to mimic the experimental configuration in (c). The phantom is designed such that we can verify our fluorescence mapping results using the direct-line-of-sight images obtained by a control camera.

optical phantom used in this study is composed of a planar tissue scaffold with an embedded MIC, a piece of porcine skin, and multiple fluorophores placed on the luminal surface. With the configuration depicted in Fig. 1(d), we can easily obtain the direct-line-of-sight images as control images that accurately depict the distributions of fluorophores on scaffold lumen. Physical properties of the phantom such as scaffold porosity and optical coefficients were kept equivalent to the vessel scaffolds used for carotid artery engineering.<sup>17</sup>

The presence of the 3-mm thick porcine skin serves two purposes. First, it mimics *in vivo* conditions,<sup>18</sup> where the presence of additional obstructive biological tissues, such as the skin of an animal, must be included in order to account for additional photon scattering and autofluorescence. Additionally, the porcine skin also enables us to evaluate the performance of our imaging system as we significantly increase imaging depth.

We used two types of fluorophores in our studies. To evaluate the resolution and depth dependence of the imaging system, we used 28- $\mu\text{m}$ -diameter green fluorescent microspheres (FP-30052-5, Spherotech Inc., Lake Forest, IL) to simulate green fluorescent protein (GFP)-labeled ECs. For a preliminary live cell study, we used GFP-labeled ECs seeded on the luminal surface of a flat 500  $\mu\text{m}$  thick scaffold.

### 2.1.2 Scaffold fabrication

Electrospinning was used to fabricate a scaffold to construct the phantom.<sup>19</sup> Briefly, bioabsorbable poly-(D, L-lactide) (PDLLA) ( $M_w = 80,000$  g/mol, SurModics Pharmaceuticals, Birmingham, AL) was suspended in a 22% w/v solution with a 3:1 ratio of tetrahydrofuran:dimethylformamide (Fisher Scientific, Fair Lawn, NJ) under gentle stirring for 4 h. Next, the polymer solution was delivered at a flow rate of 5 ml/hr through an 18 G blunt-tip needle attached to the end of a syringe. A 13 kV charge was then applied between the needle tip and a 2-in. diameter aluminum mandrel using a direct current power supply (Gamma High Voltage Research, Ormond Beach, FL). The mandrel was placed 10 cm away from the needle tip and set to rotate at a constant 60 rpm. The high voltage difference between the needle tip and the spinning mandrel drew the charged polymer solution towards the mandrel. The rapid evaporation of the solvent then generated thin strands of PDLLA polymer fibers ( $\sim 1$   $\mu\text{m}$  in diameter), which formed a finely woven scaffold sheet on the spinning mandrel as shown up close by the SEM image in Fig. 2(a). Once the scaffold sheet reached its desired thickness, it was removed from the mandrel and placed in a desiccator for 10 h to remove any residual solvent.

### 2.1.3 MIC integration

A sintering process was adapted<sup>20</sup> to selectively incorporate the MICs into the PDLLA scaffold. The MICs are made of a custom-sized, optically transparent and flexible, fused-silica hollow fiber (Polymicro Technologies, Phoenix, AZ) with an inner and outer diameter of 145 and 240  $\mu\text{m}$ , respectively. Our MIC integration process is as follows. First, a PDLLA sheet was electrospun to 300  $\mu\text{m}$  thickness and then cut into 3 cm  $\times$  2 cm rectangular mats. Next, we placed MICs on top of a PDLLA mat and covered it with a second mat, effectively sandwiching the MICs between the two scaffold mats. The scaffold mats were then compressed between glass slides with a 28 g weight in an oven at 54°C for 20 min followed by a 10 min cool down period. Through the heated compression, the PDLLA mats fused together without losing the original woven structure, while securely embedding the MICs inside as shown in Fig. 2(a). After sintering, the total thickness of the sample was

500  $\pm$  9  $\mu\text{m}$  and the distance from the luminal surface to the center of the MIC was  $\sim 200$   $\mu\text{m}$ .

### 2.2 Excitation Light Delivery

Delivery of pump light for fluorescence excitation was achieved by inserting an angle-polished fiber micro-mirror into the transparent MIC as shown in the image in Fig. 2(b). The mirror was fabricated by polishing the tip of a standard single mode fiber (SMF430, Nufern Inc., East Granby, CT) at a 45 deg angle with a 0.1- $\mu\text{m}$  grit diamond lapping film (Pace Technologies, Tucson, AR). Excitation light was coupled into the optical fiber and perpendicularly redirected by the 45 deg air-silica interface via total internal reflection as shown in Fig. 2(c). After inserting the micro-mirror into the MIC, the propagation direction of the excitation light was controlled through the translational and angular position of the inserted fiber micro-mirror.

### 2.3 Incorporation of Fluorescent Sources

The phantom studies required placing fluorescent sources on the scaffold lumen at fixed locations. We used 28  $\mu\text{m}$  diameter microspheres coated with a green fluorescent dye (FP-30052-5, Spherotech Inc., Lake Forest, IL) to mimic GFP-labeled ECs. First, the microspheres were suspended in deionized water at a 1:10 volume ratio. Next, we pipetted 1 ml of the solution onto the lumen of the phantom, which lead to a random dispersion of the microspheres. To securely attach the microsphere to the scaffold surface, a thin  $\sim 10$   $\mu\text{m}$  layer of additional PDLLA was electrospun on top of the microspheres. The added layer was thin enough to be optically transparent, yet sufficiently strong to eliminate any change in microsphere pattern during extended handling of the phantom.

### 2.4 Measuring the Scaffold Optical Properties

To quantify the optical characteristics of the electrospun PDLLA scaffold, a spectrophotometer (Cary 5000, Agilent Technologies, Santa Clara, CA) coupled with an integrating sphere (Labsphere, North Sutton, NH) was used to measure the reflectance and transmittance values from 450 to 750 nm. The optical measurements were repeated on three scaffold mats having the same thickness as the phantom ( $\pm 25$   $\mu\text{m}$  std.dev.). Prior

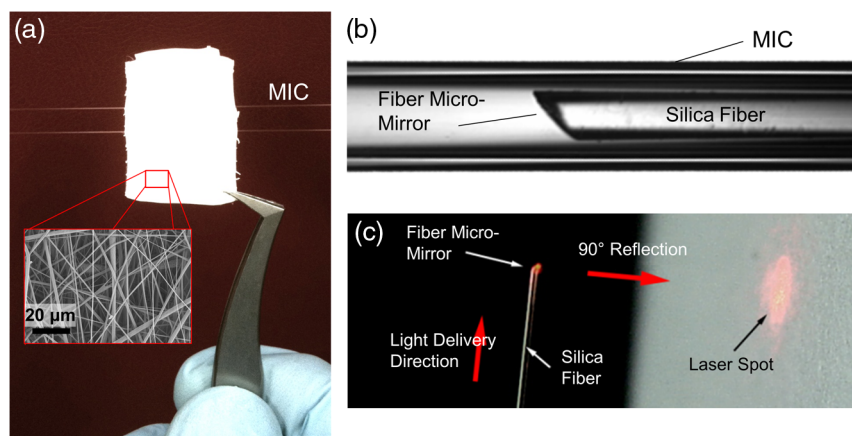


**Fig. 2** (a) A thinly woven PDLLA scaffold mat was electrospun and then cut into 3 cm  $\times$  2 cm rectangular mats. The optically turbid scaffold architecture is shown in the scanning electron microscope image. The PDLLA phantom was fabricated by placing micro-imaging channels (MICs) between two scaffold mats and heat sintering them together. (b) A microscope image of a fiber micro-mirror inserted into a MIC. (c) The 90 deg reflection of the excitation light at the polished fiber tip is used for local delivery and scanning of excitation light within the region of interest.

to the measurements, the scaffolds were immersed and saturated in Endothelial Growth Medium-2 (Lonza Biomedical, Walkersville, MD), the same cell media used for EC culturing and phantom imaging. From the reflectance and transmittance values, the absorption coefficient  $\mu_a$ , and scattering coefficient  $\mu_s$ , were calculated using the inverse adding-doubling algorithm developed by Prahl.<sup>21</sup> For the calculations, we used commonly accepted values for the refractive index ( $n = 1.38$ ) and anisotropy number ( $g = 0.9$ ) of the scaffold.<sup>9,22</sup> We calculated the MFP distance of the PDLA by using

$$\text{MFP} = \frac{1}{\mu_s}, \quad (1)$$

which models the average distance covered by a photon until a scattering event occurs. A photon undergoing several scattering events can be approximated by the TMFP based on the anisotropy number  $g$  (which relates to the degree of forward scattering) and is defined as

$$\text{TMFP} = \text{MFP} \times \frac{1}{(1 - g)}. \quad (2)$$

## 2.5 Imaging System

The scanning-fiber-based imaging method requires local excitation of the fluorophores using the fiber mirror and the detection of fluorescent signals generated at each mirror location. A schematic and a photograph of the imaging platform that can accommodate this design is shown in Fig. 3(a) and 3(b), respectively. A 473-nm laser light was coupled into an optical fiber and delivered to the sample's ROI by the fiber micro-mirror within the MIC. The laser was operated at a continuous 1 mW, with a fiber injection efficiency of  $\sim 15\%$ . The movement of the fiber micro-mirror was controlled by a custom-built two-axis

motorized scanning system consisting of a  $0.1\text{-}\mu\text{m}$ -resolution translation stage (UTM100PP.1HL, Newport, Irvine, CA) and a  $20\text{ deg/sec}$  rotation stage (URM80PE, Newport). A fiber clamp was mounted to the scanner that held the fiber in place. The distance from the fiber micro-mirror to the clamp was 15 cm. This system enabled the control of both the angular and the translational forward/backward movement of the fiber micro-mirror using a custom Labview program (National Instruments, Austin TX). The fluorescent responses generated by the fluorophores were collected by a  $2\times$  long-working distance lens (M Plan Apo 2, Mitutoyo) and captured by the electron multiplying CCD camera (EM-CCD) (iXon, Andor Inc., Belfast). The distance between the lens and the phantom was 10 cm. For fluorescence mapping, the camera was set to a full-binning mode where the EM-CCD chip's pixels were internally summed together to provide the total fluorescence intensity. In principle, we can replace the camera with a single detector such as a photomultiplier tube. However, a camera is required to quantify fluorescence distributions on the scaffold exterior surface that will be shown later. A bandpass filter (525/45 BrightLine, Semrock, Rochester, NY) was used to remove the excitation light from fluorescence signals.

## 2.6 Fiber-Scanning and Fluorescence-Mapping Procedure

The key feature of the scanning-fiber-based method is the localized fluorophore excitation. More specifically, after using the fiber mirror to deliver excitation light into the scaffold, we can assume all fluorescent signals are generated within this highly localized light spot on the luminal surface. This local light spot is referred to as an "excitation spot" and its location on the lumen is controlled by the fiber mirror position within the MIC. The illustration in Fig. 3(c) shows the excitation spot as it appears on the lumen.

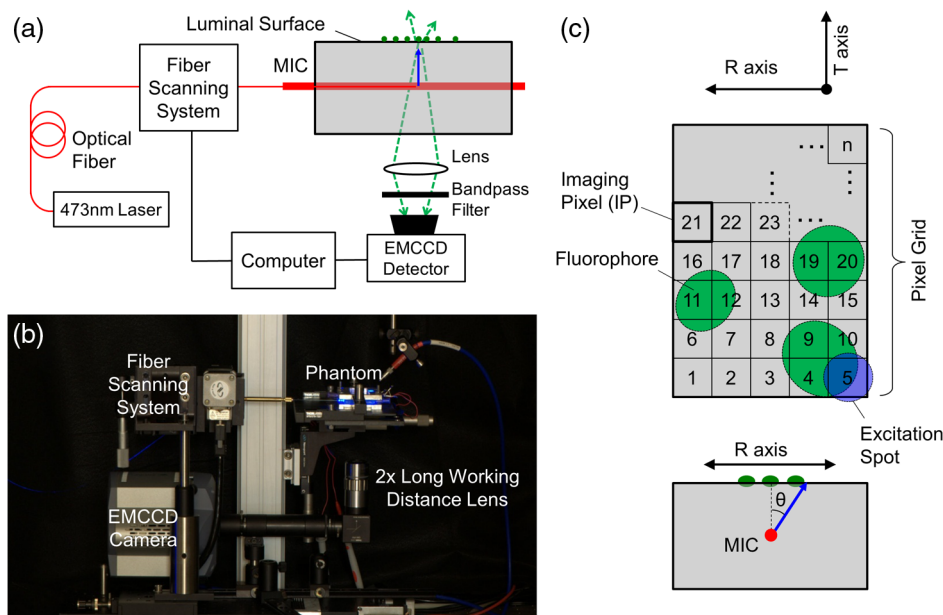


**Fig. 3** (a) Schematic and (b) photograph of the scanning-fiber-based imaging system. (c) Diagram of the imaging procedure. Using the fiber mirror, we can locally deliver excitation light to a point within the region of interest (ROI) (excitation spot). The excitation spot is moved within the ROI by rotating and translating the fiber mirror. By scanning the excitation spot according to a pixel grid, we can map the intensity responses into a digital grid to obtain fluorophore distribution.

The scanning system possesses two degrees of freedom: one is the forward/backward translation  $x$  and the other is angular rotation  $\theta$  of the fiber inside the MIC. As the excitation spot is scanned across the lumen, a fluorescence response is generated if the spot overlaps with a fluorophore. A portion of the fluorescent signal travels through the optically opaque phantom and is captured by the detector. Since all fluorescent signals are produced within the spatially-localized excitation spot, we can “reconstruct” the fluorophore distribution by using the intensity of the fluorescence signal captured by the detector. This reconstruction process is referred to as “fluorescence mapping”, and is described in detail below.

First, we selected a ROI on the lumen and divided it into a pixel grid of  $5 \times 5 \mu\text{m}^2$  imaging pixels (IP) as illustrated in Fig. 3(c). Every IP in the grid can be selectively illuminated by the excitation spot by establishing a one-to-one correspondence between the center of the spot (e.g.,  $R$  axis and  $T$  axis) and the corresponding fiber mirror position ( $x, \theta$ ). In Fig. 3(c), we define the  $R$  axis as parallel to the MIC and the  $T$  axis as perpendicular to the MIC. Note that the coordinate  $R$  is a function of the fiber rotation angle  $\theta$  and  $T$  is directly given by the linear translation  $x$  of the fiber mirror. Furthermore,  $\theta = 0$  denotes the case where the excitation light is launched directly towards the lumen.

To begin an experiment, the excitation spot was first positioned to IP = 1. The resulting fluorescence signal response value was collected by the detector and assigned to IP = 1. This process was repeated for each IP in the pixel grid by discretely scanning the excitation spot across the luminal surface. By plotting the response intensities of each IP in the pixel grid as a 2-D intensity array, we obtained a mapped image of the fluorophore distribution on the luminal surface.

To intuitively understand the validity of this imaging method, let us consider an ideal case that satisfies the following assumptions: (1) the excitation spot is contained entirely within any given IP, (2) the excitation light intensity remains constant across the lumen surface for all fiber mirror locations, and (3) the scaffold does not generate any background fluorescence (i.e., autofluorescence) as “noise.” In this ideal case, the fluorescent response assigned to each IP should be directly proportional to the brightness of the fluorophores within the corresponding IP. As a result, the image obtained through fluorescence mapping should accurately reflect the spatial distributions of fluorophores over the lumen.

This intuitive analysis also identifies three factors that may limit the performance of the fluorescence mapping method including: (1) the excitation spot may exceed the size of an IP; (2) the excitation light intensity may not remain constant over the luminal surface; and (3) the scaffold may generate autofluorescence that overwhelms the fluorescent signals produced by the fluorophores. The impacts of these three factors will be discussed in Sec. 3.

### 2.7 Excitation Spot Characterization

The intensity profile of the excitation spot was characterized using a control camera (XCD-X710, Sony, Japan) as depicted in Fig. 2(b). The camera lens was focused on the luminal surface of the phantom and pictures were taken of the excitation spot. After inserting the fiber mirror into the MIC, the excitation light was launched towards the lumen, producing a different spot profile at a given launching angle  $\theta$ , and then captured by the camera as an image. The results are described in Sec. 3.1.

### 2.8 Spectrum Measurement

The spectra of fluorescent signals as well as “noises” generated by scaffold or porcine skin autofluorescence were measured by replacing the EM-CCD camera with a spectrometer (USB2000, OceanOptics, Dunedin, FL). The imaging system remains the same otherwise.

### 2.9 Cell Culture Protocol

A human microvascular endothelium cell line (American Type Culture Collection (ATCC), Manassas, VA) labeled with enhanced GFP was used to demonstrate that our imaging method is suitable for *in vitro* and *in vivo* tissue engineering. All cells were cultured in Endothelial Growth Medium-2 (EGM-2) (Lonza Biomedical, Walkersville, MD). Before cell seeding, the scaffold with embedded MICs was sterilized using 70% ethanol for 30 min, followed by three sterile phosphate buffered saline (PBS) washes for 10 min each. The ECs were then suspended in 100  $\mu\text{L}$  of media and seeded onto the scaffold at a density of  $1 \times 10^4$  cells/cm<sup>2</sup>. The scaffold was then placed in the incubator for two hours to allow cell attachment and then was gently washed with PBS to remove any unattached cells.

## 3 Results

### 3.1 Excitation Spot Characterization

The spatial resolution of our imaging method is largely determined by the size of the excitation spot on the lumen. Therefore, it is important to quantify the properties of the excitation spot as a function of the fiber mirror launching angle  $\theta$ . The configuration described in Sec. 2.8 was used to obtain the results shown in Fig. 4(a)–4(c). The angle  $\theta$ , defined in Fig. 3(c), was swept from  $\theta$  equals to  $-50$  deg to  $+50$  deg in 1 deg increments on five different locations on the  $T$  axis. The characteristic data of the excitation spot presented in Fig. 4 shows both the average as well as the standard deviation of the five distinct  $T$  axis locations.

Figure 4(a) shows the full-width-half-maximum (FWHM) of the excitation spot size as a function of the launching angle  $\theta$ . Several intensity profiles of the excitation spot on the luminal surface are also shown in the figure as insets. It is clear that the FWHM increased as the launching angle deviated from  $\theta = 0$  deg. This phenomenon can be explained by the fact that at the angle of  $\theta = 0$  deg, excitation photons encountered the least number of scattering events as they traveled through the scaffold to the lumen. As the angle  $|\theta|$  increased, excitation photons traveled a longer distance to the lumen, thereby experiencing more scattering within the scaffold. As a result, the FWHM of the excitation spot increased as a function of the launching angle  $\theta$ . For the results in Fig. 4(a), the excitation spot FWHM was at  $21 \pm 0.8 \mu\text{m}$  at  $\theta = 0$  deg and increased by roughly 2.5 times to  $50 \pm 8.2 \mu\text{m}$  at  $\theta = \pm 50$  deg.

In Fig. 4(b), we show that the total intensity of the excitation spot decreased as  $|\theta|$  increased. The intensity value was calculated by summing all CCD camera pixel counts within the excitation spot [i.e., inset in Fig. 4(a)]. A possible explanation for this behavior is that at a larger launching angle  $|\theta|$ , the excitation photons traveled a longer distance, therefore experiencing more absorption before reaching scaffold lumen. Since the fluorescence response has a linear dependence on excitation light intensity, the fluorescence signals captured during fluorescence

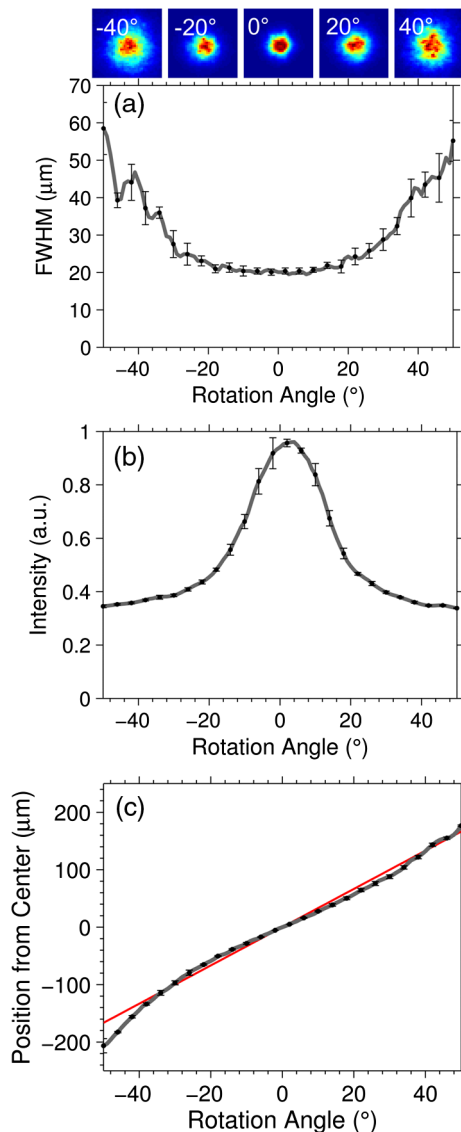


**Fig. 4** Excitation spot characterization. The plot lines are in 1 deg increments and the error is shown at every 4th point to prevent overcrowding. Error bars represent one std. dev. centered at the mean of the five trials. (a) The full-width-half-maximum of the excitation spot intensity profile on scaffold lumen is shown with respect to launching angle  $\theta$ . The insets depict the actual excitation spot profile with  $|\theta|$  equal to 0, 20, and 40 deg, respectively. (b) The intensity of the profile (summed pixels) shows a diminishing excitation spot strength at increasing angles  $|\theta|$ . (c) The excitation spot profile center position on the  $R$  axis is shown to behave nearly linearly with respect to  $|\theta|$ . From the results, we find that  $R(\theta) = 3.33 \times \theta$  based on a linear fit (red).

mapping must be renormalized as follows: At each  $|\theta|$  value, the magnitude of the fluorescent signal was boosted according to the curve in Fig. 4(b) so that the “renormalized” excitation intensity remains constant for all pixels.

Figure 4(c) shows that along the  $R$  axis, the center position of the excitation spot depends almost linearly on the fiber mirror launching angle  $\theta$ . Using a linear fit, we can relate the position of the excitation spot along the  $R$  axis versus the launching angle as  $R(\theta) = 3.33 \times \theta$ . This result indicates that for this phantom, the excitation spot can scan across a distance of 400  $\mu\text{m}$  (200  $\mu\text{m}$  on either side of  $\theta = 0$ ) on the lumen along the  $R$  axis, with a FWHM ranging from 21 to 50  $\mu\text{m}$ . The scanning range along the  $T$  axis is unlimited.

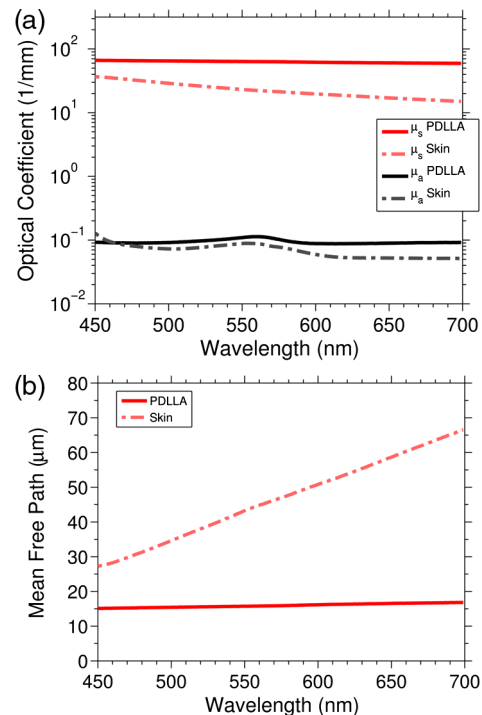


**Fig. 5** (a) The scattering coefficient ( $\mu_s$ ) of PDLLA is found to be roughly double that of porcine skin over the 450 to 700 nm range. The results also show that scattering events ( $\mu_s$ ) dominate over absorption events ( $\mu_a$ ) by more than two orders of magnitude. (b) The mean free path for PDLLA and for porcine skin.

### 3.2 Phantom Optical Properties

The optical properties of electrospun PDLLA and porcine skin (dermis and epidermis) were measured between 450 to 700 nm to determine their absorption and scattering coefficients  $\mu_a$  and  $\mu_s$ , respectively. Such values quantitatively indicate how strongly the medium absorbs and scatters light. In Fig. 5(a) we see that optical scattering is significantly stronger than optical absorption by more than two orders of magnitude. This result suggests that the resolution of optical imaging is primarily limited by optical scattering in highly turbid biological media.

Using Eq. (1) from Sec. 2.5, we can calculate the MFP of both the PDLLA and the porcine skin. The same anisotropy factor ( $g = 0.9$ ) for the  $\mu_a$  and  $\mu_s$  calculation was used to calculate the MFP, which translates to  $\text{TMFP} = 10 \times \text{MFP}$ .<sup>21</sup> Figure 5(b) shows that at the peak fluorophore emission wavelength (510 to 530 nm), the MFP is roughly 16  $\mu\text{m}$  for PDLLA and 37  $\mu\text{m}$  for porcine skin. Based on these values, the TMFP is 160  $\mu\text{m}$  for PDLLA and 370  $\mu\text{m}$  for porcine skin. We note that even for advanced modalities such as confocal and two-photon microscopes, the imaging depth is roughly limited to 1 to 2 photon TMFP,<sup>9,23,24</sup> which, in the case of our PDLLA scaffold and porcine skin phantom, is significantly less than their corresponding thickness:  $\sim 0.5$  mm for PDLLA scaffold and  $\sim 3$  mm for porcine skin.

### 3.3 Phantom Imaging Results

In testing the accuracy of our imaging method, we first captured a control image of the fluorescent microsphere distribution on the phantom lumen surface. As described in Sec. 2.1, the control image was obtained using a standard optical microscope setup to

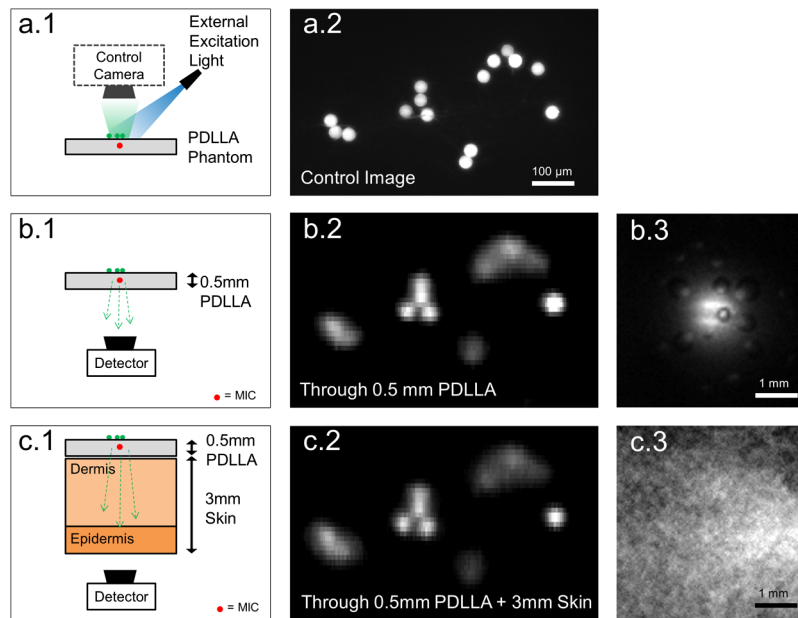


**Fig. 6** Results of fluorescence mapping. (a.1) A schematic showing how we obtain a direct-line-of-sight control image of the scaffold lumen. (a.2) An example of a control image. (b.1) Configuration for fluorescence mapping through the 0.5 mm thick PDLLA scaffold. (b.2) Mapping result through 0.5 mm PDLLA. (b.3) The spatial distribution of fluorescence signals on the bottom surface of the phantom, as captured by the EM-CCD camera. The fluorescent signals were generated by the same region of interest in (b.2) under illumination by the external excitation light. (c.1) Configuration for fluorescence mapping through the same 0.5 mm thick PDLLA scaffold and a piece of 3 mm thick porcine skin. (c.2) Results of fluorescence mapping through 0.5 mm PDLLA + 3 mm skin. (c.3) Fluorescence image on the bottom surface of the porcine skin as captured by the EM-CCD camera. We notice further “blurring” of the fluorescent signal in (c.3), yet the result of fluorescence mapping in (c.2) remain the same as the result in (b.2), which was obtained using only PDLLA scaffold.

provide an unobstructed, direct-line-of-sight, view of the luminal surface as illustrated in Fig. 6(a.1).

Prior to imaging, the sample was soaked with EGM-2. Next, the phantom was securely fastened on a glass slide. The slide with the phantom was then placed on the imaging platform and the fiber mirror was inserted into the MIC. Fiber scanning was carried out in the ROI that coincides with the control image shown in Fig. 6(a.2). After following the mapping procedure described in Sec. 2.7, we obtained the mapped image shown in Fig. 6(b.2). This configuration mimicked an *in vitro* environment of a bioengineered blood vessel with visual access to the outside surface of the vessel. When comparing the control image with the mapped image, we observe that the center position of each microsphere is in good agreement. Since the FWHM of the excitation spot is at times larger than the microsphere diameter, individual microspheres are blurred together.

Next, a 3-mm thick piece of porcine skin with an intact dermis and epidermis layer was placed under the phantom, thus further obstructing the lumen from the detector. This configuration is shown in the diagram of Fig. 6(c.1), which mimics an *in vivo* environment for a carotid artery imaging experiment. After the scanning algorithm was performed in the identical ROI, the fluorescence mapped image in Fig. 6(c.2) was produced. When comparing the fluorescence mapped image using the 0.5 mm PDLLA configuration versus the 0.5 mm PDLLA + 3 mm skin configuration, we observe that there is no significant degradation in image resolution. Therefore, the results in Fig. 6 directly demonstrate that the scanning-fiber-based method can decouple the link between imaging depth and image resolution. Fundamentally, this decoupling is due to the fact that our imaging system is not limited by the thickness of the turbid media between the lumen and the detector, but rather depends

on the signal-to-noise (SNR) of fluorescent signals. For a detailed analysis of SNR, refer to Sec. 3.5.

To compare how a standard fluorescence microscope performs in terms of resolution, we use the EM-CCD camera to capture fluorescence images on the bottom surface of the phantom, where the entire ROI on scaffold lumen was illuminated using an external excitation source. The images in Fig. 6(b.3) and Fig. 6(c.3) show the fluorescence response after traveling through 0.5 mm PDLLA and 0.5 mm PDLLA + 3 mm skin, respectively. Both images show that it is impossible to deduce the original microsphere distribution, and that adding additional turbid medium (porcine skin) causes a significant spread in the spatial distributions of fluorescent signals.

### 3.4 Imaging Resolution Analysis

We note that the result of fluorescence mapping can be modeled as a convolution of the control image with a point spread function (PSF), where the PSF describes the image “blurring” due to the finite size of the excitation spot. Mathematically, the spatial dimension of the PSF should correspond to the overall image resolution of our system.

Therefore, to quantify the overall image resolution of the fluorescence mapped image in Fig. 6, we carried out the following mathematical analysis. First, we convolved the control image with a variable-size Gaussian PSF. We note that the excitation spot profile can be closely approximated by a Gaussian PSF. By sweeping the FWHM of the Gaussian PSF from 0 to 50  $\mu\text{m}$ , we obtained various theoretically predicted fluorescence mapped images with an image resolution varying from 0 to 50  $\mu\text{m}$ . Then, the mean square error (MSE) was calculated between the theoretically predicted fluorescence mapped images

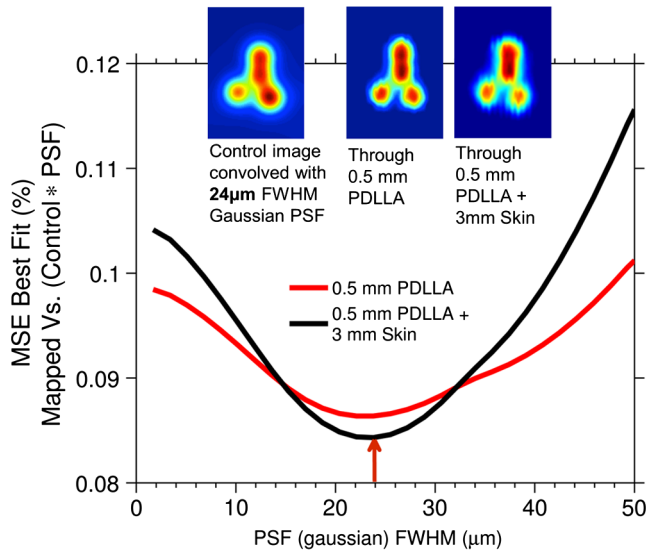


**Fig. 7** The resolution of the scanning-fiber-based method is modeled by convolving the control image with a variable Gaussian point spread function creating a theoretical mapped image. By finding the least mean square error of the difference between the theoretical and experimental results, we find the approximate resolution of the system. The result suggests that the imaging resolution is between 20 to 30  $\mu\text{m}$  at an imaging depth corresponding to 0.5 mm PDLLA plus 3 mm porcine skin.

versus the actual mapped images [i.e., the results shown in Fig. 6(b.2) or Fig. 6(c.2)]. The percentage of MSE versus the FWHM of the Gaussian PSF is plotted in Fig. 7, which shows that the smallest MSE occurs at around a 24  $\mu\text{m}$  FWHM for both with or without additional porcine skin. This matches very well with the experimental results shown at in Fig. 4(a) from  $|\theta| \sim 0$  to 30  $\mu\text{m}$ . The inserts in Fig. 7 show the experimental mapped images (through 0.5 mm PDLLA or 0.5 mm PDLLA + 3 mm skin) as well as the theoretically predicted image using a 24  $\mu\text{m}$  FWHM Gaussian PSF. With the result in Fig. 7, we conclude that the resolution of our imaging system can reach the level of 20 to 30  $\mu\text{m}$  with an imaging depth corresponding to 0.5 mm PDLLA scaffold plus 3 mm porcine skin.

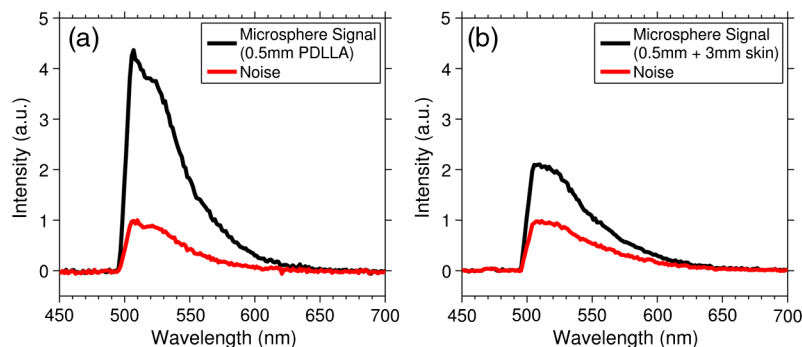


**Fig. 8** Spectral responses of microsphere signals as well as autofluorescence noises. The microsphere signal was obtained by centering the excitation spot on a single microsphere placed on the phantom lumen. The autofluorescence noise was obtained by moving the excitation spot to a location on the lumen that was free of microspheres. The signal-to-noise (SNR) is calculated as the microsphere signal divided by the autofluorescence. (a) The SNR through 0.5 mm PDLLA is around four between 510 to 545 nm. (b) The SNR through 0.5 mm PDLLA + 3 mm porcine skin is around two between 510 to 545 nm.

### 3.5 Signal Versus Noise

Figure 8 shows the spectral components of the fluorescent signals and noises generated by the microspheres and the two phantoms, respectively. These results were obtained by replacing the EM-CCD camera with a spectrometer. Specifically, the microsphere signal was measured by positioning the excitation spot to the center of a single standing microsphere and capturing the fluorescence emission spectrum. Then, we applied the same procedure to characterize noises generated by the optical phantoms. To ensure that only “noise” was captured by the spectrometer, we positioned the excitation spot on a luminal surface location that was void of any microspheres. (We used the control camera to ensure no fluorescent microspheres exist within the excitation spot.) The results are shown in Fig. 8, where we normalized the intensity of all emission spectra such that the peaks of the spectral noise were set to be one.

We define the SNR of the imaging system as the ratio between the microsphere signal and the background noise. For the 0.5 mm PDLLA experiment, the SNR is around 4 in the 510 to 540 nm range. After adding the 3-mm thick skin, the SNR dropped to two. Although a SNR of two is relatively small, it is sufficient to separate the signal from the noise to obtain the fluorescence mapped image in Fig. 6(c.2). However, if we place a thicker tissue between the phantom and the detector such that the SNR approaches unity, it would be very difficult to separate the microsphere signals from background “noises” generated by the scaffold as well as the surrounding tissue.

The results in Fig. 8 suggest that the main limitation on fluorescence mapping lies in making sure the intensity of fluorescence signals is greater than the background noise. In other words, the spatial profile of the fluorescent signal captured on the exterior surface of the scaffold or porcine skin plays no role in fluorescence mapping—only the total strength of the fluorescent signal does. More specifically, after adding the porcine skin, the fluorescence light was distributed within a much wider spatial region [Fig. 6(c.3)] compared to the case without any porcine skin [Fig. 6(b.3)]. Yet the images obtained through fluorescence mapping did not show any significant difference. Consider the following two observations: (1) for most biological tissues, optical scattering significantly exceeds optical absorption as shown in Fig. 5, and (2) the

primary impact of photon scattering is the blurring of the fluorescent signal without significantly changing its total strength. With these considerations, it is clear that the resolution is no longer limited by the scattering of the fluorescent signal. As a result, the imaging resolution of the scanning-fiber-based method is largely “decoupled” from the total imaging depth.

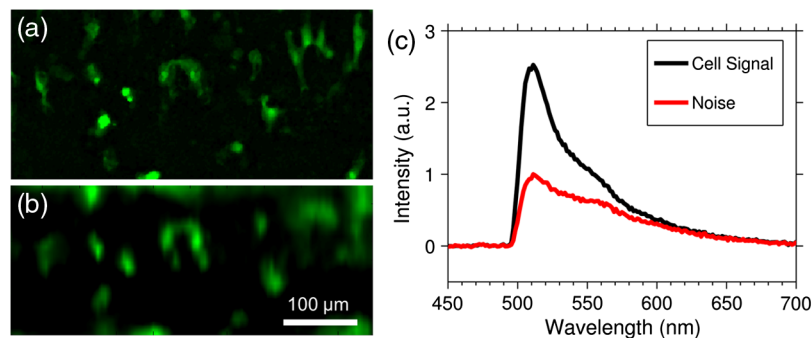
### 3.6 Endothelial Cell Imaging

Figure 9(a) shows the direct-line-of-sight control image of the GFP-labeled ECs on PDLLA scaffold lumen. The same ROI was then used for fiber scanning followed by fluorescence mapping. Following the process described in Secs. 2.7 and 3.5, we obtained the fluorescence mapped image shown in Fig. 9(b). Comparing the mapped image to the control image, it is clear that the spatial distribution of ECs obtained through fluorescence mapping is in good agreement with the control image. This result confirms that the scanning-fiber-based method can image through a 0.5-mm thick tissue scaffold and reveal the spatial distribution of ECs with single-cell-level resolution. Figure 9(c) shows that the SNR of a single GFP-labeled EC is around two for the 0.5 mm thick PDLLA phantom, which also confirms the reliability of our fluorescence mapping results.

## 4 Discussion

Due to significant photon scattering in turbid biological tissues, a major challenge in biophotonics is the conflict between imaging depth and imaging resolution. Even in the case of photoacoustic imaging, the resolution remains closely linked with imaging depth, where one can realize a spatial resolution of  $>50 \mu\text{m}$  within a depth of three photon TMFP.<sup>11,12</sup> In contrast with other imaging modalities, the method developed here can largely “decouple” the link between imaging depth and imaging resolution. The resolution of our imaging method is essentially determined by the distance between the MIC and the ROI and not by the entire thickness of the scaffold/tissue as demonstrated in Fig. 6. In principle, if system noise is sufficiently small compared with the signal strength generated by the fluorophore, we can maintain single-cell-level imaging resolution at a depth that exceeds the photon TFMP by at least one order of magnitude. In fact, using fluorescent microspheres as sources, we have shown that our imaging method is capable of achieving 20 to 30  $\mu\text{m}$  imaging resolution at an imaging depth exceeding 10 photon TMFPs (0.5 mm thick PDLLA scaffold plus three mm thick porcine skin).

The proper functioning of the imaging method presented here requires that the system signal should be stronger than the noise. This requirement makes intuitive sense: if the fluorescence response of the detector does not change regardless of whether the excitation spot coincides with the fluorophore or not, then it would be very difficult to apply the fluorescence mapping procedure to reconstruct the fluorophore distribution. Given this observation, it is worthwhile to consider several potential sources for system noise. First, we note that the spatial distribution of an excitation spot extends beyond its FWHM. Thus, during noise measurements, even though we moved the excitation spot away from any of the microspheres on the luminal surface, a small portion of the excitation light might overlap with microspheres and contribute towards the noise spectra in Fig. 8. However, noise generated by this effect should not depend significantly on the total thickness of the phantom and therefore cannot explain the reduction in system SNR after adding the porcine skin. Next, we note that during the fiber scanning process, the excitation light was directed towards the luminal surface which generates scaffold autofluorescence along the propagation path. However, the autofluorescence generated by such forward propagating excitation light would only depend on the distance between the MIC and the ROI on the luminal surface, which again is independent of the total phantom thickness. Therefore, to account for the SNR reduction observed between Fig. 8(a) and 8(b), we have to consider the fact that a small portion of the excitation light back-reflects from the luminal surface and propagates towards the exterior surface as illustrated in Fig. 10. After adding the 3-mm thick porcine skin, such back propagating excitation light would induce additional autofluorescence from the porcine skin, which would reduce the overall system SNR. In fact, many effects may induce such back-propagating light. Several examples are the Fresnel reflection at the air/MIC interface, photon scattering at the interface of the MIC and the PDLLA scaffold, and light back-scattering within the turbid PDLLA scaffold, i.e., similar to what occurs in optical coherence tomography. As discussed in Sec. 3.4, the resolution of our imaging system is closely linked to the FWHM of the excitation spot on the luminal surface. The size of the excitation spot is in turn determined by the scaffold optical property as well as the distance between the MIC and the luminal surface, both of which are largely independent of the total phantom thickness. Therefore, as long as the FWHM of the excitation light remains the same and the system SNR is sufficiently large ( $\sim 2$  or higher), the resolution of the fluorescence mapped



**Fig. 9** (a) Control image showing the actual endothelial cell (EC) distribution on scaffold lumen. (b) A fluorescence mapped image of EC distribution that corresponds to the image in (a). Comparison between the control image and the fluorescence mapped image indicates that our method can “see” through a 0.5 mm thick PDLLA scaffold with single-cell-level resolution. (c) signal-to-noise measurement for a single green fluorescent protein (GFP)-labeled EC on scaffold lumen. The SNR is around two for a 0.5 mm thick PDLLA phantom.

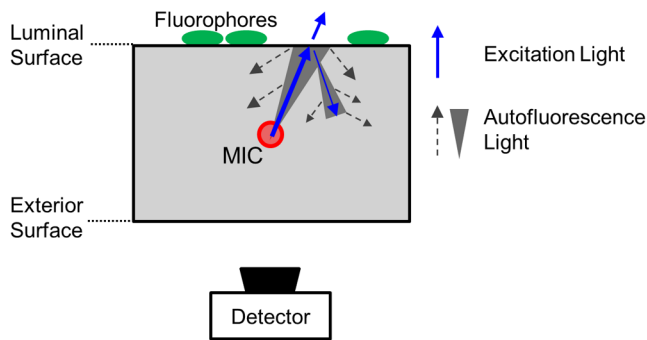


**Fig. 10** A schematic showing the potential sources for imaging system noise.

images should not depend critically on the overall thickness of the optical phantom, as can be seen from Fig. 6.

We note that the scanning-fiber-based method is well suited for tissue engineering applications. For example, the process of scaffold fabrication—a necessary step in tissue engineering—can be easily modified for embedding MICs. With proper design, we can essentially place an MIC anywhere within the tissue scaffold. Therefore, once an ROI is selected (e.g., lumen in the case of vessel engineering), we can place the MIC in close proximity to the ROI to achieve single-cell-level resolution. Secondly, since fluorescence mapping only requires total fluorescence intensity, we do not require a high numerical aperture objective lens. As a result, our imaging system can provide more than 10 cm in working distance, which is more than sufficient for the geometrical constraints imposed by most bioreactors currently in use. We point out that this practical constraint is actually very stringent in tissue engineering practices. For example, most of the commercial two-photon microscopes require focusing excitation light within a sub- $\mu\text{m}$  spot, which can only be achieved by using high numerical aperture objectives.<sup>23</sup> Such a high numerical aperture, however, generally leads to a much shorter working distance, which makes it cumbersome to integrate a functional bioreactor with a commercial two-photon or confocal microscope. A few recent examples of these types of work can be found.<sup>25,26</sup> We point out that the systems described in both references are very complex. Such complexity is mainly due to the conflict between the large geometrical dimension of a functional bioreactor and the extremely short working distance of a confocal or a two-photon microscope.

In the future, we plan to utilize the imaging method developed here for other tissue engineering studies. We are currently combining the imaging instruments with a pulsatile fluid flow bioreactor for blood vessel bioengineering studies. For such *in vitro* applications, the capability of performing non-destructive and single-cell-level imaging has a significant advantage: since we no longer need to remove the vessel from the bioreactor and subject it to frequent dissection and histological analyses, we can dynamically monitor how ECs proliferate, migrate, and respond to external stimuli such as fluid shear stress and pulsation. Given the high optical scattering within the scaffold and the geometrical constraints of the bioreactor, such a study has yet to be carried out in tissue engineering.<sup>14</sup> As a result, some of the most critical questions in tissue engineering, such as cell-cell interaction, cell-scaffold interaction, and the mechanism of neovascularization, remain not well understood. The main limitation of our method is the underlying assumption that

fluorescent-labeled cells are distributed over a 2-D surface. However, for studies involving ECs, this assumption is indeed valid and should not pose any problems. With appropriate modifications, we can potentially apply the method developed here to monitor the preconditioning of other hollow cavity tissues such as bladder, trachea, or colon, where epithelial cells play an important role in the biologically complex process of tissue regeneration.

The experimental results in this paper (Figs. 6–9) suggests that as long as the fluorescent signal is significantly stronger than scaffold autofluorescence, the resolution of our imaging system does not depend critically on system SNR and does not degrade significantly as the imaging depth increases. For example, fluorescence mapped images in Fig. 6 have almost identical image resolution despite the fact that their SNRs are quite different. Our result and analysis indicate that in order to achieve maximal imaging depth, which is very important for future *in vivo* studies, we should select a fluorophore whose emission spectrum has minimal overlap with scaffold or tissue autofluorescence. Given the spectral data in Fig. 9(b), it is clear that using a biomarker such as near-infrared quantum dots (QDs) with emission peak above 650 nm would be ideal. Such QDs can be excited by the blue laser (473 nm) used in this work. Due to the very weak autofluorescence noise at the excitation wavelength of 473 nm, we should be able to further improve imaging depth to be greater than three mm while maintaining 20 to 30  $\mu\text{m}$  image resolution. The fluorophores we used in this study unfortunately have significant spectral overlap with scaffold autofluorescence. Consequently, it is very difficult to precisely determine how much of the system noise is generated by the fluorophores and how much is caused by scaffold autofluorescence. Using the QD-labeled ECs may also enable us to more accurately quantify the behaviors of system SNRs under different tissue/scaffold thicknesses.

## 5 Conclusion

We have developed a scanning-fiber-based imaging method that can perform deep-tissue imaging with single-cell-level resolution. Our method is based on directly embedding one or more hollow core fibers within a tissue scaffold as MICs. By inserting fiber micro-mirrors into the MICs, we can locally deliver excitation light towards a specific ROI and excite the fluorophores contained within. After collecting fluorescent signals and mapping them onto a digital grid based on fiber micro-mirror location, we can reconstruct the spatial distribution of the fluorophores within the ROI. Using an optical phantom composed of fluorescent microspheres, a 500- $\mu\text{m}$  thick tissue scaffold, and a 3-mm thick porcine skin, we have demonstrated the decoupling between imaging depth and imaging resolution. Specifically, we have shown that the resolution of our fluorescence mapping results does not degrade even after we introduce the additional 3-mm thick porcine skin to the total imaging depth. As a result, we have achieved 20 to 30  $\mu\text{m}$  resolution at an imaging depth of more than 10 photon TMFPs. Finally, we have shown that we can spatially resolve single GFP-labeled ECs through a 500  $\mu\text{m}$  thick scaffold with a photon TMFP of 170  $\mu\text{m}$ .

## Acknowledgments

We would like to thank Dr. Joseph Freeman in the Department of Biomedical Engineering at Rutgers University for his advice on scaffold sintering. This research was funded by a grant from

the National Institutes of Health (NIBIB, HL098912), the National Science Foundation (CBET 0955072), and the Institute for Critical Technology and Applied Science (Holey Scaffolds, Virginia Tech).

## References

1. A. Atala et al., "Tissue-engineered autologous bladders for patients needing cystoplasty," *The Lancet* **367**(9518), 1241–1246 (2006).
2. C. T. Laurencin and J. W. Freeman, "Ligament tissue engineering: an evolutionary materials science approach," *Biomaterials* **26**(36), 7530–7536 (2005).
3. A. Raya-Rivera et al., "Tissue-engineered autologous urethras for patients who need reconstruction: an observational study," *The Lancet* **377**(9772), 1175–1182 (2011).
4. S. Petit-Zeman, "Regenerative medicine," *Nat. Biotechnol.* **19**(3), 201–206 (2001).
5. R. M. Nerem and A. Sambanis, "Tissue engineering: from biology to biological substitutes," *Tissue Eng.* **1**(1), 3–13 (1995).
6. N. D. Evans and M. M. Stevens, "Complexity in biomaterials for tissue engineering," *Nat. Mater.* **8**(6), 457–470 (2009).
7. M. P. Lutolf and J. A. Hubbell, "Synthetic biomaterials as instructive extracellular microenvironments for morphogenesis in tissue engineering," *Nat. Biotechnol.* **23**(1), 47–55 (2005).
8. L. G. Griffith and G. Naughton, "Tissue engineering—current challenges and expanding opportunities," *Science* **295**(5557), 1009–1014 (2002).
9. V. Ntziachristos, "Going deeper than microscopy: the optical imaging frontier in biology," *Nat. Meth.* **7**(8), 603–614 (2010).
10. D. J. Stephens and V. J. Allan, "Light microscopy techniques for live cell imaging," *Science* **300**(5616), 82–86 (2003).
11. H. F. Zhang et al., "Functional photoacoustic microscopy for high-resolution and noninvasive in vivo imaging," *Nat. Biotechnol.* **24**(7), 848–851 (2006).
12. V. Ntziachristos et al., "Fluorescence molecular tomography resolves protease activity in vivo," *Nat. Med.* **8**(7), 757–761 (2002).
13. J. Stitzel et al., "Controlled fabrication of a biological vascular substitute," *Biomaterials* **27**(7), 1088–1094 (2006).
14. S. J. Lee et al., "In vitro evaluation of electrospun nanofiber scaffolds for vascular graft application," *J. Biomed. Mater. Res. Part A* **83**(4), 999–1008 (2007).
15. S. Kaushal et al., "Functional small diameter neovessels using endothelial progenitor cells expanded ex vivo," *Nat. Med.* **7**(9), 1035–1040 (2001).
16. S. J. Lee et al., "Development of a composite vascular scaffolding system that withstands physiological vascular conditions," *Biomaterials* **29**(19), 2891–2898 (2008).
17. B. W. Tillman et al., "The in vivo stability of electrospun polycaprolactone-collagen scaffolds in vascular reconstruction," *Biomaterials* **30**(4), 583–588 (2009).
18. T. Shinoka et al., "Creation of viable pulmonary artery autografts through tissue engineering," *J. Thorac. Cardiovasc. Surg.* **115**(3), 536–546 (1998).
19. Q. P. Pham, U. Sharma, and A. G. Mikos, "Electrospinning of polymeric nanofibers for tissue engineering applications: a review," *Tissue Eng.* **12**(5), 1197–1211 (2006).
20. L. D. Wright et al., "Fabrication and mechanical characterization of 3D electrospun scaffolds for tissue engineering," *Biomed. Mater.* **5**(5), 055006 (2010).
21. S. A. Prael, M. J. C. van Gemert, and A. J. Welch, "Determining the optical properties of turbid media by using the adding, Åidoubling method," *Appl. Opt.* **32**(4), 559–568 (1993).
22. W. F. Cheong, S. A. Prael, and A. J. Welch, "A review of the optical properties of biological tissues," *IEEE J. Quantum Elect.* **26**(12), 2166–2185 (1990).
23. F. Helmchen and W. Denk, "Deep tissue two-photon microscopy," *Nat. Meth.* **2**(12), 932–940 (2005).
24. T. D. Wang et al., "Confocal fluorescence microscope with dual-axis architecture and biaxial postobjective scanning," *J. Biomed. Opt.* **9**, 735–742 (2004).
25. J. A. Kluge et al., "Bioreactor system using noninvasive imaging and mechanical stretch for biomaterial screening," *Ann. Biomed. Eng.* **39**(5), 1390–1402 (2011).
26. L. E. Niklason et al., "Enabling tools for engineering collagenous tissues integrating bioreactors, intravital imaging, and biomechanical modeling," *Proc. Natl. Acad. Sci.* **107**(8), 3335–3339 (2010).

## **Appendix C: Real time imaging and characterization of bioengineered blood vessels within a bioreactor using OCT**

Abhijit A. Gurjarpadhye<sup>1</sup>, MS, Bryce M. Whited<sup>1</sup>, MS, Guoguang Niu<sup>2</sup>, PhD, Kriti Sen Sharma<sup>3</sup>, William C. Vogt<sup>1</sup>, Ge Wang<sup>1,3</sup>, PhD, Yong Xu<sup>1</sup>, PhD, Shay Soker<sup>2</sup>, PhD, M Nichole Rylander<sup>1</sup>, PhD and Christopher G. Rylander<sup>1</sup>, PhD.

<sup>1</sup>School of Biomedical Engineering and Sciences, Virginia Tech – Wake Forest University, Blacksburg, VA 24061

<sup>2</sup>Wake-Forest Institute for Regenerative Medicine, Wake-Forest University, Winston-Salem, NC 27157

<sup>3</sup>Department of Electrical Engineering, Virginia Polytechnic Institute and State University, Blacksburg VA 24061, USA

### **C.1 Abstract**

#### Background and Objective:

Regenerative medicine involves the bioengineering of a functional tissue or organ by seeding living cells in a biodegradable scaffold cultured in a bioreactor. A major barrier to creating functional tissues, however, has been the inability to monitor the dynamic and complex process of scaffold maturation in real-time, making control and optimization extremely difficult. Current methods to assess maturation of bioengineered constructs, such as histology or organ bath physiology, are sample-destructive. Optical Coherence Tomography (OCT) has recently emerged as a key modality for structural assessment of native blood vessels, as well as engineered vessel mimics. The objective of this study is to monitor and assess in real time the development of bioengineered blood vessels using both free space as well as catheter-based OCT imaging in a novel quartz based bioreactor. Development of the blood vessel was characterized by changes in thickness and scattering coefficient over a 30-day period.

#### Materials and Methods:

We constructed a novel blood vessel bioreactor utilizing a rotating quartz cuvette permitting free-space OCT imaging of the vessel's outer surface. A vascular endoscopic OCT catheter was used for imaging the lumen of the vessels. The quartz cuvette permits free-space OCT imaging of the blood vessel over 360 degrees. Bioengineered blood vessels were fabricated using biodegradable polymers (15% PCL/collagen, ~200 micron thick) and seeded with CH3 10t1/2 mesenchymal cells. A swept-source OCT imaging system comprised of a 20 kHz tunable laser (Santec HSL2000) with 1300 nm central wavelength and 110nm FWHM bandwidth was used to assess the vessels. OCT images were obtained at day 1, 4, 7, 14, 21 and 30. Free-space OCT images were co-registered with endoscopic OCT images to determine the vessel wall thickness. DAPI-stained histological sections of vessels were imaged at the same time points to visualize cellular infiltration and wall thickness measurements. Non-linear curve fitting of free-space OCT data to the extended Huygen-Fresnel model was performed to determine optical scattering properties.

#### Results:

The vessel wall thickness increased from  $435 \pm 15 \mu\text{m}$  to  $610 \pm 27 \mu\text{m}$  and the scattering coefficient increased from  $3.73 \pm 0.32 \text{cm}^{-1}$  to  $5.74 \pm 0.06 \text{cm}^{-1}$  over 30 days. Histological studies showed cell migration from the scaffold surface toward the lumen and cell proliferation over the same time course.

#### Conclusions:

This study suggests that combination of free-space and catheter based OCT for blood vessel imaging provides accurate structural information of the developing blood vessel. In this study we determined that free-space OCT images could be co-registered with catheter-based OCT images to monitor structural features such as wall thickness or delamination of the developing tissue-engineered blood vessel within a bioreactor. Structural as well as optical properties obtained from OCT imaging correlate with histological sections of the blood vessel and could potentially be used as markers to non-invasively assess regeneration of the vessel. This novel method of OCT imaging and analysis could potentially be utilized to study development and tissue structure of bioengineered tissue in real time non-invasively.

## **C.2 Introduction**

Cardiovascular disease is a leading cause of morbidity and mortality worldwide, according to the World Health Organization [140]. Atherosclerosis, one of the most severe forms of vascular disease, involves the narrowing of the vessel lumen due to plaque buildup. In its advanced stages, atherosclerosis of the coronary artery may cause myocardial infarction. This vascular condition is commonly treated with a coronary artery bypass graft, in which a healthy native blood vessel from the patient's own body (saphenous vein or brachial artery) is used to create a bypass around the atherosclerotic region. However, harvesting healthy blood vessels is less than desirable and in some cases not possible due to concomitant disease or previous use [141]. Additionally, graft vessels with smaller diameter (typically <5mm) are also subject to high blood flow and therefore pose the risk of failure through thrombosis or intimal hyperplasia.

The field of vascular tissue engineering has emerged as a key technology for bypass grafting and replacement of damaged or diseased blood vessels. Bioengineering of vascular grafts involves fabrication of biocompatible and biodegradable vessels from synthetic or natural materials and subsequent seeding with vascular cells [142]. However, despite the great potential to “manufacture” histocompatible blood vessels, and other tissue/organs, regenerative medicine faces some key challenges such as monitoring the dynamic and complex biological process of tissue regeneration in real-time, which makes control and optimization extremely difficult. Histology, the gold standard used for assessment of tissue structure and composition, is a static technique that only provides a “snapshot” of the specimen at a single time point and requires that the specimen be sacrificed. This inefficiency severely limits our understanding of the biological processes associated with tissue growth during the *in vitro* pre-conditioning phase.

Optical Coherence Tomography (OCT) enables imaging of cross sectional structures in biological tissues by measuring the echo time delay of backreflected light. This imaging modality has recently been utilized in imaging native physiological and pathological blood vessels [143, 144] as well as in imaging of bioengineered blood vessel mimics [145] because of the high resolution it offers. However these studies implement a catheter-based system for imaging the vessel lumen and due to limited penetration are unable to assess the full thickness of the vessels. Therefore, a more advanced imaging method is needed to provide full-thickness images of blood vessels.

In this study, we developed a novel bioreactor that provides an imaging window for exterior imaging of the tissue-engineered blood vessels (TEBV) using free-space OCT imaging

as well as capability for endoscopic imaging. Co-registration of the exterior OCT images with catheter-based OCT imaging provides full thickness imaging of the vessel within the bioreactor over 30 days. OCT images were analyzed to provide the optical scattering coefficient over the same time period. Histological sections of identically cultured TEBV specimens were analyzed for wall thickness and cell migration/proliferation to compare to OCT images of maturing vessels, which were acquired noninvasively.

### **C.3 Materials and Methods**

Electrospun vascular scaffolds made from a composite of poly ( $\epsilon$ -caprolactone) (PCL) and type I collagen have been shown to be suitable for developing TEBVs for implantation in animal model [17, 36]. We developed TEBVs using PCL/Collagen-based scaffolds seeded with multipotent stem cells. The scaffolds were placed in a novel quartz-based bioreactor that provides a clear imaging window for free-space OCT imaging of the developing TEBVs. We used our custom-built swept-source OCT system described previously [146], for imaging of tissue-engineered blood vessels within the bioreactor. We also developed LabVIEW® and MATLAB®-based algorithms for image acquisition and post-processing for image remapping and 3D rendering. The vessel exteriors were imaged using free-space OCT while the catheter-based OCT provided luminal images. 3D models were created after obtaining multiple slices and were co-registered using specific landmarks created on the vessel holders in the bioreactors. The vessels were imaged and their geometrical and optical properties were measured at various time points.

#### **C.3.1 Tissue-Engineered Blood Vessels**

Bioengineered blood vessel scaffolds were fabricated from PCL/Collagen. Vascular scaffolds made of this material have mechanical properties similar to those of native blood vessels [95] and have been shown to be suitable for developing TEBVs for implantation in animal model [17, 36]. Scaffolds were fabricated from a blended solution, composed of PCL and collagen with a weight ratio of 1:1 in 1,1,1,3,3,3-hexafluoro-2-propanol (HFP) with a concentration of 15 % w/v. Electrospinning was conducted using a typical setup, including a high voltage power supply (Spellman High Voltage, Hauppauge, NY), a syringe pump (Medfusion 2001, Medex, Inc., Carlsbad, CA) and a rotating mandrel (Custom Design &

Fabrication, Richmond, VA - 4.8 mm diameter and 12.5 mm length) with a rotating rate of approximately 1000 rpm. The flow rate of solution, the applied voltage, and the distance between needle tip and mandrel were set to 10.0mL/h, 25kV, and 30cm respectively. Electrospun scaffolds were cross-linked by placing them over a 2.5% glutaraldehyde (GA) solution for 6 h at room temperature. Afterwards, the cross-linked scaffolds were rinsed with DI-water to remove the residue GA, and dried through lyophilization.

The scaffolds (length = 8cm, OD=5mm, wall thickness = 200-300  $\mu$ m) were first mounted over a thin fluorinated ethylene propylene (FEP) tube (OD=3mm) and both ends were then glued to the outer surface of the tube using medical-grade silicone adhesive (Figure 1). This sample configuration ensured that the scaffolds remained patent during imaging experiments and guaranteed that the cells were seeded only on the outer surface of the scaffold. This structure was sterilized using 70% ethanol and washed with sterile PBS. The scaffold was then seeded with CH3 10t1/2 pluripotent mesenchymal cells (American Type Culture Collection – ATCC) at a cellular density of 500,000 cells per ml. A small segment (~1 cm) of silicone tube was used to create a bridge between the dispensing needle and the FEP tube, as demonstrated in the schematic (Figure C.1). Additionally, a non-cellularized (control) scaffold was kept immersed in media for the duration of the study and was imaged along with the cellularized TEBV.

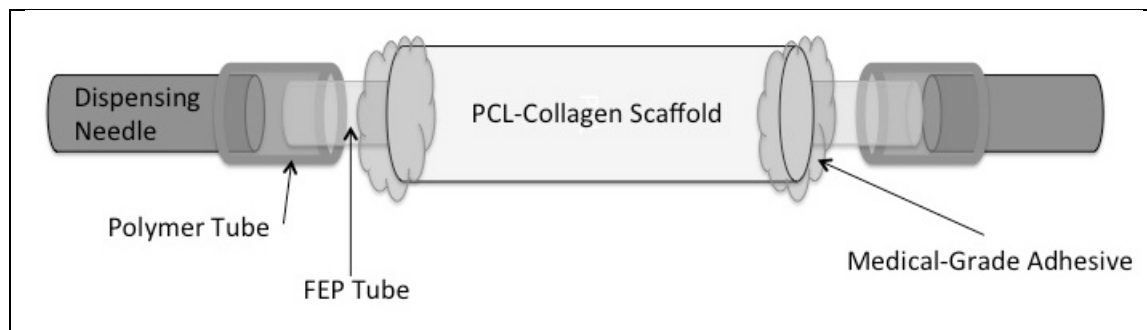
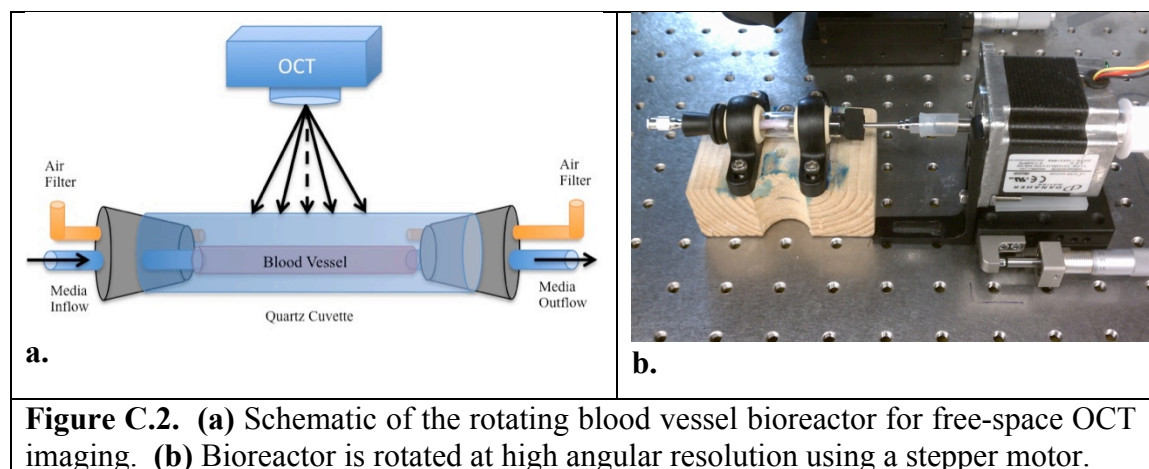


**Figure C.1.** Schematic of the PCL-Collagen scaffold mounted within the bioreactor. The FEP tube provides mechanical support for the scaffold and ensures its patency.

### C.3.2 Bioreactor Design

The development of a multi-imaging modality to study the growth of a bioengineered blood vessel requires a bioreactor suitable for OCT imaging of the vessel, in addition to providing a biologically active and sterile environment for seeded cells.



OCT imaging of a blood vessel in free-space requires an imaging window on the bioreactor. Due to its high absorption in the IR range, normal glass such as borosilicate can attenuate the OCT signal. Quartz offers a better alternative owing to its low absorption coefficient within the same spectral range. A bioreactor using quartz cuvette was created to house the vessel and to facilitate OCT imaging. Figure C.2a represents a schematic of the quartz bioreactor, which provides a sterile environment for the bioengineered blood vessel and functions as an imaging window for free-space OCT scanning. The cylindrical quartz cuvette allows for vessel scanning over 360°. Large bore stainless steel needles were used to mechanically support the blood vessel inside the bioreactor such that the vessel will be held in the center of the cuvette, and to provide growth media to the cells. Sterilizable rubber stoppers were used to seal both the ends of the cuvette. The bioreactor was mounted in two bearings and rotated at the desired speed and angular steps using a high-precision stepper motor (T21NRLH-LDN-NS-00, National Instruments), as shown in Figure C.2b.

### C.3.3 Swept-Source OCT

A high-speed custom-built SS-OCT system was used, which is comprised of a swept laser source (HSL-2000, Santec Corp., Hackensack, NJ) that provides ~110nm wavelength scan range around 1300 nm central wavelength at a scan rate of 20 kHz. This system offers an axial (in-depth) resolution of ~13  $\mu$ m in air. OCT catheter (Volcano Corporation) was used for catheter-based OCT of the TEBV through its lumen.

### C.3.4 OCT Image Acquisition

The TEBVs within the bioreactor were imaged using free-space OCT as well as catheter-based OCT. The tissue-engineered blood vessels were imaged prior to cell-seeding and then on days 1, 4, 7, 14, 21 and 30. The bioreactor is rotated using a stepper motor (T21NRLH-LDN-NS-00, National Instruments), with respect to a laterally moving point source in free-space OCT. The catheter as well as fiber-optic rotary joint (FORJ, MJP-131-28-FA, Princetel, Inc. Hamilton NJ 08619) rotates inside the lumen of the TEBV, which is translated laterally using linear translation stage (Newport UTM100CC.1, Newport Corp.) for catheter-based imaging. Segments of the TEBV were scanned in spiral pattern and the data was further processed and transformed into polar coordinates to produce a series of 2D cross-sectional OCT images. The image acquisition and processing codes were written in LabVIEW®. For catheter-based OCT imaging, a reference image was acquired at each time point to record the baseline, which was then removed from each catheter-based OCT image of the TEBVs using background subtraction.

### C.3.5 Resolution

Collimated OCT beam was focused on the specimen using a 35 mm plano-convex lens (AC254-035-C-ML, Thorlabs). Beam spot size was calculated to be 25  $\mu\text{m}$ . Typically, 160,000 A-scans were acquired helically per vessel segment of 1000  $\mu\text{m}$ . Each B-scan, comprising 4000 A-scans represented one 2D cross-section of the vessel, offered an angular resolution of  $0.09^\circ$  or  $\sim 400\mu\text{m}$  on the surface of the vessel. 40 slices were acquired over 1000 $\mu\text{m}$  length offering 25 $\mu\text{m}$  lateral resolution matching the beam spot size. Axial resolution is dependent on the laser source center wavelength and bandwidth and was calculated to be 13 $\mu\text{m}$  in air.

### C.3.6 Scaffold Thickness

Large-bore needles and polymer tubes that hold the two ends of the TEBV were visible in the exterior and interior OCT imaging and thus served as landmarks for image registration. 3D models created using multiple 2D slices from exterior and interior OCT were overlapped to create a full-thickness 3D model of the TEBV. Five 2D slices of this model were randomly chosen and within each slice, the wall thickness was assessed at ten sites along the circumference of the section, as shown in Figure C.3. Average wall thickness was determined by first calculating the average thickness for each of the five sections.

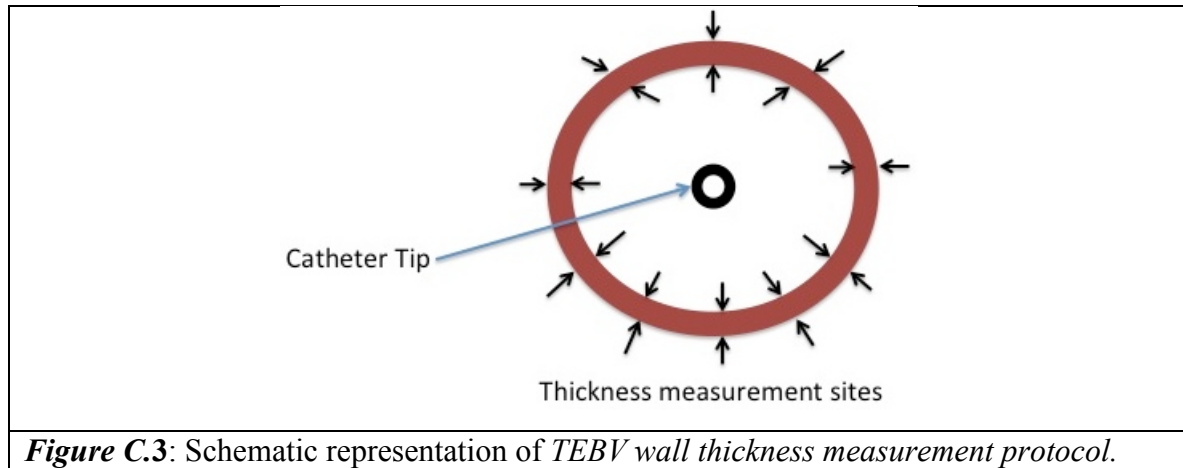


**Figure C.3:** Schematic representation of *TEBV* wall thickness measurement protocol.

### C.3.7 Scattering Coefficient

Thrane *et al* [147] developed a model that analyzes the heterodyne OCT signal as a function of depth. This model accounts for multiple scattering effects based on the extended Huygen-Fresnel principle (EHF) [148], and thus the depth profile of OCT is a function of scattering coefficient ( $\mu_s$ ) and  $g$  of the specimen. Five 2D slices of the TEBV were chosen randomly and all 4000 A-scans were averaged within each slice to obtain an average A-scan profile. A MATLAB®-based non-linear curve-fitting algorithm was used to fit this profile data to the model in order to extract  $\mu_s$  for each slice.

#### Histology:

A small segment of the developing bioengineered blood vessel cultured separately was sectioned for histological evaluation on D1, 4, 7, 14, 21 and 30. After embedding the scaffolds in the optimal cutting temperature compound (O.C.T. compound, Tissue-Tek), 13  $\mu$  m thick histological cross sections were cut with a Microm HM 550 (Microm, Waldorf, Germany) and stained with DAPI (Vector Laboratories, Burlingame, CA) to visualize cell nuclei [149]. A Leica MI6000-B microscope (Leica, Wetzlar, Germany) with 10X objective was used to obtain both polarized bright field and fluorescent images of the scaffolds. The brightness, gain, and exposure were held constant for all images. Histological images were also used to perform thickness measurements for comparing with OCT-based thickness results.

## C.4 Results

### C.4.1 OCT Imaging

The TEBVs were imaged prior to their cellularization, and then on day 1, 4, 7, 14, 21 and 30. Structures supporting the scaffolds, such as the dispensing needles and polymer tubes were visible in the OCT images and were used for co-registration of OCT images obtained from

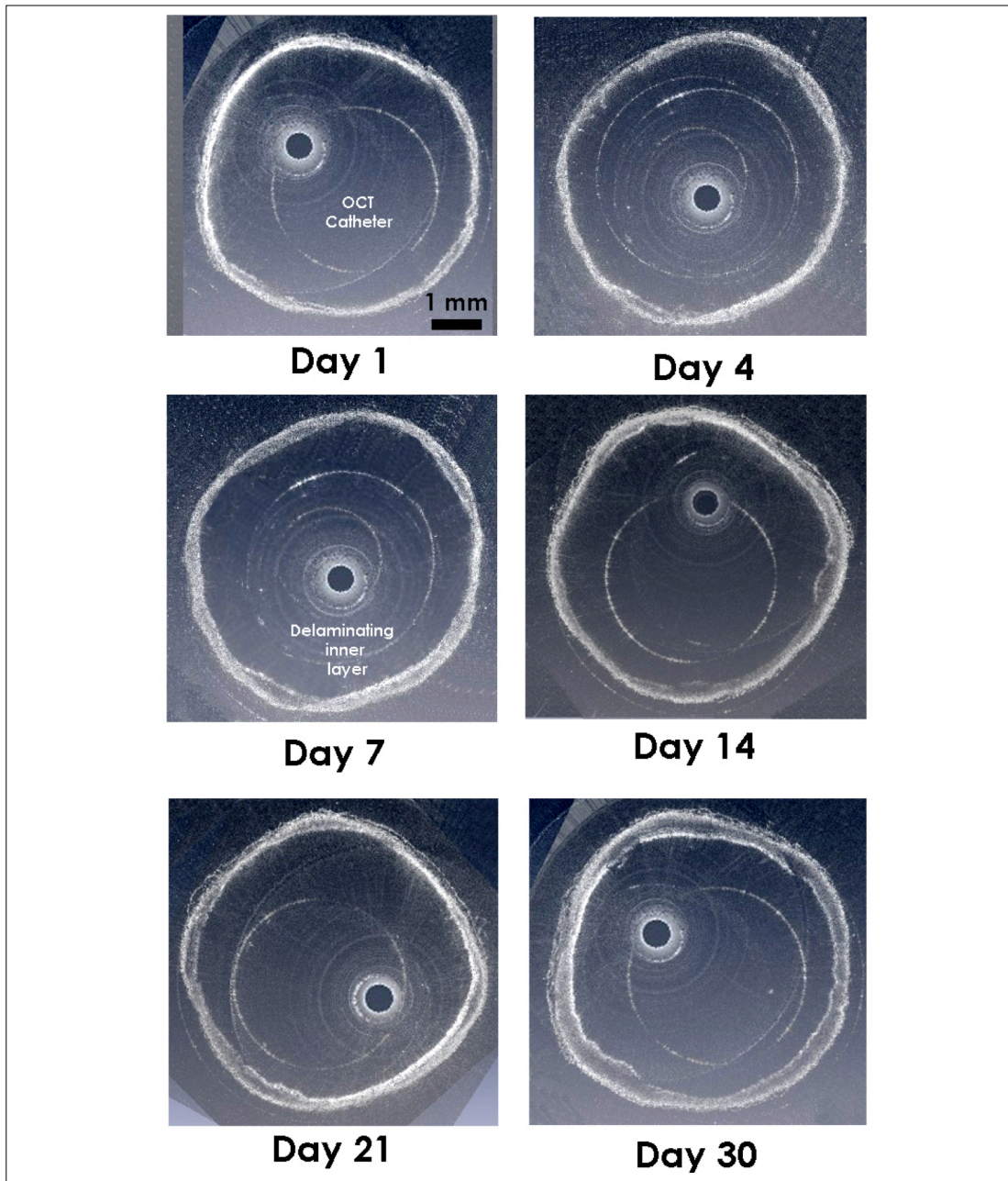


**Figure C.4:** Representative cross-sectional co-registered OCT images of the TEBV at different time-points, using co-registered free-space and catheter-based images. Scale bars = 1 mm

free-space and catheter-based OCT. Figure C.4 shows co-registered cross-sectional images of the blood vessels during scaffold maturation from day 1 through 30. As seen in the image Day 7, some scaffolds experienced delamination of the lumen layer.

#### C.4.2 Scaffold Thickness

Using the co-registered free-space and catheter-based OCT images of the TEBVs, the wall thickness of each vessel was measured at each time point in the study. While the average thickness of the developing TEBVs appears to increase from day 1 ( $430 \pm 15 \mu\text{m}$ ) to day 30 ( $610 \pm 30 \mu\text{m}$ ), as shown in Figure C.5a, it remained relatively constant over the length of a given vessel at each time point (data not shown). The thickness of the non-cellularized scaffold (control scaffold) immersed in media for 30 days, however, did not show a significant change in thickness (Figure C.5b).

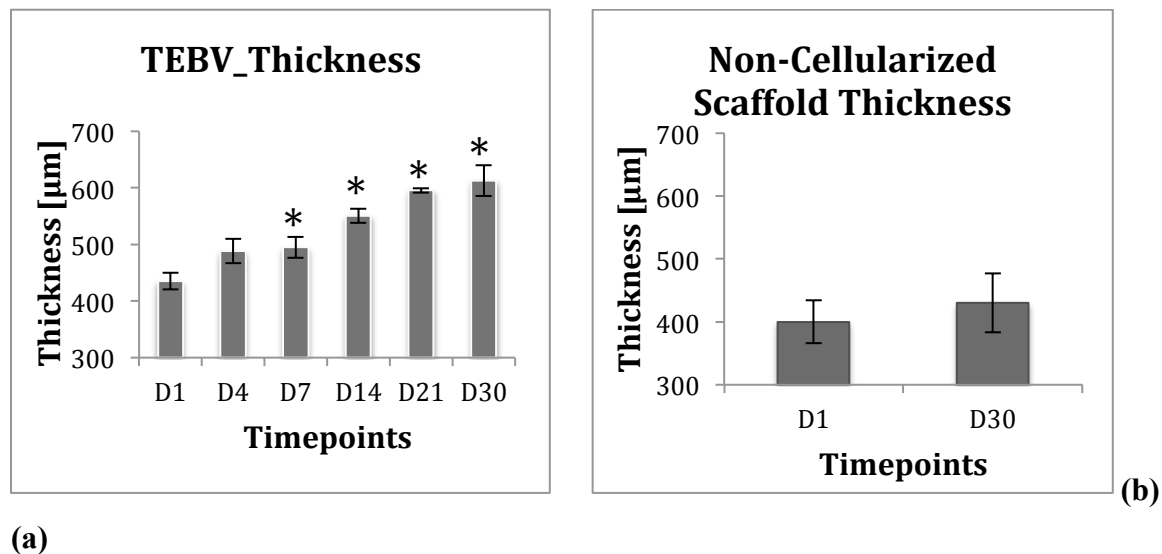
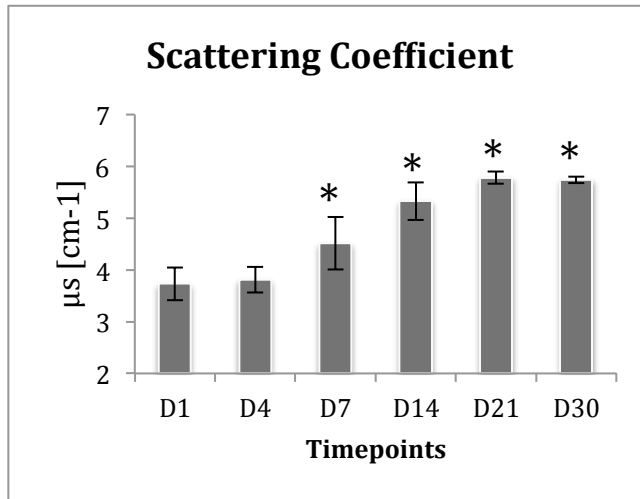


**Fig C.5:** Average wall thickness of the TEBV at different time points. (a) Mean wall thickness of individual cellularized TEBVs ( $n=10$ ) increase over time, whereas (b) mean wall thickness ( $n=3$ ) of non-cellularized/control scaffolds remain constant over time. \* =  $p < 0.05$  when compared with D1.

#### C.4.3 Scaffold Scattering Coefficient

The scattering coefficient of the maturing TEBVs was calculated by non-linear curve fitting of the free-space-based OCT data to the EHF model. The  $\mu_s$  for all three TEBVs

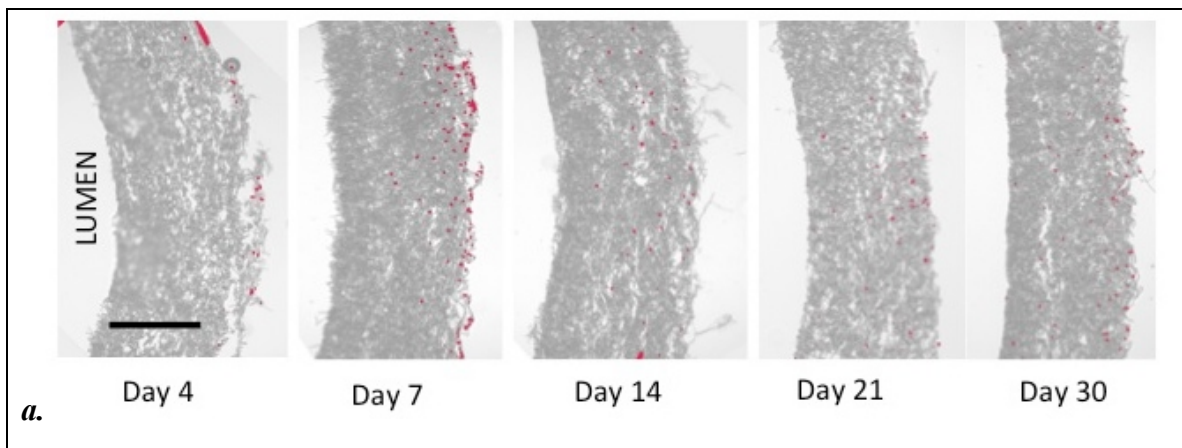
increased over time ( $\mu_s=3.733\pm0.318\text{ cm}^{-1}$  on day 1 to  $\mu_s=5.737\pm0.061\text{ cm}^{-1}$  on day 30), as shown in Figure C.6. Change in  $\mu_s$  between day 21 and day 30 appears to be insignificant. However, in all the TEBVs, the scattering coefficient at any time point remained consistent throughout the length of the vessel (data not shown).



**Figure C.6:** Average scattering coefficient of the TEBVs increases over time, suggesting that the TEBVs become more scattering ( $n=3$ ) in the first three weeks of culture after cell-seeding.  $*=p<0.01$  when compared with D1.

#### C.4.4 Cell migration

Cellular infiltration was assessed by imaging DAPI-stained histological sections of the cellularized control TEBV. These images show gradual migration of the cells toward the lumen of the TEBV over time. While the cells were small in number on day 4 and populated only the outer section of the scaffold thickness, later time point evaluations suggest that the cells have migrated throughout the thickness of the scaffold and appear to have proliferated.



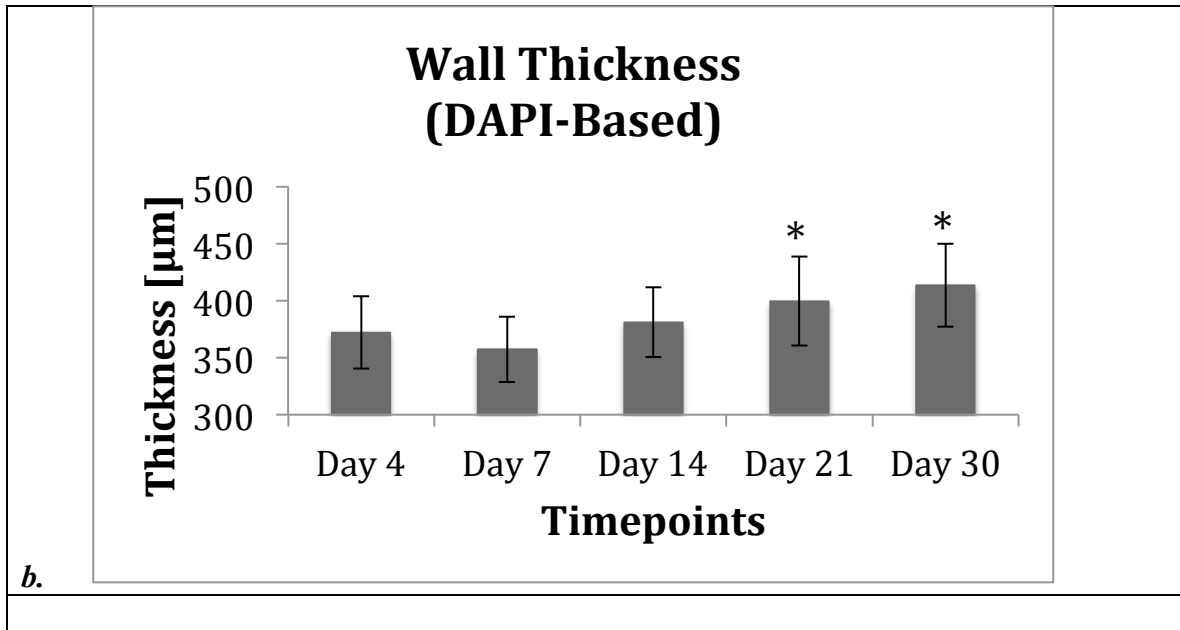


**Figure C.7** (a) DAPI stained histology images of the tissue-engineered blood vessels. Faded background shows the scaffold structure while the red dots indicate the location of cell nuclei. (Scale bar = 250 μm). (b) Plot shows average wall thickness of the control TEBV using the DAPI-stained histology images. \*= $p < 0.01$  when compared with D4.

Wall thickness values of the control TEBV, measured using the DAPI-stained images, show a similar trend of thickness increase as observed in the three TEBVs using OCT.

### C.5 Discussion

Endovascular OCT has found wide clinical applications including high-resolution imaging of vascular pathology as well as systemic response to interventional procedures such as stenting [143]. However, endovascular or free-space OCT cannot independently yield full-thickness images of developing TEBVs because of highly scattering nature of the scaffolding material [145, 150]. Our results, nonetheless, show that dual imaging of bioengineered blood vessels using both luminal (catheter based) and exterior (free space) approach can provide full thickness imaging of the blood vessel.

This study shows, for the first time, a real time and non-destructive evaluation of bioengineered blood vessel development using OCT. Central to the design of our bioreactor was the quartz tube that results in minimal signal attenuation, thereby providing a clear window for monitoring and imaging the bioengineered construct from the outside. The large-bore stainless steel needles and valves permit access to the interior of the vessel for luminal imaging using an

OCT catheter. As demonstrated in this study, the quartz bioreactor can be effectively used for both luminal as well as exterior imaging of the blood vessel.

Quantitative data extracted in this study include scaffold wall thickness and scaffold scattering coefficient during scaffold incubation in the bioreactor over a 30-day period. We observed that the thickness of the TEBVs increased steadily from ( $430\pm 15\mu\text{m}$ ) on day 1 to ( $590\pm 10\mu\text{m}$ ) on day 21. Histological sections of the control TEBV at same time points indicated that the seeded cells proliferated and migrated towards the lumen of the vessel, to occupy the full thickness of the scaffold by day 21. The change in scaffold thickness may be due to cell proliferation and/or cell-mediated scaffold remodeling. Ju *et al* [37] recently showed that when the pore size of PCL-Collagen-based electrospun scaffolds is large enough, the cells could proliferate and infiltrate to the scaffold interior. They observed that when the bilayered scaffolds are seeded with SMCs, the cell migration and proliferation results an overall increase in scaffold thickness over a 28-day period. Proliferation and infiltration of the CH3 10t1/2 cells in our TEBVs over 30 days may have exhibited similar phenomenon where the cells, while spreading throughout the scaffolds, remodeled the scaffold to increase scaffold thickness. Thickness calculated from the histological sections obtained at same time points as those calculated for other TEBVs using OCT imaging demonstrated the same trend in thickness increase; however smaller in magnitude. The discrepancy between thicknesses measured by OCT and histology may have arisen due to scaffold dehydration during scaffold embedding and freezing to obtain sections.

Signals obtained from free-space-based OCT imaging of the TEBVs were used to extract scattering coefficients of the specimens. Similar to the thickness trend, the  $\mu_s$  increased steadily over 21 days. Lack of significant change in  $\mu_s$  of non-cellularized scaffold suggests that the cellularization and scaffold remodeling may be responsible for the changing  $\mu_s$ . Proliferation of cells and their density may impact the optical properties of the TEBV. Previously, Levitz *et al* [151] showed that the scattering coefficient of the developing collagen gels increased with increase in cell density. However, minimal change in  $\mu_s$  between days 21 and 30 in our study appears in contrast with their results. Presence of PCL in the scaffold and synthesis of collagen by the CH3 10t1/2 cells may be the contributing factors to such incremental change. Additionally, as we observed using histology, the cells had colonized the entire thickness of the scaffold by day 21, which may have reduced cell proliferation.

Although OCT offers high-resolution images of the blood vessel structure, it fails to provide information about the cell-cell and cell-scaffold interactions. Monitoring these interactions is also crucial to control the process of tissue-engineering of such vessels. Ability to visualize these dynamic processes may enable us to control more precisely blood vessel development. The use of bioluminescent and fluorescent proteins as reporters, in particular, has enabled powerful and flexible strategies to monitor gene expression, protein interactions, and cellular behavior in real-time. Hofmann *et al* [152] demonstrated the use of Fluorescence molecular tomography (FMT) to monitor cell migration within the scaffold. OCT can be integrated with FMT for simultaneous structural and functional imaging of the development of tissue-engineered blood vessels. Further experiments will be performed to study the utility of OCT in simultaneous imaging with fluorescence.

In summary, we developed a novel bioreactor for OCT imaging of bioengineered blood vessels and demonstrated its utility in monitoring the development of the vessels and quantifying their geometrical and optical properties. Vessel parameters such as the wall thickness as well as the scattering coefficient increased in a time dependent manner suggesting that these parameters could be used as effective markers to study blood vessel development using OCT. This technique is extremely valuable for tissue regeneration since it not only offers the ability to non-destructively assess structural development of the growing tissue-engineered constructs but also provides opportunity for process optimization. Non-destructive imaging of developing vessels will make it possible to eliminate structurally defective vessels such as ones with polymer delamination or layer separation as these vessels may cause mechanical failure upon implantation.

OCT imaging of a TEBV in the novel bioreactor suggest that this method can be effectively used to monitor structural features of the blood vessel within a bioreactor non-destructively. This novel setup of OCT imaging could potentially be utilized to study physiological development and tissue structure of bioengineered blood vessels in real time. Additionally, this bioreactor can be used for OCT imaging and real-time evaluation of various other luminal constructs, such as tracheas, which are being tissue-engineered [153] with minimal modifications.

## **C.6 Acknowledgements**

This study was funded by a grant from the NIH/NHLBI (R01 HL098912). We also acknowledge the support of the American Society for Laser Medicine and Surgery in the form of a travel grant to the ASLMS 2012 conference in Kissimmee, FL.

## References

- [1] Minino AM MS, Xu J, Kochanek KD. . Deaths: Final data for 2008. National Vital Statistics Reports National Center for Health Statistics. 2011;59.
- [2] Aird WC. Phenotypic heterogeneity of the endothelium: I. Structure, function, and mechanisms. *Circ Res*. 2007;100:158-73.
- [3] Crowther MA. Pathogenesis of atherosclerosis. *Hematology / the Education Program of the American Society of Hematology American Society of Hematology Education Program*. 2005:436-41.
- [4] Grech ED. ABC of interventional cardiology: percutaneous coronary intervention. I: history and development. *BMJ*. 2003;326:1080-2.
- [5] Huynh T, Abraham G, Murray J, Brockbank K, Hagen PO, Sullivan S. Remodeling of an acellular collagen graft into a physiologically responsive neovessel. *Nat Biotechnol*. 1999;17:1083-6.
- [6] Betz RR. Limitations of autograft and allograft: new synthetic solutions. *Orthopedics*. 2002;25:s561-70.
- [7] Ricco JB, Marchand C, Neau JP, Marchand E, Cau J, Febrer G. Prosthetic carotid bypass grafts for atherosclerotic lesions: a prospective study of 198 consecutive cases. *European journal of vascular and endovascular surgery : the official journal of the European Society for Vascular Surgery*. 2009;37:272-8.
- [8] Jensen LP, Lepantalo M, Fossdal JE, Roder OC, Jensen BS, Madsen MS, et al. Dacron or PTFE for above-knee femoropopliteal bypass. a multicenter randomised study. *European journal of vascular and endovascular surgery : the official journal of the European Society for Vascular Surgery*. 2007;34:44-9.
- [9] Tomizawa Y. Vascular prostheses for aortocoronary bypass grafting: a review. *Artif Organs*. 1995;19:39-45.
- [10] Griffith LG, Naughton G. Tissue engineering--current challenges and expanding opportunities. *Science*. 2002;295:1009-14.
- [11] Mohiuddin MM. Clinical xenotransplantation of organs: why aren't we there yet? *PLoS Med*. 2007;4:e75.
- [12] Shireman PK, Pearce WH. Endothelial cell function: biologic and physiologic functions in health and disease. *AJR Am J Roentgenol*. 1996;166:7-13.
- [13] Cines DB, Pollak ES, Buck CA, Loscalzo J, Zimmerman GA, McEver RP, et al. Endothelial cells in physiology and in the pathophysiology of vascular disorders. *Blood*. 1998;91:3527-61.
- [14] Seifalian AM, Tiwari A, Hamilton G, Salacinski HJ. Improving the clinical patency of prosthetic vascular and coronary bypass grafts: the role of seeding and tissue engineering. *Artif Organs*. 2002;26:307-20.
- [15] Williamson MR, Black R, Kielty C. PCL-PU composite vascular scaffold production for vascular tissue engineering: attachment, proliferation and bioactivity of human vascular endothelial cells. *Biomaterials*. 2006;27:3608-16.
- [16] L'Heureux N, Dusserre N, Konig G, Victor B, Keire P, Wight TN, et al. Human tissue-engineered blood vessels for adult arterial revascularization. *Nat Med*. 2006;12:361-5.

- [17] Lee SJ, Liu J, Oh SH, Soker S, Atala A, Yoo JJ. Development of a composite vascular scaffolding system that withstands physiological vascular conditions. *Biomaterials*. 2008;29:2891-8.
- [18] Sarkar S, Salacinski HJ, Hamilton G, Seifalian AM. The mechanical properties of infrainguinal vascular bypass grafts: their role in influencing patency. *European journal of vascular and endovascular surgery : the official journal of the European Society for Vascular Surgery*. 2006;31:627-36.
- [19] Davies PF. Flow-mediated endothelial mechanotransduction. *Physiol Rev*. 1995;75:519-60.
- [20] Quint C, Kondo Y, Manson RJ, Lawson JH, Dardik A, Niklason LE. Decellularized tissue-engineered blood vessel as an arterial conduit. *Proceedings of the National Academy of Sciences of the United States of America*. 2011;108:9214-9.
- [21] Malek AM, Alper SL, Izumo S. Hemodynamic shear stress and its role in atherosclerosis. *JAMA : the journal of the American Medical Association*. 1999;282:2035-42.
- [22] Mott RE, Helmke BP. Mapping the dynamics of shear stress-induced structural changes in endothelial cells. *Am J Physiol Cell Physiol*. 2007;293:C1616-26.
- [23] Kakisis JD, Liapis CD, Sumpio BE. Effects of cyclic strain on vascular cells. *Endothelium : journal of endothelial cell research*. 2004;11:17-28.
- [24] Sumpio BE, Widmann MD, Ricotta J, Awolesi MA, Watase M. Increased ambient pressure stimulates proliferation and morphologic changes in cultured endothelial cells. *J Cell Physiol*. 1994;158:133-9.
- [25] Salwen SA, Szarowski DH, Turner JN, Bizios R. Three-dimensional changes of the cytoskeleton of vascular endothelial cells exposed to sustained hydrostatic pressure. *Medical & biological engineering & computing*. 1998;36:520-7.
- [26] Schwartz EA, Bizios R, Medow MS, Gerritsen ME. Exposure of human vascular endothelial cells to sustained hydrostatic pressure stimulates proliferation. Involvement of the  $\alpha$ V integrins. *Circ Res*. 1999;84:315-22.
- [27] Chen GP, Ushida T, Tateishi T. Scaffold design for tissue engineering. *Macromolecular Bioscience*. 2002;2:67-77.
- [28] Deutsch M, Meinhart J, Fischlein T, Preiss P, Zilla P. Clinical autologous in vitro endothelialization of infrainguinal ePTFE grafts in 100 patients: a 9-year experience. *Surgery*. 1999;126:847-55.
- [29] Herring MB. Endothelial cell seeding. *J Vasc Surg*. 1991;13:731-2.
- [30] Badylak SF, Lantz GC, Coffey A, Geddes LA. Small intestinal submucosa as a large diameter vascular graft in the dog. *The Journal of surgical research*. 1989;47:74-80.
- [31] Weinberg CB, Bell E. A blood vessel model constructed from collagen and cultured vascular cells. *Science*. 1986;231:397-400.
- [32] Peter SJ, Miller MJ, Yasko AW, Yaszemski MJ, Mikos AG. Polymer concepts in tissue engineering. *J Biomed Mater Res*. 1998;43:422-7.
- [33] Stitzel J, Liu J, Lee SJ, Komura M, Berry J, Soker S, et al. Controlled fabrication of a biological vascular substitute. *Biomaterials*. 2006;27:1088-94.
- [34] Sill TJ, von Recum HA. Electrospinning: applications in drug delivery and tissue engineering. *Biomaterials*. 2008;29:1989-2006.
- [35] Boland ED, Matthews JA, Pawlowski KJ, Simpson DG, Wnek GE, Bowlin GL. Electrospinning collagen and elastin: preliminary vascular tissue engineering. *Front Biosci*. 2004;9:1422-32.

- [36] Tillman BW, Yazdani SK, Lee SJ, Geary RL, Atala A, Yoo JJ. The in vivo stability of electrospun polycaprolactone-collagen scaffolds in vascular reconstruction. *Biomaterials*. 2009;30:583-8.
- [37] Ju YM, Choi JS, Atala A, Yoo JJ, Lee SJ. Bilayered scaffold for engineering cellularized blood vessels. *Biomaterials*. 2010;31:4313-21.
- [38] Li WJ, Mauck RL, Cooper JA, Yuan X, Tuan RS. Engineering controllable anisotropy in electrospun biodegradable nanofibrous scaffolds for musculoskeletal tissue engineering. *J Biomech*. 2007;40:1686-93.
- [39] Bashur CA, Dahlgren LA, Goldstein AS. Effect of fiber diameter and orientation on fibroblast morphology and proliferation on electrospun poly(D,L-lactic-co-glycolic acid) meshes. *Biomaterials*. 2006;27:5681-8.
- [40] Bashur CA, Shaffer RD, Dahlgren LA, Guelcher SA, Goldstein AS. Effect of fiber diameter and alignment of electrospun polyurethane meshes on mesenchymal progenitor cells. *Tissue engineering Part A*. 2009;15:2435-45.
- [41] Choi JS, Lee SJ, Christ GJ, Atala A, Yoo JJ. The influence of electrospun aligned poly(epsilon-caprolactone)/collagen nanofiber meshes on the formation of self-aligned skeletal muscle myotubes. *Biomaterials*. 2008;29:2899-906.
- [42] Ma Z, Kotaki M, Inai R, Ramakrishna S. Potential of nanofiber matrix as tissue-engineering scaffolds. *Tissue Eng*. 2005;11:101-9.
- [43] Pham QP, Sharma U, Mikos AG. Electrospinning of polymeric nanofibers for tissue engineering applications: a review. *Tissue Eng*. 2006;12:1197-211.
- [44] Schnell E, Klinkhammer K, Balzer S, Brook G, Klee D, Dalton P, et al. Guidance of glial cell migration and axonal growth on electrospun nanofibers of poly-epsilon-caprolactone and a collagen/poly-epsilon-caprolactone blend. *Biomaterials*. 2007;28:3012-25.
- [45] Dunn GA, Heath JP. A new hypothesis of contact guidance in tissue cells. *Experimental cell research*. 1976;101:1-14.
- [46] Xu CY, Inai R, Kotaki M, Ramakrishna S. Aligned biodegradable nanofibrous structure: a potential scaffold for blood vessel engineering. *Biomaterials*. 2004;25:877-86.
- [47] Herring M, Baughman S, Glover J, Kesler K, Jesseph J, Campbell J, et al. Endothelial seeding of Dacron and polytetrafluoroethylene grafts: the cellular events of healing. *Surgery*. 1984;96:745-55.
- [48] Jarrell BE, Williams SK, Stokes G, Hubbard FA, Carabasi RA, Koolpe E, et al. Use of freshly isolated capillary endothelial cells for the immediate establishment of a monolayer on a vascular graft at surgery. *Surgery*. 1986;100:392-9.
- [49] Baitella-Eberle G, Groscurth P, Zilla P, Lachat M, Muller-Glauser W, Schneider J, et al. Long-term results of tissue development and cell differentiation on Dacron prostheses seeded with microvascular cells in dogs. *J Vasc Surg*. 1993;18:1019-28.
- [50] Li S, Henry JJ. Nonthrombogenic approaches to cardiovascular bioengineering. *Annu Rev Biomed Eng*. 2011;13:451-75.
- [51] Naito Y, Shinoka T, Duncan D, Hibino N, Solomon D, Cleary M, et al. Vascular tissue engineering: towards the next generation vascular grafts. *Adv Drug Deliv Rev*. 2011;63:312-23.
- [52] Zilla P, Bezuidenhout D, Human P. Prosthetic vascular grafts: wrong models, wrong questions and no healing. *Biomaterials*. 2007;28:5009-27.
- [53] Li S, Bhatia S, Hu YL, Shiu YT, Li YS, Usami S, et al. Effects of morphological patterning on endothelial cell migration. *Biorheology*. 2001;38:101-8.

- [54] Uttayarat P, Perets A, Li M, Pimton P, Stachelek SJ, Alferiev I, et al. Micropatterning of three-dimensional electrospun polyurethane vascular grafts. *Acta Biomater.* 2010;6:4229-37.
- [55] Pham QP, Sharma U, Mikos AG. Electrospun poly(epsilon-caprolactone) microfiber and multilayer nanofiber/microfiber scaffolds: characterization of scaffolds and measurement of cellular infiltration. *Biomacromolecules.* 2006;7:2796-805.
- [56] Crombez M, Chevallier P, Gaudreault RC, Petitclerc E, Mantovani D, Laroche G. Improving arterial prosthesis neo-endothelialization: application of a proactive VEGF construct onto PTFE surfaces. *Biomaterials.* 2005;26:7402-9.
- [57] Zisch AH, Schenk U, Schense JC, Sakiyama-Elbert SE, Hubbell JA. Covalently conjugated VEGF--fibrin matrices for endothelialization. *Journal of controlled release : official journal of the Controlled Release Society.* 2001;72:101-13.
- [58] Szmitko PE, Fedak PW, Weisel RD, Stewart DJ, Kutryk MJ, Verma S. Endothelial progenitor cells: new hope for a broken heart. *Circulation.* 2003;107:3093-100.
- [59] Rotmans JI, Heyligers JM, Verhagen HJ, Velema E, Nagtegaal MM, de Kleijn DP, et al. In vivo cell seeding with anti-CD34 antibodies successfully accelerates endothelialization but stimulates intimal hyperplasia in porcine arteriovenous expanded polytetrafluoroethylene grafts. *Circulation.* 2005;112:12-8.
- [60] Baguneid M, Murray D, Salacinski HJ, Fuller B, Hamilton G, Walker M, et al. Shear-stress preconditioning and tissue-engineering-based paradigms for generating arterial substitutes. *Biotechnol Appl Biochem.* 2004;39:151-7.
- [61] Dardik A, Liu A, Ballermann BJ. Chronic in vitro shear stress stimulates endothelial cell retention on prosthetic vascular grafts and reduces subsequent in vivo neointimal thickness. *Journal of vascular surgery : official publication, the Society for Vascular Surgery [and] International Society for Cardiovascular Surgery, North American Chapter.* 1999;29:157-67.
- [62] Inoguchi H, Tanaka T, Maehara Y, Matsuda T. The effect of gradually graded shear stress on the morphological integrity of a huvec-seeded compliant small-diameter vascular graft. *Biomaterials.* 2007;28:486-95.
- [63] L'Heureux N, McAllister TN, de la Fuente LM. Tissue-engineered blood vessel for adult arterial revascularization. *N Engl J Med.* 2007;357:1451-3.
- [64] Nieponice A, Soletti L, Guan J, Deasy BM, Huard J, Wagner WR, et al. Development of a tissue-engineered vascular graft combining a biodegradable scaffold, muscle-derived stem cells and a rotational vacuum seeding technique. *Biomaterials.* 2008;29:825-33.
- [65] Niklason LE, Gao J, Abbott WM, Hirschi KK, Houser S, Marini R, et al. Functional arteries grown in vitro. *Science.* 1999;284:489-93.
- [66] Yazdani SK, Tillman BW, Berry JL, Soker S, Geary RL. The fate of an endothelium layer after preconditioning. *Journal of vascular surgery : official publication, the Society for Vascular Surgery [and] International Society for Cardiovascular Surgery, North American Chapter.* 2010;51:174-83.
- [67] Ott MJ, Ballermann BJ. Shear stress-conditioned, endothelial cell-seeded vascular grafts: improved cell adherence in response to in vitro shear stress. *Surgery.* 1995;117:334-9.
- [68] Ahn SJ, Costa J, Emanuel JR. PicoGreen quantitation of DNA: effective evaluation of samples pre- or post-PCR. *Nucleic Acids Res.* 1996;24:2623-5.

- [69] O'Toole SA, Sheppard BL, McGuinness EP, Gleeson NC, Yoneda M, Bonnar J. The MTS assay as an indicator of chemosensitivity/resistance in malignant gynaecological tumours. *Cancer Detect Prev.* 2003;27:47-54.
- [70] Blum JS, Temenoff JS, Park H, Jansen JA, Mikos AG, Barry MA. Development and characterization of enhanced green fluorescent protein and luciferase expressing cell line for non-destructive evaluation of tissue engineering constructs. *Biomaterials.* 2004;25:5809-19.
- [71] Kuhn LT, Liu Y, Advincula M, Wang YH, Maye P, Goldberg AJ. A nondestructive method for evaluating in vitro osteoblast differentiation on biomaterials using osteoblast-specific fluorescence. *Tissue Eng Part C Methods.* 2010;16:1357-66.
- [72] Georgakoudi I, Rice WL, Hronik-Tupaj M, Kaplan DL. Optical spectroscopy and imaging for the noninvasive evaluation of engineered tissues. *Tissue Eng Part B Rev.* 2008;14:321-40.
- [73] Denk W, Strickler JH, Webb WW. Two-photon laser scanning fluorescence microscopy. *Science.* 1990;248:73-6.
- [74] Diaspro A, Bianchini P, Vicidomini G, Faretta M, Ramoino P, Usai C. Multi-photon excitation microscopy. *Biomed Eng Online.* 2006;5:36.
- [75] Bonnema GT, Cardinal KO, McNally JB, Williams SK, Barton JK. Assessment of blood vessel mimics with optical coherence tomography. *Journal of biomedical optics.* 2007;12:024018.
- [76] Chen CW, Betz MW, Fisher JP, Paek A, Chen Y. Macroporous Hydrogel Scaffolds and Their Characterization By Optical Coherence Tomography. *Tissue Eng Part C-Me.* 2011;17:101-12.
- [77] Kricka LJ. Application of bioluminescence and chemiluminescence in biomedical sciences. *Methods Enzymol.* 2000;305:333-45.
- [78] de Boer J, van Blitterswijk C, Lowik C. Bioluminescent imaging: emerging technology for non-invasive imaging of bone tissue engineering. *Biomaterials.* 2006;27:1851-8.
- [79] Vilalta M, Jorgensen C, Degano IR, Chernajovsky Y, Gould D, Noel D, et al. Dual luciferase labelling for non-invasive bioluminescence imaging of mesenchymal stromal cell chondrogenic differentiation in demineralized bone matrix scaffolds. *Biomaterials.* 2009;30:4986-95.
- [80] Kim P, Chung E, Yamashita H, Hung KE, Mizoguchi A, Kucherlapati R, et al. In vivo wide-area cellular imaging by side-view endomicroscopy. *Nature methods.* 2010;7:303-5.
- [81] Cameron A, Davis KB, Green G, Schaff HV. Coronary bypass surgery with internal-thoracic-artery grafts--effects on survival over a 15-year period. *N Engl J Med.* 1996;334:216-9.
- [82] Conte MS. The ideal small arterial substitute: a search for the Holy Grail? *Faseb J.* 1998;12:43-5.
- [83] Grenier G, Remy-Zolghadri M, Guignard R, Bergeron F, Labbe R, Auger FA, et al. Isolation and culture of the three vascular cell types from a small vein biopsy sample. *In Vitro Cell Dev Biol Anim.* 2003;39:131-9.
- [84] Kaushal S, Amiel GE, Guleserian KJ, Shapira OM, Perry T, Sutherland FW, et al. Functional small-diameter neovessels created using endothelial progenitor cells expanded ex vivo. *Nat Med.* 2001;7:1035-40.

- [85] Sieminski AL, Hebbel RP, Gooch KJ. Improved microvascular network in vitro by human blood outgrowth endothelial cells relative to vessel-derived endothelial cells. *Tissue engineering*. 2005;11:1332-45.
- [86] Langille BL, Graham JJ, Kim D, Gotlieb AI. Dynamics of shear-induced redistribution of F-actin in endothelial cells in vivo. *Arterioscler Thromb*. 1991;11:1814-20.
- [87] Flemming RG, Murphy CJ, Abrams GA, Goodman SL, Nealey PF. Effects of synthetic micro- and nano-structured surfaces on cell behavior. *Biomaterials*. 1999;20:573-88.
- [88] Liliensiek SJ, Wood JA, Yong J, Auerbach R, Nealey PF, Murphy CJ. Modulation of human vascular endothelial cell behaviors by nanotopographic cues. *Biomaterials*. 2010;31:5418-26.
- [89] Uttayarat P, Toworfe GK, Dietrich F, Lelkes PI, Composto RJ. Topographic guidance of endothelial cells on silicone surfaces with micro- to nanogrooves: orientation of actin filaments and focal adhesions. *J Biomed Mater Res A*. 2005;75:668-80.
- [90] Heath DE, Lannutti JJ, Cooper SL. Electrospun scaffold topography affects endothelial cell proliferation, metabolic activity, and morphology. *J Biomed Mater Res A*. 2010;94:1195-204.
- [91] Veleva AN, Heath DE, Johnson JK, Nam J, Patterson C, Lannutti JJ, et al. Interactions between endothelial cells and electrospun methacrylic terpolymer fibers for engineered vascular replacements. *J Biomed Mater Res A*. 2009;91:1131-9.
- [92] Jiang XY, Takayama S, Qian XP, Ostuni E, Wu HK, Bowden N, et al. Controlling mammalian cell spreading and cytoskeletal arrangement with conveniently fabricated continuous wavy features on poly(dimethylsiloxane). *Langmuir*. 2002;18:3273-80.
- [93] Kreke MR, Sharp LA, Lee YW, Goldstein AS. Effect of intermittent shear stress on mechanotransductive signaling and osteoblastic differentiation of bone marrow stromal cells. *Tissue Eng Part A*. 2008;14:529-37.
- [94] Silver AE, Vita JA. Shear-stress-mediated arterial remodeling in atherosclerosis: too much of a good thing? *Circulation*. 2006;113:2787-9.
- [95] Lee SJ, Yoo JJ, Lim GJ, Atala A, Stitzel J. In vitro evaluation of electrospun nanofiber scaffolds for vascular graft application. *J Biomed Mater Res A*. 2007;83:999-1008.
- [96] Aird WC. Phenotypic heterogeneity of the endothelium: II. Representative vascular beds. *Circ Res*. 2007;100:174-90.
- [97] Lim SH, Liu XY, Song H, Yarema KJ, Mao HQ. The effect of nanofiber-guided cell alignment on the preferential differentiation of neural stem cells. *Biomaterials*. 2010;31:9031-9.
- [98] Yin Z, Chen X, Chen JL, Shen WL, Hieu Nguyen TM, Gao L, et al. The regulation of tendon stem cell differentiation by the alignment of nanofibers. *Biomaterials*. 2010;31:2163-75.
- [99] Williams C, Wick TM. Perfusion bioreactor for small diameter tissue-engineered arteries. *Tissue engineering*. 2004;10:930-41.
- [100] Humphries JD, Wang P, Streuli C, Geiger B, Humphries MJ, Ballestrem C. Vinculin controls focal adhesion formation by direct interactions with talin and actin. *J Cell Biol*. 2007;179:1043-57.
- [101] Barbee KA, Davies PF, Lal R. Shear stress-induced reorganization of the surface topography of living endothelial cells imaged by atomic force microscopy. *Circ Res*. 1994;74:163-71.

- [102] Mueller RL, Rosengart TK, Isom OW. The history of surgery for ischemic heart disease. *The Annals of thoracic surgery*. 1997;63:869-78.
- [103] MacNeill BD, Pomerantseva I, Lowe HC, Oesterle SN, Vacanti JP. Toward a new blood vessel. *Vasc Med*. 2002;7:241-6.
- [104] L'Heureux N, Paquet S, Labbe R, Germain L, Auger FA. A completely biological tissue-engineered human blood vessel. *FASEB journal : official publication of the Federation of American Societies for Experimental Biology*. 1998;12:47-56.
- [105] Nerem RM, Seliktar D. Vascular tissue engineering. *Annual review of biomedical engineering*. 2001;3:225-43.
- [106] Pankajakshan D, Agrawal DK. Scaffolds in tissue engineering of blood vessels. *Can J Physiol Pharmacol*. 2010;88:855-73.
- [107] Behrendt D, Ganz P. Endothelial function. From vascular biology to clinical applications. *The American journal of cardiology*. 2002;90:40L-8L.
- [108] Heyligers JM, Arts CH, Verhagen HJ, de Groot PG, Moll FL. Improving small-diameter vascular grafts: from the application of an endothelial cell lining to the construction of a tissue-engineered blood vessel. *Annals of vascular surgery*. 2005;19:448-56.
- [109] Lamm P, Juchem G, Milz S, Schuffenhauer M, Reichart B. Autologous endothelialized vein allograft: a solution in the search for small-caliber grafts in coronary artery bypass graft operations. *Circulation*. 2001;104:I108-14.
- [110] Seifalian AM, Tiwari A, Hamilton G, Salacinski HJ. Improving the clinical patency of prosthetic vascular and coronary bypass grafts: the role of seeding and tissue engineering. *Artificial organs*. 2002;26:307-20.
- [111] Thomas AC, Campbell GR, Campbell JH. Advances in vascular tissue engineering. *Cardiovascular pathology : the official journal of the Society for Cardiovascular Pathology*. 2003;12:271-6.
- [112] Quint C, Kondo Y, Manson RJ, Lawson JH, Dardik A, Niklason LE. Decellularized tissue-engineered blood vessel as an arterial conduit. *Proceedings of the National Academy of Sciences of the United States of America*. 2011;108:9214-9.
- [113] Kaushal S, Amiel GE, Guleserian KJ, Shapira OM, Perry T, Sutherland FW, et al. Functional small-diameter neovessels created using endothelial progenitor cells expanded ex vivo. *Nature medicine*. 2001;7:1035-40.
- [114] de Mel A, Jell G, Stevens MM, Seifalian AM. Biofunctionalization of biomaterials for accelerated in situ endothelialization: a review. *Biomacromolecules*. 2008;9:2969-79.
- [115] Stegemann JP, Kaszuba SN, Rowe SL. Review: advances in vascular tissue engineering using protein-based biomaterials. *Tissue engineering*. 2007;13:2601-13.
- [116] Dardik A, Liu A, Ballermann BJ. Chronic in vitro shear stress stimulates endothelial cell retention on prosthetic vascular grafts and reduces subsequent in vivo neointimal thickness. *Journal of vascular surgery : official publication, the Society for Vascular Surgery [and] International Society for Cardiovascular Surgery, North American Chapter*. 1999;29:157-67.
- [117] Williams C, Wick TM. Perfusion bioreactor for small diameter tissue-engineered arteries. *Tissue engineering*. 2004;10:930-41.
- [118] Yazdani SK, Tillman BW, Berry JL, Soker S, Geary RL. The fate of an endothelium layer after preconditioning. *Journal of vascular surgery : official publication, the Society for Vascular Surgery [and] International Society for Cardiovascular Surgery, North American Chapter*. 2010;51:174-83.

- [119] Hofmann MC, Whited BM, Criswell T, Rylander MN, Rylander CG, Soker S, et al. A Fiber-Optic-Based Imaging System for Nondestructive Assessment of Cell-Seeded Tissue-Engineered Scaffolds. *Tissue engineering Part C, Methods*. 2012.
- [120] Hofmann MC, Whited BM, Mitchell J, Vogt WC, Criswell T, Rylander C, et al. Scanning-fiber-based imaging method for tissue engineering. *J Biomed Opt*. 2012;17:066010.
- [121] Durand E, Scoazec A, Lafont A, Boddaert J, Al Hajzen A, Addad F, et al. In vivo induction of endothelial apoptosis leads to vessel thrombosis and endothelial denudation: a clue to the understanding of the mechanisms of thrombotic plaque erosion. *Circulation*. 2004;109:2503-6.
- [122] Frangos JA, Eskin SG, McIntire LV, Ives CL. Flow effects on prostacyclin production by cultured human endothelial cells. *Science*. 1985;227:1477-9.
- [123] Chien S. Mechanotransduction and endothelial cell homeostasis: the wisdom of the cell. *American journal of physiology Heart and circulatory physiology*. 2007;292:H1209-24.
- [124] Estrada R, Giridharan GA, Nguyen MD, Roussel TJ, Shakeri M, Parichehreh V, et al. Endothelial cell culture model for replication of physiological profiles of pressure, flow, stretch, and shear stress in vitro. *Analytical chemistry*. 2011;83:3170-7.
- [125] Wu GD, Jin YS, Salazar R, Dai WD, Barteneva N, Barr ML, et al. Vascular endothelial cell apoptosis induced by anti-donor non-MHC antibodies: A possible injury pathway contributing to chronic allograft rejection. *J Heart Lung Transpl*. 2002;21:1174-87.
- [126] Engbers-Buijtenhuijs P, Buttafoco L, Poot AA, Geelkerken RH, Feijen J, Vermes I. Analysis of the balance between proliferation and apoptosis of cultured vascular smooth muscle cells for tissue-engineering applications. *Tissue engineering*. 2005;11:1631-9.
- [127] Bran GM, Stern-Straeter J, Hormann K, Riedel F, Goessler UR. Apoptosis in bone for tissue engineering. *Archives of medical research*. 2008;39:467-82.
- [128] Coyle CH, Mendralla S, Lanasa S, Kader KN. Endothelial cell seeding onto various biomaterials causes superoxide-induced cell death. *Journal of biomaterials applications*. 2007;22:55-69.
- [129] Kader KN, Yoder CA. Endothelial cell death on biomaterials: Theoretical and practical aspects of investigation. *Mat Sci Eng C-Bio S*. 2008;28:387-91.
- [130] Heath DE, Lannutti JJ, Cooper SL. Electrospun scaffold topography affects endothelial cell proliferation, metabolic activity, and morphology. *J Biomed Mater Res A*. 2010;94A:1195-204.
- [131] Bondar B, Fuchs S, Motta A, Migliaresi C, Kirkpatrick CJ. Functionality of endothelial cells on silk fibroin nets: Comparative study of micro- and nanometric fibre size. *Biomaterials*. 2008;29:561-72.
- [132] Ntziachristos V. Going deeper than microscopy: the optical imaging frontier in biology. *Nature methods*. 2010;7:603-14.
- [133] Zhu Y, Wang A, Patel S, Kurpinski K, Diao E, Bao X, et al. Engineering Bi-layer Nanofibrous Conduits for Peripheral Nerve Regeneration. *Tissue Eng Part C Methods*. 2011.
- [134] Li D, Wang YL, Xia YN. Electrospinning nanofibers as uniaxially aligned arrays and layer-by-layer stacked films. *Adv Mater*. 2004;16:361-6.
- [135] Schmidt D, Asmis LM, Odermatt B, Kelm J, Breyman C, Gossi M, et al. Engineered living blood vessels: functional endothelia generated from human umbilical cord-derived progenitors. *The Annals of thoracic surgery*. 2006;82:1465-71; discussion 71.

- [136] Lin MZ, McKeown MR, Ng HL, Aguilera TA, Shaner NC, Campbell RE, et al. Autofluorescent proteins with excitation in the optical window for intravital imaging in mammals. *Chemistry & biology*. 2009;16:1169-79.
- [137] O'Callaghan CJ, Williams B. Mechanical strain-induced extracellular matrix production by human vascular smooth muscle cells: role of TGF-beta(1). *Hypertension*. 2000;36:319-24.
- [138] Ueno H, Nakamura F, Murakami M, Okumura M, Kadosawa T, Fujinag T. Evaluation effects of chitosan for the extracellular matrix production by fibroblasts and the growth factors production by macrophages. *Biomaterials*. 2001;22:2125-30.
- [139] Gareau DS, Bargo PR, Horton WA, Jacques SL. Confocal fluorescence spectroscopy of subcutaneous cartilage expressing green fluorescent protein versus cutaneous collagen autofluorescence. *Journal of biomedical optics*. 2004;9:254-8.
- [140] Patnaik JL, Byers T, DiGuseppi C, Dabelea D, Denberg TD. Cardiovascular disease competes with breast cancer as the leading cause of death for older females diagnosed with breast cancer: a retrospective cohort study. *Breast Cancer Res*. 2011;13:R64.
- [141] Sybrandy JE, Wittens CH. Initial experiences in endovenous treatment of saphenous vein reflux. *Journal of vascular surgery : official publication, the Society for Vascular Surgery [and] International Society for Cardiovascular Surgery, North American Chapter*. 2002;36:1207-12.
- [142] Peck M, Gebhart D, Dusserre N, McAllister TN, L'Heureux N. The evolution of vascular tissue engineering and current state of the art. *Cells, tissues, organs*. 2012;195:144-58.
- [143] Karanasos A, Ligthart J, Witberg K, van Soest G, Bruining N, Regar E. Optical Coherence Tomography: Potential Clinical Applications. *Current cardiovascular imaging reports*. 2012;5:206-20.
- [144] Jaguszewski M, Landmesser U. Optical Coherence Tomography Imaging: Novel Insights into the Vascular Response After Coronary Stent Implantation. *Current cardiovascular imaging reports*. 2012;5:231-8.
- [145] Bonnema GT, Cardinal KO, McNally JB, Williams SK, Barton JK. Assessment of blood vessel mimics with optical coherence tomography. *J Biomed Opt*. 2007;12:024018.
- [146] Gurjarpadhye AA, Vogt WC, Liu Y, Rylander CG. Effect of Localized Mechanical Indentation on Skin Water Content Evaluated Using OCT. *International journal of biomedical imaging*. 2011;2011:817250.
- [147] Thrane L, Yura HT, Andersen PE. Analysis of optical coherence tomography systems based on the extended Huygens-Fresnel principle. *J Opt Soc Am A*. 2000;17:484-90.
- [148] Lutomirski RF, Yura HT. Propagation of a finite optical beam in an inhomogeneous medium. *Applied optics*. 1971;10:1652-8.
- [149] Whited BM, Whitney JR, Hofmann MC, Xu Y, Rylander MN. Pre-osteoblast infiltration and differentiation in highly porous apatite-coated PLLA electrospun scaffolds. *Biomaterials*. 2011;32:2294-304.
- [150] J. K. Barton DBDP, S. K. Williams, B. Ford, and M. R. Descour. Imaging vascular implants with optical coherence tomography. *Proceedings of SPIE*. 2000;3915:8.
- [151] Levitz D, Hinds MT, Choudhury N, Tran NT, Hanson SR, Jacques SL. Quantitative characterization of developing collagen gels using optical coherence tomography. *J Biomed Opt*. 2010;15:026019.
- [152] Hofmann MC, Whited BM, Criswell T, Rylander MN, Rylander CG, Soker S, et al. A fiber-optic-based imaging system for nondestructive assessment of cell-seeded tissue-engineered scaffolds. *Tissue Eng Part C Methods*. 2012;18:677-87.

[153] Jungebluth P, Moll G, Baiguera S, Macchiarini P. Tissue-engineered airway: a regenerative solution. *Clinical pharmacology and therapeutics*. 2012;91:81-93.